Spring 2022

Measurement of Correlations Between Neutral Pions and Charged Hadrons with Respect to the Event Plane in Heavy Ion Collisions with ALICE

Michael Henry Oliver
Yale University Graduate School of Arts and Sciences, michael.oliver.137@gmail.com

Abstract

Measurement of Correlations Between Neutral Pions and Charged Hadrons with Respect to the Event Plane in Heavy Ion Collisions with ALICE

Michael Henry Oliver
2022

In Ultra-Relativistic Heavy Ion collisions, such as those done at the Large Hadron Collider (LHC) and Relativistic Heavy Ion Collider (RHIC), the high energy densities create an exotic state of matter not seen since the first few microseconds past the Big Bang, a Quark Gluon Plasma (QGP) where quarks and gluons are not confined into hadronic bound states.

The properties and evolution of this matter can be studied using a naturally existing probe: the hard QCD (Quantum Chromo-Dynamics) jets that are produced in partonic hard scatters at the beginning of the collisions. Similarly to the x-rays in medical Computed Tomography, the escaping jets reflect the transverse structure of the medium. However, this analogy breaks down in two key ways. The QGP, unlike the human body, is rapidly evolving on the same timescale of the jet's passing through of the medium. Additionally, the interaction of the jet with the QGP is not fully understood and may modify the structure of jets beyond a simple attenuation. The field of studying these jet-medium interactions, called jet tomography, is advanced by the research in this thesis using correlations high momentum π^0 mesons and hadrons arising from the same jet-producing hard scatter process. The focus in this study is on experimentally varying the path-length traversed by the involved jets by examining the correlations with respect to the reaction plane of the colliding ions. This is done using Pb–Pb collisions measured by ALICE detector at the LHC at $\sqrt{s_{\mathrm{NN}}} = 5.02\ \mathrm{TeV}$.

Measurement of Correlations Between Neutral Pions and Charged Hadrons with Respect to the Event Plane in Heavy Ion Collisions with ALICE

A Dissertation
Presented to the Faculty of the Graduate School
of
Yale University
in Candidacy for the Degree of
Doctor of Philosophy

by
Michael Henry Oliver

Dissertation Director: John W Harris

May 2022

Elwood: It’s 106 miles to Chicago, we got a full tank of gas, half a pack of cigarettes, it’s dark... and we’re wearing sunglasses.

Jake: Hit it.

Contents

1 Introduction **1**

1.1 Standard Model . . . 1
1.2 Quantum Chromodynamics . . . 2
1.2.1 Jets . . . 3
1.3 Quark-Gluon Plasma . . . 5
1.3.1 Theory . . . 5
1.3.2 Evidence for the QGP . . . 5
1.4 Jet-Medium Interactions . . . 12
1.4.1 Coherence Effects . . . 12
1.4.2 Observation of Jet Quenching . . . 13
1.4.3 Role of Fluctuations . . . 14
1.5 Previous Measurements . . . 15
1.5.1 Jet-Hadron Correlations . . . 15
1.5.2 ALICE π^0-Hadron Correlations . . . 16
1.5.3 STAR and PHENIX π^0 and $\gamma-$Hadron Correlations . . . 18
1.5.4 CMS Jet-Track Correlations . . . 19
1.5.5 ALICE Jet-Hadron Correlations . . . 19
1.5.6 ATLAS Jet Flow . . . 20

2 Experiment: ALICE at the LHC **22**

2.1 Large Hadron Collider . . . 22
2.2 Coordinates and Variables . . . 24
2.2.1 Coordinates . . . 24
2.2.2 Centrality . . . 25
2.2.3 Event Plane . . . 26
2.3 A Large Ion Collider Experiment . . . 26
2.3.1 Central Barrel Tracking . . . 27
2.3.2 Calorimetry . . . 29
2.3.3 Forward Detectors . . . 30

2.4 Trigger . . . 33
2.4.1 Minimum Bias . . . 33
2.4.2 EMCal Trigger . . . 33

3 π^0-Hadron Correlations 35
3.1 Event Selection . . . 37
3.1.1 Data Sample . . . 37
3.1.2 Centrality Selection . . . 38
3.1.3 Event Trigger . . . 39
3.2 Clusters and Tracks . . . 40
3.2.1 Track Selection . . . 40
3.2.2 Clusterization . . . 42
3.2.3 Cluster S‘election . . . 46
3.3 Track Cluster Correction . . . 49
3.3.1 Cluster Veto . . . 49
3.3.2 Hadronic Correction . . . 50
3.4 π^0 Identification . . . 57
3.4.1 Cluster Cuts . . . 57
3.4.2 Cluster Pair Cuts . . . 58
3.4.3 Invariant Mass . . . 61
3.4.4 Cut Optimization . . . 66
3.4.5 Final Invariant Mass Distributions and Cuts . . . 67
3.4.6 Final π^0-Candidate Distributions . . . 69
3.4.7 π^0 Purity Determination . . . 71
3.5 Correlations . . . 75
3.6 Mixed-Event Correction . . . 76
3.6.1 Constructing Mixed-Events . . . 77
3.6.2 Two-Stage Event Mixing . . . 77
3.6.3 Normalization of Mixed-Events Correlations . . . 79
3.7 Projections in $\Delta\eta, \Delta\phi$ . . . 81
3.7.1 Mixed-Event Correction Skew . . . 82
3.8 π^0 Impurity Correction . . . 85
3.8.1 Tools for Validation in ALICE Monte Carlo . . . 86
3.8.2 Sideband Selection . . . 87
3.8.3 First Test . . . 87
3.8.4 Sideband Theory: Why the First Test Failed . . . 89
3.8.5 Extrapolation . . . 93
3.9 Flow Subtraction . . . 94
3.9.1 Reaction Plane Fit . . . 95
3.9.2 Event Plane Resolution . . . 96

3.9.3 Reaction Plane Fit Parameters . . . 97
3.9.4 Results of Flow Subtraction . . . 101
3.10 Systematic Uncertainties . . . 104
3.10.1 Pseudorapidity Cut Uncertainty . . . 104
3.10.2 Mixed Event Correction Uncertainty . . . 105
3.10.3 π^0 Purity . . . 106
3.10.4 Impurity Correction . . . 107
3.10.5 Tracking Efficiency . . . 107
3.10.6 Flow Subtraction Uncertainty . . . 112
3.10.7 $\Delta\phi$ Integration Window. . . . 115
3.10.8 Summary of Systematic Uncertainties . . . 116
3.11 Results . . . 120
3.11.1 Observable Definitions . . . 120
3.11.2 Gamma Triggered Results . . . 121
3.11.3 Comparison to Theory . . . 123

4 Jet Energy Loss Models **126**
4.1 JEWEL . . . 126
4.1.1 JEWEL Configuration . . . 127
4.2 JEWEL Parameters . . . 130
4.2.1 Monte Carlo Configuration . . . 130
4.2.2 Longitudinal Asymmetry Bug . . . 131
4.2.3 Validation of Configuration . . . 132
4.3 Monte Carlo Analysis with JEWEL . . . 133
4.3.1 MC Event Generator Analysis . . . 133
4.3.2 Flow Toy Model . . . 137
4.4 Surface Bias in JEWEL . . . 139
4.5 JEWEL Predictions . . . 144
4.5.1 Jet-Hadron Correlations at 2.76 TeV . . . 144
4.5.2 Jet-Hadron Correlations at 5.02 TeV . . . 148
4.5.3 π^0-Hadron Correlations at 5.02 TeV . . . 148
4.5.4 Direct γ-Hadron Correlations . . . 150
4.6 Discussion and Analysis . . . 155
4.7 Jet-Medium Interactions in JEWEL . . . 155
4.7.1 Energy Loss . . . 155
4.7.2 Scattering Centers . . . 156
4.7.3 Event Plane Dependence . . . 157
4.7.4 Centrality Dependence . . . 157
4.7.5 System Dependence . . . 158
4.8 Concluding Notes . . . 161

5 Results and Discussion **162**
5.1 Future Possibilities . . . 165
5.1.1 Flow in Events With High p_{T} Triggers . . . 165
5.1.2 New Data and Reconstruction . . . 165
5.1.3 Additional Model Comparison . . . 165
5.1.4 Correlations with Direct Photons . . . 166

A Software **168**
A.1 Alice Collaboration Software . . . 168
A.2 π^0 Analysis Specific Software . . . 168
A.3 Monte Carlo Generator Analysis Software . . . 168

B Configurations **169**
B.1 EMCal Corrections Framework . . . 169

C Fit Function Implementations in ROOT **171**

D π^0-identification plots **179**

E π^0-hadron Plots **182**
E.1 Raw Correlations . . . 182

F π^0 Impurity Correction Plots **190**

G Flow Correction Plots **193**
G.1 Observables . . . 201
G.1.1 Systematic uncertainties by source . . . 201
G.1.2 Yield Results by Event Plane . . . 202
G.1.3 Yield Results by Event Plane with Model Comparisons . . . 202
G.1.4 Sigma Widths by Event Plane . . . 204

H EMCal Trigger Simulation **206**

Appendix **208**

Bibliography **208**

List of Figures

1.1 The Standard Model of Particle Physics. Figure credit: Wikimedia 2
1.2 Running of the QCD coupling as a function of energy scale [1] 4
1.3 Early and modern phase diagrams of QCD, mapped in terms of the temperature T and the baryon density (ρ_B) or baryon chemical potential (μ_B). 6
1.4 The temperature dependence of the pressure, energy density, and entropy in QCD, as determined by lattice QCD calculations by [2]. 6
1.5 Nuclear suppression factor R_{AA} for a variety of particles as measured by PHENIX at $\sqrt{s_{\mathrm{NN}}} = 200$ GeV (left) [3] and as measured by CMS at $\sqrt{s_{\mathrm{NN}}} = 5.02$ TeV (right) [4]. 7
1.6 Jet R_{AA} as measured by the ALICE, ATLAS, and CMS experiments at the LHC [5]. 7
1.7 Diagrams describing the geometric and hydrodynamic source of elliptical flow in a heavy-ion collision. Diagrams from [5]. 8
1.8 Variation in flow parameters in Au–Au collisions at $\sqrt{s_{\mathrm{NN}}} = 200$ GeV as measured by STAR and PHENIX, with comparison to results from relativistic hydrodynamic models [6]. 9
1.9 Flow of mesons (full markers) and baryons (empty markers) measured by PHENIX in Au–Au collisions at $\sqrt{s_{\mathrm{NN}}} = 200$ GeV, presented as functions of p_{T} and KE_T [7]. 10
1.10 Measurement by ALICE of strange particles in Pb–Pb, p–Pb, and pp collisions [8]. 11
1.11 Quarkonia suppression in heavy-ion collisions vs their binding energy [4]. 11
1.12 Energy loss mechanisms cartoon 12
1.13 STAR Dihadron Correlation measurement for Au–Au collisions published in 2003[9]. 13
1.14 Diagram of dijets traversing a medium from different starting points, and a resulting asymmetry in the dijet momenta, as represented by vectors. . . 14

1.15 Dijet asymmetry as measured by CMS and as modelled by the JEWEL model. On the left, good agreement is found between the CMS Pb–Pb measurement and the JEWEL predictions. On the right, the asymmetry distribution is shown for JEWEL's standard mode (in which jet sources are realistically distributed within the medium) and a central production, wherein all jets come from the exact center of the event. The two distributions are largely indistinguishable [10]. 15
1.16 Azimuthal correlations of jets and charged hadrons in Au–Au and pp collisions as measured by the STAR experiment [11]. 16
1.17 Yield differences in Au–Au and pp collisions in STAR's jet-hadron correlations measurement. At high associated p_{T}, significant suppression in Au–Au collisions is observed, while yields are enhanced at low p_{T}[11]. . 17
1.18 Yield ratios for π^0-hadron correlations measured in pp and Pb–Pb collisions at $\sqrt{s_{\mathrm{NN}}} = 2.76\ \mathrm{TeV}$, with comparisons to the AMPT and JEWEL models, and an NLO pQCD model [12]. 17
1.19 PHENIX results on γ-hadron correlations in Au–Au collisions. On the left, the ratio of the per-trigger yield for γ-hadron collisions between Au–Au and pp and the ratio between d-Au and pp collisions are shown. The d-Au collisions show no sign of modification, while the Au–Au collisions do. On the right, the yield modification is presented for different trigger momenta. 18
1.20 Yields of particles associated with jets in Pb–Pb and pp collisions recorded by CMS [13]. On the top row, correlations between jets and hadrons in Pb–Pb and pp collisions. From left to right, the panels shift from peripheral to central events. The difference in per-trigger yields between Pb–Pb and pp collisions is shown in the lower row. 19
1.21 Ratio of hadron yield correlated with jets measured in-plane vs out-of-plane by ALICE in Pb–Pb collisions at $\sqrt{s_{\mathrm{NN}}} = 2.76\ \mathrm{TeV}$ [14]. The ratios for the nearside are shown on the left, and away-side, where more significant dependence is expected, is shown on the right. 20
1.22 Azimuthal anisotropies of jets in Pb–Pb collisions by the ATLAS experiment. The raw distribution of jets with respect to the 2nd order event plane is shown at left, while v_2 and v_3 measurements at different p_{T} are shown at right, with comparison with the LIDO model implementing collisional and radiative losses [15]. 21

2.1 Diagram of the Large Hadron Collider with the four main LHC experiments. Not drawn to scale (figure from [16]). 23
2.2 Schematic of the ALICE experimental site at LHC Interaction Point 2 [17]. 24

2.3 Cartoon of the geometry of a heavy ion collision. Participant and spectator nucleons are labelled in purple and orange, respectively. 25
2.4 Diagram of the ALICE experiment, with labels for each subdetector. . . . 27
2.5 The Inner Tracking System is shown as the green detector layers around the beam pipe. 28
2.6 Schematics of the TPC. An overview is shown on the left, while a schematic of the readout chambers at the endplates are shown on the right. Electric fields propagate freed electrons from charged particles to the readout wire chambers at the end plates. 28
2.7 A schematic of the larger section of the EMCal. 10 full supermodules and 2 $1/3$-supermodules are included. 30
2.8 Diagram of the DCal positioned opposite the EMCal within the central barrel [18]. 31
2.9 Diagram of the VZERO detector and its location within the central barrel. 31
2.10 Time-of-flight for signals in the V0-A and V0-C, plotted separately in the top plot and correlated in the lower plot. The correlations between the signals allows discrimination between proton-gas collisions and proton-proton collisions by the V0 detectors [19]. 32

3.1 Diagram expressing the blueprint of this analysis. Jets oriented out-of-plane are expected to lose more energy than jets orientated in-plane. . . . 35
3.2 Flow chart of the major steps of this analysis. 36
3.3 VZERO amplitude distribution, divided into centrality ranges. Overlaid is the result from a Glauber MC simulation [20]. 38
3.4 EMCal trigger rejection factor (RF) for the γ trigger. 39
3.5 Centrality distributions in Minimum Bias and EMCal Gamma-triggered events, as well as the centrality distributions when 10 GeV cluster requirement is applied. 40
3.6 Tracking efficiency in η and in φ of the reconstructed track for central (left) and peripheral (right) event collisions 41
3.7 Projected tracking efficiencies for central (left), peripheral (right). 42
3.8 Projected tracking efficiencies for central (left), peripheral (right) collisions. First row is the standard efficiency model used for the correction obtained with tracks of $p_{\mathrm{T}} > 0.15\,\mathrm{GeV}/c$. The second row shows a model obtained with higher momentum tracks $p_{\mathrm{T}} > 1\,\mathrm{GeV}/c$and the third row shows a model that only has a p_{T} dependence but no η dependence. The left and right columns show the 0-10% central and 50-80% most central, respectively. 44

3.9 Cell level display of ALICE EMCal clusterization. Each collection of cells would be combined as a single cluster by the V1 algorithm, while the partitions by the V2 or V1+unfolding are outlined with red and blue lines. Figures from [21] 45
3.10 Left: cluster time vs. p_{T} of events with an EGA trigger, right: time distribution for three intervals of cluster momenta. 47
3.11 Fraction of clusters in the vicinity of a bad channel (panel 1), a SM edge (panel 2), and neither one of the two (panel 3). The fraction is given for all clusters and γ candidates. 48
3.12 Track cluster matching, MB, (30-50% Centrality). On the left are the correlations in $\Delta\eta$ and on the right are the correlations in $\Delta\phi$. The top plots show the raw distributions, the bottom plots show the distributions after the other cut ($\Delta\eta$ or $\Delta\phi$) has been applied. 50
3.13 $5 \leq p_T < 7$ GeV/c cluster pairs in MB 10-30% Central events. 51
3.14 Comparison of mass peak position with the different MIP energies. 52
3.15 Comparison of mass peak widths with the different MIP energies. 53
3.16 Comparison of mass peak position with the different MIP energies in EMCal Gamma triggered events. 54
3.17 Comparison of mass peak widths with the different MIP energies in EMCal Gamma triggered events. 55
3.18 π^0 candidates vs the event plane for different track-cluster corrections (MB, 30-50% central on left, EGA 30-50% central on right). Fits including v_2 and v_4 terms are overlayed. 56
3.19 Testing three different ranges for the asymmetry cut in MB data, 30-50% central events. 58
3.20 Testing three different ranges for the asymmetry cut in EGA data, 30-50% central events. 59
3.21 Invariant mass distribution with different minimum opening angle cuts, in MB 30-50% centrality events. 60
3.22 Ratio of the invariant mass distribution with different minimum opening angle cuts to the distribution without an opening angle, in EGA-triggered 30-50% centrality events, for 2 p_{T} bins. 60
3.23 Example mass spectra for 0-10% central minimum bias events, in different p_{T} bins. 61
3.24 Comparison of different fit peak functions, fitting the MC True π^0 signal. Centrality 30-50% in MC production 16h2. The cuts used here are $0.1 < \sigma^2_{\mathrm{long}} < 0.5$, and $\theta > 0.017$. 63

3.25 Invariant mass distribution fitting with Mixed-Events for 0-10% central events in MC production 16h2. The mixed-event background is shown in gray on the left plot, where it is normalized to a high mass region near 0.8 GeV/c^2. On the right, the invariant mass distribution is analyzed using the available MC information. 65
3.26 Breakdown of position swapped background method for 0-10% events in 16h2, a production with minimum bias HIJING + Pythia jets. The position swapped distribution (black squares) is close in shape to the true background (red squares), but differs at low invariant mass. The difference can be attributed to the preserved correlations of π^0 and η decay photons, in cyan and orange, respectively. 66
3.27 χ^2/NDF for different combination of σ^2_{long} (labelled λ^2_0 in the plots) and θ_c cut paramters in MB, 0-10% central events. Red squares indicate bins where the χ^2/NDF id below an arbitrary threshold of 1.75 67
3.28 χ^2/NDF for different combination of σ^2_{long} (labelled λ^2_0 in the plots) and θ_c cut paramters in MB, 10-30%, 30-50%, 50-80% central events. 68
3.29 Peak significance (yield / $\sqrt{\text{background}}$) for different combination of σ^2_{long} (labelled λ^2_0 in the plots) and θ_c cut paramters in MB, 0-10% central events. 68
3.30 Peak significance (yield / $\sqrt{\text{background}}$) for different combination of σ^2_{long} (labelled λ^2_0 in the plots) and θ_c cut paramters in MB, 10-30%, 30-50%, 50-80% central events. 68
3.31 Invariant Mass for the p_{T} ranges 5-7,7-9, and 9-11 GeV/c for the Pb–Pb 15o minimum bias, 30-50% central data set. 70
3.32 Invariant Mass for the p_{T} ranges 11-14,14-17 GeV/c for the Pb–Pb 15o EGA triggered event, Central 30-50% data set. 70
3.33 Distribution of accepted π^0-candidates in MB events (30-50% central events). 71
3.34 Distribution of accepted π^0-candidates in EGA-triggered events (30-50% central events). 71
3.35 Residuals of fits with the different ranges for the $5 \leq p_T < 7$ GeV/c (left) and the ratio of the reconstructed purity to the true purity (right). 73
3.36 Residuals of fits with the different ranges for the $11 \leq p_T < 14$ GeV/c (left), χ^2/NDF for the fit ranges (middle), and the ratio of the reconstructed purity to the true purity (right). 73
3.37 π^0 purity vs p_{T} for different event-plane angles, in EGA-triggered, 30-50% central events. Error bars are the quadratic sum of the statistical and systematic uncertainties. 75
3.38 A raw correlation function for Same Event pairs corresponding to events with primary vertex $0 \leq z < 2$ cm and π^0_{Cand} triggers between 11 and 14 GeV/c. 76
3.39 Single-stage event mixing method schematic. 78

3.40 Two-stage event mixing method schematic. 79
3.41 mixed-event π^0-hadron correlations for EGA-triggerd 30-50% central events with $11 \leq p_{\mathrm{T}}^{\mathrm{trigger}} < 14$ GeV/c and $0.2 < p_{\mathrm{T}}^{\mathrm{assoc}} < 0.4$ GeV/c. Each plot is a different z-vertex range. 80
3.42 mixed-event π^0-hadron correlations for EGA-triggerd 30-50% central events with $11 \leq p_{\mathrm{T}}^{\mathrm{trigger}} < 14$ GeV/c. Starting from the top left, each plot is a bin of the associated hadron p_{T}. 81
3.43 Raw π^0-hadron correlations projected onto the $\Delta\eta$ axis for 2.5-4 GeV/c associated particles. The nearside $\Delta\phi$ region is plotted in black points, and the awayside region is scaled to match the nearside region using the $0.6 < |\Delta\eta| < 1.2$ region. These are from EGA Triggered events, 30-50% centrality range, 11-14 GeV/c $p_{\mathrm{T}}^{\mathrm{trig}}$. 82
3.44 Raw π^0-hadron correlations projected onto the $\Delta\eta$ axis with the scaled awayside correlations subtracted from the nearside for 2.5-4 GeV/c. These are from EGA Triggered events, 30-50% centrality range, 11-14 GeV/c $p_{\mathrm{T}}^{\mathrm{trig}}$s. A fit using the sum of two gaussians is performed. 83
3.45 Projected correlations onto the $\Delta\eta$ axis. From left to right and top to bottom, the p_{T} range of the associated particles is changed. 83
3.46 Correlations projected onto the $\Delta\eta$ axis for 30-50% EGA-triggered events, 11-14 GeV/c $p_{\mathrm{T}}^{\mathrm{trig}}$, 0.4-0.8 GeV/$c$ hadrons. The event-plane dependent skew in $\Delta\eta$ is significant at low p_T^a, and is the analysis' limiting factor in reaching lower p_T^a 84
3.47 Pseudo-data plots shaded to display the definition of the near $\Delta\eta$ and far $\Delta\eta$ regions (shown on the left) the nearside far $\Delta\eta$ region and awayside region (right). 84
3.48 Projected π^0_{Cand}-hadron correlations, projected on to $\Delta\varphi$ for π^0_{Cand} in the 11-14 GeV/c p_{T} range. The near $\Delta\eta$ regions are in black full markers, while the far $\Delta\eta$ region is show in empty violet markers. 85
3.49 Cartoon of general sideband method. 85
3.50 π^0-Candidate peak and 3 sidebands for $5 \leq p_T < 7$ GeV/c, 10-30% central MB event. 88
3.51 Sidebands used in the first test of the sideband subtraction, with simulated events in MC production LHC16h2, 0-10% central events. 88
3.52 Comparison of sideband-subtracted correlations in MC with the MC true π^0-hadron correlations. This is using the closest two sidebands to the π^0 peak, without any extrapolation applied. These correlations for triggers in the p_{T} range 5-7 GeV/c. 89
3.53 Correlation with the event plane of π^0-candidates and sideband triggers, from the $5-7$ GeV/c, 30-50% central MB events. 90

3.54 Invariant mass distribution for cluster pairs in the LHC16h2 MC production in the 5-7 (upper left) and 11-14 (upper right) GeV/cwindows. The background is broken up into the correlated background (cluster pairs that share a common ancestor) and the uncorrelated background (cluster pairs with no common ancestor). The relative fractions of the correlated and uncorrelated fractions are shown in the lower plots. 91
3.55 Comparison of sideband-subtracted correlations in MC with the MC true π^0-hadron correlations. This is using extrapolation function 4, with all three sidebands. These correlations for triggers in the p_{T} range 11-14 GeV/c. 94
3.56 Diagram of in-plane, mid-plane, and out-of-plane regions used in this analysis, alongside the mathematical description. Figure from the ALICE jet-hadron analysis [14] 96
3.57 Fits of tracks to v_2 (left) and v_3 (right) in EGA-triggered 30-50% central events. 98
3.58 Comparison of flow parameters for charged calculated directly in this analysis between MB and EGA-triggered events, for 30-50% central events. . 99
3.59 Comparison (for 11-14 GeV/c, 30-50% central EGA-triggered events) of parameter v_2^a from the RPF method with no fixed parameters, from fitting the tracks vs the event plane in the same events, and the ALICE published data with a cumulant method in MB events. 99
3.60 Comparison (for 11-14 GeV/c, 30-50% central EGA-triggered events) of parameter v_2^t from the RPF method with no fixed parameters and from fitting the π^0 vs the event plane (after applying a sideband subtraction) in the same events. 100
3.61 Comparison (for 11-14 GeV/c, 30-50% central EGA-triggered events) of parameter $v_3^t v_3^a$ from the RPF method and from fitting the tracks vs the event plane in the same events. 101
3.62 Comparison (for 11-14 GeV/c, 30-50% central EGA-triggered events) of parameter v_4^a from the RPF method, from fitting the tracks vs the event plane in the same events, and the ALICE published data with a cumulant method in MB events. 101
3.63 Comparison (for 11-14 GeV/c, 30-50% central EGA-triggered events) of parameter v_4^t from the RPF method and from fitting the tracks vs the event plane in the same events. 102

3.64 Plots of the reaction plane fit process. In the top row, the π^0-hadron correlations in the near-$\Delta\eta$ (signal dominated) and far-$\Delta\eta$ (background dominated) regions are plotted for triggers in-plane, mid-plane, and out-of-plane and finally all triggers. In the second row, the far-$\Delta\eta$ region is plotted along with individual components of the RPF. In the third row, the residuals of the far $\Delta\eta$ region vs the RPF. The darkened points in the nearside region are those used for the fit. In the final row, the subtracted near-$\Delta\eta$ correlations are shown, with any over-subtraction highlighted. . 103
3.65 Awayside yield out/in event plane ratio with different $\Delta\eta$ cut options are shown on the left. On the right, variance in the points on the right are used to calculate the systematic uncertainty thhat is shown on the right. 105
3.66 Ratio of different mixed event correlation correction options to the default value. Four $p_{\mathrm{T}}^{\mathrm{assoc}}$ bins are shown. The data is for raw π^0-hadron correlations in the $11 - 14\ \mathrm{GeV}/c$ bin, 30-50% central EGA-triggered events. . . 106
3.67 Final results with varying of the purity value used in the sideband subtraction by $\pm$ the uncertainty in the purity. 107
3.68 Tracking efficiency in different centrality bins. 109
3.69 Example plots of the efficiency vs ρ_M. 109
3.70 Slopes ($d\epsilon/d\rho_M$) of the efficiency vs particle density plots. 110
3.71 Flow values as found by ALICE [22]. 111
3.72 Reaction Plane Fit of 30-50% Central, EGA-Triggered events, 11-14 GeV/c π^0s using reactionPlaneFit python implementation by [23] 113
3.73 Covariance matrix sampling for the RPF with 11-14 GeV/c π^0s, 1.5-2.5 GeV/c associated particles. The diagonal plots show the 1-D distribution of each parameter, while the off-diagonal plots show the correlations between parameters. 113
3.74 Variations of the $v_3^t v_3^a$ parameter in EGA-triggered 30-50% central events. The parameters used for each fit are labeled in green and blue, while the calculated $v_3^t v_3^a$ values are shown in purple. 114
3.75 Effect of the $v_3^t v_3^a$ variation on the out/in awayside yield ratio. 114
3.76 Variation of the choice of how many low assoc. p_{T} bins are used to fit the $v_{2,t}$ and $v_{4,t}$ parameters via the RPF. The fixing is not implemented in RPF Method 2, leaving the $v_{2,t}$ and $v_{4,t}$ parameters free. 115
3.77 Effect of the FixV2 variation on the out/in awayside yield ratio. 115
3.78 Out/In yield ratios with different integration windows for fitting. 116
3.79 Out/In σ ratios with different integration windows for fitting. 117
3.80 Systematic uncertainty in the nearside out/in yield ratio by contribution. . 117
3.81 Systematic uncertainty in the awayside out/in yield ratio by contribution. . 118
3.82 Systematic uncertainty in out/in width (sigma) ratio by contribution. . . . 118
3.83 Systematic uncertainties by source for away-side yields (inclusive). 119

3.84 Systematic uncertainties by source for near-side yields (inclusive). 119
3.85 Near-side yields (all-angles) for π^0 range 11-14 GeV/c in 30-50% central EGA-trigger events. 121
3.86 Away-side yields (all-angles) for π^0 range 11-14 GeV/c in 30-50% central EGA-trigger events. 122
3.87 Near-side widths with σ parameter (all-angles) for π^0 range 11-14 GeV/c in 30-50% central EGA-trigger events. 122
3.88 Away-side widths with σ parameter (all-angles) for π^0 range 11-14 GeV/c in 30-50% central EGA-trigger events.. 123
3.89 Near-side (left) and away-side (right) Yield Ratios 30-50%, EGA-triggered events. 123
3.90 Nearside yields (all angles) with JEWEL model comparisons. 124
3.91 Awayside yields (all angles) with JEWEL model comparisons. 124
3.92 Near-side (left) and away-side (right) Yield Ratios 30-50%, EGA-triggered events. 125

4.1 JEWEL temperature distribution at $t = 0.95$ fm/c in Pb–Pb event at $\sqrt{s_{\mathrm{NN}}} = 5.02\,\mathrm{TeV}$, in units of GeV (left) and hard-scatter vertex distribution (right), for an event in the 5% centrality percentile. The x and y axes are the positions within the x-y plane in units of fm. 127
4.2 Temperature distribution in the $y = 0$ plane of an event in units of fm vs time in the longitudinally expanding medium model used by JEWEL, for a Pb–Pb event at $\sqrt{s_{\mathrm{NN}}} = 5.02\,\mathrm{TeV}$ in the 5% centrality percentile. The z-axis gives the temperature in GeV. 128
4.3 Estimation of inelastic nuclear cross section σ_{NN} at 5.02 TeV, using proton-proton cross section plot from [1]. 129
4.4 Hard scatter angular correlation in $(\Delta\eta, \Delta\phi)$ with different triggers in JEWEL's proton-proton mode. Left: R=0.2 full (tracks + clusters) jets , right: π^0s. 129
4.5 Hard scatter angular correlation in $(\Delta\eta, \Delta\phi)$ with different triggers in Pb–Pb, 30-50% Central events, JEWEL without recoils. Left: R=0.2 full (tracks + clusters) jets, middle: π^0s, right: direct photons. 130
4.6 Hard scatter p_{T} correlation with different triggers in Pb–Pb, 30-50% Central events, JEWEL without recoils. The correlations are normalized per column (p_T^{parton}). Left: R=0.2 full (tracks + clusters) jets, middle: π^0s, right: direct photons. 130
4.7 Distribution of final state particles in η and φ in JEWEL with recoils enabled. On the left is the distribution before the longitudinal bug fix, where a significant skew is present. On the right is the distribution after the fix has been applied, and no apparent bias or skew is observable. 132

4.8 Validation of JEWEL configuration by comparing jet R_{AA} to independently produced JEWEL predictions. 132
4.9 $\Delta\eta$ correlations in π^0-hadron correlations with and without recoils, for π^0s in the $11-14\ \mathrm{GeV}/c$ range, associated hadrons in the $2.5-4\ \mathrm{GeV}/c$ range in 30-50% central events. 135
4.10 $\Delta\varphi$ correlations in different $\Delta\eta$ regions with JEWEL (with recoils) 30-50% cent. events. No pedestal correction is applied here. 135
4.11 $\Delta\varphi$ correlations in different $\Delta\eta$ regions with JEWEL (with recoils) 30-50% cent. events. The pedestal correction is applied here. 136
4.12 Measured Track transverse momentum spectra for Minimum Bias Events. 138
4.13 Cartoon diagrams of geometric bias in dijet and gamma-jet events. 139
4.14 Normalized vertex radius distribution under different requirements in Pb–Pb JEWEL w/o recoils in the 0-10% centrality range. 140
4.15 Difference in p_{T} between leading jet and matched hard scatter parton, correlated with the radius R of the hard scatter in Pb–Pb 0-10% central events in JEWEL w/o recoils. A profile is overlaid with the uncertainty in the mean as the error bars. 141
4.16 Diagram of rotated jet vertex coordinates. 141
4.17 Hard-scatter vertex distribution for PbPb ($\sqrt{s_{\mathrm{NN}}} = 5.02\ \mathrm{TeV}$) 0-10% JEWEL w/o recoils in the rotated jet vertex coordinates with projections onto the x_{jet} and y_{jet} axes. The surface bias parameter S is calculated from the x_{jet} projection. 142
4.18 Hard-scatter vertex distribution for Au–Au ($\sqrt{s_{\mathrm{NN}}} = 200\ \mathrm{GeV}$) 0-10% JEWEL w/o recoils in the rotated jet vertex coordinates with projections onto the x_{jet} and y_{jet} axes. The surface bias parameter S is calculated from the x_{jet} projection. 143
4.19 Comparison of the R = 0.2 jet cross sections in pp collisions at RHIC and LHC energies calculated with PYTHIA 6 (left) and a diagram explaining how the hardness of the jet p_{T} spectrum affects the number of jets that can start inside the medium and lose energy to arrive at the same $p_{\mathrm{T}}^{\mathrm{final}}$ of a jet starting at the surface. 143
4.20 Jet Response matrix for R=0.2 anti-k_{T} jets in the 2.76 TeV jet-hadron correlations analysis, for jets at all angles relative to the event plane. 145
4.21 Comparison of fit functions used for 2-3 GeV/c associated hadrons and 20-40 GeV/c jets, in JEWEL w/o recoils, 30-50% centrality. 146
4.22 JEWEL w/o recoils model predictions for awayside yield out/in ratio in jet-hadron correlations for Pb–Pb at $\sqrt{s_{\mathrm{NN}}} = 2.76\ \mathrm{TeV}$ in 30-50% centrality events. 147

4.23 JEWEL with recoils model predictions for awayside yield out/in ratio in jet-hadron correlations for Pb–Pb at $\sqrt{s_{\rm NN}} = 2.76$ TeV in 30-50% centrality events. 147
4.24 JEWEL model (w/o recoils on the left, with recoils on the right) predictions for awayside yield out/in ratio in jet-hadron correlations for Pb–Pb at $\sqrt{s_{\rm NN}} = 5.02$ TeV in 30-50% centrality events. 148
4.25 JEWEL model (w/o recoils on the left, with recoils on the right) predictions for awayside yield out/in ratio in jet-hadron correlations for Pb–Pb at $\sqrt{s_{\rm NN}} = 5.02$ TeV in 0-10% centrality events. 149
4.26 Nearside (left) and awayside (right) out/in yield ratios for π^0-hadron correlations in Pb–Pb at $\sqrt{s_{\rm NN}} = 5.02$ TeV, 30-50% central events, JEWEL without recoils. 149
4.27 Nearside (left) and awayside (right) out/in width (sigma) ratios, JEWEL without recoils. 150
4.28 Nearside (left) and awayside (right) out/in yield ratios for π^0-hadron correlations in Pb–Pb at $\sqrt{s_{\rm NN}} = 5.02$ TeV, 30-50% central events, JEWEL with recoils. 150
4.29 Nearside (left) and awayside (right) out/in width (sigma) for π^0-hadron correlations in Pb–Pb at $\sqrt{s_{\rm NN}} = 5.02$ TeV, 30-50% central events, JEWEL with recoils. 151
4.30 Feynmann diagrams for the hard scattering processes included in JEWEL's boson-jet hard scatter processes, sourced from [24]. 151
4.31 Direct γ-hadron correlations in JEWEL PbPb collisions w/o recoils at $\sqrt{s_{\rm NN}} = 5.02$ TeV, 30-50% central, with trigger direct photons in $11 < p_T < 14 \mathrm{GeV}/c$. 152
4.32 Awayside peak for π^0-hadron (left) and direct γ-hadron (right) correlations in PbPb correlations simulated with JEWEL w/o recoils, 30-50% centrality with trigger particles in the range $11 < p_T < 14$ GeV/c. 152
4.33 Awayside Out/In yield ratio for direct γ-hadron correlations in Pb–Pb JEWEL events w/o recoils at $\sqrt{s_{\rm NN}} = 5.02$ TeV in 30-50% centrality, $11 \leq p_{\rm T}^{\gamma} < 14$ GeV/c. 153
4.34 Awayside Out/In yield ratio for direct γ-hadron correlations in Pb–Pb JEWEL events without recoils (left) and with recoils (right) at $\sqrt{s_{\rm NN}} = 5.02$ TeV in 30-50% centrality, $40 \leq p_{\rm T}^{\gamma} < 50$ GeV/c. 153
4.35 D_{AA} in jet-hadron measurements by STAR ([11]) and D_{RP}. 154
4.36 D_{RP} in direct γ-hadron correlations in Pb–Pb at $\sqrt{s_{\rm NN}} = 5.02$ TeV for 30-50% central events in JEWEL without recoils. 154
4.37 Momentum difference between reconstructed jets ($20 < p_{\rm T} < 40$ GeV/c) and the matched hard scatter parton, in Pb–Pb events $\sqrt{s_{\rm NN}} = 5.02$ TeV in JEWEL w/o recoils in 30-50% centrality. 156

4.38 Number of scattering centers in different event plane angles encountered by jets tagged by direct photons in the p_{T} range 20-40 GeV/c in JEWEL Pb–Pb events at $\sqrt{s_{\mathrm{NN}}} = 5.02$ TeV in the 30-50% centrality range. . . . 157
4.39 Average number of scattering centers direct photon-tagged jets interact with in Pb–Pb events at $\sqrt{s_{\mathrm{NN}}} = 5.02$ TeV in different centrality ranges. 158
4.40 Ratio of the number of scattering centers sampled by jets in JEWEL out-of-plane relative to in-plane 159
4.41 Out/In ratios for the average number of scattering centers with which jets interact in JEWEL in different centrality bins, with a comparison between the Pb–Pb collisions at $\sqrt{s_{\mathrm{NN}}} = 5.02$ TeV and Au–Au collisions at $\sqrt{s_{\mathrm{NN}}} = 200$ GeV. 160

5.1 Near-side (left) and away-side (right) yield ratios in 30-50% centrality, EGA-triggered events. 162
5.2 Out/In yield ratios in three experimental measurements. 163
5.3 Distribution of hard-scatter parton p_{T} producing π^0 triggers in the p_{T} range 11-14 GeV/c in pp collisions at $\sqrt{s} = 5.02$ TeV, produced with JEWEL's vacuum mode (equivalent to PYTHIA6). The distributions are divided by parton configuration. The first entry (q or g) indicates the type of parton that produced the π^0 (with no distinction between quarks and anti-quarks). 164
5.4 Out/in yield ratio I_{RP} and p_{T}-weighted yield difference D_{RP} for direct γ-hadron correlations with 40-50 GeV/c γ triggers in JEWEL with recoils in 30-50% central events. 166

D.1 Invariant Mass for the PbPb 15o Minimum Bias, Central 0-10% data set. . 179
D.2 Invariant Mass for the PbPb 15o Minimum Bias, Central 10-30% data set. 179
D.3 Invariant Mass for the p_{T} ranges 5-7,7-9, and 9-11 GeV/c for the PbPb 15o Minimum Bias, Central 30-50% data set. 180
D.4 Invariant Mass for the PbPb 15o Minimum Bias, Central 50-80% data set. 180
D.5 Invariant Mass for the PbPb 15o EGA triggered event, Central 0-10% data set. 180
D.6 Invariant Mass for the PbPb 15o EGA triggered event, Central 10-30% data set. 181
D.7 Invariant Mass for the p_{T} ranges 11-14,14-17 GeV/c for the PbPb 15o EGA triggered event, Central 30-50% data set. 181
D.8 Invariant Mass for the PbPb 15o EGA triggered event, Central 50-80% data set. 181

E.1 Raw π^0-hadron correlations for trigger range 11-14 GeV/c, all-Angles, 0-10% Cent., EGA-trigger 183

E.2 Raw π^0-hadron correlations for trigger range 11-14 GeV/c, in-plane, 0-10% Cent., EGA-trigger 183
E.3 Raw π^0-hadron correlations for trigger range 11-14 GeV/c, mid-plane, 0-10% Cent., EGA-trigger 184
E.4 Raw π^0-hadron correlations for trigger range 11-14 GeV/c, out-of-plane, 0-10% Cent., EGA-trigger 184
E.5 Raw π^0-hadron correlations for trigger range 11-14 GeV/c, all-angles, 10-30% Cent., EGA-trigger 185
E.6 Raw π^0-hadron correlations for trigger range 11-14 GeV/c, in-plane, 10-30% Cent., EGA-trigger 185
E.7 Raw π^0-hadron correlations for trigger range 11-14 GeV/c, mid-plane, 10-30% Cent., EGA-trigger 186
E.8 Raw π^0-hadron correlations for trigger range 11-14 GeV/c, out-of-plane, 10-30% Cent., EGA-trigger 186
E.9 Raw π^0-hadron correlations for trigger range 11-14 GeV/c, all-angles, 30-50% Cent., EGA-trigger 187
E.10 Raw π^0-hadron correlations for trigger range 11-14 GeV/c, all-angles, 50-90% Cent., EGA-trigger 187
E.11 Raw π^0-hadron correlations for trigger range 11-14 GeV/c, in-plane, 50-90% Cent., EGA-trigger 188
E.12 Raw π^0-hadron correlations for trigger range 11-14 GeV/c, mid-plane, 50-90% Cent., EGA-trigger 188
E.13 Raw π^0-hadron correlations for trigger range 11-14 GeV/c, out-of-plane, 50-90% Cent., EGA-trigger 189

F.1 Sideband subtraction in $\Delta\varphi$ with for π^0 in the p_{T} range 11-14 GeV/c. 30-50% centrality EGA-triggered events. From left to right and top to bottom, the plots increase in associated hadron p_{T}. 190
F.2 Sideband subtraction in $\Delta\eta$ with for π^0 in the p_{T} range 11-14 GeV/c. 30-50% centrality EGA-triggered events. From left to right and top to bottom, the plots increase in associated hadron p_{T}. 191
F.3 Comparison of sideband-subtracted correlations in MC with the MC true π^0-hadron correlations. This is using extrapolation function 4, with all three sidebands. These correlations for triggers in the p_{T} range 11-14 GeV/c. 192

G.1 χ^2/NDF for the Reaction Plane fit for π^0 triggers in the $11-14\mathrm{GeV}/cp_{\mathrm{T}}$ range, 30-50% centralEGA-triggered events. 193
G.2 $v_1^t v_1^a$ for the Reaction Plane fit for π^0 triggers in the $11-14\mathrm{GeV}/cp_{\mathrm{T}}$ range, 30-50% centralEGA-triggered events. 194

G.3 v_2^a for the Reaction Plane fit for π^0 triggers in the $11-14\mathrm{GeV}/cp_\mathrm{T}$ range, 30-50% centralEGA-triggered events. 194
G.4 v_2^a for the Reaction Plane fit for π^0 triggers in the $11-14\mathrm{GeV}/cp_\mathrm{T}$ range, 30-50% centralEGA-triggered events. 195
G.5 $v_3^t v_3^a$ for the Reaction Plane fit for π^0 triggers in the $11-14\mathrm{GeV}/cp_\mathrm{T}$ range, 30-50% centralEGA-triggered events. 195
G.6 v_2^a for the Reaction Plane fit for π^0 triggers in the $11-14\mathrm{GeV}/cp_\mathrm{T}$ range, 30-50% centralEGA-triggered events. 196
G.7 v_2^a for the Reaction Plane fit for π^0 triggers in the $11-14\mathrm{GeV}/cp_\mathrm{T}$ range, 30-50% centralEGA-triggered events. 196
G.8 11-14 GeV/c π^0, 0.2-0.4 GeV/c $p_\mathrm{T}^\mathrm{assoc}$,30-50% central, EGA-triggered events 197
G.9 11-14 GeV/c π^0, 0.4-0.8 GeV/c $p_\mathrm{T}^\mathrm{assoc}$, 30-50% central, EGA-triggered events 197
G.10 11-14 GeV/c π^0, 0.8-1.5 GeV/c $p_\mathrm{T}^\mathrm{assoc}$, 30-50% central, EGA-triggered events 198
G.11 11-14 GeV/c π^0, 1.5-2.5 GeV/c $p_\mathrm{T}^\mathrm{assoc}$, 30-50% central, EGA-triggered events 198
G.12 11-14 GeV/c π^0, 2.5-4 GeV/c $p_\mathrm{T}^\mathrm{assoc}$, 30-50% central, EGA-triggered events 199
G.13 11-14 GeV/c π^0, 4-7 GeV/c $p_\mathrm{T}^\mathrm{assoc}$, 30-50% central, EGA-triggered events 199
G.14 11-14 GeV/c π^0, 7-11 GeV/c $p_\mathrm{T}^\mathrm{assoc}$,30-50% central, EGA-triggered events 200
G.15 11-14 GeV/c π^0, 11-17 GeV/c $p_\mathrm{T}^\mathrm{assoc}$, 30-50% central, EGA-triggered events 200
G.16 Systematic uncertainties by source for near-side in-plane yields. 201
G.17 Systematic uncertainties by source for near-side mid-plane yields. 201
G.18 Systematic uncertainties by source for near-side out-of-plane yields. . . . 202
G.19 Systematic uncertainties by source for away-side in-plane yields. 202
G.20 Systematic uncertainties by source for away-side mid-plane yields. 203
G.21 Systematic uncertainties by source for away-side out-of-plane yields. . . . 203
G.22 Nearside yields in each event plane bin. 203
G.23 Awayside yields in each event plane bin. 204
G.24 Nearside yields with JEWEL model comparison. 204
G.25 Awayside yields in-plane, mid-plane, and out-of-plane with JEWEL comparison. 204
G.26 Near-side RMS widths in each event plane bin. 204
G.27 Awayside RMS widths in each event plane bin. 205

H.1 Neutral jet turn-on curve for the EMCal Jet Patch trigger, with data drawn as markers and the results of the trigger simulation. Three different jet resolution parameters are used. 207

List of Tables

3.1 Parameters obtained by fitting the efficiency distributions as a function of p_{T} (p_0-p_9) and η (p_{10}-p_{21}) for different centralities. For the η distributions there are two values reported. One for the η efficiency for tracks with p_{T} ($0.15 - 30$ GeV/c) and in brackets for tracks with p_{T} ($1 - 30$ GeV/c). . . 43
3.2 Parameters for the EMCal clusterization in this analysis. 46
3.3 Cluster cuts in the GetAcceptCluster() function. 47
3.4 Cluster cuts in the AccClusterForAna() function 47
3.5 Peak fit functions implemented in the code (phase1/fitAlgos.cc). Each peak function also has an overall normalization parameter giving the yield of the peak (not written in this table). Named functions represent the implementation in ROOT's TMath. G represents a Gaussians normalized to unity. The Crystal Ball variables are defined in eq. 3.11 62
3.6 Event pool bins for the 2-cluster event mixing. 64
3.7 Background fit functions implemented in the code (phase1/fitAlgos.cc). Each peak function also has an overall normalization parameter (not written in this table). $\mathrm{Poly}_n(x)$ is implemented as $\sum_{j=0}^{n} \frac{a_j}{j!} x^j$. Other named functions represent the implementation in ROOT's TMath. 66
3.8 Final cuts for the π^0 candidates 69
3.9 Invariant mass central values and cuts for the Pb–Pb 15o minimum bias data set. 69
3.10 Invariant mass central values and widths for the Pb–Pb 15o EGA triggered data set. 69
3.11 Final set of background fit functions used to evaluate the uncertainty in the purity. 72
3.12 Table of fit ranges investigated. 73
3.13 π^0 purity values with statistical and systematic uncertainties for the EGA-triggered data. 74
3.14 π^0 purity values with statistical and systematic uncertainties for the EGA-triggered data. 74

3.15 Bin information for $\Delta\eta$, $\Delta\varphi$. 75
3.16 Centrality bins for this analysis. 75
3.17 Associated hadron p_{T} bins. 76
3.18 Settings for the mixed-event pool. 77
3.19 Settings for the mixed-event pool with event plane angle mixing. 77
3.20 Monte Carlo Modes for Correlations 87
3.21 Sideband extrapolation functions. Functions are defined such that the parameter A is the value for $x = m_{peak}$, which is fixed to the location of the π^0 peak found in this analysis. Subsets are the list of masks determining which sidebands are included (e.g. 101 denotes sidebands 1 and 3) 92
3.22 Mixed Event correction parameter variations tested. 105
3.23 Average $dN/d\eta$ and ρ_M per centrality bin, as produced in the LHC16g1 MC production, and as measured by ALICE in $\sqrt{s_{\mathrm{NN}}}$=5.02 TeV PbPb collisions[25]. MC uncertainties are only statistical, while the data uncertainties included systematic uncertainties. 108

4.1 JEWEL Parameters. 131
4.2 JEWEL Medium Parameters. 131
4.3 JEWEL Production Statistics 131
4.4 Dijet fit functions tried for event generator analysis. 137
4.5 Details of individual fit functions for the σ width parametrization. The modified gaussian formula is described in [26]. The exact implementations of the fits are given in Appendix C. 137
4.6 Toy Model Particle Distribution. Landau(x, μ, c) is the unnormalized Landau distribution available in ROOT's TMath Library. 138
4.7 Toy Model Parameters 138
4.8 Table of parameters for the v_n used in the toy model. 139
4.9 Settings and bins for the JEWEL jet-hadron correlations analysis. 144

Chapter 1

Introduction

1.1 Standard Model

As of this writing, 4.9% of this universe is understood by human scientists through the formulation known as the Standard Model of particle physics. This theory describes the known elementary particles (organized in Figure 1.1) and their interactions in terms of gauge theory with a small number of groups:

$$SU(3) \times SU(2)_L \times U(1) \tag{1.1}$$

The $SU(3)$ group corresponds to the strong interaction, representing rotations in the space of the three color charges of Quantum Chromodynamics (QCD), while $SU(2)_L \times U(1)$ represent the electroweak interaction. The latter is spontaneously broken into the weak and electromagnetic interactions via the Higgs mechanism, resulting in the three massive W^+, W^-, and Z bosons and the massless photon. This Higgs mechanism also gives mass to elementary fermions, and is popularly (outside of the physics community) thought to give mass to most of the known matter in the universe. However, of course, most mass in baryonic matter comes from the strong nuclear interaction, as evidenced by the fact that the valence quarks in protons and neutrons account for less than 2% of their mass. The remaining mass derives from the rich interactions of gluon and quark fields confined within strongly interacting bound particles, known as hadrons. This thesis studies those interactions using high energy quarks and gluons as probes of a form of nuclear matter in which quarks and gluons are unconfined, known as the quark-gluon plasma.

The remaining 95.1% of the universe is not of interest to this thesis.

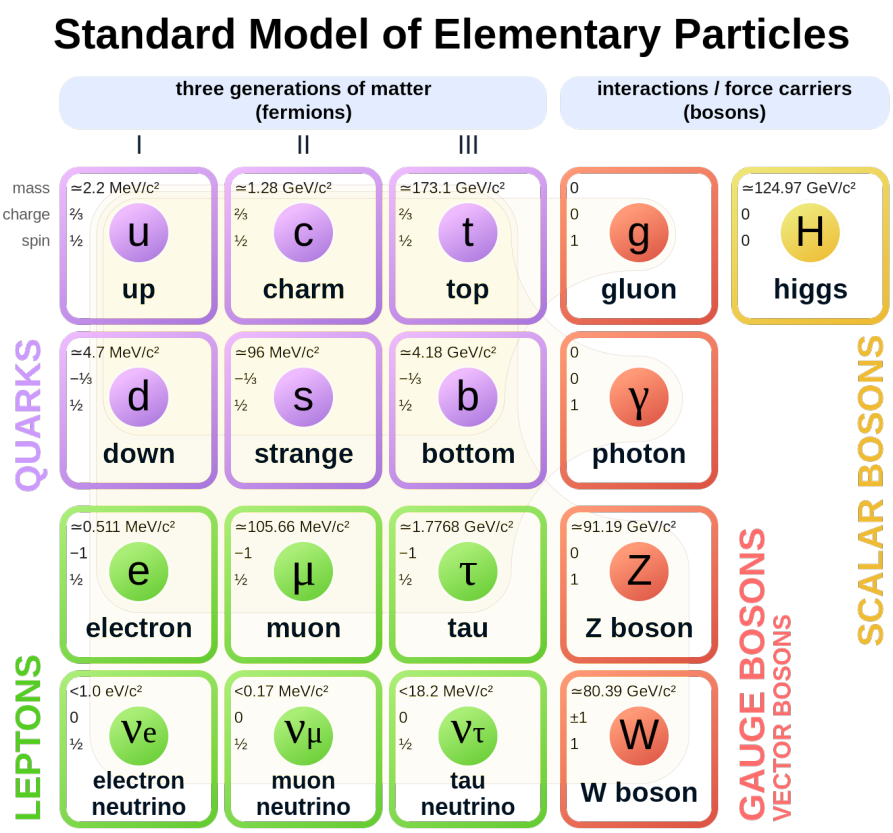

Figure 1.1: The Standard Model of Particle Physics. Figure credit: Wikimedia

1.2 Quantum Chromodynamics

Quantum Chromodynamics is the theory describing the strong nuclear interaction between quarks and gluons, and it is a Yang-Mills theory of the $SU(3)$ non-abelian symmetry group, which is described by the following lagrangian:

$$\mathcal{L} = \overline{\psi}(i\not{D} - m)\psi - \frac{1}{4}(G^i_{\mu\nu})^2 \tag{1.2}$$

Expanding the equation using the formula for the covariant derivative $D_\mu = \partial_\mu igA^a_\mu t^a$ and gluon field tensor $F_{\mu\nu} = \partial_\mu A^a_\nu - \partial_\nu A^a_\mu + gf^{abc}A^b_\mu A^c_\nu$ gives the following:

$$\begin{aligned}\mathcal{L} = \overline{\psi}(i\not{\partial} - m)\psi - \frac{1}{4}(\partial_\mu A^a_\nu - \partial_\nu A^a_\mu)^2 + gA^a_\mu\overline{\psi}\gamma^\mu t^a\psi \\ - gf^{abc}(\partial_\mu A^a_\nu)A^{\mu b}A^{\nu c} - \frac{1}{4}g^2(f^{eab}A^a_\mu A^b_\nu)(f^{ecd}A^{\mu c}A^{\nu d})\end{aligned} \tag{1.3}$$

The components with three and four factors of the gauge vector field indicate that the

gluon fields are self-interacting, unlike the gauge field of the electromagnetic theory. During the renormalization necessary to exclude divergences in the theory, the self-interaction of the gluon fields results in an important feature of QCD. Specifically, quantum corrections to the coupling strength reveal that the coupling strength decreases at higher energy scales. This can be seen in the Callan-Symanzik β function (at the one-loop level), which describes how the coupling strength evolves as a function of the renormalization energy scale M, for Yang-Mills theories [27]:

$$\beta(g) \equiv M\frac{\partial}{\partial M}g = -\frac{g^3}{(4\pi)^2}\left[\frac{11}{3}C_2(G) - \frac{4}{3}n_f C(r)\right] \tag{1.4}$$

Here, $C_2(G)$ is the quadratic Casimir operator of the given representation r of the gauge group ($SU(3)$ for QCD), n_f is the number of fermions participating in the interaction, and $C(r)$ is the constant in the orthogonality relation $tr[t_r^a t_r^b] = C(r)\delta^{ab}$ for r. For the N-vector adjoint representation of $SU(N)$, we can use the results that $C_2(r) = N$ and $C(r) = \frac{1}{2}$ get Equation 1.5.

$$\beta(g) = -\frac{g^3}{(4\pi)^2}\left[\frac{11}{3}N - \frac{2}{3}n_f\right] \tag{1.5}$$

The interesting consequence of this equation is that for $n_f < 16.5$, the β function is negative, indicating that g decreases as M increases and vice versa, which is the opposite behavior as the running coupling[1] in Quantum Electro-Dynamics. Since there are only 6 fermion fields taking part in the strong interaction, this is the case, as can be seen in measurements of the strong coupling constant at different energy scales such as those shown in Figure 1.2.

This results in two key effects in QCD: confinement at low energies and asymptotic freedom at high energies. At low energies and long distances, the strong coupling strength becomes stronger, approaching $O(1)$ where perturbative techniques (including Equation 1.4) are no longer valid. The strength of the strong interaction increasing with distance results in quarks being confined in bound states that have no net color charge. In contrast, at high energies, the coupling strength becomes small enough that individual quarks and gluons can scatter and become deconfined from hadrons.

1.2.1 Jets

Jets are a QCD phenomenon that spans the energy scales from the range of asymptotic freedom to confinement. In high energy collisions between hadrons, partons from each hadron can interact in a hard scattering event at a high energy scale that can be mod-

[1] Joke: A quantum field theorist picks up the phone. "Hello, is your theory's coupling constant running?" "Why , yes, it evolves as a function of the energy scale of the interactions according to the Callan-Symanzik β function." "Well, then you'd better go catch it!"

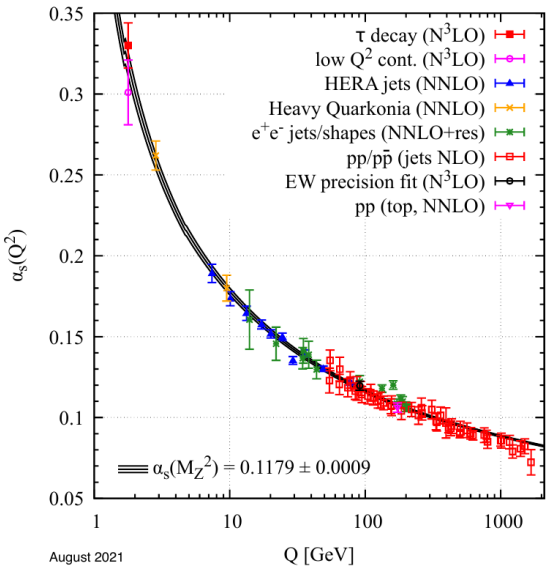

Figure 1.2: Running of the QCD coupling as a function of energy scale [1]

elled through perturbative QCD. From the hard scatter, high energy quarks and gluons are practically free to travel a short time before fragmenting into multiple quarks and gluons through gluon emission, pair production, and gluon splitting. This can be understood intuitively by noting that the quarks and gluons produced in hard scatters begin highly off-shell, and hence can only "exist" for a short time before shedding their virtuality through fragmentation.

In the process of fragmentation, quantum interference between gluon emissions results in a condition known as angular ordering in which subsequent emissions are restricted to smaller and smaller cones. As a result, the free parton converts into a collimated spray of partons. As the energies of individual partons decrease, the strength of the interaction between them increases, to the point at which they can no longer remain free. At that point, the quarks and gluons are confined into new hadrons, in a process called hadronization, which cannot be modelled with perturbative QCD.

An assumption that is used in studying the phenomenon of jets in hadronic collisions is that the physics at different scales and times in the event can be modelled separately, an assumption called factorization. This concept is often expressed in formulas for the production of final state particles from nucleon-nucleon collisions:

$$\sigma^{n_1 n_2 \to h+X} = f_i^{n_1}(x_1, Q^2) \otimes f_j^{n_2}(x_2, Q^2) \otimes \sigma^{ij \to k+X}(x_1 p_{n_1}, x_2 p_{n_2}, Q^2) \otimes D_{k \to h}(z, Q^2) \tag{1.6}$$

This describes the (assumed to be independent) processes of finding partons i and j in nucleons n_1 and n_2 carrying momentum fractions x_1 and x_2, the hard scatter between said

partons resulting in parton k, which fragments and hadronizes into a final state including a hadron h carrying transverse momentum fraction $z \equiv p_{\mathrm{T}}^{h}/p_{\mathrm{T}}^{k}$. The parton distribution functions $f(x, Q^2)$ are measured in deeply inelastic scattering experiments, and their evolution as a function of Q^2 can be extrapolated by evolution equations known as the Dokshitzer-Gribov-Lipatov-Altarelli-Parisi (DGLAP) equations. The hard scattering can be modelled well with perturbative QCD, usually resulting in a final states of two opposing jets. The fragmentation function can be modelled at the partonic level with perturbative QCD, while the hadronization stage cannot, and is modelled by phenomenological models such as PYTHIA [28], HERWIG [29], and SHERPA [30] .

1.3 Quark-Gluon Plasma

1.3.1 Theory

It has long been proposed that at sufficiently high temperature nuclear matter undergoes a phase transition to a state where quarks are no longer confined in individual hadrons. This is often presented in the form of the QCD phase diagram, with variables of the temperature, T, and the baryon chemical potential, μ_B, which is the energy cost of adding a new baryon. This potential, also understandable as the net baryonic density is nonzero but low for normal baryonic matter and extremely large in neutron stars. In heavy ion collisions, as the center of mass energy per nucleon pair, $\sqrt{s_{\mathrm{NN}}}$, increases, the T increases while the μ_B decreases, such that collisions at the LHC probe the high T, low μ_B corner of the diagram. Early and modern versions of the QCD phase diagram are shown in Figure 1.3. Calculations with lattice QCD (see Figure 1.4) have predicted a crossover transition around a temperature of 155 MeV at $\mu_B = 0$, while a first order phase transition is predicted at larger μ_B, with a critical point at an undetermined location [4].

1.3.2 Evidence for the QGP

The experimental evidence that the QGP has been been produced in heavy-ion collisions at RHIC and the LHC includes several independent types of measurements: the quenching of jets and high p_{T} hadrons, the observation of hydrodynamic flow, the enhancement of strangeness, and the suppression of quarkonia.

Jet Quenching

As high p_{T} partons/jets are produced in a very short time frame at the beginning of the collision, they traverse and interact with the medium as it forms. As the medium is strongly interacting with free quarks and gluons, the jets interact with the medium, losing some of their initial energy. The result of this and the falling p_{T} spectra of jets, is that at high p_{T}, the

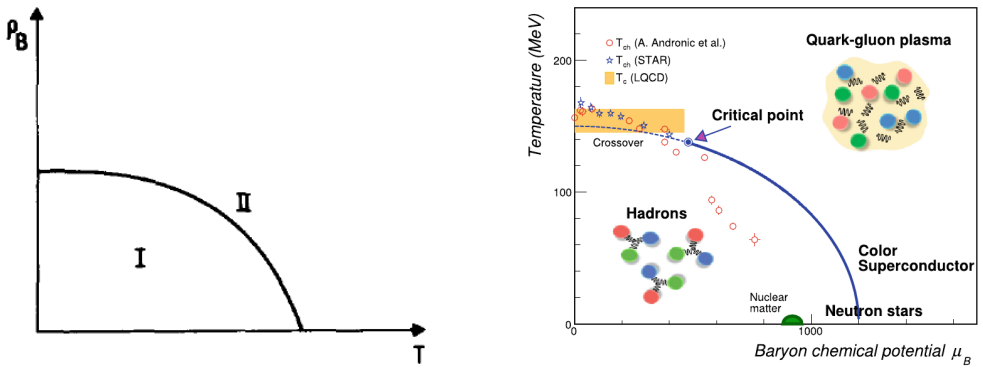

(a) QCD phase diagram as proposed in 1975 [31].

(b) Modern view of the QCD phase diagram [4].

Figure 1.3: Early and modern phase diagrams of QCD, mapped in terms of the temperature T and the baryon density (ρ_B) or baryon chemical potential (μ_B).

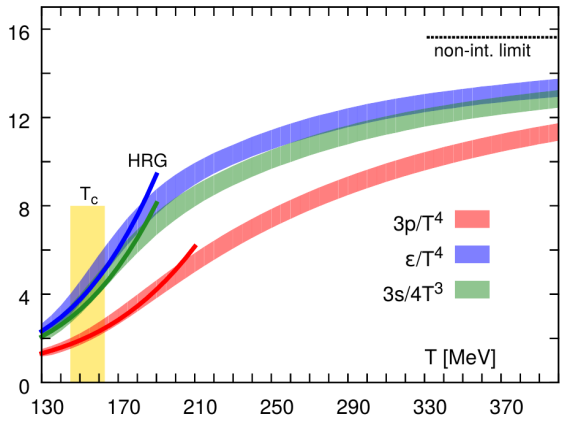

Figure 1.4: The temperature dependence of the pressure, energy density, and entropy in QCD, as determined by lattice QCD calculations by [2].

number of jets and hadrons in a given p_{T} bin will be reduced in comparison to what would be measured without a medium. Since we cannot turn off the medium in these collisions, in order to make this comparison the spectra of jets and hadrons is measured in pp collisions for reference. To account for the fact that heavy-ion collisions involve more than one nucleon-nucleon collision that may produce these jets, the pp measurement is scaled by the number of binary collisions between nucleons in the two nuclei, as calculated using a simulation called a Glauber model [32]. Then the effect of the medium can be measured by comparing the heavy ion and pp measurements in an observable ratio R_{AA}, as defined in Equation 1.7:

$$R_{AA} = \frac{1}{\langle N_{coll} \rangle} \frac{dN^{AA}/dp_{\mathrm{T}}}{dN^{pp}/dp_{\mathrm{T}}} \tag{1.7}$$

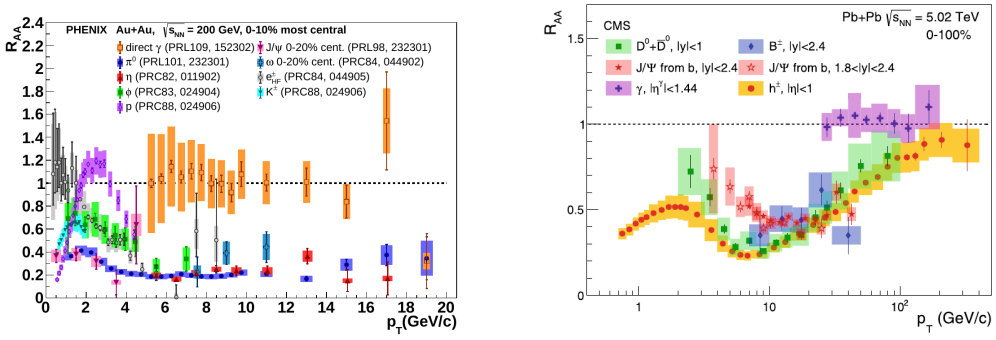

Figure 1.5: Nuclear suppression factor R_{AA} for a variety of particles as measured by PHENIX at $\sqrt{s_{\mathrm{NN}}} = 200$ GeV (left) [3] and as measured by CMS at $\sqrt{s_{\mathrm{NN}}} = 5.02$ TeV (right) [4].

If jets are losing energy, then their p_{T} spectra will be shifted to lower p_{T} resulting in an $R_{AA} < 1$. Measurements of the R_{AA} for a wide range of particles and two different collision energies is shown in Figure 1.5. One particularly interesting R_{AA} is that for single photons (excluding photons from hadronic decays), which is notable for not showing any suppression at all. This is expected, as photons do not interact strongly, and thus should traverse the medium unchanged.

In jets reconstructed using the anti-k_T clustering with a number of jet resolution parameters, similar quenching is observed, as seen in Figure 1.6.

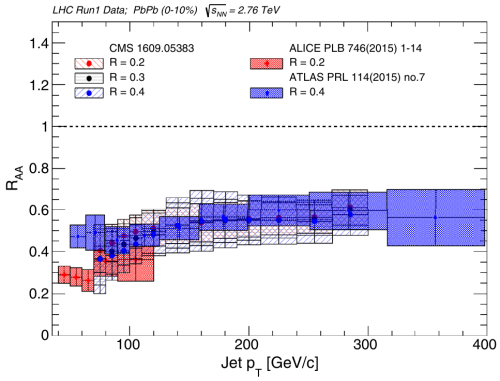

Figure 1.6: Jet R_{AA} as measured by the ALICE, ATLAS, and CMS experiments at the LHC [5].

Measurements of the R_{AA} can also be affected by non-QGP effects, such as the different parton distributions measured in nucleons in and outside of nuclei. For this reason, there is also a large interest in measuring R_{pA}, the ratio for collisions between single protons and heavy ions. More in-depth theoretical and experimental information on jet quenching is provided in Section 1.4

Hydrodynamic Flow

Another central piece of evidence for the existence of the quark-gluon plasma is the appearance of hydrodynamic flow during the evolution of the collision. In the immediate aftermath of a heavy-ion collision, the medium is contained in the overlap region of the two nuclei, as the remnants of the nuclei continue, as shown in Figure 1.7. In collisions that are not perfectly head on (impact parameter $b = 0$ fm), the medium has a non-spherical shape, typically described as an almond. Around the surface of the medium, the flatter parts (in the reaction plane defined by the x and z axes) have a higher density gradient that relativistic hydrodynamics predict will translate to a higher transverse momentum in the reaction plane, which will be conserved by the hadronization phase and reflected in an anisotropy in the final state.

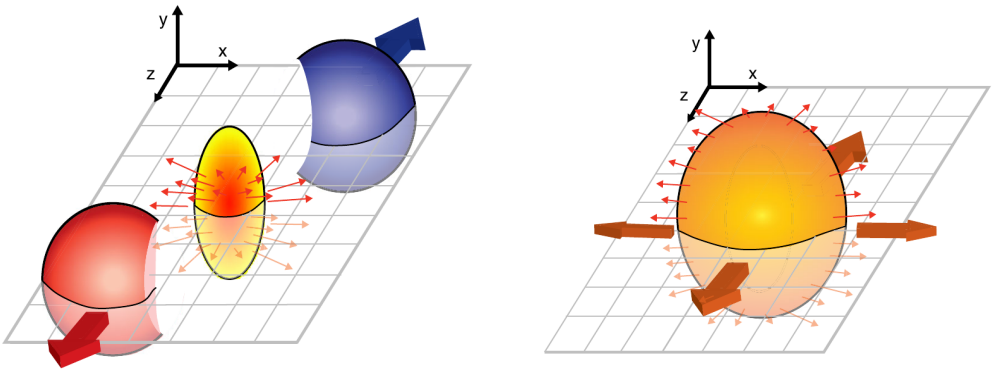

Figure 1.7: Diagrams describing the geometric and hydrodynamic source of elliptical flow in a heavy-ion collision. Diagrams from [5].

The azimuthal anisotropy in a single event or a class of events can be characterized by a Fourier series, such as that in Equation 1.8, in which ϕ is the azimuthal angle of final state particles, and ψ_n is called the event plane angle of order n. The first few terms are referred to as the directed, elliptical, and triangular flow for $n = 1, 2$ and 3, respectively.

$$E\frac{d^3N}{d^3p} = \frac{d^2N}{2\pi p_{\mathrm{T}} dp_{\mathrm{T}} dy}\left(1 + \sum_{n=1}^{\infty} 2v_n \cos(n(\phi - \Psi_n))\right) \tag{1.8}$$

Experimental measurements of anisotropies point to the existence of a hydrodynamic phase involving free quarks in a number of ways. One is that the flow coefficients are well described by models of relativistic hydrodynamics in heavy-ion collisions, such as those described in [6]. Those models use an initial state with realistic density fluctuations, and then evolve it using relativistic hydrodynamics. Then the v_n values are calculated per event, with the variation between events calculated for comparison with data. With values for the shear viscosity to entropy ratio (η/S) of 0.12 for Au–Au collisions at $\sqrt{s_{\mathrm{NN}}} = 200$ GeV and 0.2 for Pb–Pb collisions at $\sqrt{s_{\mathrm{NN}}} = 2.76$ TeV, the data are well

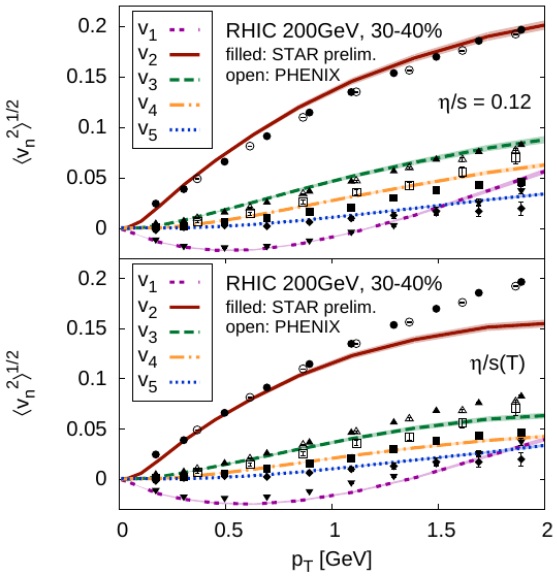

Figure 1.8: Variation in flow parameters in Au–Au collisions at $\sqrt{s_{\rm NN}} = 200$ GeV as measured by STAR and PHENIX, with comparison to results from relativistic hydrodynamic models [6].

described by hydrodynamical calculations, as can be seen for Au–Au collisions in Figure 1.8.

Another observed feature supporting the flow interpretation of the anisotropies of final state particles is found when examining the flow coefficients for identified particles by type, which show a feature called NCQ (number of constituent quark) scaling. As can be seen in Figure 1.9, baryons (which have 3 constituent quarks) and mesons (which have 2 constituent quarks) have significantly different flow parameters. However, when the v_n and $p_{\rm T}$ values are scaled down by the number of constituent quarks, the measured values between particles of different mass and quark contents coincide, as viewable in the difference between the plots in Figure 1.9. This is consistent with a hydrodynamic phase of quarks as hadrons measured at momentum $p_{\rm T}$ are likely composed from n quarks with momentum $p_{\rm T}/n$, and the coalescence of n quarks should be proportional to the product of the azimuthal distribution of the 2 or 3 quarks. This should be roughly equivalent to $n_q v_2$, which can seen through multiplying the fourier series:

$$\begin{aligned} P_{n_q=3} &\propto (1 + 2v_2\cos(2\Delta\phi) + \dots)^3 \\ &= 1 + 3*2*v_2\cos(2\Delta\phi) + 3*4*v_2^2\cos^2(2\Delta\phi) + 8*v_2^2\cos^3(\Delta\phi) + \dots \end{aligned} \quad (1.9)$$

The term proportional to $\cos(2\Delta\phi)$ is multiplied by 3, and a similar argument can be made for hadrons composed of 2 quarks.

This scaling is found to be even more accurate when the p_{T} variable is replaced by the variable $KE_T = m_T - m$, where m_T is called the transverse mass, and is given by $m_T = \sqrt{p_{\mathrm{T}}^2 + m^2}$ [7].

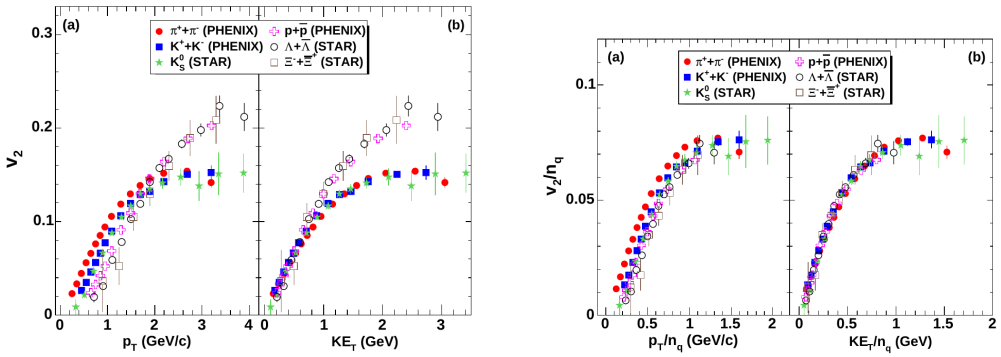

Figure 1.9: Flow of mesons (full markers) and baryons (empty markers) measured by PHENIX in Au–Au collisions at $\sqrt{s_{\mathrm{NN}}} = 200$ GeV, presented as functions of p_{T} and KE_T [7].

Strangeness Enhancement

It has been predicted that in the QGP, there is large production of strange quarks and anti-quarks that will be reflected in an enhancement of strange hadrons in the final state, relative to collisions between single hadrons. This can be understood through the gluonic degrees of freedom and through the chemical equilibration at temperatures above the threshold for producing $s\bar{s}$ pairs [33]. The enhancement of strange particle production in heavy-ion collisions is observable in Figure 1.10, where their production (normalized by the production of pions) is significantly large for Pb–Pb collisions than in pp collisions.

Quarkonia

In the high temperature and strongly interacting medium of the QGP, it has been predicted that bound states of heavy quark-antiquark pairs will be "dissolved" by the medium [34]. This dissolution can be caused by thermal gluons absorbed by the quarks as well as color screening of the interaction between the pair. In particular, for excited states of quarkonia, such as $\psi(2s)$ for the J/ψ meson and $\Upsilon(2s)$ for the Υ meson, there should be additional suppression due to the lower binding energies of these states, a pattern that has indeed been measured, as seen in measurements by CMS in Figure 1.11. While this has been proposed as a means of measuring the temperature of the QGP, this is complicated by the observation that quarkonia are less suppressed at the LHC than at RHIC, even though the higher temperature of the medium at the LHC should dissolve quarkonia at a higher rate. This is currently understood as arising from the coalescence of heavy quarks in the medium into quarkonia [33].

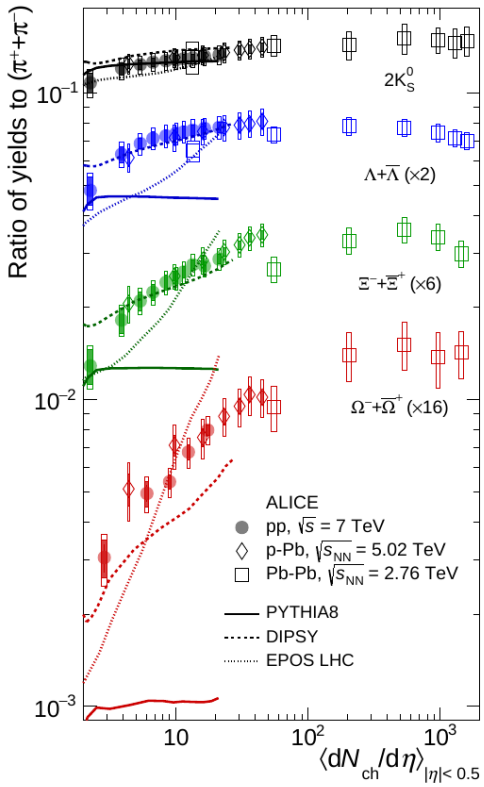

Figure 1.10: Measurement by ALICE of strange particles in Pb–Pb, p–Pb, and pp collisions [8].

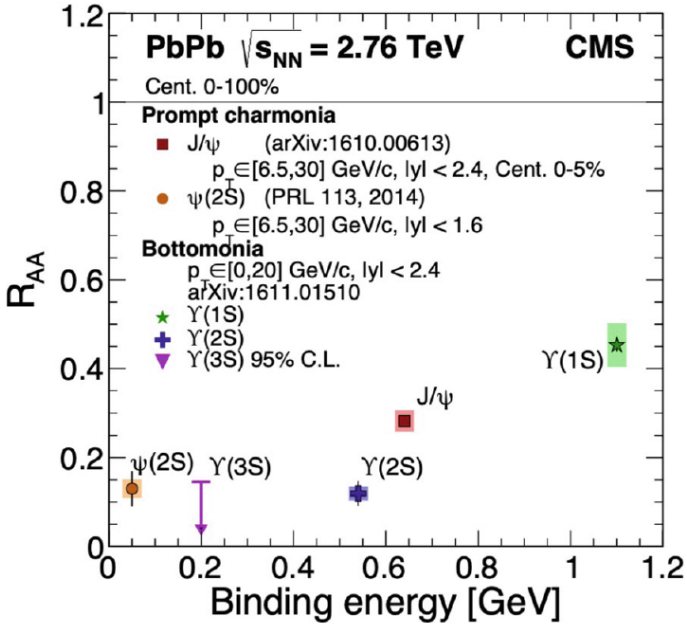

Figure 1.11: Quarkonia suppression in heavy-ion collisions vs their binding energy [4].

1.4 Jet-Medium Interactions

Jets travelling through the strongly coupled QGP medium are thought to lose energy through two primary means: elastic collisions with partons in the medium, and medium-induced radiation (expressed visually in Figure 1.12). The medium-induced radiation occurs in the QCD equivalent of bremsstrahlung radiation, where the presence of a color-charged medium allows the partons in the jet to radiate gluons. As described in [33] and [35], these can be expressed as elastic and radiative transport coefficients $\hat{e}$ and $\hat{q}$. The elastic energy loss, which is more significant for heavy quarks, causes an energy loss proportional to the path-length traversed by the jet. In contrast, radiative energy loss causes energy loss that is quadratic as a function of path-length. Additionally, gluons are thought to lose energy due to their higher Casimir factor ($C_2(\text{gluon}) = 3$, $C_2(\text{quark}) = 4/3$), which can be understood intuitively by the greater number of possible color configurations for a gluon interacting with additional partons. This results in significantly more interactions for gluon jets than for quark jets. The resulting energy loss through length L of the medium can be roughly expressed as such :

$$\Delta E \propto C_2 \hat{e} L + C_2 \hat{q} L^2 \tag{1.10}$$

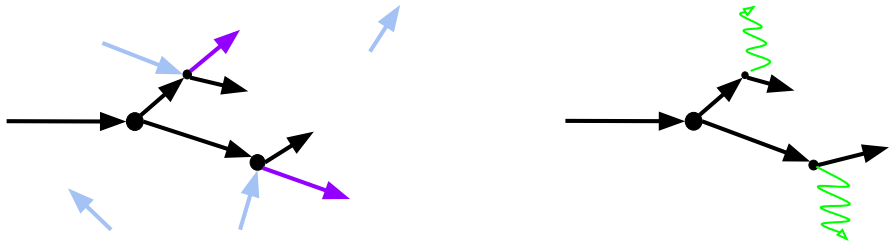

(a) Collisional energy loss (b) Radiative energy loss

Figure 1.12: Energy loss mechanisms cartoon

It should be noted that the radiative component results in a significant amount of the parton's energy being emitted in the plane transverse to the direction of the parton.

1.4.1 Coherence Effects

One important complication in the jet-medium interaction comes from the effect of color coherence. As the parton shower evolves, quarks and gluons emit more quarks and gluons, each of which can then lose energy in the medium. However, when these splittings occur at sufficiently small angles and transverse (to the jet) momenta, the medium does not resolve the split partons as separate particles and color-charges, instead interacting with the split pair as a single parton. This is described by a parameter known as the formation

time $t_f = 2\omega/k_{\mathrm{T}}^2$, where ω is the gluon energy and k_{T} is the transverse momentum of the emission. When this t_f is greater than the mean free path of the parton in the medium, then the splitting is not "resolved" by the medium. As a result, the medium interacts coherently with the split parton pair, as if the splitting never happened [36]. This is also known as the non-abelian Landau-Pomeranchuk-Migdal (LPM) effect.

1.4.2 Observation of Jet Quenching

One notable demonstration of jet quenching in a semi-inclusive measurement is the early dihadron correlations in Au–Au collisions published by the STAR collaboration in 2003, as shown in Figure 1.13. In this measurement, correlations in relative azimuthal angle ($\Delta\varphi$) are recorded between pairs of hadrons in pp and Au–Au collisions at $\sqrt{s_{\mathrm{NN}}} = 200\,\mathrm{GeV}$, as well as d–Au collisions to study cold nuclear matter effects. The primary features are the peaks at $\Delta\varphi = 0$ and $\Delta\varphi = \pi$. The near-side peak at (at $\Delta\varphi = 0$) appears due to correlations between hadrons that arose from the same hard parton. On the away-side (at $\Delta\varphi = 0$), as a significant peak can be seen corresponding to the other parton from the hard scatter in d–Au and pp collisions. However, this peak is absent in Au–Au collisions, a finding that is attributed to energy lost by the recoiling jet, and is strong evidence of an opaque medium.

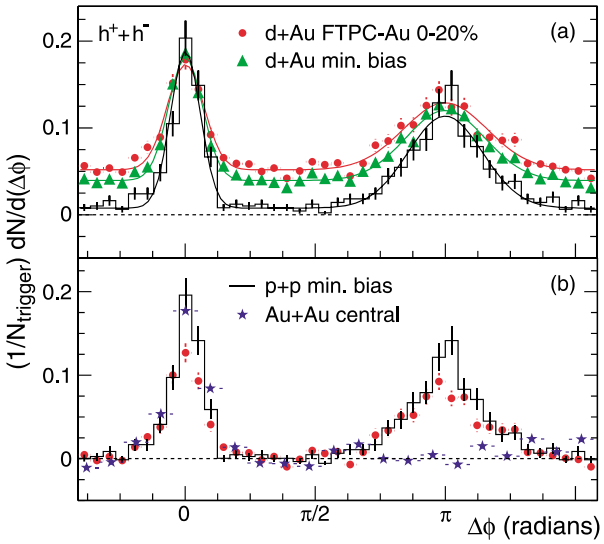

Figure 1.13: STAR Dihadron Correlation measurement for Au–Au collisions published in 2003[9].

1.4.3 Role of Fluctuations

Unfortunately for physicists focused on the idea of jet tomography, event-by-event and even jet-by-jet fluctuations play large roles in what can actually be measured. One source of fluctuations is that the initial state is not actually a simple almond shape, and has significant fluctuations between events. This is confirmed by measurements of odd flow coefficients in the final state, which could otherwise not exist. Another fluctuation source is that the energy loss is expected to vary between quarks and gluons due to the Casimir factors and different fragmentation functions. Due to the color coherence effect, differences in fragmentation function between jets result in differences in energy loss. Finally, the probabilistic nature of the collisional and radiative loss should set a minimum amount of fluctations in energy loss, that will be present even between events with the same exact initial conditions.

One particularly interesting theoretical result highlights the role that fluctuations play in jet quenching measurements, this is the study of the dijet asymmetry distribution in JEWEL by [10]. The dijet asymmetry is defined for a pair of jets in Equation 1.11, where $p_{\mathrm{T},1}$ is the p_{T} of the higher p_{T} jet. For balanced dijets, this A_j variable should be peaked near 0. Larger values of the A_j are expected, on average, for heavy ion collisions, as many jet pairs will have one jet lose more energy than the other. This can be explained intuitively from a geometric perspective, as shown in Figure 1.14.

$$A_J \equiv \frac{p_{\mathrm{T},1} - p_{\mathrm{T},2}}{p_{\mathrm{T},1} + p_{\mathrm{T},2}} \tag{1.11}$$

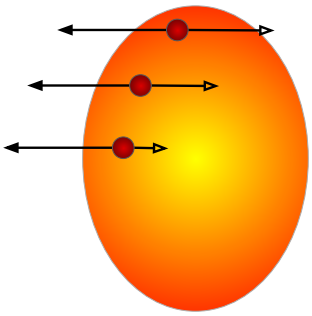

Figure 1.14: Diagram of dijets traversing a medium from different starting points, and a resulting asymmetry in the dijet momenta, as represented by vectors.

As shown in the left plot of Figure 1.15, the JEWEL A_j distribution is consistent with that measured by CMS for jets in Pb–Pb collisions. A surprising result from the study is shown in the right plot, where the JEWEL A_j distribution is indistinguishable from the A_j found in a modified version of JEWEL where all jets are forced to start in the exact center of the event. In this version, there is no possible asymmetry in the path-lengths traversed by the jets, meaning that the geometric explanation shown in Figure 1.14 may

not represent the dominant source of the dijet asymmetry. Instead, the asymmetry in the JEWEL model arises from fluctuations in the jet-medium interaction. Specifically, these fluctuations are driven by fluctuations in the fragmentation pattern of the parton shower, where jets with wider fragmentation lose more energy[10]. The JEWEL model does not include fluctuations in the medium density itself, so conclusions cannot be drawn about the relative importance of medium fluctuations and jet fragmentation fluctuations.

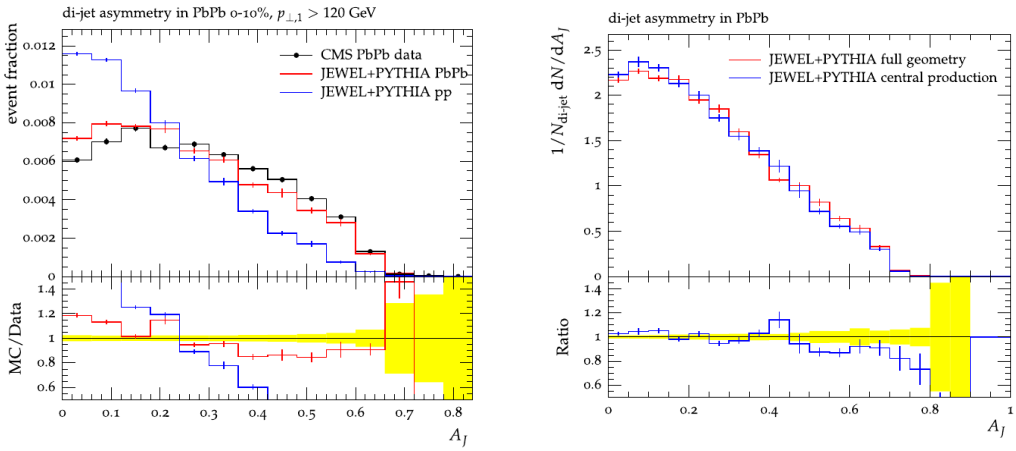

Figure 1.15: Dijet asymmetry as measured by CMS and as modelled by the JEWEL model. On the left, good agreement is found between the CMS Pb–Pb measurement and the JEWEL predictions. On the right, the asymmetry distribution is shown for JEWEL's standard mode (in which jet sources are realistically distributed within the medium) and a central production, wherein all jets come from the exact center of the event. The two distributions are largely indistinguishable [10].

1.5 Previous Measurements

In this section, several similar measurements to those in this thesis are reviewed.

1.5.1 Jet-Hadron Correlations

One well-known measurement using correlations to measure jet energy loss is the measurement of jet-hadron correlations in Au–Au and pp collisions at $\sqrt{s_{\text{NN}}} = 2.76$ TeV by the STAR experiment.

In this experiment, R=0.4 jets were reconstructed from charged particles measured by tracking and neutral particles measured with the STAR Barrel Electromagnetic Calorimeter, after which the azimuthal correlations between charged hadrons and the jets were measured. Examples of such correlations are shown in Figure 1.16. For high p_{T} charged particles, there is a noticeable suppression in the awayside peak at $\Delta\phi = \pi$. However,

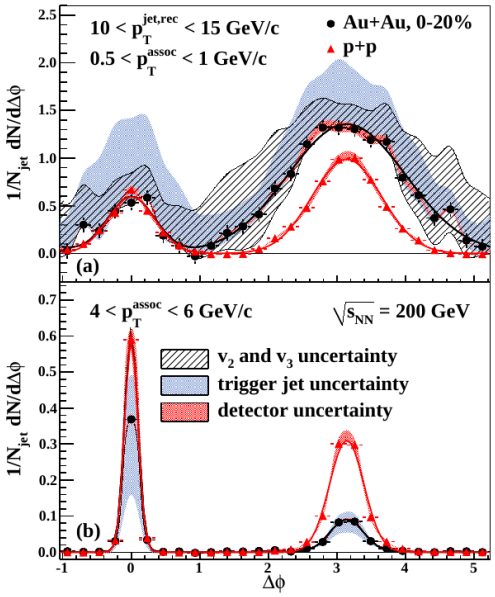

Figure 1.16: Azimuthal correlations of jets and charged hadrons in Au–Au and pp collisions as measured by the STAR experiment [11].

at low p_{T}^{assoc}, there is a relative enhancement. This can be understood through the conservation of momentum, where the energy lost by the high energy components of jets is transferred to many particles at lower energies.

To study this effect further, an observable was defined using the differences in yields of associated particles in a given p_{T} range in heavy-ion and pp collisions, scaled by the mean p_{T} in the range:

$$D_{AA} = Y_{AA}(p_{\mathrm{T}}^{assoc}) * < p_{\mathrm{T}}^{assoc,AA} > - Y_{pp}(p_{\mathrm{T}}^{assoc}) * < p_{\mathrm{T}}^{assoc,pp} > \tag{1.12}$$

In Figure 1.17, the D_{AA} is plotted for jets in two p_{T} ranges. The D_{AA} variable is interesting, as one can see if the redistribution of the awayside ($\Delta\phi \approx \pi$) jet's energy to associated particles is completely accounted for, which is the case if the sum of all D_{AA} values across the full p_{T} range of associated particles is consistent with 0.

1.5.2 ALICE π^0-Hadron Correlations

ALICE has previously published ([12]) π^0-hadron correlations for Pb–Pb collisions at 0-10% centrality at $\sqrt{s_{\mathrm{NN}}} = 5.02$ TeV, with pp collisions at the same energy for reference. Similarly to the STAR jet-hadron correlations measurement, the yields of associated particles were compared between pp and heavy-ion collisions. In this case, both the yields around the nearside and awayside peaks were compared using the ratio $I_{AA} \equiv Y_{AA}/Y_{pp}$, as seen in Figure 1.18. The awayside yields show the expected pattern of suppression at

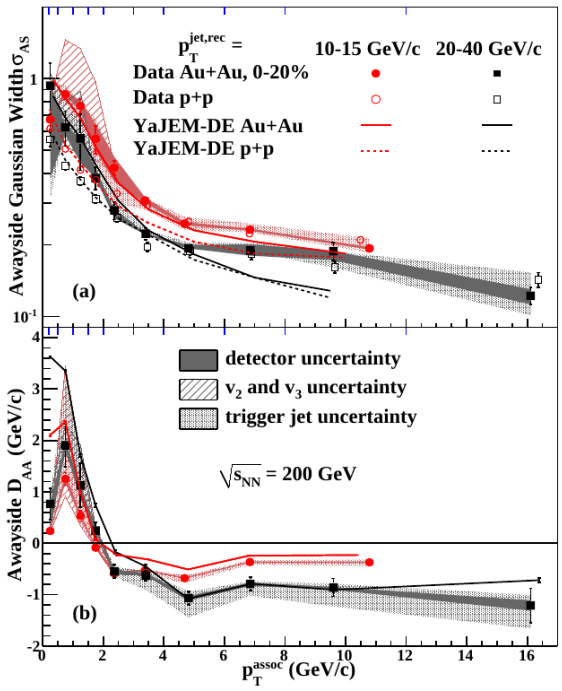

Figure 1.17: Yield differences in Au–Au and pp collisions in STAR's jet-hadron correlations measurement. At high associated p_{T}, significant suppression in Au–Au collisions is observed, while yields are enhanced at low p_{T}[11].

high p_{T}^{assoc} at least partially balanced out by enhancement at low p_{T}^{assoc}, and the compared models generally agree. Interestingly, the nearside shows some enhancement at low p_{T} that neither of the compared models (JEWEL and AMPT) seem to describe well.

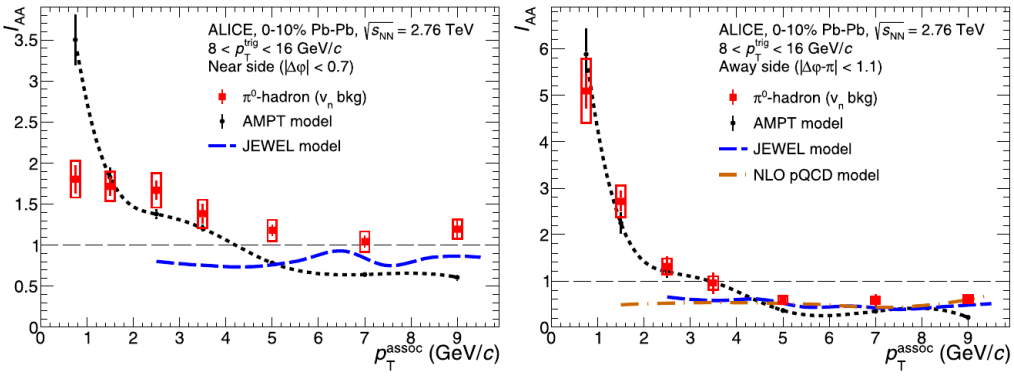

Figure 1.18: Yield ratios for π^0-hadron correlations measured in pp and Pb–Pb collisions at $\sqrt{s_{\mathrm{NN}}} = 2.76$ TeV, with comparisons to the AMPT and JEWEL models, and an NLO pQCD model [12].

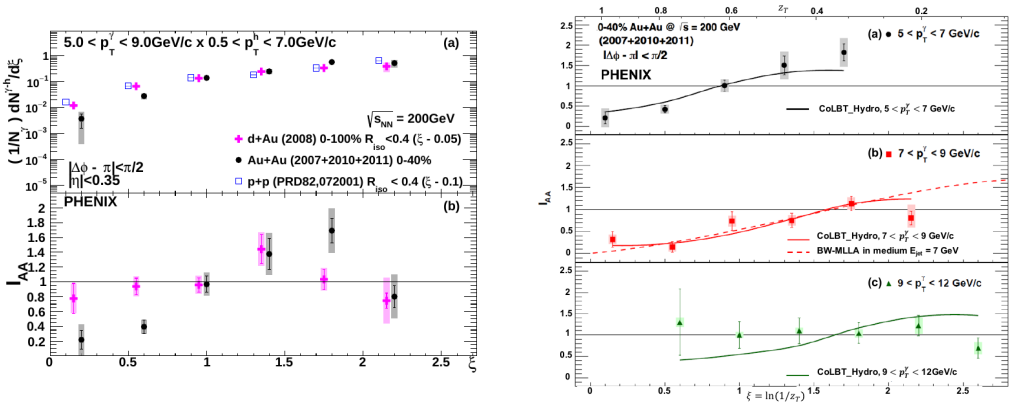

Figure 1.19: PHENIX results on γ-hadron correlations in Au–Au collisions. On the left, the ratio of the per-trigger yield for γ-hadron collisions between Au–Au and pp and the ratio between d-Au and pp collisions are shown. The d-Au collisions show no sign of modification, while the Au–Au collisions do. On the right, the yield modification is presented for different trigger momenta.

1.5.3 STAR and PHENIX π^0 and $\gamma-$Hadron Correlations

The STAR and PHENIX experiments have produced many analyses studying jet physics using π^0 and γ triggers. ([37],[38],[39],[40],[41]). These include *pion*eering[2] a technique in which π^0-hadron correlations are used to subtract the background contribution that decay photons from π^0s add to measurements of γ-hadron correlations, which was actually part of the original inspiration for the research in this thesis.

Some results for γ-hadron correlations are shown in Figure 1.19. In these, focus is on the yields of hadrons on the awayside (opposite the trigger photon), with calculation of the I_{AA} yield ratio. These results are presented as functions of $\xi \equiv \ln(1/z_T)$, where $z_T = p_{\mathrm{T}}^{assoc}/p_{\mathrm{T}}^{\gamma}$ is the ratio of the p_{T} of the associated particle relative to the p_{T} of the trigger particle, a photon in this case. For direct photons, this is a particularly accurate measurement of the fragmentation function of the jet, as the photon carries roughly the same p_{T} as the initial parton that produced the awayside jet. Low ξ corresponds to high p_{T} associated particles, and this is where suppression is seen relative to pp collisions; but no suppression is observed in d–Au collisions. In the right figure, where the I_{AA} is shown for different trigger p_{T}, the turnover between suppression and enhancement can be seen to shift to higher ξ (lower z_T) in a manner consistent with the model comparisons. It should be noted that, in terms of the p_{T}^{assoc}, the turnover point is roughly constant, staying in the 3-4 GeV/c region, an effect first noted in the measurement by STAR [41].

[2] Intentional pun

1.5.4 CMS Jet-Track Correlations

Another similar measurement that was made by the CMS collaboration is shown in Figure 1.20. In that measurement, correlations of particles near reconstructed jets are analyzed and compared between Pb–Pb and pp collisions to study the effect of the medium on jets. These measurements show a significant enhancement of low p_{T} particles in and around a jet in Pb–Pb collisions that increases in more central events. Above a p_{T} of 3 GeV/c there is no significant difference observed.

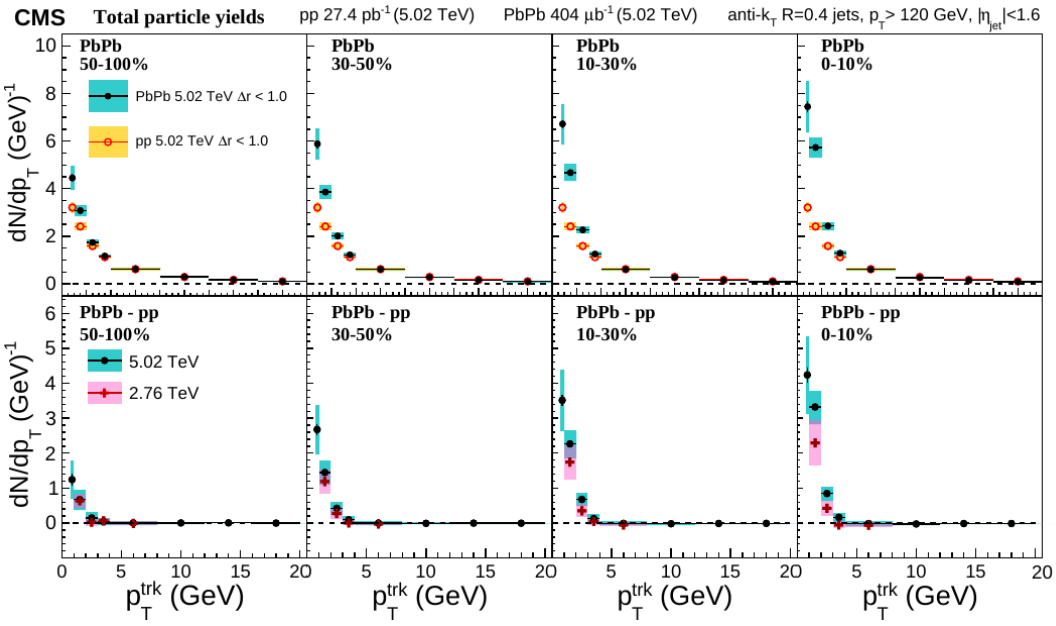

Figure 1.20: Yields of particles associated with jets in Pb–Pb and pp collisions recorded by CMS [13]. On the top row, correlations between jets and hadrons in Pb–Pb and pp collisions. From left to right, the panels shift from peripheral to central events. The difference in per-trigger yields between Pb–Pb and pp collisions is shown in the lower row.

1.5.5 ALICE Jet-Hadron Correlations

Another study that must be mentioned is the measurement of jet-hadron correlations relative to the event plane in Pb–Pb collisions at $\sqrt{s_{\mathrm{NN}}} = 2.76$ TeV by ALICE [14]. In this study, the correlations are measured separately for jets in different angles relative to the event plane. This allows the usage of a background estimation technique called the Reaction Plane Fit (more details are provided in Section 3.9 and in [42]). This also allows for the experimental variation of the path-length traversed by jets, by comparing the associated particles for jets in-plane (where jets traverse less of the medium) to out-of-plane (where jets traverse more of the medium). In the analysis, the ratio between yields out-plane were

compare to those found in-plane. Path-length dependence of jet energy loss may then be observed as suppression (Yield ratio < 1) at high p_{T}^{assoc}, possibly with enhancement at low p_{T}^{assoc} as observed in the STAR jet-hadron analysis described in Section 1.5.1. The results are presented, along with a prediction using the JEWEL model, in Figure 1.21. Overall, no statistically significant event-plane dependence is seen, which is consistent with the small amount of event-plane dependence seen in the JEWEL model. One conclusion of the paper was that this non-observation of path-length dependence may be due to the effect of fluctuations in jet energy loss, similar to those studied in the JEWEL dijet asymmetry paper ([10]).

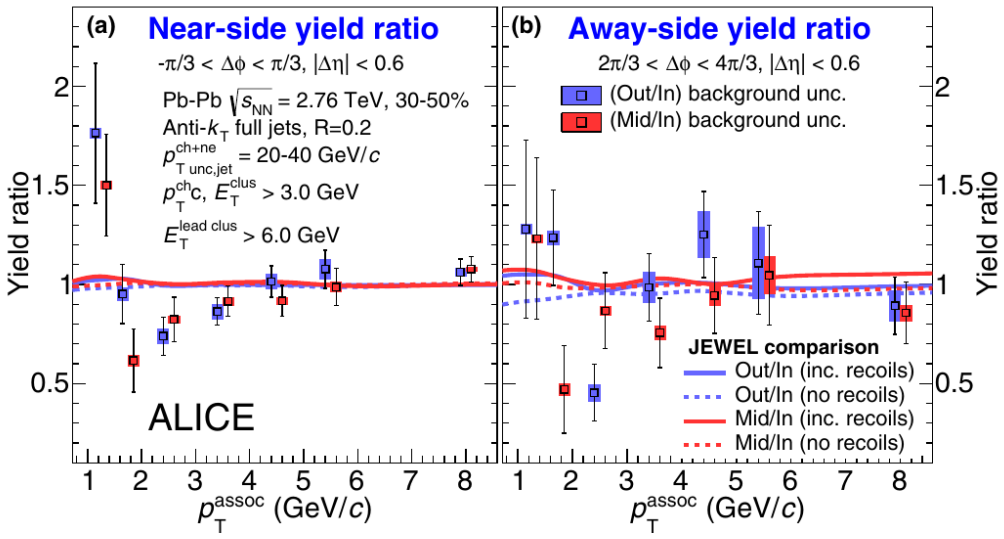

Figure 1.21: Ratio of hadron yield correlated with jets measured in-plane vs out-of-plane by ALICE in Pb–Pb collisions at $\sqrt{s_{\mathrm{NN}}} = 2.76$ TeV [14]. The ratios for the nearside are shown on the left, and away-side, where more significant dependence is expected, is shown on the right.

The JEWEL predictions in this analysis were produced by the author of this thesis, and the process of producing them and more predictions are described in chapter 4.

1.5.6 ATLAS Jet Flow

A recent result that appears to have successfully measured event plane dependence of jets is a paper submitted for publication by the ATLAS collaboration of the flow coefficients of jets at high p_{T} [15]. While nonzero flow coefficients of particles at low p_{T} is attributed to the anisotropically expanding and flowing medium, the most likely cause for azimuthal anisotropy at high p_{T} is the geometric effect of different path-lengths traversed by jets angled out-of-plane vs in-plane. As visible in Figure 1.22, the flow coefficient results are consistent with predictions made with a jet energy loss model.

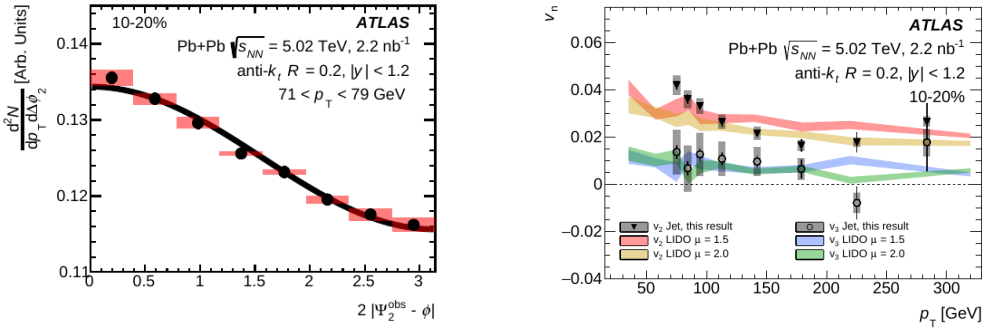

Figure 1.22: Azimuthal anisotropies of jets in Pb–Pb collisions by the ATLAS experiment. The raw distribution of jets with respect to the 2nd order event plane is shown at left, while v_2 and v_3 measurements at different p_{T} are shown at right, with comparison with the LIDO model implementing collisional and radiative losses [15].

Chapter 2

Experiment: ALICE at the LHC

This research on the interactions of QCD jets with the quark-gluon plasma was done using a large ion collider experiment, specifically the experiment known as ALICE (A Large Ion Collider Experiment).

ALICE is a multipurpose detector dedicated to measuring heavy ion collisions at the highest center-of-mass energies ever achieved, using beams of Lead ions and protons (and occasionally Xenon ions) produced and accelerated at the Large Hadron Collider (LHC) at CERN, the European Organization for Nuclear Research, on the border of France and Switzerland.

The ALICE detector is focused on measuring and identifying the thousands of charged particles produced in the central ($|\eta| < 1$) region in heavy ion collisions, using multiple layers of tracking detectors. In addition, ALICE has several specialized detectors, including two electromagnetic calorimeters in the midrapidity and a muon tracking arm operating in the forward (large $|\eta|$) region on one side of the detector. There are additional forward calorimeters and counters that play vital roles in determining when a collision occurs, as well as measuring various characteristics of the event.

In this chapter, we start by introducing the LHC and then outline the coordinates and variables that will be necessary to describe the details of ALICE's subdetectors. Then the detectors relevant to this thesis in ALICE's central barrel are reported, specifically the Inner Tracking System (ITS) and Time Projection Chamber (TPC). Following this, we discuss the calorimetry, with emphasis on the Electromagnetic Calorimeter (EMCal). Finally, we discuss the forward detectors and the trigger system of ALICE.

2.1 Large Hadron Collider

The Large Hadron Collider is currently the largest hadron collider in the world, located at and around CERN's sites in Geneva. It was built into the preexisting tunnel for the Large Electron Position collider, with the purpose of colliding hadrons at the highest energies

achieved in a human-made collider. The primary goals of the LHC were to discover the Higgs boson and to serve as a discovery machine for physics beyond the Standard Model. The former was achieved in 2012 ([43], [44]), while the latter is an ongoing effort.

The LHC consists of a 27 km circumference ring around which hadrons are sent at ultra-relativistic velocities in two counter-rotating beams. The beams cross at four interaction points, at which the four primary LHC experiments are located, as visible in Figure 2.1.

During most of the running time of the LHC, the machine collides beams of protons, however for a dedicated time during most operating years heavy ion beams (Pb^{208}) are collided for the purpose of studying the quark-gluon plasma that has been found to be formed in those collisions. During the heavy ion periods, collisions between protons and Lead ions are generated, primarily to study non-QGP effects of collisions involving Lead ions. There are also periods in which proton-proton collisions are created at $\sqrt{s_{\mathrm{NN}}} = 2.76\ \mathrm{TeV}$ and $\sqrt{s} = 5.02\ \mathrm{TeV}$, instead of the maximum energies achievable, to provide a baseline for measurements in Pb–Pb collisions.

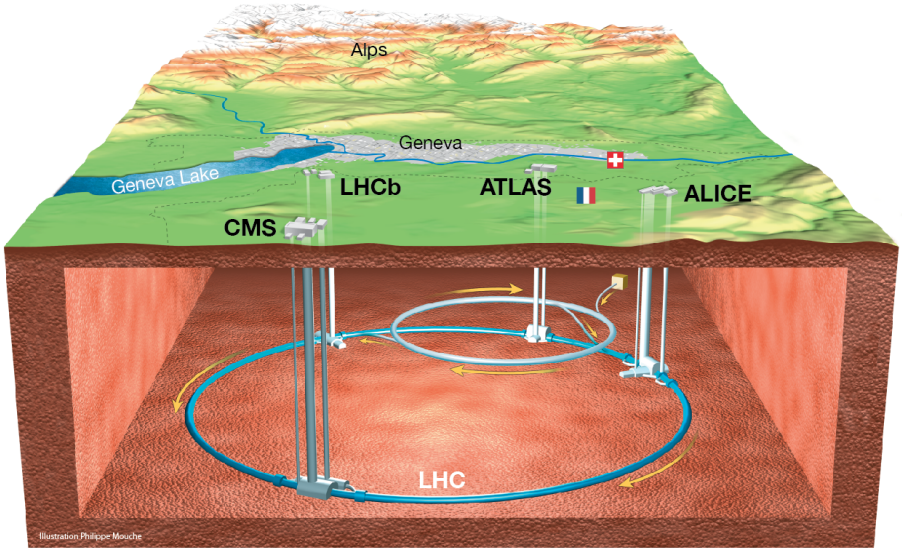

Figure 2.1: Diagram of the Large Hadron Collider with the four main LHC experiments. Not drawn to scale (figure from [16]).

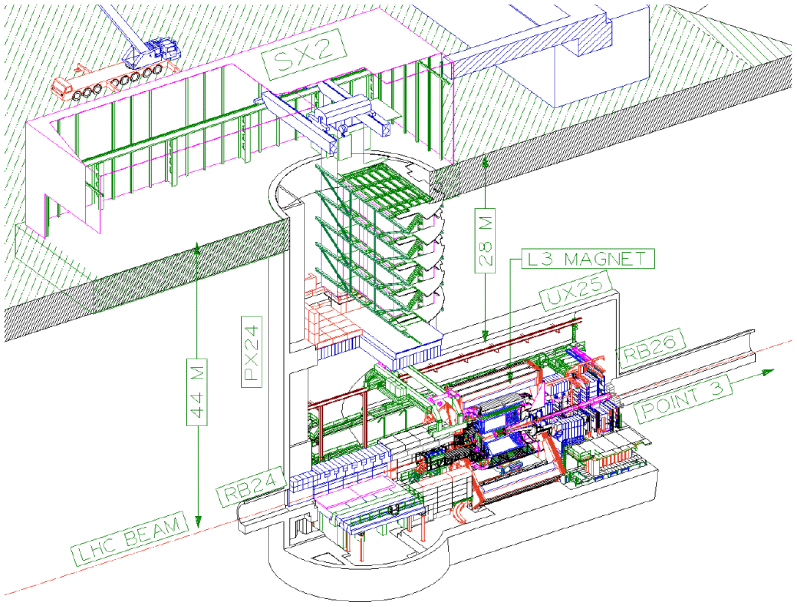

Figure 2.2: Schematic of the ALICE experimental site at LHC Interaction Point 2 [17].

2.2 Coordinates and Variables

2.2.1 Coordinates

The coordinates used in the ALICE detector are described relative to the nominal central interaction point within the beam pipe. The beam axis defines the z-axis, with the positive z direction being anticlockwise and negative z being clockwise around the LHC defining the A-side and C-side of the ALICE detector[1]. In Figure 2.2, the negative z direction is towards interaction point 3 (the interaction points at the LHC are numbered clockwise) . The x and y axes are then defined by the horizontal and vertical directions, respectively.

Particles in the ALICE experiment are generally described in the coordinates of transverse momentum p_{T}, azimuthal angle φ, angle θ relative to the beam axis and pseudorapidity η, defined in Equation 2.1. Pseudorapidity is closely related to the rapidity variable, y defined in Equation 2.2, and the variables are identical for a massless particle. Rapidity is the theoretically ideal particle as it in Lorentz invariant for boosts along the beam direction. However, determining the rapidity of an individual particle requires knowledge of its mass, whereas η can be determined just from the angle of the particle.

$$\eta \equiv -\ln[\tan(\theta/2)] = \frac{1}{2}\ln\left(\frac{|\mathbf{p}|+p_z}{|\mathbf{p}|-p_z}\right) \tag{2.1}$$

[1]By coincidence, at ALICE this can by memorized by the A-side going towards ATLAS and the C-side going towards CMS

$$y \equiv \frac{1}{2} \ln \left(\frac{E + p_z}{E - p_z} \right) \tag{2.2}$$

An approximation for y as a function of η is given in Equation 2.3, from an expansion in m/p_{T}.

$$y \approx \eta - \frac{1}{2} \tanh \eta \, (m/p_T)^2 \tag{2.3}$$

From this it can be observed that the difference between the variables increases with η and with m/p_{T}. As a result, particle distributions that are constant in y will have a η-dependence at low p_{T}.

2.2.2 Centrality

An important and useful parameter for analyzing heavy-ion collisions is the impact parameter between the two colliding nuclei. It is defined as the distance (in the plane perpendicular to the beam axis) between the centers of the nuclei, as shown in Figure 2.3. Nucleons that interact with nucleons from the other nucleus are called participant nucleons and contribute energy to the medium that is formed. Nucleons that do not are known as spectator nucleons, which continue along the beam direction.

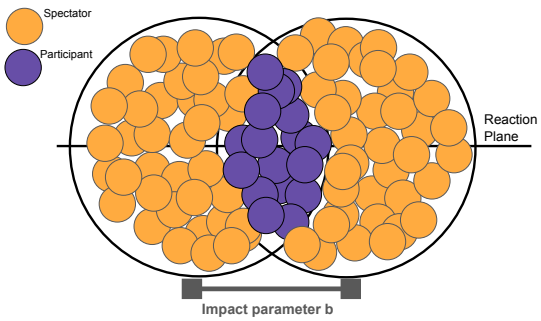

Figure 2.3: Cartoon of the geometry of a heavy ion collision. Participant and spectator nucleons are labelled in purple and orange, respectively.

The number of particles with low momentum transverse to the beam ($p_{\mathrm{T}} \equiv \sqrt{p_x^2 + p_y^2}$) produced in the final state is proportional to the total number of participating nucleons. A shorter impact parameter results in more soft (low p_{T}) particles in the final state, which can be leveraged to estimate the impact parameter from the multiplicity of particles measured by detectors. This is generally done using a model called a Glauber model, in which the nucleon-nucleon cross section and the assumption that nucleons are distributed within the nuclei according to a Woods-Saxon function. Then the number of participants are estimated for ranges of the impact parameter. Ultimately, events are classified according to

percentile in the multiplicity distribution. This distribution is called the centrality distribution, with 0% central referring to the highest multiplicity and most central events, and 100% central referring to low multiplicity, peripheral events. More details, specifically for how this is done with the ALICE detector, are provided in [45].

2.2.3 Event Plane

As mentioned in Section 1.3.2, the distribution in particles in heavy ion events can be characterized by a Fourier series:

$$E\frac{d^3N}{d^3p} = \frac{d^2N}{2\pi p_{\mathrm{T}} dp_{\mathrm{T}} dy}\left(1 + \sum_{n=1}^{\infty} 2v_n \cos(n(\phi - \Psi_n))\right)$$

The angles Ψ_n are referred to as the n^{th}-order event-plane, and can be determined by calculating the q_n vector, which has the direction Ψ_n and has a scale proportional to the flow terms v_n.

$$\begin{aligned} q_{n,x} &= \frac{1}{S}\sum_i S_i \cos(n\varphi_i), \\ q_{n,y} &= \frac{1}{S}\sum_i S_i \sin(n\varphi_i), \end{aligned} \tag{2.4}$$

The individual weight S_i is usually taken to be 1. Then the n^{th} order event-plane angle is given by:

$$\Psi_n = \tan^{-1}(q_{n,y}/q_{n,x}) \tag{2.5}$$

More details on the q_n-vector determination are provided in [45]. One method to determine the flow parameter v_n of various particles is to fit their distribution relative to Ψ_n. It is good practice to avoid bias from auto-correlations by using separate sets of of particles for the Ψ_n and v_n determination. This is typically done by requiring a pseudorapidity gap between the two sets of particles.

2.3 A Large Ion Collider Experiment

In Figure 2.4, a schematic of the ALICE detector is displayed, where the position of individual subdetectors are labelled.

In the following sections, we discuss the ALICE central barrel, the calorimetry, the forward detectors, and some details of the ALICE event trigger.

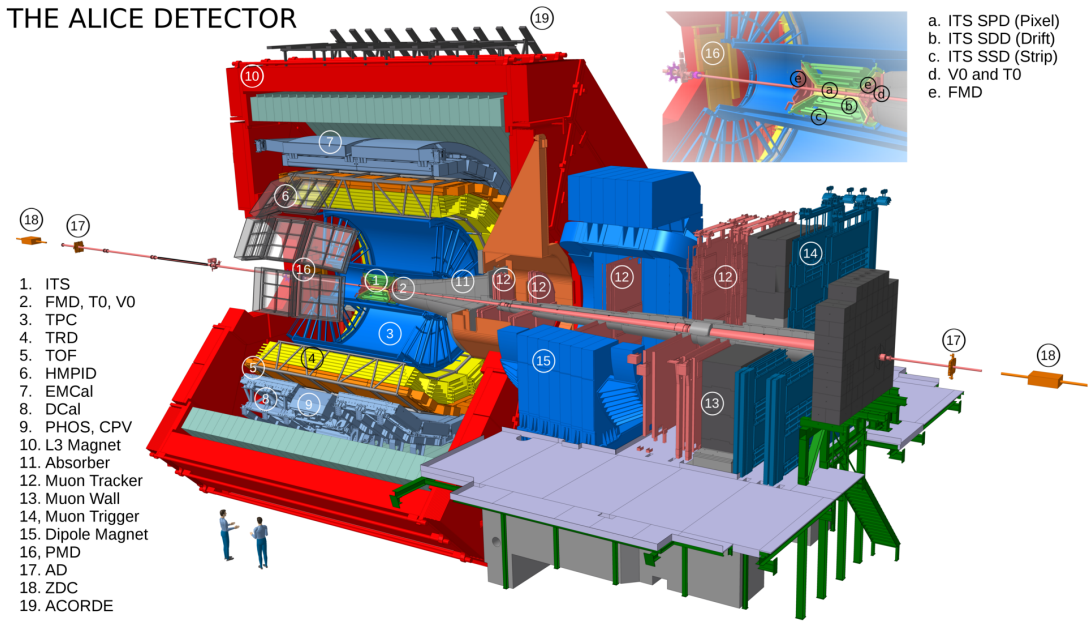

Figure 2.4: Diagram of the ALICE experiment, with labels for each subdetector.

2.3.1 Central Barrel Tracking

The central barrel of ALICE consists of four main subdetectors listed in order moving output from the beam: the Inner Tracking System (ITS), the Time Projection Chamber (TPC) the Transition Radiation Detector (TRD), and the Time-of-Flight detector (TOF)

ITS

The ALICE ITS is composed of three subdetectors, each with two layers of silicon tracking detectors. They are the first detector encountered by particles from the collision, with the innermost layer, called the Silicon Pixel Detectors (SPD) starting at 3.9 cm from the interaction point. Outside the SPD are the Silicon Drift Detectors (SDD), and Silicon micro-Strip Detectors (SSD). These are each visible in Figure 2.5, as the green detectors around the beam pipe. The ITS serves as a key part of the charged-particle tracking in the ALICE central barrel. In addition, the ITS is used to locate the vertex of the primary interaction and the vertices of strange-particle heavy flavor decays with a precision around 12 μm [17].

Time Projection Chamber (TPC)

The ALICE Time Projection Chamber (TPC) serves both to measure the momentum of charged particles as they ionize atoms in the gas contained within, as well as to identify particles according to the energy they deposit. The electrons freed from the ionization

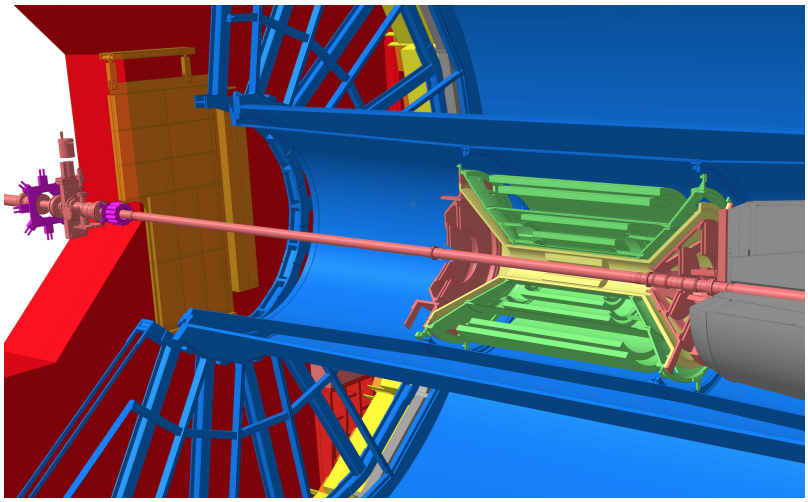

Figure 2.5: The Inner Tracking System is shown as the green detector layers around the beam pipe.

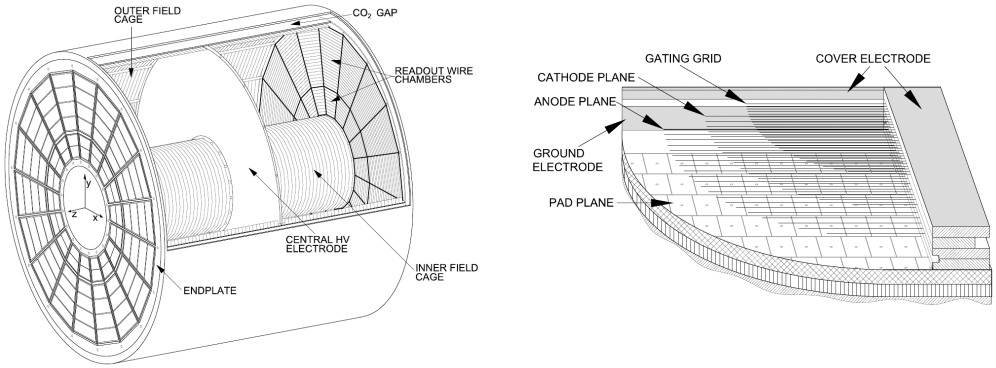

Figure 2.6: Schematics of the TPC. An overview is shown on the left, while a schematic of the readout chambers at the endplates are shown on the right. Electric fields propagate freed electrons from charged particles to the readout wire chambers at the end plates.

drift through the electric field within the TPC towards the two endplates, visible in Figure 2.6. The x-y coordinates of energy deposits is determined by the position of the signal from the electrons within the readout chambers. The z position of the ionization can be calculated using the relative timing of the primary interaction and when the electrons arrive at the chambers. The strength of the signal measured depends on how much energy the charged particles deposit, which depends on the mass and momentum of the particle. This is described by the Bethe formula [1], and can be used to identify the particles.

Transition Radiation Detector (TRD)

The Transition Radiation Detector (TRD), found between radii of 2.9-3.68 m from the interaction point, serves two purposes: high p_{T} electron identification and triggering on

high p_{T} charged particles. High momentum electrons passing through radiator layers emit X-rays that ionize gas in Multi-Wire Proportional Chambers. Charged particles also produce an ionization signal that is useful for triggering on high p_{T} particles and which can be included with the tracking in the ITS and TPC to improve tracking resolution [17].

Time-of-Flight (TOF)

The Time-of-Flight (TOF) detector is a layer of Multi-gap Resistive-Plate Chamber (MRPC) between the radii of 370 cm and 399 cm. Charged particles traversing the TOF ionize a gas under a high electric field, quickly creating a gas avalanche. Unlike other gas detectors such as the TPC, there is no significant drift time for signals, resulting in a superior timing resolution. The primary purpose of the TOF is to measure the time it takes for charged hadrons to reach the TOF from the interaction point, giving the velocity of the particles. In combination with the momentum measured in the ITS and TPC, this allows identification of charged pions and kaons up to 2.5 GeV/c and protons up to 4 GeV/c [17]. This is particularly useful for measurements for reconstructing less stable hadrons.

2.3.2 Calorimetry

Around the ALICE central barrel, two electromagnetic calorimeters are included in ALICE: the ElectroMagnetic Calorimeter (EMCal) and Photon Spectrometer (PHOS).

Electromagnetic Calorimeter

The ALICE EMCal is designed to aid the study of jet quenching by measuring photons and neutral mesons, including those produced by jets.

The EMCal is composed of 6 cm $\times$ 6 cm towers of alternating layers of $PbWO_4$ and lead. Each tower (sometimes called a cell) is of angular size $\Delta\phi \times \Delta\eta = 0.0143 \times 0.0143$ The towers are organized into large "super modules" that can be seen in Figure 2.7.

In Run 2 of the LHC, an extension of the EMCal called the Dijet Calorimeter (DCal) was added, opposite the existing EMCal section. The EMCal and the DCal together cover the φ ranges of $80 < \phi < 187°$ and $260 < \phi < 327°$ [18]. The positioning is shown in Figure 2.8.

The effective energy range is from 0 to 250 GeV and the energy resolution of the EMCal is parametrized in a formula given in Equation 2.6

$$\frac{\sigma}{E} = \sqrt{A^2 + B^2/E + C^2/E^2} \tag{2.6}$$

The parameters have been determined for the EMCal to be: $A = 1.7\%, B = 11.3\%$ and $C = 4.8\%$.

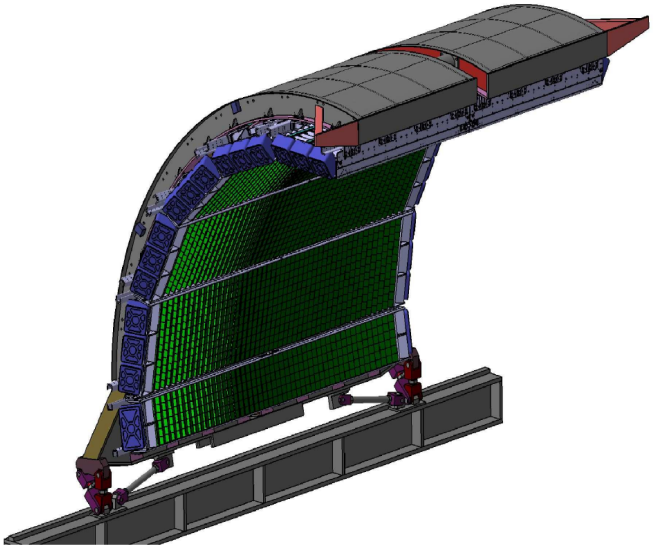

Figure 2.7: A schematic of the larger section of the EMCal. 10 full supermodules and 2 $1/3$-supermodules are included.

Photon Spectrometer (PHOS)

The Photon Spectrometer (PHOS) is an electromagnetic calorimeter similar to the EMCAL, but with finer angular resolution due to a smaller tower size of 2.2 cm $\times$ 2.2 cm and finer energy resolution. It covers a smaller acceptance and has a lower energy range (0-100 GeV) than the EMCal [17].

2.3.3 Forward Detectors

Vertex 0 (V0) Detector

The V0 detector consists of two discs of segmented scintillator counters, called VZERO-A and VZERO-C (also written as V0A and V0C), located on either side of the interaction point, on the A-side and C-side respectively, as shown in Figure 2.9. They have an asymmetric configuration determined by the constraint that the V0C is required to be in front of the hadronic absorber serving the muon arm. This results in an asymmetric coverage in η, with the V0A covering $2.8 < \eta < 5.1$ and V0C covering $-3.7 < \eta < -1.7$.

As the number of particles interacting with the V0 increases monotonically with the event centrality, the signal in the V0 can be used as a measurement of event centrality. Additionally, the angular distribution of hits in the V0 can be used to estimate the event plane angles, although the event plane resolution is particularly poor for the 4th order event plane due to the granularity of the detector.

The V0 also plays a key role in the event trigger system. The minimum bias (MB) trigger (intended to trigger on any inelastic collision without significant bias from any

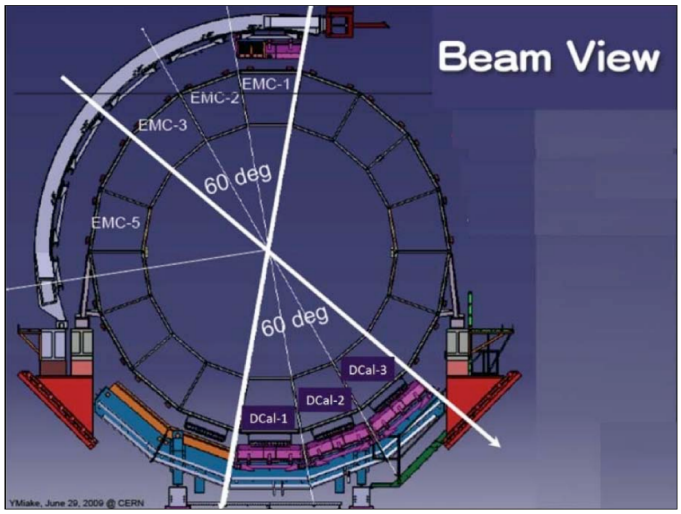

Figure 2.8: Diagram of the DCal positioned opposite the EMCal within the central barrel [18].

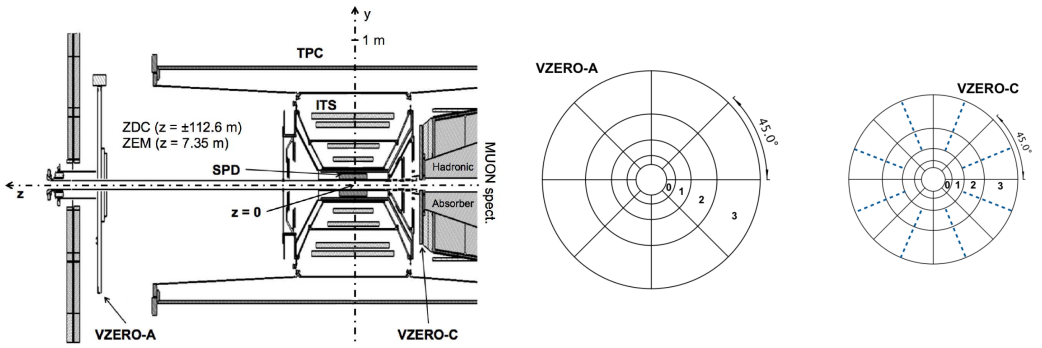

Figure 2.9: Diagram of the VZERO detector and its location within the central barrel.

variable or specific physical effect) typically used the detection of particles in both the V0A and V0C. This requirement allows the removal of events produced by interactions between a beam particle and a gas particle within the LHC, as detailed in Figure 2.10. Beam-gas collisions typically deposit energy in one side or the other, but not both, which can be understood simply from considering the center-of-mass frame of the beam-gas system [19].

Zero Degree Calorimeter

The Zero Degree Calorimeter (ZDC) consists of sets of hadronic calorimeters approximately 116 m from the interaction point. The ZDC is designed to measure spectator nucleons from heavy ion collisions. They consist of neutron calorimeters at 0° in the collision coordinate system, and proton calorimeters offset to account for the fact that the charged protons are offset slightly by the magnetic fields.

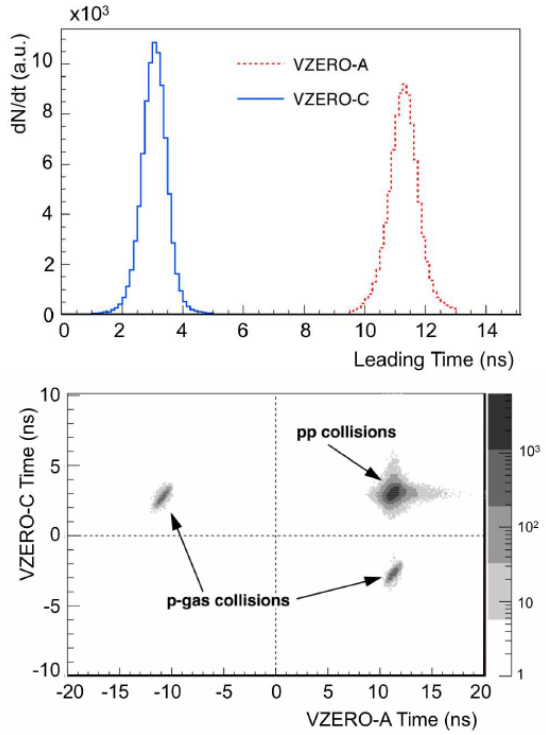

Figure 2.10: Time-of-flight for signals in the V0-A and V0-C, plotted separately in the top plot and correlated in the lower plot. The correlations between the signals allows discrimination between proton-gas collisions and proton-proton collisions by the V0 detectors [19].

2.4 Trigger

The ALICE detector has several dedicated event triggers designed to pick out events of interest, such as those with high energy clusters in the EMCal or with muons detected by the muon tracking arm, as well as events of no particular interest (Minimum Bias).

Event triggers are classified into level 0 (L0), level 1 (L1), and level 2 (L2) triggers. Level 0 triggers take the shortest amount of time to be evaluated per event.

2.4.1 Minimum Bias

A Minimum Bias (MB) trigger is designed to measure events in which an interaction between the nuclei or protons in the beam has occurred, but without any bias towards any type of event. A counter-example would be an event trigger that is more efficient in more central events, which would bias the distribution of events towards more central events. Many analyses, including analyses using dedicated triggers, also require a MB trigger to allow cross section measurements without relying on trigger simulations. Additionally, MB data is required for analysis focused on measuring flow and other bulk characteristics of the event.

As described in Section 2.3.3, the ALICE MB trigger uses coincidence between the V0A and V0C detectors to identify events with an inelastic collision occurring between the beams.

2.4.2 EMCal Trigger

The EMCal provides two levels of event trigger, starting with an L0 trigger using sliding window patches of 4×4 towers, requiring energy above a threshold typically set at 2.5 GeV. This trigger is evaluated by Trigger Readout Unit (TRU) electronics boards, of which there are three for each full supermodule of the EMCal. The level 1 trigger is evaluated by a Summary Trigger Unit (STU) board, of which there is one for the main EMCal section and one for the DCal.

The EMCal L1 trigger sums the energy deposited in a sliding window of different sizes. The Gamma patch is a window of 4×4 towers, like the L0 trigger, except that its window can cross the boundary between TRUs. The Jet patch is a sliding window in 32×32 towers.

Before the patches are compared to threshold, an estimate of the underlying event background is subtracted in Pb–Pb collisions. This is necessary to avoid the effective threshold of the trigger changing between different centrality ranges. In Run 1 of the LHC (2010-2013), this estimate was determined using the energy deposited in the V0 detector. In Run 2 (2015-2018), the background energy for the main EMCal section was determined from the median energy of patches in the DCal, and vice-versa.

In many data-taking periods there are two energy thresholds for each type of L1 trigger. For the 2015 Pb–Pb data set that this dissertation uses, only one energy threshold existed for each L1 trigger: 10 GeV for the Gamma patch and 20 GeV for the Jet patch.

Chapter 3

π^0-Hadron Correlations

The primary purpose of this thesis research has been to continue the effort to measure path-length dependence of jets in the QGP using the angle of jets relative to the event-plane to tune the path-length traversed by the jets within the same event.

In this analysis, high p_{T} π^0 mesons are used as a proxy for jets, in order to study dijet events. Hadrons correlated with the π^0 trigger can be used to measure the jet that produced the π^0 and the recoiling jet opposite it in azimuthal angle. By studying these correlations as a function of the angle between the π^0 and the reaction plane, we hope to measure path-length dependent effects through the ellipticity of the medium. This is expressed visually in Figure 3.1.

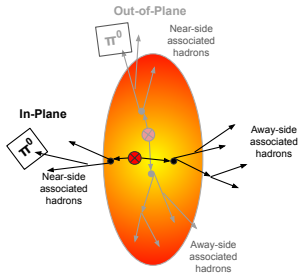

Figure 3.1: Diagram expressing the blueprint of this analysis. Jets oriented out-of-plane are expected to lose more energy than jets orientated in-plane.

One advantage of π^0s as a triggers for correlations is that high p_{T} π^0s set off the EMCal Gamma patch L1 trigger (described in Section 2.4.2), yielding significant statistics. Another advantage is that the transverse momentum of the π^0 is relatively simple to determine, in comparison to reconstructed jets. For jets, the clustering algorithms add a significant number of particles from the underlying event, which cannot be trivially removed. One disadvantage of π^0s or any single hadron as a trigger is that the connection to the initial parton p_{T} is weaker, as π^0s can arise from initial partons with a wide range of

initial p_{T}. However, requiring a π^0 trigger biases the triggered events towards those with jets that fragmented with a large fraction of their p_{T} in a single particle (the measured π^0).

This chapter is organized around the steps of this analysis, starting with how events were selected for this analysis. After that, the analysis follows the flow chart provided in Figure 3.2.

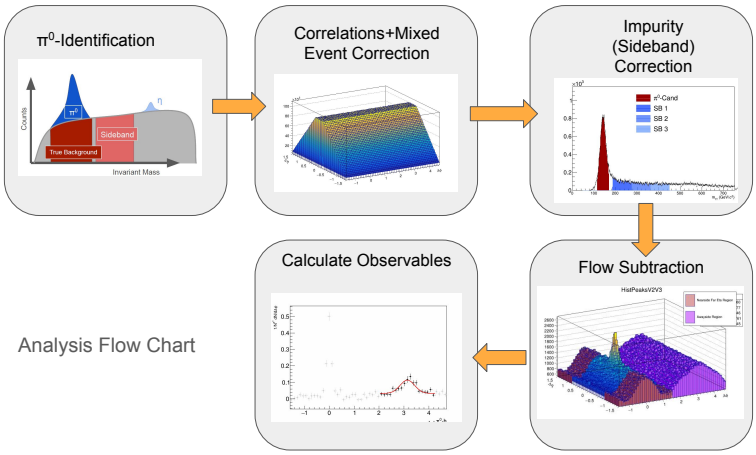

Figure 3.2: Flow chart of the major steps of this analysis.

The method for identifying π^0 candidates with the EMCal is described in Section 3.4.

After candidates for measured π^0 particles have been identified, it is necessary to calculate the purity of the π^0 sample, the fraction of π^0 candidates that correspond to true π^0s and not the combinatorial background from pairing clusters. This is necessary in order to apply the impurity correction, in which we remove the contribution from tracks correlated with the combinatorial background cluster pairs. This is one of the key challenges in this analysis, due to kinematic cutoff and the correlated background. The full procedure for determining the π^0 purity and our uncertainty in the parameter is given in 3.4.7.

After π^0 candidates have been selected, the next step is to measure their correlations in $\Delta\eta$ and $\Delta\varphi$ with charged tracks measured by ALICE's central barrel tracking. The first steps of this, including a correction for the tracking efficiency as a function of track p_{T} and η, are described in Section 3.5. These raw correlations still reflect effects of the finite acceptance of the detector, as well as some ϕ-dependence in the tracking efficiency. In order for the correlations to be comparable to theory and other experiments, the correlations are corrected for these effects with a mixed event correction, described in Section 3.6. Intermediate results at this stage are presented in Section 3.7, including some preliminary analysis.

At this point, the correlations reflect a combination of correlations between tracks and real π^0s and correlations between tracks and background cluster pairs. This is problematic, as the background pairs have different sources and thus create different correlations.

This represents a unique challenge for the analysis due to the lack of useable lower mass sideband region in the invariant mass spectrum for π^0s. This challenge and how it is met is described in Section 3.8.

After the correlations are corrected to reflect only those between charged hadrons and real π^0s, the next step is to extract the correlations that are due to high p_{T} jet physics. Specifically, the correlated particles that arise from the same high p_{T} hard scatter in the event. However, there are additional correlations that arise from the bulk features of the collision that are not the target of this analysis and act as a background.[1] The subtraction of this background is described in Section 3.9.

The following Section 3.10 delves into the calculation of systematic uncertainties that apply to final results. The final results are given with their uncertainties are provided in Section 3.11, including a comparison to theory predictions with the JEWEL model (which is described in more detail in 4.1).

3.1 Event Selection

The events used in this analysis were selected on a number of criteria, including ensuring that the subdetectors important for this analysis were running properly.

3.1.1 Data Sample

This analysis encompasses the Pb–Pb collision data set of 2015, during Run 2 of the LHC. Data is recorded by ALICE in continuous periods of time called runs, that typically last several hours. One purpose of this is to ensure that the data is organized into periods within which the detector properties and configuration are unchanging. Later, in offline analysis, quality assurance checks are done on a per-period basis, resulting in a table allowing the convenient definition of data sets of multiple runs in which specified subdetectors are performing well.

The analysis was performed on Pb–Pb at $\sqrt{s_{\mathrm{NN}}} = 5.02\ \mathrm{TeV}$ TeV. For the analysis period LHC15o with the first pass of reconstruction ("pass1"). A data set was defined that ensured that the following detectors were included in data-taking and functioning nominally:

- Inner Tracking detectors: SSD, SPD, SDD
- Time Projection Chamber
- Forward detectors: V0, ZDC

[1] Somewhere out there, a paper is being written on flow physics in which jet-related correlations are dismissed as background.

- Calorimeters: EMC

In the ALICE analysis train system the data set is called: LHC15o_pass1_AOD194 and includes the following runs:
246945, 246928, 246846, 246845, 246844, 246810, 246809, 246808, 246807, 246805, 246804, 246766, 246765, 246760, 246759, 246758, 246757, 246751, 246750, 246495, 246493, 246488, 246487, 246434, 246424, 246272, 246271, 246225, 246222, 246217, 246115, 246113, 246089, 246087, 246053, 246052, 246042, 246037, 246003, 246001, 245963, 245954, 245952, 245949, 245833, 245831, 245829, 245705, 245702, 245700, 245683

3.1.2 Centrality Selection

In this analysis, the standard ALICE determination of event centrality is used, which is the multiplicity in the VZERO detector. The number of particles in the VZERO varies as a monotonic function of the number of nucleons participating in the collision, which it turn is a function of the impact parameter b between the nuclei. This allows the classification of Pb–Pb events in approximate percentiles of the impact parameter, as shown in Figure 3.3. The 0-10% range represents the most central collisions (with the smallest impact parameter), while 90-100% are the most peripheral (with the largest impact parameter).

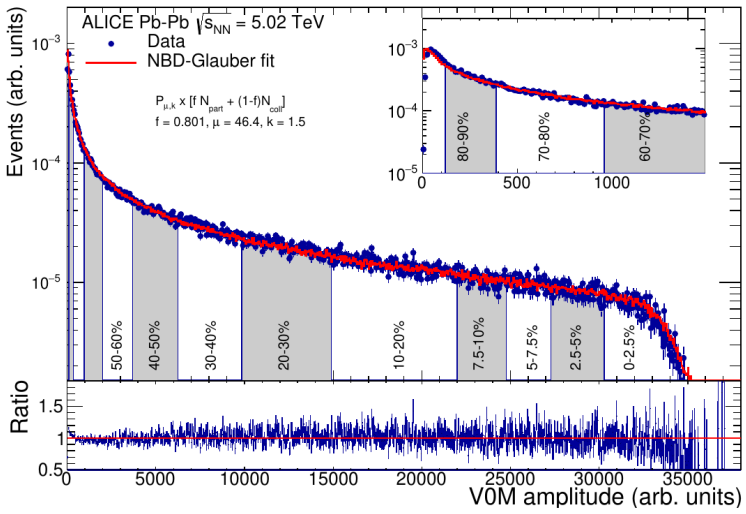

Figure 3.3: VZERO amplitude distribution, divided into centrality ranges. Overlaid is the result from a Glauber MC simulation [20].

This analysis examined events in the centrality ranges: 0-10%, 10-30%, 30-50%, and 50-90%, but the focus is on the 30-50% range, where the difference between the path-length traversed through the medium by out-of-plane jets and in-plane jets is expected to be significant and where the mixed event correction (see Section 3.6) worked as designed.

3.1.3 Event Trigger

The data used in the analysis consisted of events passing one of two trigger conditions: the Minimum Bias (MB) and EMCal Gamma (GA) trigger.

Mininum Bias Trigger

As described in Section 2.4, the MB trigger uses the detection of particles by the V0-A and V0-C detectors.

EMCal Trigger

This analysis makes extensive use of the EMCal Gamma (EGA) patch trigger. In the 2015o Pb–Pb period, the EGA trigger had a single threshold of 10 GeV. The performance of the trigger is quantified by the rejection factor (RF), which is the effective number of MB events rejected by the trigger. It is calculated by taking the ratio of spectra with the EGA trigger and the spectra with the MB. The determination of this is shown in Figure 3.4.

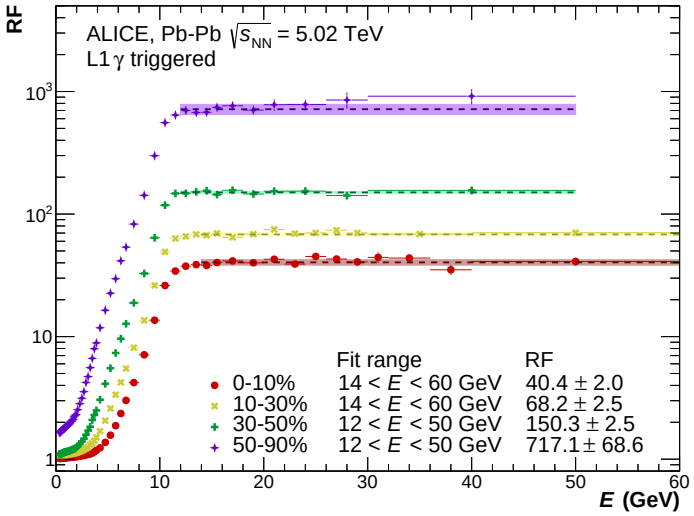

Figure 3.4: EMCal trigger rejection factor (RF) for the γ trigger.

One important characterization of the EMCal trigger is how it impacts the centrality distribution of events, relative to Minimum Bias. If the background subtraction procedure for the trigger is not performing well, then central events will have a lower effective energy threshold, introducing an unnatural bias towards more central events. However, some natural bias is expected, as more high energy clusters are expected as events become more central, as they are produced in proportion to the number of binary collisions N_{coll}. To test if this is true, the centrality distribution under a few different conditions is studied, as shown in Figure 3.5. To test if the EGA trigger's centrality bias is consistent with the N_{coll}

scaling effect, a quick offline emulation of the trigger is applied to the MB distribution, in which it is required that the event have a cluster above the trigger threshold of 10 GeV. It was found that the centrality bias with the EGA trigger was reasonably consistent with the 10 GeV cluster requirement.

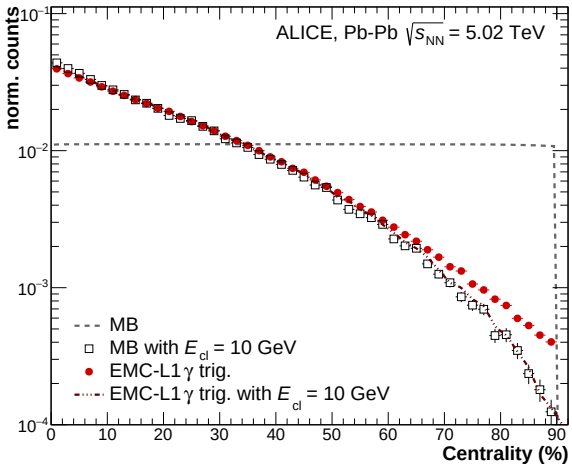

Figure 3.5: Centrality distributions in Minimum Bias and EMCal Gamma-triggered events, as well as the centrality distributions when 10 GeV cluster requirement is applied.

3.2 Clusters and Tracks

3.2.1 Track Selection

The track selection is done within the EMCal correction framework. This analysis uses hybrid tracks. All tracks with $0.15 < p_{\mathrm{T}} < 30\,\mathrm{GeV}/c$ and $-0.9 < \eta < 0.9$ were included into the analysis.

Tracking Efficiency

The selected tracks in the analysis were corrected for their finite reconstruction efficiency. In order to estimate the efficiency, Monte Carlo simulations were used (LHC16g1, Hijing min bias anchored to LHC15o). Figure 3.6 shows the 2D tracking efficiency in η and φ. The efficiency was determined by relating reconstructed tracks at detector level (matched to a particle level track) with a track at particle level (restricted to stable, charged particles)[2].

Since the η and φ inhomogeneity can be partially corrected for by the mixed event correction the main focus is on the varying reconstruction efficiency as a function of track p_{T}. Ideally the efficiency correction would be done in 3 dimensions, however, since this

[2]This tracking efficiency calculation and parametrization was done by Dr. Eliane Epple (LANL).

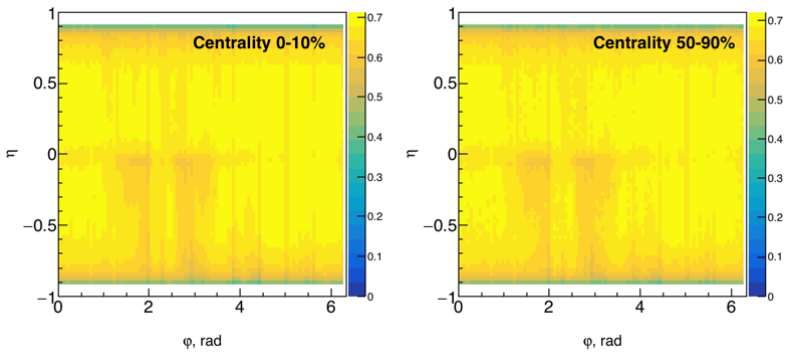

Figure 3.6: Tracking efficiency in η and in φ of the reconstructed track for central (left) and peripheral (right) event collisions

is overly complex we reduced the correction to two dimensions. As the acceptance varies more in η than in φ we developed a model for a 2D η-p_{T} dependent correction. The projections in p_{T} and η were fitted with functions in order to have a model with a continuous efficiency trend. Figure 3.7 shows the fitted projections for 0-10% and 50-90%, respectively (also fitted were the 10-30% and 30-50% centralities).

The fit of the distributions was carried out for p_{T} and η independently. Additionally, the low and high momentum part of the p_{T} spectrum was fitted by two independent functions, and the negative and positive η regions were fitted independently. The functions used for the fit are listed below:

$$\epsilon(p_{\mathrm{T}},\eta) = \left(\begin{array}{ll} p_0 - p_1 \cdot \frac{1}{p_{\mathrm{T}}} + p_2 \cdot e^{(\frac{p_{\mathrm{T}}-p_3}{p_4})^2} & (p_{\mathrm{T}} \leq 3.5) \\ p_5 + p_6 \cdot p_{\mathrm{T}} + p_7 \cdot p_{\mathrm{T}}^2 + p_8 \cdot p_{\mathrm{T}}^3 + p_9 \cdot p_{\mathrm{T}}^4 & (p_{\mathrm{T}} > 3.5) \end{array} \right) \times SF \times \quad (3.1)$$

$$\left(\begin{array}{ll} p_{10} \cdot e^{-(\frac{p_{11}}{0.91+\eta})^{p_{12}}} + p_{13} \cdot \eta + p_{14} \cdot e^{(\frac{\eta+0.04}{p_{15}})^2} & (\eta \leq -0.04) \\ p_{16} \cdot e^{-(\frac{p_{17}}{0.91-\eta})^{p_{18}}} + p_{19} \cdot \eta + p_{20} \cdot e^{(\frac{\eta+0.04}{p_{21}})^2} & (\eta > -0.04) \end{array} \right) \quad (3.2)$$

There is an additional scale factor, SF, that takes into account that the two parts were fitted individually and avoids a double correction. It is determined by the maximum of the η function. The fit showed an overall good description of the distributions resulting in the 22 parameters for the four centrality regions listed in Table 3.1. Since the low and high momentum part of the track spectrum had a significantly different distribution in η, two fit versions were performed. One over the full p_{T} spectrum (see middle row of Fig. 3.7) and one restricting the momenta to $> 1\,\mathrm{GeV}/c$(lowest row of Fig. 3.7). This leads to the two sets of parameter values displayed for parameters 10-21 in Table 3.1. The values in the brackets denote the results of the fit of the high momentum region.

The parameters in Table 3.1 together with Eq. 3.1 were used to develop a 2D model for the efficiency. By default the efficiency correction was done for the parameters not in

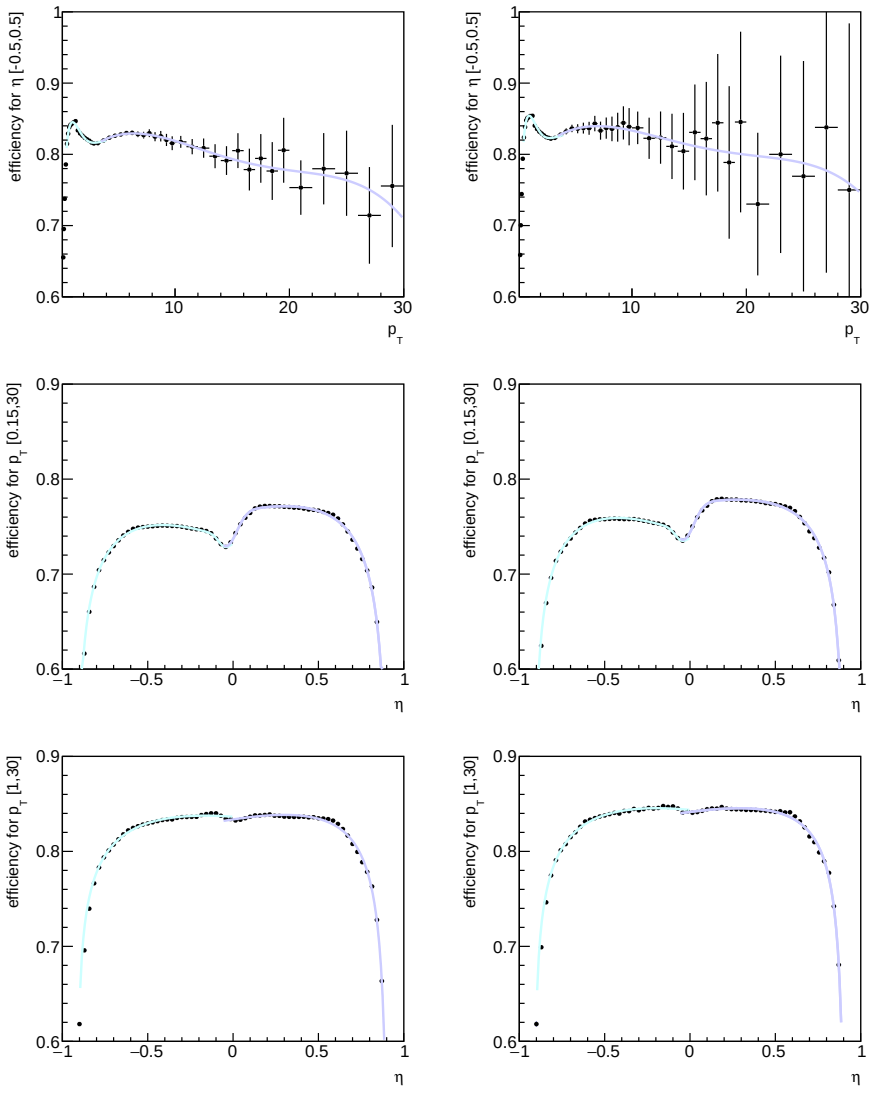

Figure 3.7: Projected tracking efficiencies for central (left), peripheral (right).

brackets in Table 3.1. Two variations were tested.https://www.overleaf.com/project/5d5eea8d2d10bd438fb
One for the parameters obtained with the fit to the higher momentum component (values in brackets in Table 3.1) and a second variation omitting the η dependence of the efficiency. These three models are displayed in Fig. 3.8.

3.2.2 Clusterization

In analyses using the ALICE EMCal, several algorithms are available to build clusters from the array of energies measured in each cell. Before clusterization, cells that have been determined to be malfunctioning are removed from analysis. These algorithms then work

Table 3.1: Parameters obtained by fitting the efficiency distributions as a function of p_{T} (p_0-p_9) and η (p_{10}-p_{21}) for different centralities. For the η distributions there are two values reported. One for the η efficiency for tracks with p_{T} ($0.15 - 30$ GeV/c) and in brackets for tracks with p_{T} ($1 - 30$ GeV/c).

Parameter	0-10%	10-30%	30-50%	50-90%
p_0	0.8350	0.8213	0.8381	0.8437
p_1	0.0621	0.0527	0.0648	0.0668
p_2	0.0986	0.0867	0.1052	0.1083
p_3	0.2000	0.1970	0.1478	0.2000
p_4	1.0124	1.1518	1.0320	0.9741
p_5	0.7568	0.7469	0.7628	0.7677
p_6	0.0277	0.0300	0.0263	0.0255
p_7	-0.0034	-0.0038	-0.0032	-0.0030
p_8	$0.1506 \cdot 10^{-3}$	$0.1704 \cdot 10^{-3}$	$0.1443 \cdot 10^{-3}$	$0.1260 \cdot 10^{-3}$
p_9	$-0.0023 \cdot 10^{-3}$	$-0.0026 \cdot 10^{-3}$	$-0.0023 \cdot 10^{-3}$	$-0.0019 \cdot 10^{-3}$
p_{10}	1.0086 (1.1330)	0.9726 (1.1979)	0.9076 (1.0597)	1.1259 (1.1182)
p_{11}	0.0074 (0.0011)	0.0066 (0.0010)	0.0065 (0.0014)	0.0105 (0.0014)
p_{12}	0.2404 (0.1785)	0.2543 (0.1465)	0.3216 (0.2239)	0.1961 (0.1959)
p_{13}	-0.1230 (-0.0623)	-0.1167 (-0.0577)	-0.1130 (-0.0619)	-0.1330 (-0.0675)
p_{14}	-0.0107 (0)	-0.0113 (0)	-0.0107 (0)	-0.0103 (0)
p_{15}	0.0427 (0)	0.0400 (0)	0.0456 (0)	0.0440 (0)
p_{16}	0.8579 (0.8871)	0.8729 (0.8912)	0.8521 (0.8851)	0.8421 (0.8849)
p_{17}	0.0088 (0.0066)	0.0122 (0.0079)	0.0073 (0.0059)	0.0066 (0.0059)
p_{18}	0.4697 (0.5648)	0.4537 (0.5454)	0.4764 (0.5721)	0.5061 (0.5932)
p_{19}	0.0772 (0.0593)	0.0965 (0.0703)	0.0668 (0.0524)	0.0580 (0.0505)
p_{20}	-0.0352 (0)	-0.0328 (0)	-0.0363 (0)	-0.0379 (0)
p_{21}	0.0645 (0)	0.0623 (0)	0.0668 (0)	0.0651 (0)

by starting with a seed cell, which has a large energy deposit above a "seed" threshold. Then cells sharing an edge with the seed and above a cell energy threshold are added to the cluster. What happens next depends on which algorithm is used. Several algorithms are used in ALICE, the two most popular being the V1 and V2/V3([3]) In the V1 algorithm, cells above the cell threshold and bordering a cell in the cluster are added to the cluster, and this process iterates until there are no neighboring cells above threshold available to add. In high multiplicity events, this can result in anomalously large clusters combining energy deposits from multiple particles. This can be characterized by counting the number of local maxima (NLM) in a cluster and requiring that clusters used in an analysis have only 1.

The V2/V3 clusterizer adds cells together similarly, but does not add a cell if its energy

[3] V3 is identical to V2, except that it is more efficient. However, V2 is often the name used in descriptions.

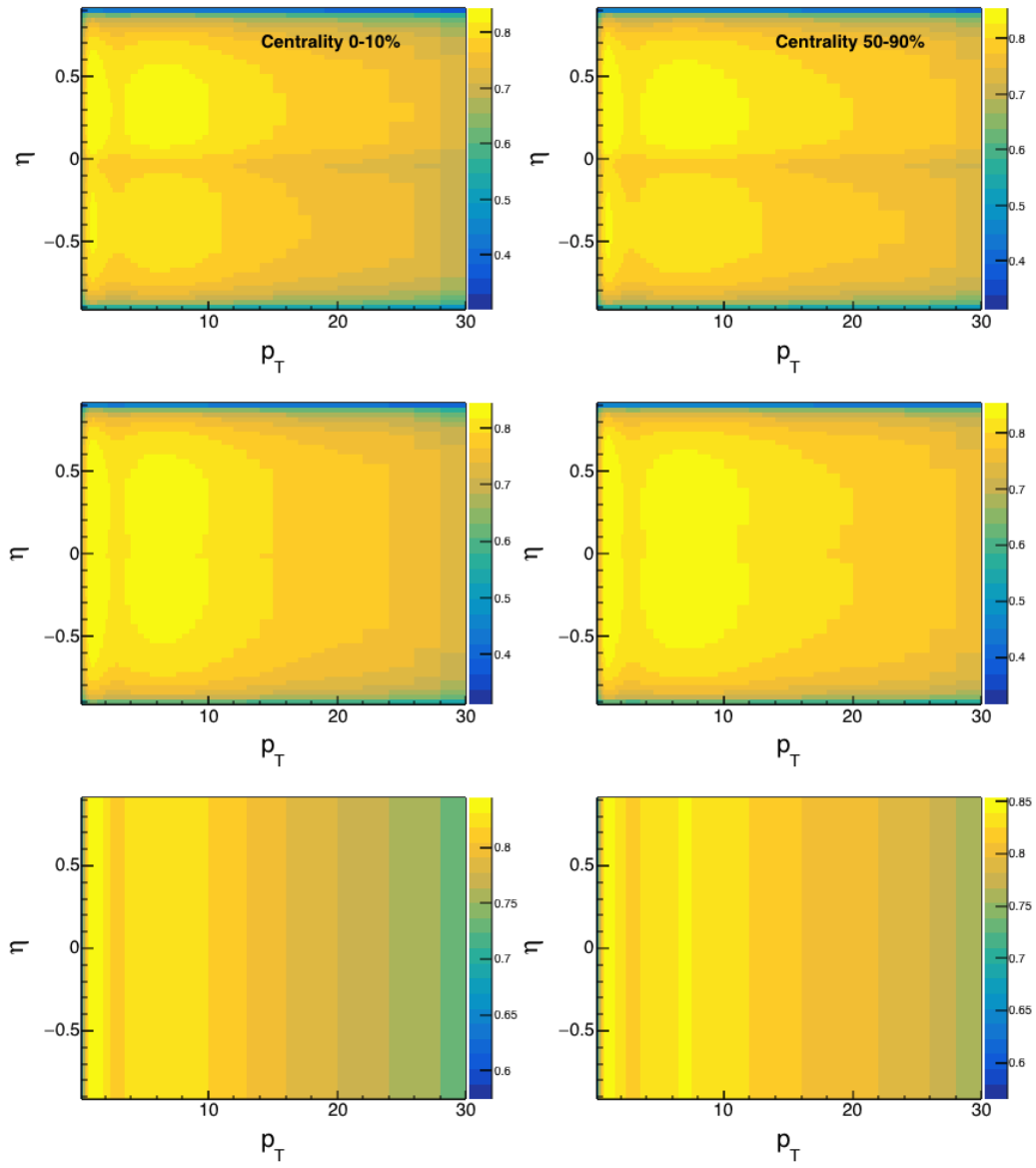

Figure 3.8: Projected tracking efficiencies for central (left), peripheral (right) collisions. First row is the standard efficiency model used for the correction obtained with tracks of $p_{\mathrm{T}} > 0.15\,\mathrm{GeV}/c$. The second row shows a model obtained with higher momentum tracks $p_{\mathrm{T}} > 1\,\mathrm{GeV}/c$and the third row shows a model that only has a p_{T} dependence but no η dependence. The left and right columns show the 0-10% central and 50-80% most central, respectively.

is greater than the neighboring cell already in the cluster. This serves to avoid combining energy deposits from neighboring particles, and forces the number of local maxima to always be 1. This is considered to be the default clusterization algorithm for Pb–Pb collisions.

In the V1+unfolding algorithm, the V1 clusterizer is initially used, but then a procedure similar to the V2/V3 clusterizer is applied to divide the cluster into subclusters. Then the energy of cells on the borders between subclusters is split between the two clusters.

The different clusterizers are explained visually in Figure 3.9. This analysis uses the V2/V3 clusterizer, but in principle could be done with the V1+unfolding algorithm as well. The clusterizer parameters for this analysis are listed in Table 3.2.

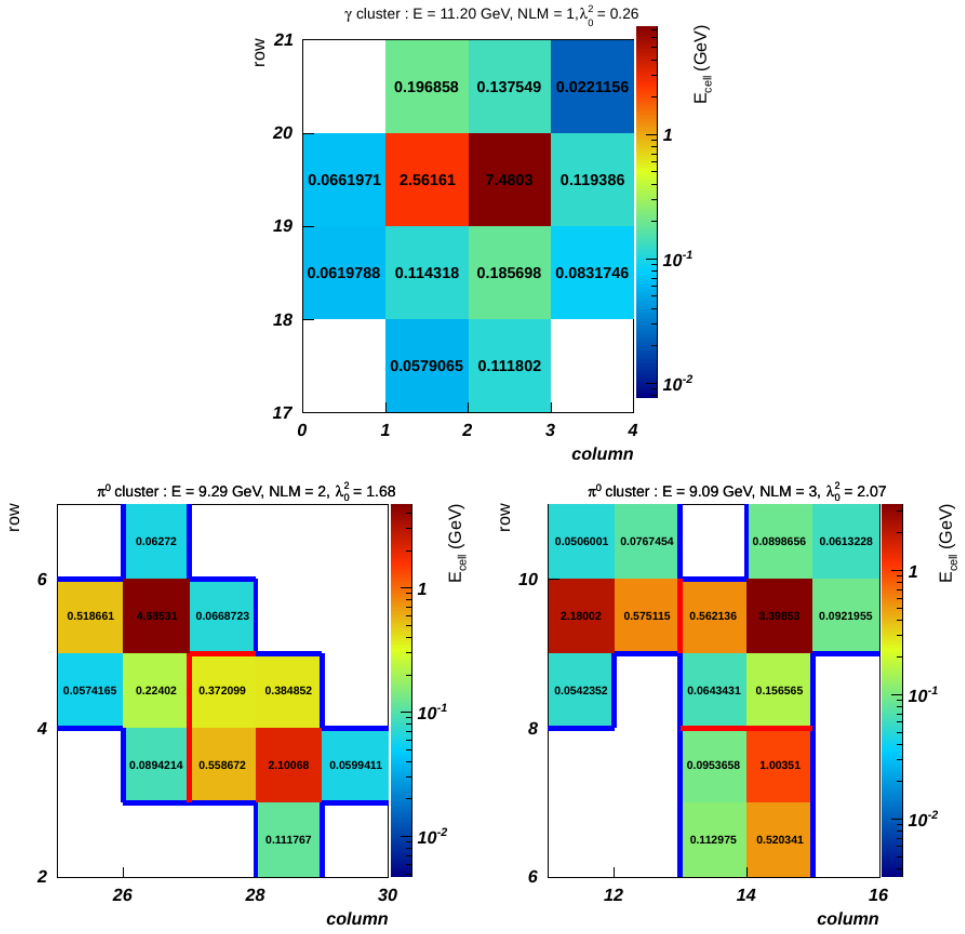

Figure 3.9: Cell level display of ALICE EMCal clusterization. Each collection of cells would be combined as a single cluster by the V1 algorithm, while the partitions by the V2 or V1+unfolding are outlined with red and blue lines. Figures from [21]

For the cell correction the new EMCal correction framework is used (AliEmcalCorrectionTask). The individual corrections configuration file that is used is included in appendix Section B.1.

Modules enabled were:

- CellEnergy,

- CellBadChannel,
- CellTimeCalib,
- Clusterizer,
- ClusterExotics,
- ClusterNonLinearity,
- ClusterTrack Matcher,

In the Clusterizer part additional settings enabled were:

- clusterizer: kClusterizerv3
- recalDistToBadChannels: true

The clusterization was done with

Table 3.2: Parameters for the EMCal clusterization in this analysis.

Description	Value
Seed thresh.	500 MeV
E_{min} cell	100 MeV
clusterizer	V3
non lin. corr.	kBeamTestCorrectedv3

3.2.3 Cluster S‘election

Clusters were selected by the GetAcceptCluster() function of the AliClusterContainer class. There cluster cuts (ApplyClusterCuts) and kinematic cuts (ApplyKinematicCuts) are applied. The cut values for these selections are listed in Table 3.3. Further selection cuts were applied, which are summarized in Table 3.4. Figure 3.10 shows the time distribution on which the cut is applied.

In this analysis, we do not apply any fiducial volume cuts on the cluster position (defined by the maximum cell energy within the cluster). We include all clusters for the analysis, no matter if they are right next to a bad channel or a supermodule edge. In general, there is a significant fraction of clusters affected by a vicinity to a bad cell or a supermodule border. Figure 3.11 shows the percentage of clusters that is close to a bad cell and/or a border (defined by the position of the maximum energy cell in the cluster). The fraction is similar for all clusters and clusters with cluster shapes in the typical γ-region. Since 30% of clusters would be rejected by a typical fiducial volume cut (one cell away from border and bad channels) these type of clusters were more closely investigated.

Table 3.3: Cluster cuts in the GetAcceptCluster() function.

Cut	Value	Comment
IsEMCal	kTRUE	Throws out PHOS clusters
Cluster Time	$\pm$ 50 ns	See Figure 3.10
fExoticCut	kTRUE	Rejects exotic clusters
minPt, maxPt	0, 1000.	GeV/c
minE, maxE	$> 2\,\mathrm{GeV}/c$, 1000	Rejects low energy clusters
minEta, maxEta	-0.7,0.7	No cut, see Sec. 3.2.3

Table 3.4: Cluster cuts in the AccClusterForAna() function

Cut	Value	Comment
Number of cells	> 1	Throws out one cell clusters
NLM	< 2	Number of local maxima in the cluster
λ_0^2	$0.1 - 0.5$	Cluster shape parameter.
Track matching	kTRUE	$\lvert\Delta\eta\rvert < 0.010 + (p_T + 4.07)^{-2.5}$, $\lvert\Delta\varphi\rvert < 0.015 + (p_T + 3.65)^{-2}$see Sec. 3.3.1
E/p matching cut	None	Intensively tested, see Sec. 3.3.1

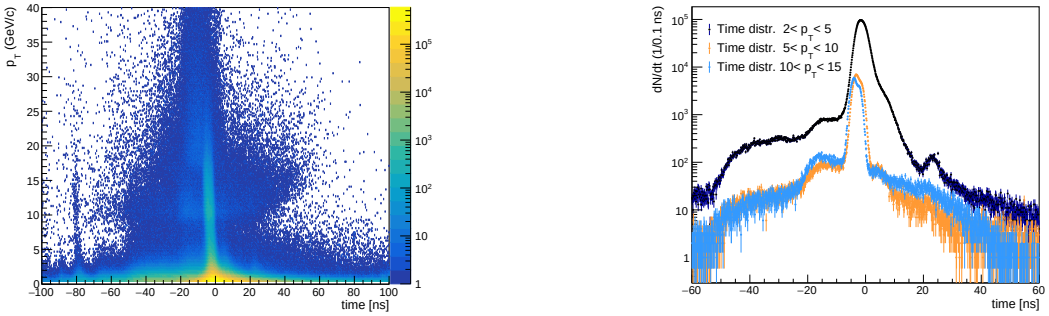

Figure 3.10: Left: cluster time vs. p_{T} of events with an EGA trigger, right: time distribution for three intervals of cluster momenta.

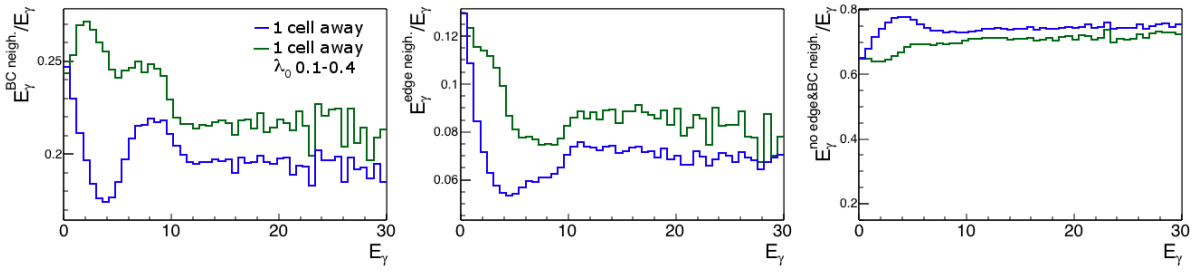

Figure 3.11: Fraction of clusters in the vicinity of a bad channel (panel 1), a SM edge (panel 2), and neither one of the two (panel 3). The fraction is given for all clusters and γ candidates.

3.3 Track Cluster Correction

While the Electromagnetic Calorimeter is intended for measuring photons and electrons, other particles in the event will also deposit energy. Some of these are massive charged particles, such as charged hadrons and muons, that deposit a small amount of energy in the detector. These so-called "Mininum Ionizing Particles" (MIPs) are estimated to deposit an average of 234 MeV, based on simulations with GEANT4 and an analysis of test beam results.

The contribution of charged particles to EMCal clusters is generally a problem for physics analyses, as it can lead to particles being counted twice in analyses. For this analysis, they are of concern because of their impact on reconstructed π^0s.

During analysis, the tracks of charged particles are extrapolated to their intersection with the EMCAL. Then for each EMCal cluster, nearby tracks which may have contributed partially or fully to the cluster can be identified. The tracks are labelled as matched if their extrapolated position differs from the cluster by less than the track p_{T}-dependent cuts given in Equations 3.3 and 3.4:

$$|\Delta\eta| < 0.010 + (p_T + 4.07)^{-2.5} \tag{3.3}$$

$$|\Delta\varphi| < 0.015 + (p_T + 3.65)^{-2} \tag{3.4}$$

We have tested several strategies for using applying tracking information to improve performance on measuring π^0s. We have primarily considered applying a veto on clusters with well-matched tracks and applying a hadronic correction. For purposes of comparison, the π^0 candidate analysis has also been done with neither a veto nor matching.

The next section presents the track matching cluster veto, which was investigated but ultimately not used.

3.3.1 Cluster Veto

We apply a track p_T dependent track-cluster matching that is commonly used in ALICE measurements. The angular correlation of potential cluster-track matches is shown in Figure 3.12.

After clusters have been matched to tracks, we compare the cluster energy and track momenta by calculating $E_{\text{clus}}/p_{\text{track}}$. By removing clusters that have at least one matched track such that $E_{\text{clus}}/p_{\text{track}}$ is near 1, we can remove clusters likely produced by electrons, as electrons deposit all of their energy in the EMCal and their energy is approximately equal to their momentum at these energies due to the low mass of electrons.

To optimize this cut, an analysis was done over a subset of the LHC16h4 Monte Carlo production (π^0s and ηs injected in MB HIJING). Invariant mass spectra were computed

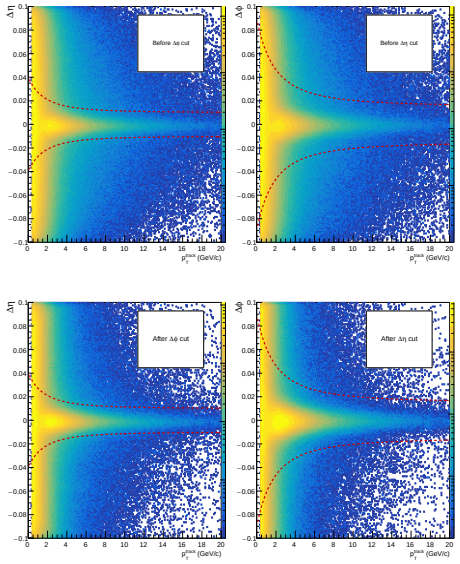

Figure 3.12: Track cluster matching, MB, (30-50% Centrality). On the left are the correlations in $\Delta\eta$ and on the right are the correlations in $\Delta\phi$. The top plots show the raw distributions, the bottom plots show the distributions after the other cut ($\Delta\eta$ or $\Delta\phi$) has been applied.

for pairs of clusters, focusing on the π^0 peak in various p_T bins. Using the Monte Carlo cluster information, pairs were matched to either true π^0 signals (the two clusters came from the same π^0) or background. This signal and background was integrated around the π^0 peak, and the peak significance $\frac{\text{Signal}}{\sqrt{\text{Background}}}$ was calculated. This was done while varying either the upper or lower cut on $E_{\text{clus}}/p_{\text{track}}$. While varying the lower (upper) cut, the upper (lower) was fixed at 1.4 (0.6).

To optimize the cut, we seek the highest peak significance. For the lower cut, the cut values 0.05, 0.1, and 0.2 consistently give the highest peak significance. For the upper cut, increasing the cut above 1.3 yields lower peak significance. The final $\frac{\text{Signal}}{\sqrt{\text{Background}}}$ cut that was considered was [0.1,1.2].

3.3.2 Hadronic Correction

An alternative to vetoing clusters that have matched tracks, intended to remove the contribution of charged hadrons and electrons to the clusters, is to directly subtract the energy from the clusters. For each track matched to a cluster, we subtract the energy deposited by a minimum-ionizing particle (MIP), which describes most of the hadrons hitting the EMCal.

This has the advantage of removing the contribution of MIPs to photon clusters, and hence, improving resolution of π^0 identification via invariant mass.

This approach is also attractive for this analysis because it is expected to impact π^0 detection efficiency less in high multiplicity events.

The disadvantage of this approach is that electron clusters will not be removed, instead having the estimated MIP energy subtracted. These electron clusters will then be part of the combinatorial background of cluster pairs.

Initially, we used an energy of 290 MeV for the MIP. This value corresponds to an estimate based on GEANT3 simulations of the detectors. This value has been updated for data to 234 MeV, a value consistent with GEANT4 simulations and test beam data. It will be appropriate to still use 290 MeV for GEANT3 based simulations, although GEANT4 simulations would be greatly preferred.

It may be of some value to note the impact of this update, to see if the analysis is particularly sensitive to this parameter.

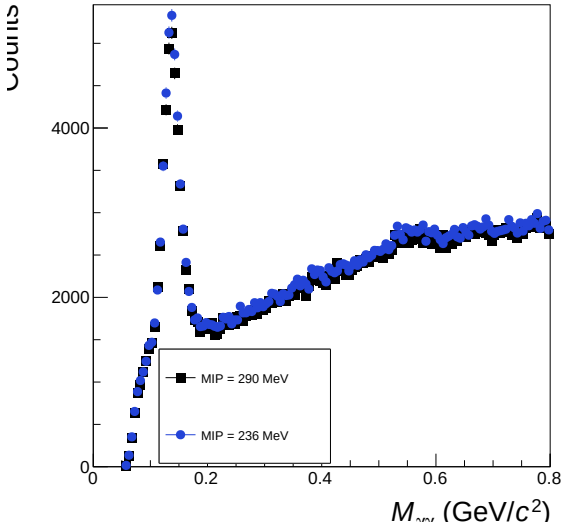

Figure 3.13: $5 \leq p_T < 7$ GeV/c cluster pairs in MB 10-30% Central events.

A comparison of the analysis with 290 MeV and 236 MeV as the hadronic correction energy was done. There are only minor changes to the peak parameters found, as seen in Figures 3.13, 3.14, 3.15, 3.16, and 3.17. In MB events, using the more accurate MIP energy seems to improve the resolution of the π^0 peak (decrease the width, σ) for events in centrality 0-50%, while the resolution may worsen slightly in the 50-80% bin.

One important aspect to consider when choosing what correction to apply is how it affects the efficiency of the π^0 measurement. In particular, it is important to know if the efficiency is significantly reduced at high multiplicities, such as those encountered along the direction of the reaction plane.

As can be seen in Figure 3.18, there is no significant change in the shape of the distribution of π^0-candidates vs the event plane.

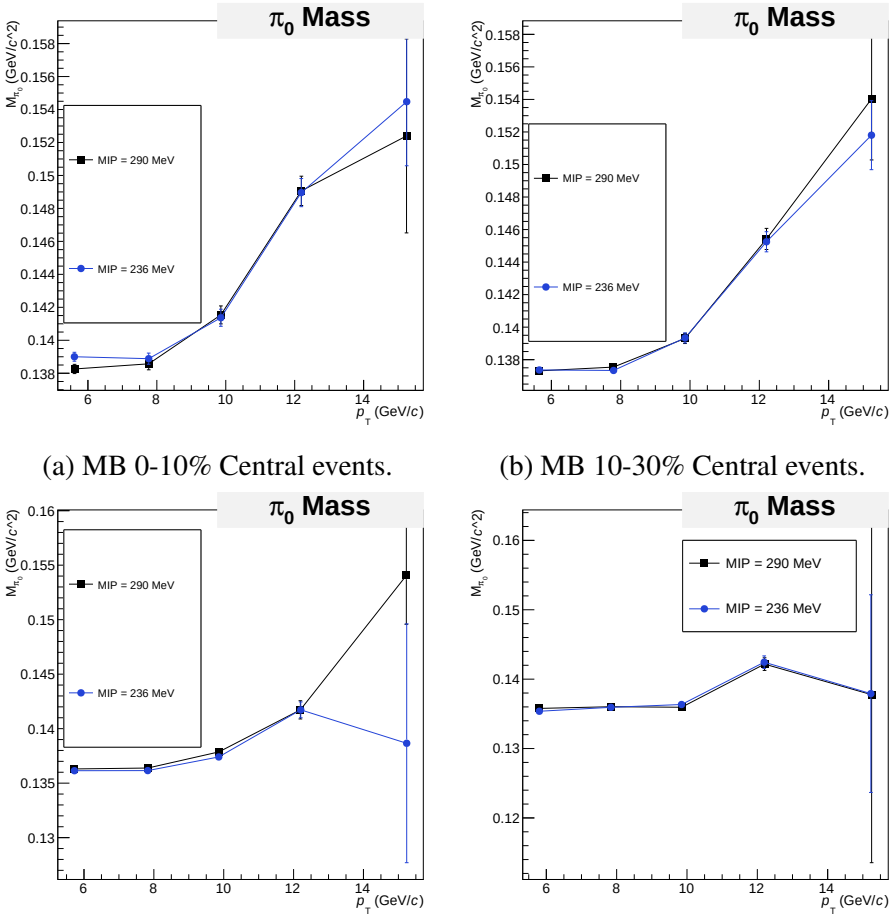

(a) MB 0-10% Central events.

(b) MB 10-30% Central events.

(c) MB 30-50% Central events.

(d) MB 50-80% Central events.

Figure 3.14: Comparison of mass peak position with the different MIP energies.

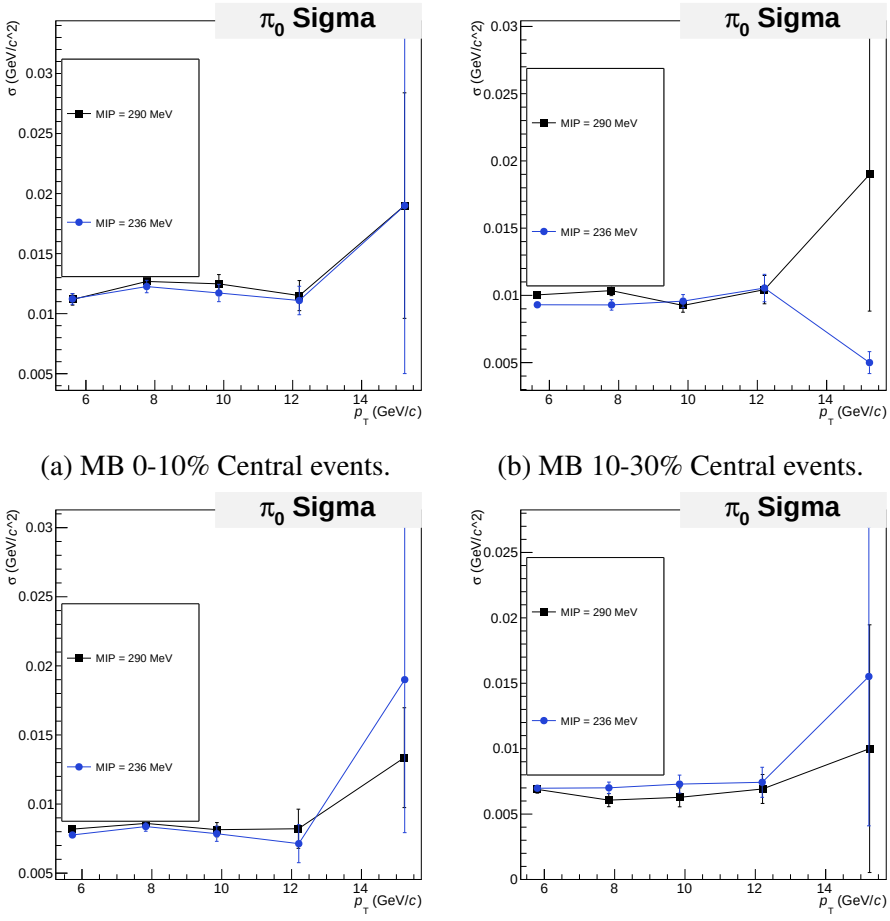

(a) MB 0-10% Central events.

(b) MB 10-30% Central events.

(c) MB 30-50% Central events.

(d) MB 50-80% Central events.

Figure 3.15: Comparison of mass peak widths with the different MIP energies.

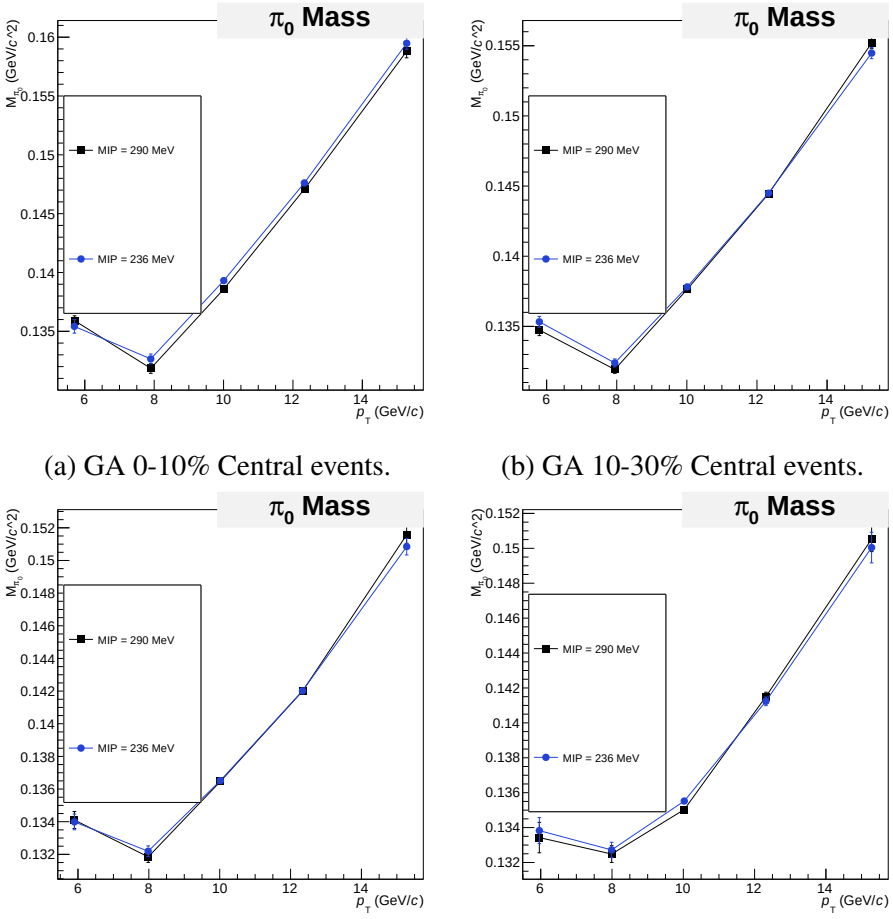

(a) GA 0-10% Central events.

(b) GA 10-30% Central events.

(c) GA 30-50% Central events.

(d) GA 50-80% Central events.

Figure 3.16: Comparison of mass peak position with the different MIP energies in EMCal Gamma triggered events.

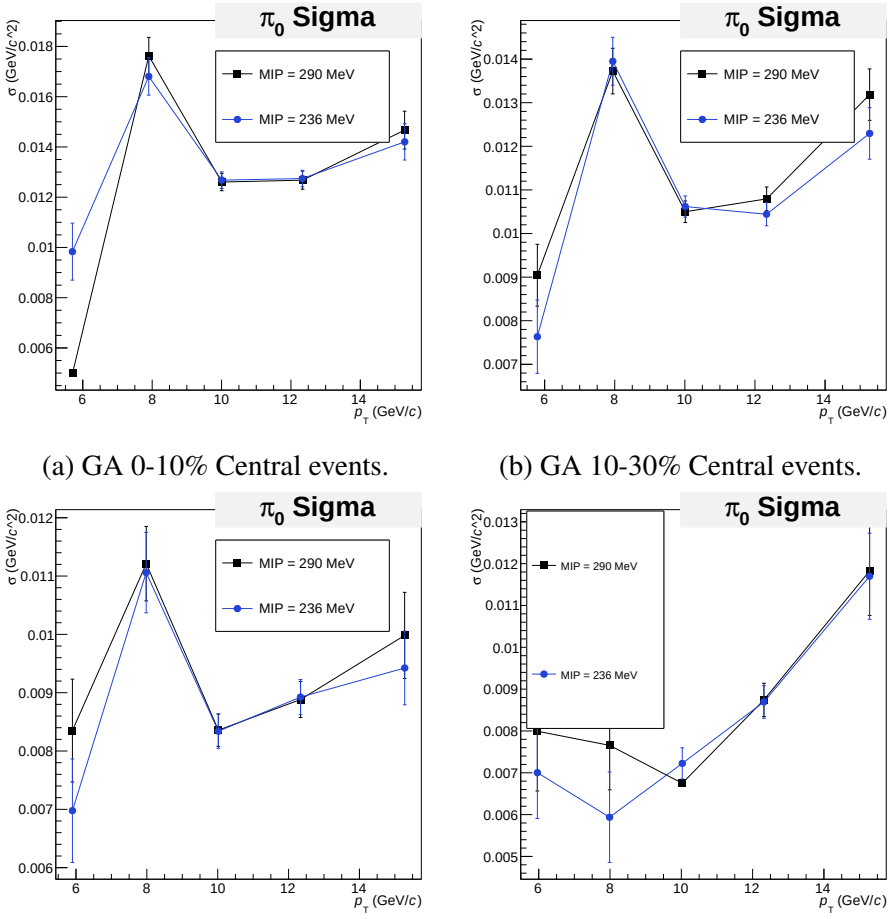

(a) GA 0-10% Central events.

(b) GA 10-30% Central events.

(c) GA 30-50% Central events.

(d) GA 50-80% Central events.

Figure 3.17: Comparison of mass peak widths with the different MIP energies in EMCal Gamma triggered events.

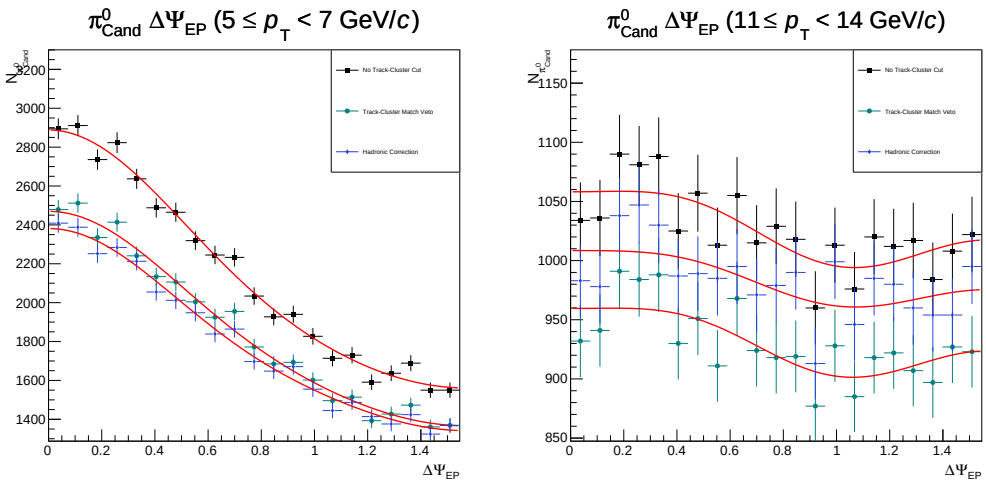

Figure 3.18: π^0 candidates vs the event plane for different track-cluster corrections (MB, 30-50% central on left, EGA 30-50% central on right). Fits including v_2 and v_4 terms are overlayed.

3.4 π^0 Identification

In this analysis, π^0s are identified using pairs of energy clusters in the EMCal. This is one among many methods that are available with the ALICE detector. Other methods make use of the PHOS detectors, as well as conversions of photons to e^+e^- pairs within the central barrel.

3.4.1 Cluster Cuts

Several cuts are applied to the EMCal clusters before they are used to reconstruct π^0 candidates. The most basic cut applied is requiring a 2 GeV minimum cluster energy, which conserves processing time and memory. The focus of this analysis has been on π^0s in an intermediate p_T range of $5 - 17$ GeV/c. The phase space of cluster pairs with p_T above 5 GeV/c and invariant mass near 135 MeV (the π^0 mass) is unaffected by this cut.

Shower Shape

Photons produce very circular clusters, while merged π^0 clusters and charged hadrons produce more elliptical clusters. This can be used to exclude some non-photonic clusters by cutting on the shower shape. This is done by quantifying the shape via covariances $\sigma_{\eta\eta}$, $\sigma_{\eta\varphi}$, and $\sigma_{\varphi\varphi}$, which are defined by:

$$\sigma^2_{\alpha\beta} = \sum_i \frac{w_i \alpha_i \beta_i}{w_{\text{tot}}} - \sum_i \frac{w_i \alpha_i}{w_{\text{tot}}} \sum_i \frac{w_i \beta_i}{w_{\text{tot}}} \tag{3.5}$$

The variables α_i and β_i are the indices in the η or φ axis of cell i, while w_{tot} is the sum of weights w_i, which are defined by:

$$w_i = \max(0, w_0 + \ln(E_i/E)) \tag{3.6}$$

where E_i is the energy in cell i and E is the total energy in the cluster. The parameter w_0 is fixed to 4.5 to exclude cells with less than 1.1% of the cluster energy.

Then we characterize each cluster with the shower shape variable σ^2_{long}, defined as such:

$$\sigma^2_{\text{long}} = \frac{\sigma_{\eta\eta} + \sigma_{\varphi\varphi}}{2} + \sqrt{\frac{(\sigma_{\eta\eta} - \sigma_{\phi\varphi})^2}{4} + \sigma^2_{\eta\varphi}} \tag{3.7}$$

The circular clusters formed by photons typically have a σ^2_{long} near 0.25, while hadrons and merged clusters have larger σ^2_{long}. A standard cut used in ALICE is to require $0.1 < \sigma^2_{\text{long}} < 0.5$[46]. For this analysis, an in-depth study was performed to see if this cut is optimal for this analysis, detailed in Section 3.4.4.

3.4.2 Cluster Pair Cuts

Two cuts on properties of cluster pairs are applied to optimize statistics and the signal-to-background ratio. An additional consideration is the ease of modelling the combinatorial background.

Asymmetry

For high p_{T} cluster pairs, cutting out highly asymmetric cluster pairs reduces the combinatorial background from low-energy clusters paired with high-energy clusters. As with most experimental cuts, it removes some signal with some background. To evaluate whether to apply such a cut, we can make direct comparisons of the results with and without the cut. In Figures 3.19 and 3.20, the maximum range of acceptance asymmetry values is varied while examining the invariant mass spectrum for a single p_{T} bin and the calculated ratio of signal to total for all five p_{T} bins. Apart from the 14-17 GeV/c bin for minimum bias data (which has negligible statistics with the current cuts), no significant effect is observed. A stronger asymmetry dependence would likely be seen if the minimum cluster energy cut were lower (currently 2 GeV).

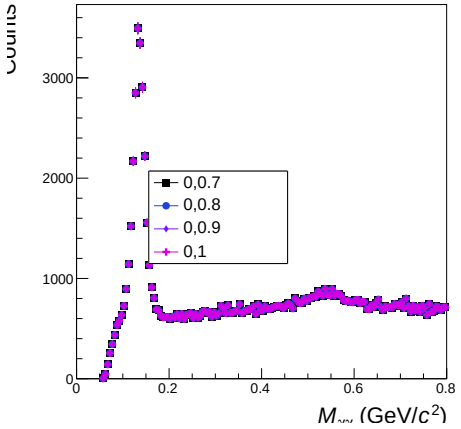

(a) Invariant mass spectra for MB 30-50% centrality events, $5 \leq p_{\mathrm{T}} < 7$ GeV/c with different asymmetry cuts (see legend) applied.

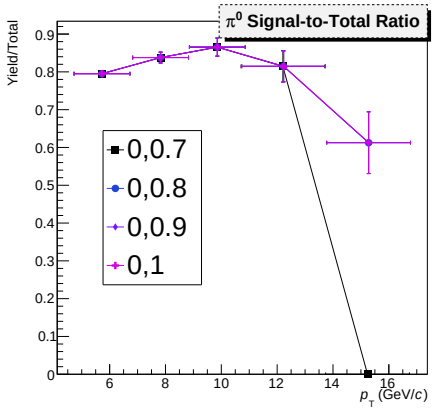

(b) Estimated π^0 purity (yield/total) for MB 30-50% centrality events, in different p_{T} bins with different asymmetry cuts (see legend) applied.

Figure 3.19: Testing three different ranges for the asymmetry cut in MB data, 30-50% central events.

Opening Angle Cut

In similar analyses by ALICE, a minimum opening angle cut is applied for pairs of clusters. The purpose of this is to improve the performance of mixed-event techniques (in

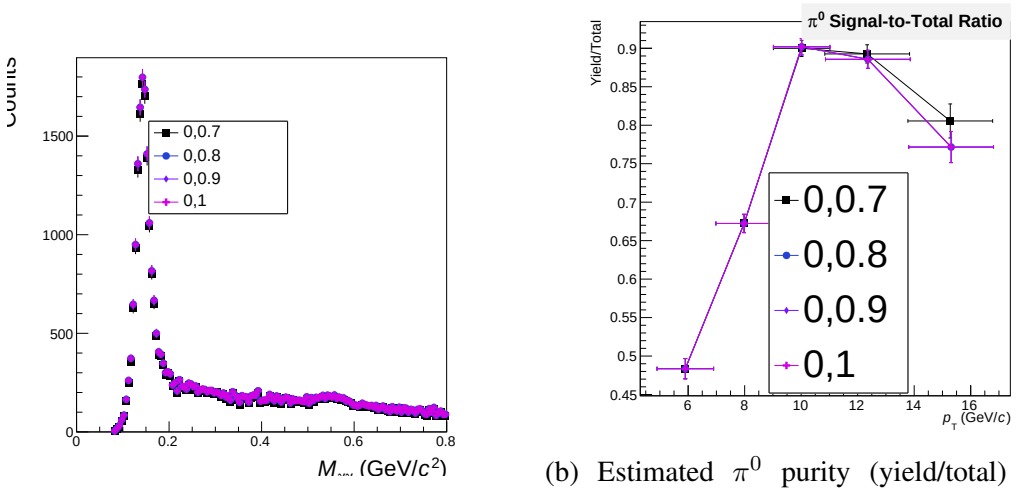

(a) Invariant mass spectra for EGA 30-50% centrality events, $11 \leq p_{\mathrm{T}} < 14$ GeV/c with different asymmetry cuts applied.

(b) Estimated π^0 purity (yield/total) for EGA 30-50% centrality. events, in different p_{T} bins with different asymmetry cuts (see legend) applied.

Figure 3.20: Testing three different ranges for the asymmetry cut in EGA data, 30-50% central events.

which clusters from different but similar events are paired to produce a signal-free invariant mass distribution) to model the background from combinatorial cluster pairs. The underlying idea is that in the data, there is an effective opening angle cut that occurs due to cluster merging: clusters sufficiently close to this will be merged, even with the V2 clusterizer. Without an opening angle cut, the mixed-event invariant mass distribution will not have this cutoff. Inconveniently, the cutoff from merging is not an exact cutoff, but depends on the shape of the two clusters. The event mixing technique is not effective at high p_{T} due to the correlated background from jets, which will be investigated in Section 3.4.3.

As described more in Section 3.4.3, the background estimation technique is entirely based on functional fits. However, such a method still has an issue from cluster merging. While the physical background shape before detector effects may be assumed to be a smooth function, we know that the shape of the background will have a cutoff at small opening angles, which a smooth functional fit may have trouble describing. This same problem also applies to the signal fit. One feasible approach that was investigated was to include a cutoff function acting as an envelope to the signal and background functions.

To avoid having too many free parameters, the envelope function is determined first, before the final fit. To simplify the shape of the cutoff, a sharp opening angle minimum cut is applied. Then the invariant mass spectra is compared with and without the opening angle cut, to determine the shape of the cutoff in the mass spectra. The can be modelled analytically, but it still depends on the actual cluster distributions, particularly the asymmetry distribution.

To help parametrize the shape, a wide range of opening angle cuts was applied. The effect of the cutoff shifting with the opening angle is shown for two different p_{T} bins in Figure 3.21.

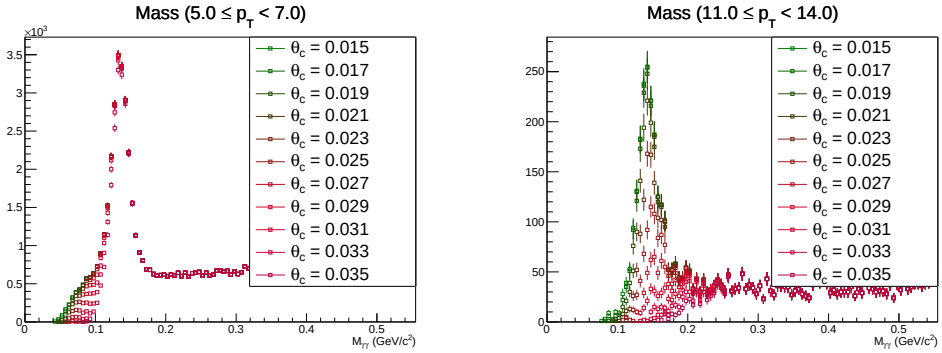

Figure 3.21: Invariant mass distribution with different minimum opening angle cuts, in MB 30-50% centrality events.

The next step is to calculate the ratio between the distributions (shown in Figure 3.22) with and without the cut, and fit it to the following function:

$$\begin{aligned} G(m_{\gamma\gamma}) &= \mathrm{Erf}(z) * \Theta(z), \\ z &= \lambda(m_{\gamma\gamma} - m_0) \end{aligned} \tag{3.8}$$

Where the Erf and Θ is the Error function and the Heaviside functions, respectively. The m_0 parameter gives the precise cutoff, while λ parametrizes the slope of the cutoff.

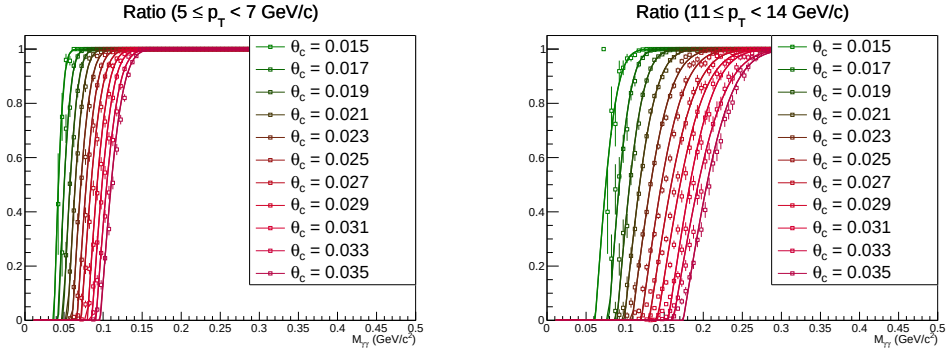

Figure 3.22: Ratio of the invariant mass distribution with different minimum opening angle cuts to the distribution without an opening angle, in EGA-triggered 30-50% centrality events, for 2 p_{T} bins.

It was found that different values were needed for the signal and background fits, as the π^0 decay photons have a different asymmetry distribution than the background. The values for the signal are determined using the cluster pairs from the same event. The parameters

for the background are determined by performing the opening angle ratio fit on cluster pairs from mixed events.

The signal and background functions are each multiplied by the corresponding cutoff function when fitting. This prevents the background parameters from being effected by the detector-dependent angle effects.

3.4.3 Invariant Mass

The π^0 candidates used in this analysis are found from calculating the invariant mass of pairs of clusters from the same event, adding the clusters together as massless four-vectors. The resultant invariant mass formula is given in eq. 3.9.

$$m_{\gamma\gamma} = \sqrt{2E_1E_2(1-\cos(\theta_{\gamma\gamma}))} \tag{3.9}$$

E_1, E_2 are the energies of the two clusters, while $\theta_{\gamma\gamma}$ is the opening angle between the two clusters. The invariant mass spectra are analyzed in bins of the transverse momentum of the pair, similarly described in eq. 3.10. The momentum bins in this analysis were chosen to correspond to those in the PHENIX publications [38]. A small adjustment is made so that the fourth momentum bin starts at the plateau of the turn-on curve ($\approx 11\mathrm{GeV}/c$) for clusters with the EMCal Gamma trigger. Example plots of the invariant mass distributions in different p_{T} bins are shown in Figure 3.23.

$$p_T = (E_1 + E_2)\cos(\theta_{\gamma\gamma}) \tag{3.10}$$

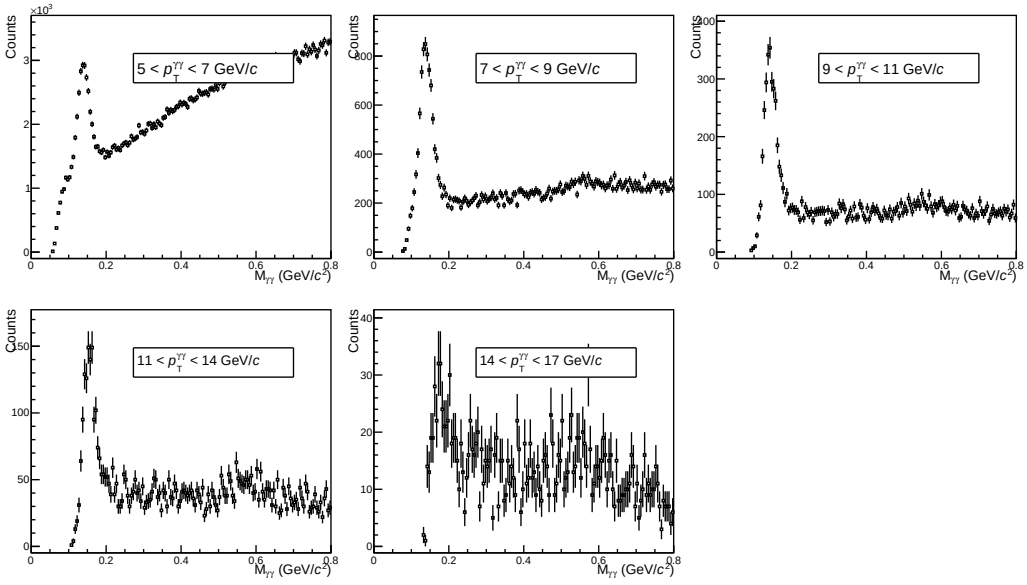

Figure 3.23: Example mass spectra for 0-10% central minimum bias events, in different p_{T} bins.

Invariant Mass in Monte Carlo

Peak Fits

Several functions have been tried for describing the shape of the π^0 peak, and even more for the shape of the background. The peak function should be roughly Gaussian, but may require an extended tail, such as in the Crystal Ball function. These tails, both for low $m_{\gamma\gamma}$ and high $m_{\gamma\gamma}$ describe situations where one or both clusters lost or gained energy. Lost energy can be expected when one photon undergoes pair conversion in the material before the EMCal. Gained energy is expected when one cluster has energy from both the decay photon and a third particle, such as a charged hadron depositing a small amount of energy. The higher energy tail can be diminished by requiring a stricter cut on the shape parameter λ_0^2 for the clusters, which is typically larger for clusters coming from two overlapping particles. A full list, with the implementation and parameter lists, is available in Table 3.5. The η peak is fit as a simple Gaussian peak, simultaneously with the π^0 peak and the background.

Function	Implementation Form
Gaussian	$\mathrm{G}(x,\mu,\sigma)$
GausExp (left)	$\mathrm{G}(x,\mu,\sigma)+(x<\mu)*\mathrm{Exp}((x-\mu)/\lambda)(\mathrm{G}(0,0,\sigma)-\mathrm{G}(x,\mu,\sigma))$
GausExp (right)	$\mathrm{G}(x,\mu,\sigma)+(x>\mu)*\mathrm{Exp}(-(x-\mu)/\lambda)(\mathrm{G}(0,0,\sigma)-\mathrm{G}(x,\mu,\sigma))$
GausExp (both)	$\mathrm{G}(x,\mu,\sigma)+(x<\mu)*\mathrm{Exp}((x-\mu)/\lambda)(\mathrm{G}(0,0,\sigma)-\mathrm{G}(x,\mu,\sigma))+(x>\mu)*\mathrm{Exp}(-(x-\mu)/\lambda)(\mathrm{G}(0,0,\sigma)-\mathrm{G}(x,\mu,\sigma))$
Crystal Ball (left)	$N\begin{cases}\exp(-\frac{x-\mu}{2\sigma^2}), & x-\mu\geq-\sigma\alpha\\ A*(B-\frac{x-\mu}{\sigma})^{-n}, & x-\mu<-\sigma\alpha\end{cases}$
Crystal Ball (right)	$N\begin{cases}\exp(-\frac{x-\mu}{2\sigma^2}), & x-\mu\leq\sigma\alpha\\ A*(B+\frac{x-\mu}{\sigma})^{-n}, & x-\mu>\sigma\alpha\end{cases}$
Breit-Wigner	$\mathrm{BreitWigner}(x,\mu,\sigma*\sqrt{2\ln(2)})$
Voigt	$\mathrm{Voigt}(x-\mu,\sigma,\gamma,4)$

Table 3.5: Peak fit functions implemented in the code (phase1/fitAlgos.cc). Each peak function also has an overall normalization parameter giving the yield of the peak (not written in this table). Named functions represent the implementation in ROOT's TMath. G represents a Gaussians normalized to unity. The Crystal Ball variables are defined in eq. 3.11

The crystal ball fit function is described in Equation 3.11.

$$\begin{aligned} A=\left(\frac{n}{|\alpha|}\right)^n\exp(-\frac{|\alpha|^2}{2}), B=\frac{n}{|\alpha|}-|\alpha|, N=\frac{1}{\sigma(C+D)},\\ C=\frac{n}{|\alpha|}\frac{1}{n-1}\exp(-\frac{|\alpha|^2}{2}), D=\sqrt{\frac{\pi}{2}}\left(1+\mathrm{erf}(\frac{|\alpha|}{\sqrt{2}})\right)\end{aligned} \tag{3.11}$$

The different fit functions are applied to the MC true π^0 signal in Figure 3.24. It can be observed from this figure that some fit functions, such as the GausExp (both sides) work much better than the other.

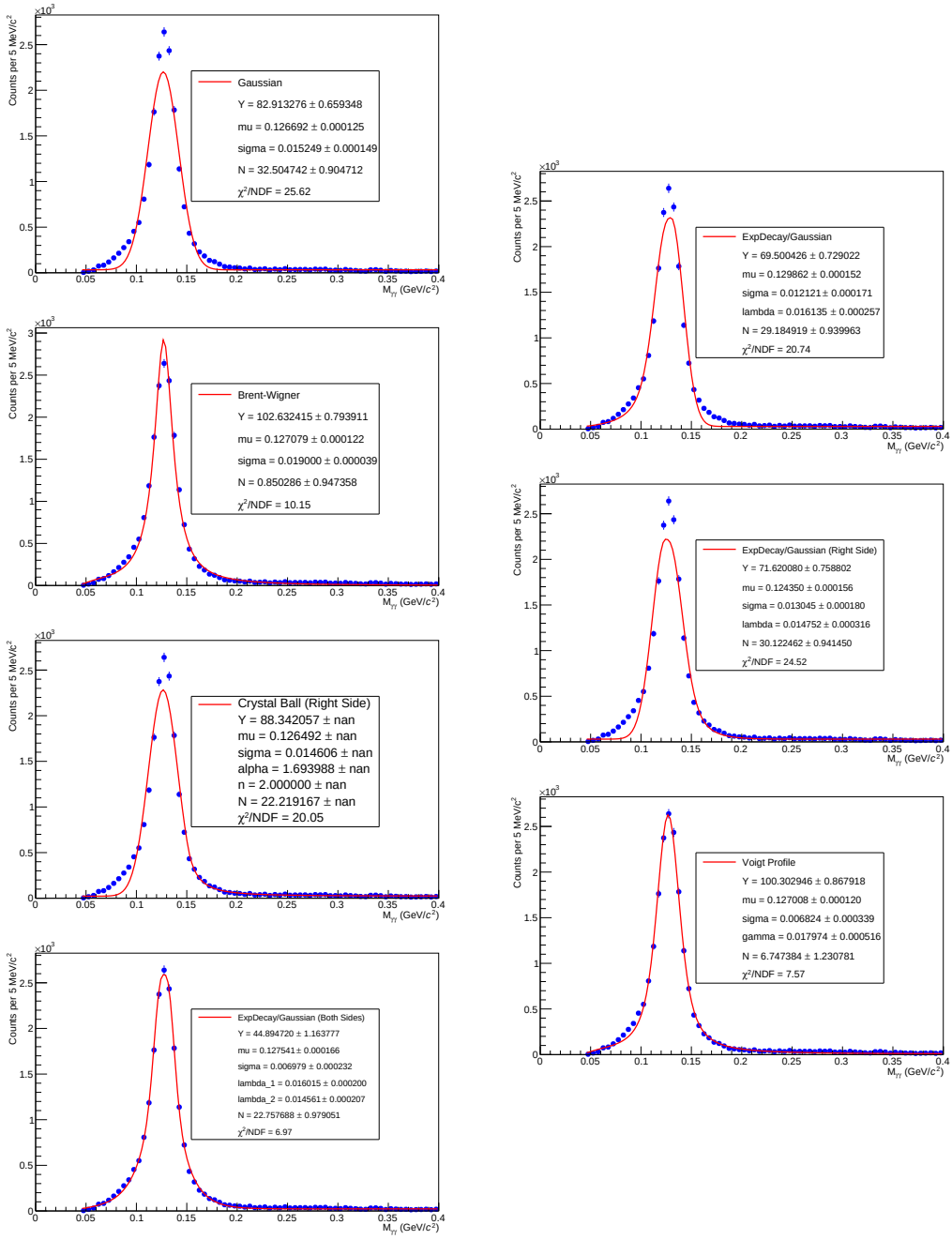

Figure 3.24: Comparison of different fit peak functions, fitting the MC True π^0 signal. Centrality 30-50% in MC production 16h2. The cuts used here are $0.1 < \sigma^2_{\text{long}} < 0.5$, and $\theta > 0.017$.

Background Modelling

Several methods were investigated with the goal of modelling the combinatorial background under the π^0 peak. Ultimately, none of these could describe the correlated portion of the background, which dominates for higher p_{T} cluster pairs.

Rotational Background Pairs

In the simplest method for modeling the combinatorial background, we decorrelated the cluster pairs by taking one cluster and rotating it to a random position within the acceptance. For more statistics, in the low $m_{\gamma\gamma}$, high p_T region, these positions can be weighted towards lower opening angles (with appropriate weighting for the entries). An investigation was done to see if this kind of re-weighting could be used to change the opening angle distribution found when rotating to match the opening angle distribution in data.

This investigation eventually led to the opening angle efficiency parametrization.

Mixed-Event Cluster Pairs

One method investigated for modelling the background was a traditional mixed-event method, wherein clusters are combined with clusters from different (but similar) events. The EventPoolManager object within AliPhysics was used for this, with pool binning given in Table 3.6. In general, it has been found that this method does not describe the background well, in particular at higher p_T, where much of the background is not of the uncorrelated type that can be modelled with mixed-events. An example of this can be seen in Figure 3.25.

Table 3.6: Event pool bins for the 2-cluster event mixing.

Axis	Bins
EMCal Multiplicity	0,100,200,300,1000
Z Vertex (cm)	-10,-6,-3,-1,1,3,6,10

Position Swapped Pairs

Another method for modelling the invariant mass background is swapping the position of clusters within the same event. The advantage of this method is that the background cluster pairs have the same opening angle distribution as the real distribution. This is desirable as it means the background distribution matches the opening angle cutoff from cluster merging and the angular correlations from jets and flow.

This method was implemented with a step at each real cluster pair. In this step, a third cluster from the event is either chosen at random or every possible third cluster is used. Then the second cluster is moved to the position of the third cluster, keeping its

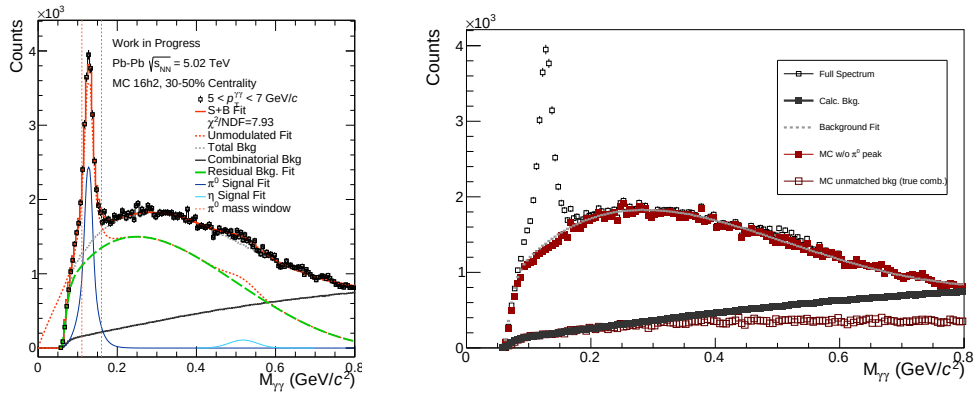

Figure 3.25: Invariant mass distribution fitting with Mixed-Events for 0-10% central events in MC production 16h2. The mixed-event background is shown in gray on the left plot, where it is normalized to a high mass region near 0.8 GeV/c^2. On the right, the invariant mass distribution is analyzed using the available MC information.

original energy. Then the invariant mass and transverse momentum are recalculated for a background distribution.

It was found that this method is not viable for this analysis due to the preserved π^0 peak. The angular correlation between clusters from π^0 and η decays is still preserved by the position swapping, albeit transformed, as visible in Figure 3.26. These preserved distributions appear when the position swapping procedure acts on a pair of clusters where one is a true π^0 or η decay photon and the second is uncorrelated. If the third cluster was the matching decay photon. One method to correct for this is to calculate how the shape of a prior π^0 signal is transformed by the procedure, as detailed in [47]. To apply a method here, it would be necessary to extend it to a p_{T}-differential analysis, which would require a π^0 prior distribution as a function of mass and p_{T}. This creates a recursion issue, although it is in principle possible to solve recursively.

Background Fits

Many options for the background function have been tried, all of them either polynomials or polynomials multiplied by another function. For most backgrounds functions, Bernstein polynomials were used, as they have the useful feature that they can be kept strictly non-negative by limiting their coefficients to be non-negative. This is extremely useful for modelling distributions and spectra for which any negative background would have no physical meaning. This an other commendations for fitting spectra are found in [48]. The full list of attempted background fit functions used is given in Table 3.7.

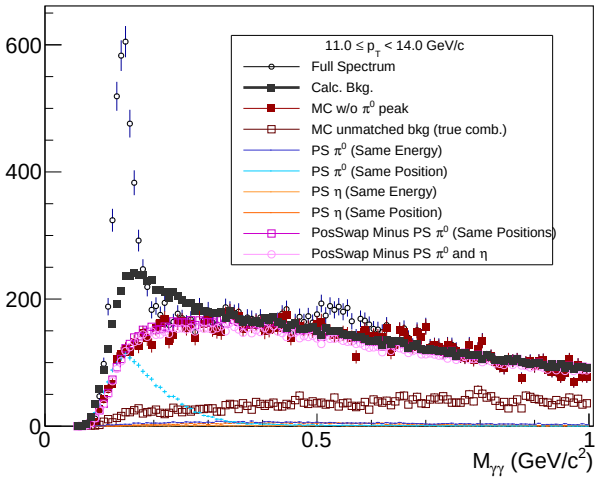

Figure 3.26: Breakdown of position swapped background method for 0-10% events in 16h2, a production with minimum bias HIJING + Pythia jets. The position swapped distribution (black squares) is close in shape to the true background (red squares), but differs at low invariant mass. The difference can be attributed to the preserved correlations of π^0 and η decay photons, in cyan and orange, respectively.

Table 3.7: Background fit functions implemented in the code (phase1/fitAlgos.cc). Each peak function also has an overall normalization parameter (not written in this table). $\text{Poly}_n(x)$ is implemented as $\sum_{j=0}^{n} \frac{a_j}{j!} x^j$. Other named functions represent the implementation in ROOT's TMath.

Function	Implementation Form	Parameters
(n^{th} order)-Polynomial	$\text{Poly}_n(x)$	$a_0, \ldots, a_n$
Exp*Bern(2)	$\text{Exp}(-\lambda * x)\left(\sum_{\nu=0}^{2} a_\nu \binom{2}{\nu} x^\nu (1-x)^{2-\nu}\right)$	λ, a_0, a_1, a_2
Exp*Bern(3)	$\text{Exp}(-\lambda * x)\left(\sum_{\nu=0}^{3} a_\nu \binom{3}{\nu} x^\nu (1-x)^{3-\nu}\right)$	$\lambda, a_0, \ldots, a_3$
ExpDecay*Bern(2)	$(x > c)(1 - \exp(-x/\lambda^2) \sum_{\nu=0}^{2} a_\nu \binom{2}{\nu} x^\nu (1-x)^{2-\nu}$	λ, a_0, a_1, a_2
ExpDecay*Bern(3)	$(x > c)(1 - \exp(-x/\lambda^2) \sum_{\nu=0}^{3} a_\nu \binom{3}{\nu} x^\nu (1-x)^{3-\nu}$	$\lambda, a_0, a_1, a_2, a_3$
Bern(3)	$\sum_{\nu=0}^{3} a_\nu \binom{3}{\nu} x^\nu (1-x)^{3-\nu}$	$a_0, \ldots, a_3$
Bern(4)	$\sum_{\nu=0}^{4} a_\nu \binom{4}{\nu} x^\nu (1-x)^{4-\nu}$	$a_0, \ldots, a_4$
Bern(5)	$\sum_{\nu=0}^{5} a_\nu \binom{5}{\nu} x^\nu (1-x)^{5-\nu}$	$a_0, \ldots, a_5$

3.4.4 Cut Optimization

When deciding on the final cuts to apply for accepting π^0 candidates, three priorities must be balanced: the size of the sample, the purity of the sample, and our uncertainty in the purity. The purpose of prioritizing the size is practically self-explanatory; in any experiment counting a quantity N, the relative statistical uncertainty scales with $1/\sqrt{N}$. It is also desirable to have a relatively pure sample, to minimize the contribution of combinatorial cluster pairs to the measurement. Finally, in choosing the cuts we may prioritize our

confidence in determining the purity. As we are applying an impurity correction via a sideband and errors in the purity will propagate to the sideband-subtracted correlations. The two goals can be balanced by optimizing the peak significance, defined by $S_p = Y/\sqrt{B}$, the signal yield divided by the square root of the background count. Another goal to consider is the uncertainty in the purity, which we also want to minimize. One quick way to quantify our uncertainty in the purity is to examine the χ^2/NDF of the invariant mass fits.

To scan for the best set of cuts, a procedure was done in which the S_p and χ^2/NDF was calculated for each combination of opening angle cut and σ^2_{long}. These scans are shown graphically in Figures 3.27 and 3.28 for MB events and 3.29 and 3.30.

Ultimately, it was found that the default cuts used in ALICE for the σ^2_{long} were adequate, while different opening angle cuts were found to be best in low p_{T} data from MB events and high p_{T} data from EGA-triggered events.

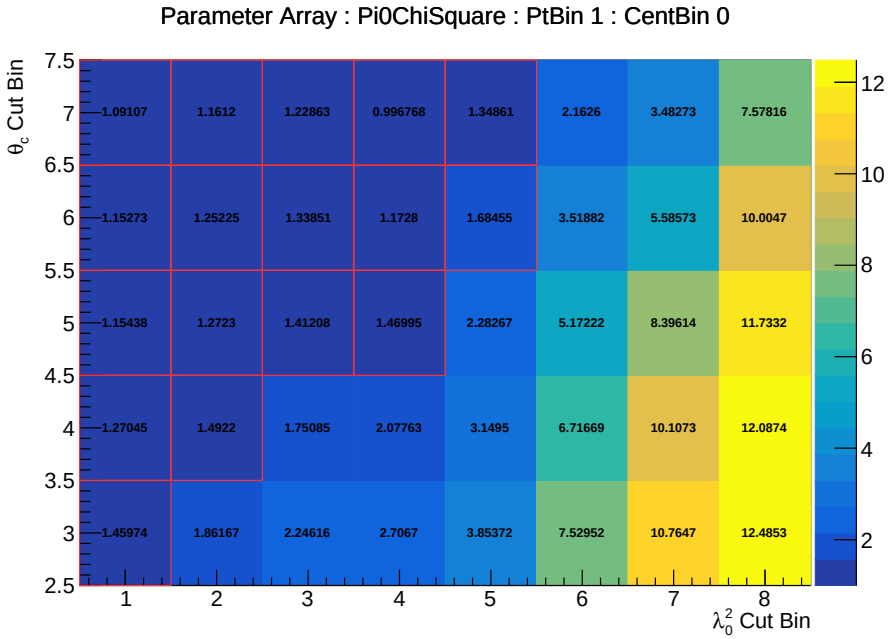

Figure 3.27: χ^2/NDF for different combination of σ^2_{long} (labelled λ^2_0 in the plots) and θ_c cut paramters in MB, 0-10% central events. Red squares indicate bins where the χ^2/NDF id below an arbitrary threshold of 1.75

3.4.5 Final Invariant Mass Distributions and Cuts

The final cuts used in the analysis are summarized in Table 3.8.

The final π^0 mass peak positions and widths for MB and EGA-triggered data are given in Tables 3.9 and 3.10, respectively. The final invariant mass windows used are determined by $\mu \pm 3\sigma$.

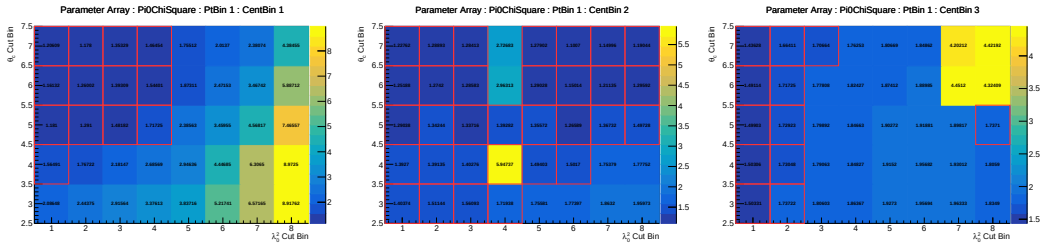

Figure 3.28: χ^2/NDF for different combination of $\sigma^2_{\rm long}$ (labelled λ_0^2 in the plots) and θ_c cut paramters in MB, 10-30%, 30-50%, 50-80% central events.

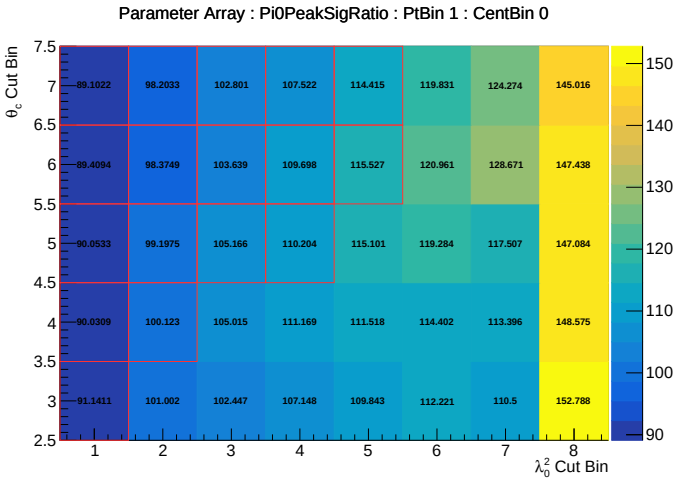

Figure 3.29: Peak significance (yield / $\sqrt{\text{background}}$) for different combination of $\sigma^2_{\rm long}$ (labelled λ_0^2 in the plots) and θ_c cut paramters in MB, 0-10% central events.

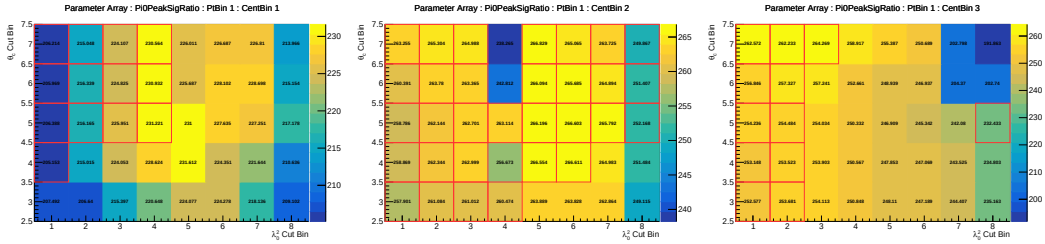

Figure 3.30: Peak significance (yield / $\sqrt{\text{background}}$) for different combination of $\sigma^2_{\rm long}$ (labelled λ_0^2 in the plots) and θ_c cut paramters in MB, 10-30%, 30-50%, 50-80% central events.

The final (after deciding all cuts) invariant mass distributions are shown for the 30-50% centrality range for MB and EGA-triggered events in Figures 3.31 and 3.32. One single+background fit is plotted on each of them, with the background-subtracted distribution shown in red.

Table 3.8: Final cuts for the π^0 candidates

Cut	MB	EGA
$\sigma^2_{\text{long}}(Max)$	0.5	0.5
$\theta_c(Min)$	23 mRad	17mRad
α	1.0	1.0

Table 3.9: Invariant mass central values and cuts for the Pb–Pb 15o minimum bias data set.

Centrality	p_{T}	μ	σ
0-10%	5-7	0.138998	0.011146
	7-9	0.139368	0.011566
	9-11	0.141303	0.011338
	11-14	0.148221	0.011077
10-30%	5-7	0.137308	0.009240
	7-9	0.137660	0.009207
	9-11	0.139410	0.009374
	11-14	0.144601	0.011105
30-50%	5-7	0.136108	0.007751
	7-9	0.135959	0.008359
	9-11	0.137340	0.007867
	11-14	0.141563	0.006892
50-80%	5-7	0.135356	0.006977
	7-9	0.135408	0.006724
	9-11	0.135935	0.007251
	11-14	0.141102	0.007834

Table 3.10: Invariant mass central values and widths for the Pb–Pb 15o EGA triggered data set.

Centrality	p_{T}	μ	σ
0-10%	11-14	0.147529	0.012747
	14-17	0.158139	0.013998
10-30%	11-14	0.144848	0.010878
	14-17	0.153996	0.012375
30-50%	11-14	0.142265	0.008908
	14-17	0.151094	0.009553
50-80%	11-14	0.140655	0.008444
	14-17	0.150016	0.011205

3.4.6 Final π^0-Candidate Distributions

The final distribution of π^0-candidates in η and ϕ within the detector are presented in Figures 3.33 (MB events) and 3.34 (EGA events). Several common features are notable

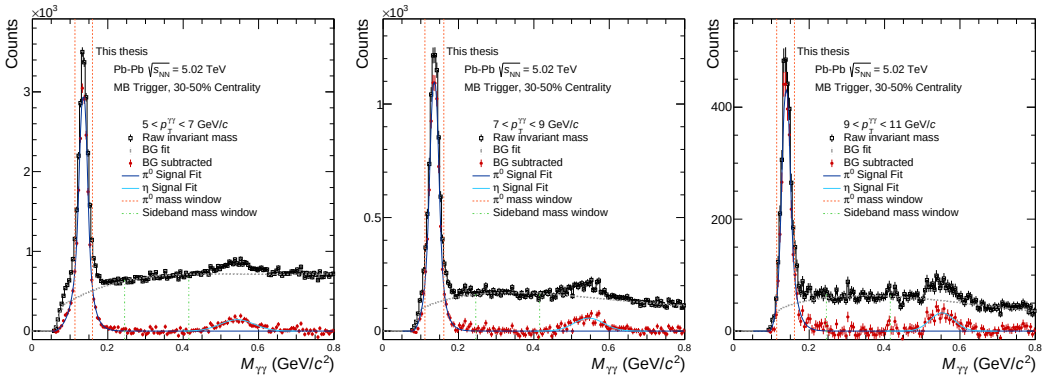

Figure 3.31: Invariant Mass for the p_{T} ranges 5-7,7-9, and 9-11 GeV/c for the Pb–Pb 15o minimum bias, 30-50% central data set.

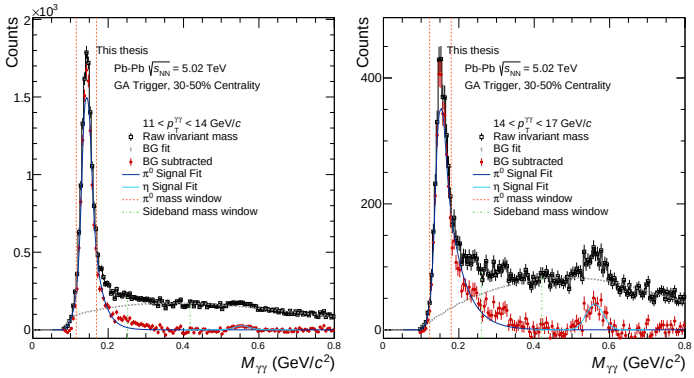

Figure 3.32: Invariant Mass for the p_{T} ranges 11-14,14-17 GeV/c for the Pb–Pb 15o EGA triggered event, Central 30-50% data set.

in both distributions, including the overall acceptance of the EMCal and DCal. Horizontal stripes of lower π^0 yields are caused by the edges between different supermodules of the EMCal. Horizontal stripes are caused by the material of the support structure for the Transition Radiation Detector in front of the EMCal. Small holes in the distribution are caused by bad cells in the EMCal and their removal from the analysis, as explained in Section 3.4.1.

In the EGA-triggered events, some regions have significantly lower yields than in MB, such as those around 0.4 in η in the lower right regions of the main EMCal. These dips are due to masking of Trigger Readout Units in the EMCal trigger configuration during data-taking. This was done to avoid "hot channels" in the EMCal that produced spurious signals.

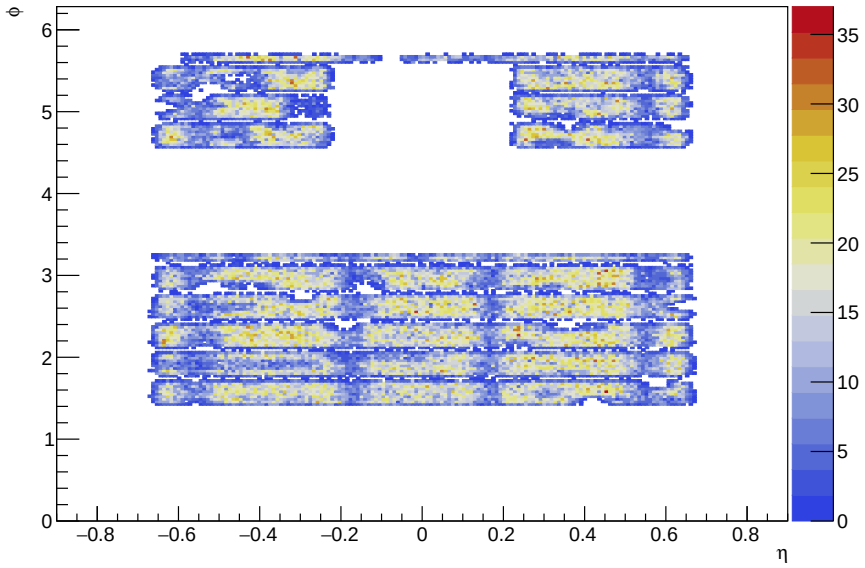

Figure 3.33: Distribution of accepted π^0-candidates in MB events (30-50% central events).

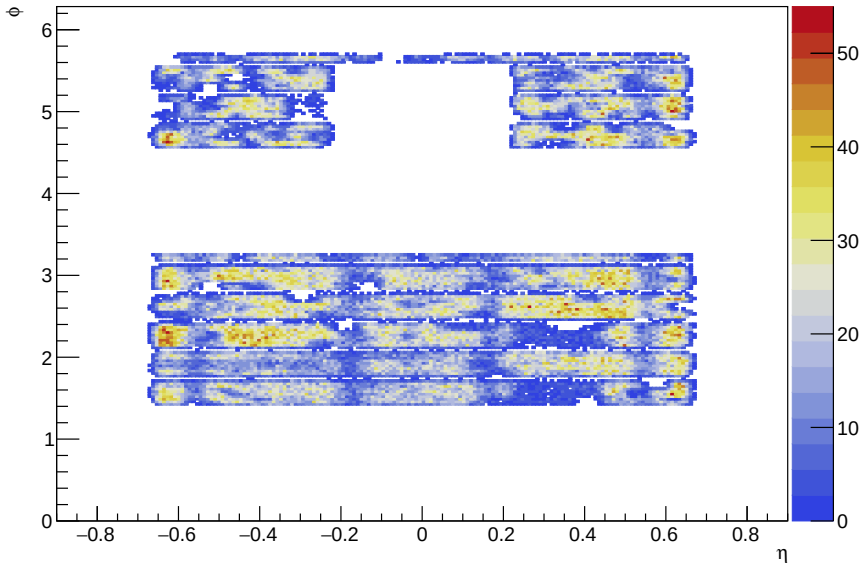

Figure 3.34: Distribution of accepted π^0-candidates in EGA-triggered events (30-50% central events).

3.4.7 π^0 Purity Determination

Establishing an accurate measure of the purity of the π^0_{Cand} sample selected by a given mass window serves two key purposes in this analysis. One is to give metrics by which to optimize data cuts. It is to the benefit of the analysis to increase the purity of the π^0

signal, so as to minimize contamination by the correlations between charged particles and the combinatorial background cluster pairs.

The second use for the purity is to apply an impurity correction to subtract the contribution to the π^0_{Cand}-hadron correlations from background pair-hadron correlations. While the full details of this correction are described in Section 3.8, actual magnitude of the purity is one key input into this correction.

The purity for each π^0 p_{T} bin is calculated by integrating the counts in the invariant mass range $(\mu - 3\sigma, \mu + 3\sigma)$ to give the total, subtracting the background component of the signal+background, and integrating the background-subtracted distribution in the same range.

The final value for the purity that is used in the impurity correction is taken from the average of the purity calculated with a wide range of background fit functions and fit ranges.

Fit Background Function

Due to the mass cutoff from kinematics (limiting the statistics to the left of the π^0 peak) and the correlated background, inferring the shape of the combinatorial background of cluster pairs of invariant mass near the π^0 peak is extremely difficult, and represents one of the largest sources of uncertainty in this measurement. This is addressed by using a wide range of background functions to reflect this uncertainty. The final set of functions used for determining the systematic uncertainty in the purity are given in Table 3.11.

Table 3.11: Final set of background fit functions used to evaluate the uncertainty in the purity.

Background Function
Exp*Bern(2)
Exp*Bern(3)
ExpDecay*Bern(3)
Bern(3)
Bern(4)
Bern(5)

Fit Range

The range over which the final fit of the peak + background function to the invariant mass is a somewhat arbitrary choice, and so should be varied to investigate a systematic uncertainty in the purity determination. An initial set of ranges to investigate is outlined in Tab. 3.12, where we vary the maximum value. Results of this are shown in Figures 3.35 and 3.36.

Table 3.12: Table of fit ranges investigated.

Option	0 (Default)	1	2	3	4	5	6	7	8	9
Fit Max	1.0	0.35	0.4	0.45	0.5	0.6	0.65	0.7	0.75	0.8

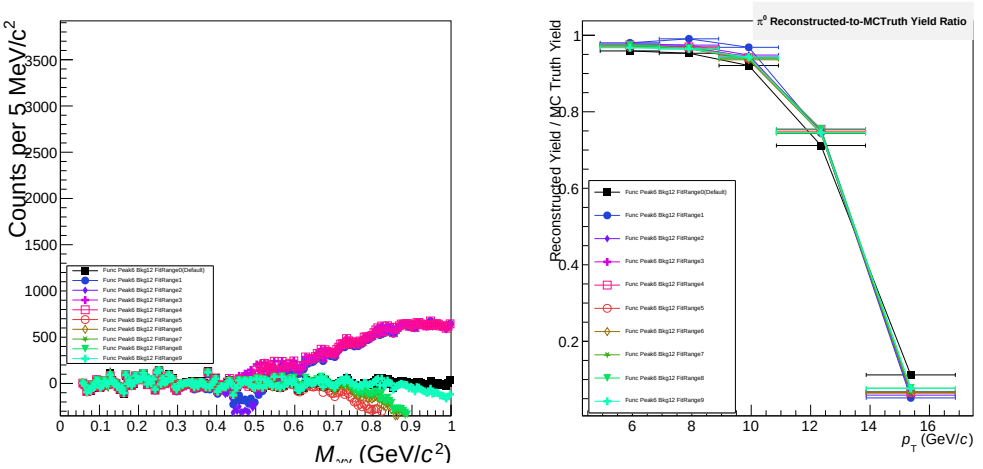

Figure 3.35: Residuals of fits with the different ranges for the $5 \leq p_T < 7$ GeV/c (left) and the ratio of the reconstructed purity to the true purity (right).

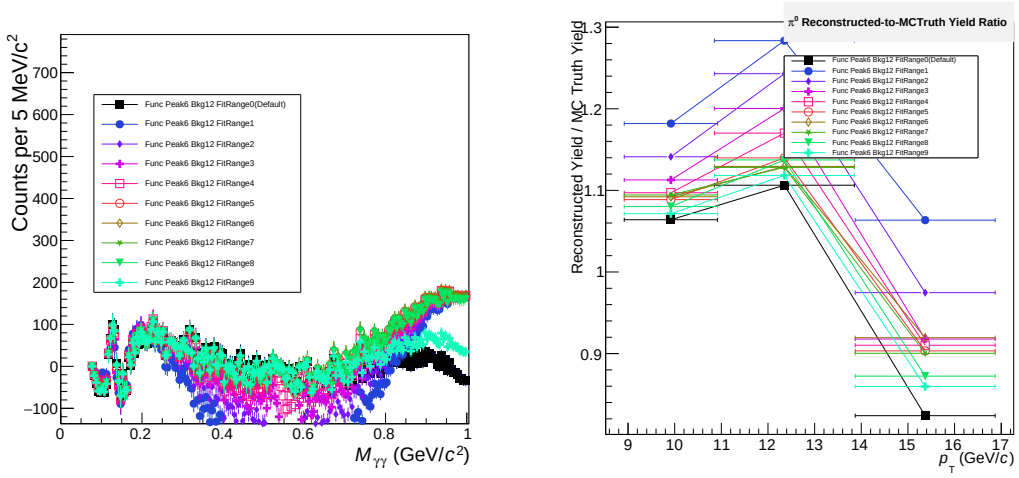

Figure 3.36: Residuals of fits with the different ranges for the $11 \leq p_T < 14$ GeV/c (left), χ^2/NDF for the fit ranges (middle), and the ratio of the reconstructed purity to the true purity (right).

Final π^0 Purity Uncertainty

To evaluate the final systemetic uncertainty, each combination of fit range listed in Table 3.12 and each background function listed in Table 3.11 was used, with the final purity values taken as the average. The variance of the values is taken as the systematic uncertainty

and the statistical uncertainty taken from one combination. The total uncertainty in the purity is taken as the sum in quadrature of these values. The π^0 purity and the uncertainties are given in Tables 3.13 and 3.14.

Table 3.13: π^0 purity values with statistical and systematic uncertainties for the EGA-triggered data.

Centrality Range	p_{T} Range (GeV/c)	π^0 purity $\pm$ (stat uncert.) $\pm$ (sys uncert.)
30-50%	5-7	$0.792 \pm 0.010 \pm 0.005$
	7-9	$0.838 \pm 0.018 \pm 0.010$

Table 3.14: π^0 purity values with statistical and systematic uncertainties for the EGA-triggered data.

Centrality Range	p_{T} Range (GeV/c)	π^0 purity $\pm$ (stat uncert.) $\pm$ (sys uncert.)
30-50%	11-14	$0.915 \pm 0.012 \pm 0.013$
	14-17	$0.907 \pm 0.024 \pm 0.017$

Event-Plane Dependence

There are physically motivated reasons to expect that the π^0-purity may vary with the event-plane. Specifically, the higher multiplicity of tracks aimed at the EMCal when the π^0 is in-plane may add more background pairs. This is concerning, as incorrectly subtracting too much or too little background in different event-plane bins could create a fake event-plane dependence, or mask a true one. To address this, the π^0 purity is calculated separately in each event-plane. These are shown for EGA-triggered data in Figure 3.37. No significant event-plane dependence is detectable at high p_{T} given the error bars.

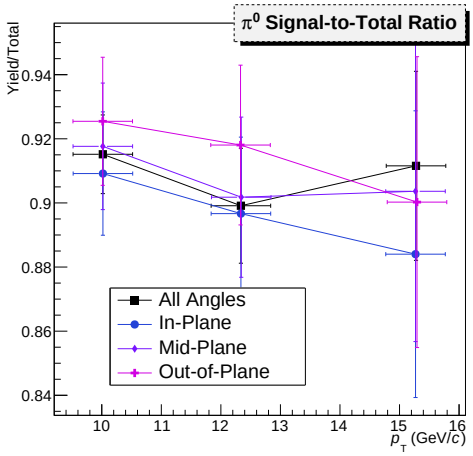

Figure 3.37: π^0 purity vs p_{T} for different event-plane angles, in EGA-triggered, 30-50% central events. Error bars are the quadratic sum of the statistical and systematic uncertainties.

3.5 Correlations

π^0_{Cand}-hadron and sideband-hadron correlations are measured by counting the number of hadrons in each bin of centrality, event plane, trigger p_{T} bin, associated p_{T} bin, $\Delta\eta$ = $\eta^{\mathrm{trigger}} - \eta^{\mathrm{hadron}}$, and $\Delta\varphi$ = $\varphi^{\mathrm{trigger}} - \varphi^{\mathrm{hadron}}$, and the z-vertex of the primary interaction within the beam. The correlations are corrected for the efficiency as a function of η and p_{T} as the correlations are saved, giving us raw same-event correlations:

$$Y(\Delta\eta, \Delta\varphi)^{SE} = \frac{1}{\epsilon(\eta, p_{\mathrm{T}})} \frac{d^2 N_{\mathrm{assoc}}}{d\Delta\eta d\Delta\varphi} \tag{3.12}$$

The bins in which the correlation are saved are provided in Tables 3.15, 3.16, and 3.17.

Table 3.15: Bin information for $\Delta\eta$, $\Delta\varphi$.

	#bins	range
$\Delta\eta$	80	[-2,2]
$\Delta\varphi$	54	$[-\pi/2, 3\pi/2]$

Table 3.16: Centrality bins for this analysis.

Bin	0	1	2	3
Centrality	0-10%	10-30%	30-50%	50-90%

Table 3.17: Associated hadron p_{T} bins.

Bin	0	1	2	3	4	5	6	7
p_T (GeV/c)	0.2-0.4	0.4-0.8	0.8-1.5	1.5-2.5	2.5-4	4-7	7-11	11-17

3.6 Mixed-Event Correction

Finite acceptance effects of the detector can be corrected with the help of correlations from mixed-event. An example of an uncorrected correlation function $Y(\Delta\eta, \Delta\varphi)^{SE}$ is displayed in Figure 3.38. The overall structure in $\Delta\eta$ is due to acceptance effects, from the fact that we are correlating triggers in the $-0.7 < \eta < 0.7$ region with $-0.9 < \eta < 0.9$. This effect needs to be corrected to measure an accurate correlation function. This is done using a mixed-event correction, in which mixed-event correlations are produced using trigger particles and hadrons from different, but similar events.

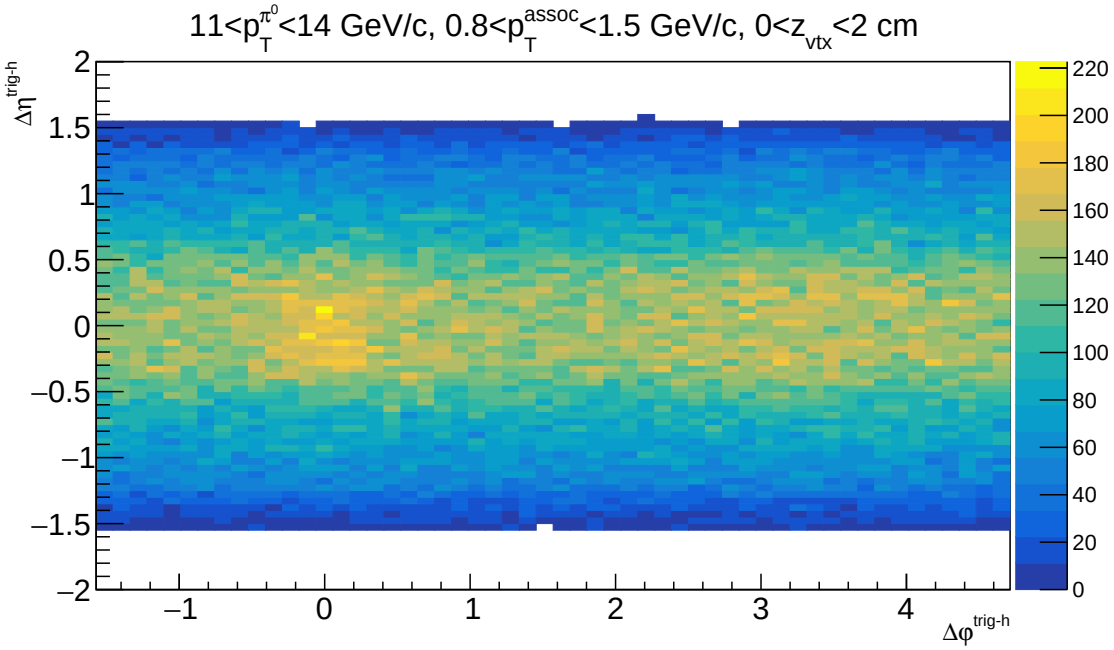

Figure 3.38: A raw correlation function for Same Event pairs corresponding to events with primary vertex $0 \leq z < 2$ cm and π^0_{Cand} triggers between 11 and 14 GeV/c.

The mixed-event corrected correlations are found by dividing same-event correlations by mixed-event corrections:

$$C(\Delta\eta) = \frac{Y(\Delta\eta, \Delta\varphi)^{SE}}{Y(\Delta\eta, \Delta\varphi)^{ME}} \tag{3.13}$$

3.6.1 Constructing Mixed-Events

The construction of the mixed-event works as follows. A trigger particle candidate is combined with a track from another event. While the trigger particle can stem from a Gamma-triggered event, the tracks can only come from a MB event selection, since they will otherwise be biased into the direction of the calorimeter. Additionally, the trigger and the track must come from events that are similar enough. For this analysis 8 bins in centrality and 10 bins in z-vertex position were chosen, listed in Table 3.18. In the final analysis with EMCal-Gamma triggered events, the angle of the 2nd-order event plane within the detector was added as an additional parameter in the event mixing, with 6 bins, listed in Table 3.19.

Table 3.18: Settings for the mixed-event pool.

Property	Value	Comment
MaxEvents	-1	No limit on events in pool
TrackDepth	50,000	
NCentBins	8	0,10,20,30,40,50,60,80,100
nZvtxBins (cm)	10	-10,-8,-6,...,6,8,10
nEPBins	2	Used only to separate odd, even events

Table 3.19: Settings for the mixed-event pool with event plane angle mixing.

Property	Value	Comment
MaxEvents	-1	No limit on events in pool
TrackDepth	50,000	
NCentBins	8	0,10,20,30,40,50,60,80,100
nZvtxBins (cm)	10	-10,-8,-6,...,6,8,10
nEPBins	14	$-7\pi/6, -\pi, -5\pi/6$,...,$5\pi/6, \pi, 7\pi/6$
		Positive and negative used to distinguish odd and even events.

3.6.2 Two-Stage Event Mixing

Early in the analysis, it was found that the existing mixed-event procedure was not producing sufficient statistics. The cause of this can be understood from how the event mixing works in practice on the LHC computing grid, where analyses are parallelized as thousands (typically 6,000 to 14,000 for these analyses) of separate processes, each examining a small subset of the dataset.

In the old procedure, diagrammed in Figure 3.39, hereafter referred to as single-stage event mixing, each job on the grid stores tracks from MB events as it analyzes them. The jobs wait until they have a threshold before they are labelled as "ready", meaning that they have stored some minimum number of tracks or events. In addition, the mixed-event pools are allowed to "fill," at which point the first MB events saved will be removed. These steps are done so that the tracks in the first analyzed events are not given significantly more weight than tracks from later events. Both of these steps unnecessarily decrease the available statistics in mixed-event. However, the primary issue with single-stage mixing is that trigger particles from one can only be mixed with tracks from events analyzed by the same job. As there are thousands of jobs, this clearly decreases the available mixed-event correlations by a factor in the thousands.

The new approach that was used is to save the mixed-event pools from all jobs and merge them together after the first run over the data as explained in the diagram in Figure 3.40. To keep the size of the pool small, the mixing is reversed such that the pool stored π^0-candidate triggers instead of the tracks. Then in a second run over the dataset, the individual analysis jobs load the global pool, and correlate tracks from the events they analyze with triggers from the global pool.

While this method doubles the run time (as two "trains" are needed), the statistical improvement in the mixed-events is greater than 10^3. The method requires a downscale to the mixed-event sampling to keep the run-time of jobs within limits imposed by the grid.

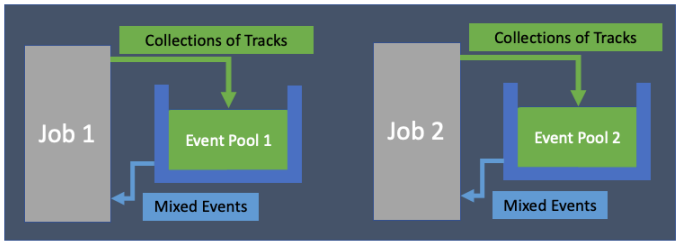

Figure 3.39: Single-stage event mixing method schematic.

Avoiding Same Event within Mixed-Events

One major complication of merging the particle pool used in event mixing is that it makes it difficult to ensure that the trigger particle and the associated particle are not, in fact, from the same event. This was trivial to avoid when producing event pools on-the-fly, as a new event's same-event correlations can be calculated before that event's particles are added to the pool. Since the entire population of π^0-candidates is being saved to the trigger pool, the event that the π^0 came from will be used again in the second pass. This is automatically avoided for analyzing EGA-triggered events, as the π^0 candidates come from the EGA-triggered events, while the mixed-events use tracks from MB events. Thus

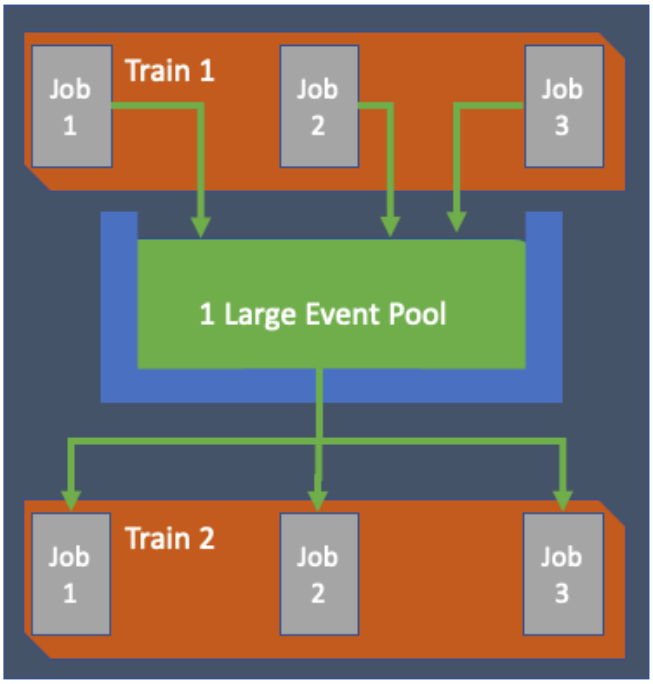

Figure 3.40: Two-stage event mixing method schematic.

the issue only exists for analyzing MB data. To address this, a hash function is used to divide the events into two categories: odd and even. The hash function returns the same result for the event each time. When storing π^0 candidates for the trigger pool, the triggers are divided into odd and even events. Then during the event mixing, odd triggers are used for even events and vice versa, thus ensuring that a π^0 candidate is not used with the same event during event mixing.

3.6.3 Normalization of Mixed-Events Correlations

The standard method in mixed-event corrections is to normalize the correlation function such that $Y(\Delta\eta = 0, \Delta\varphi = 0)^{ME} = 1$. This assumes that the detector acceptance for the associated particle overlaps with and includes the acceptance for the trigger particle such that we always expect to detect an associated particle perfectly aligned with the trigger particle.

As can be seen clearly in the $\Delta\phi$-projected mixed-event correlations in Figure 3.41, which shows the $\Delta\varphi$ projection of mixed-event correlations, there is a relative suppression in the mixed-event correlations near $\Delta\phi = 0$, especially for low p_{T}^{assoc}.

There is also a noticeable effect at high $p_{\mathrm{T}}^{\mathrm{assoc}}$ in which vertical striations appear, which is particularly visible in the 2D mixed event correlations shown in 3.42. The bands with fewer correlations correspond to the edges of the TPC sectors. This can occur because

both the EMCal and the TPC have the same azimuthal segmentation. The effect appears at high p_{T} due to the fact that lower p_{T} tracks curve more, minimizing the effect of the blind sections between sectors.

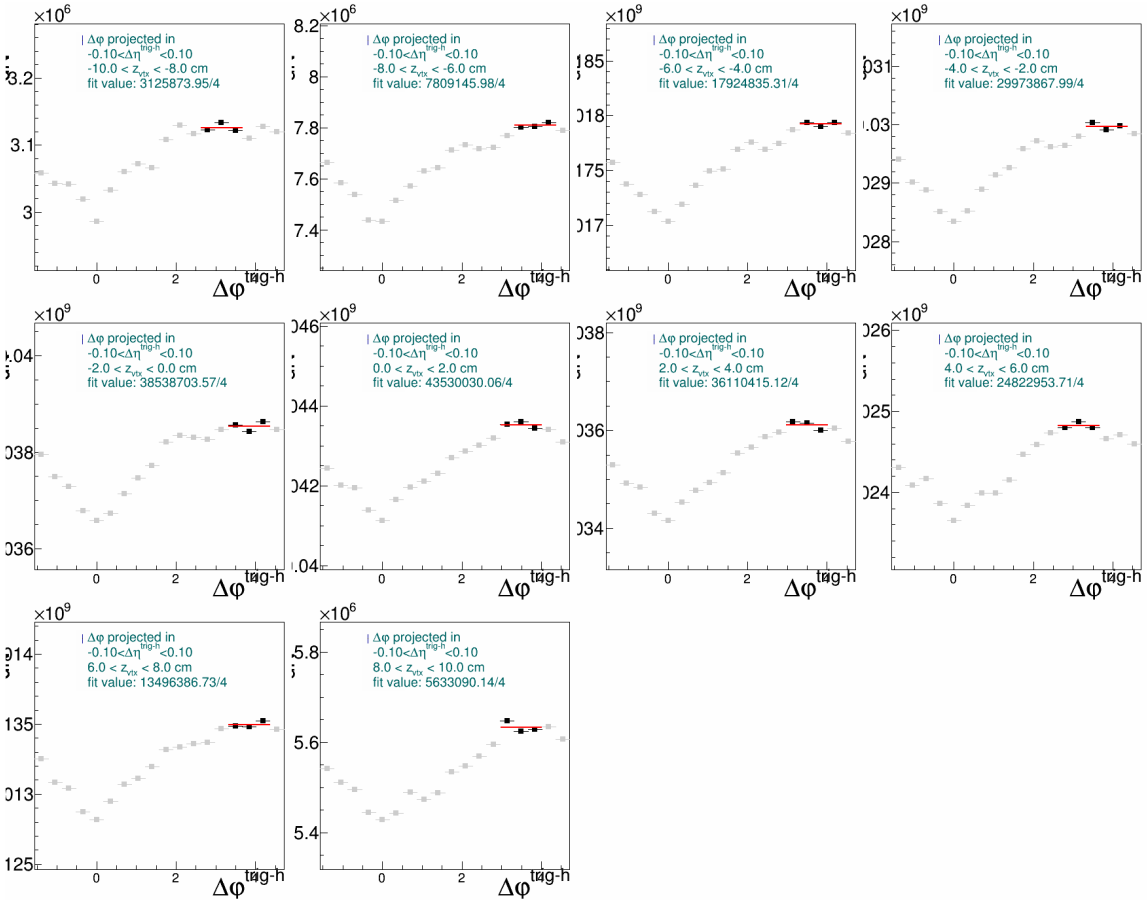

Figure 3.41: mixed-event π^0-hadron correlations for EGA-triggerd 30-50% central events with $11 \leq p_{\mathrm{T}}^{\mathrm{trigger}} < 14$ GeV/c and $0.2 < p_{\mathrm{T}}^{\mathrm{assoc}} < 0.4$ GeV/c. Each plot is a different z-vertex range.

As a result of the depletion near $\Delta\phi = 0$, normalizing the mixed-event correlations to unity there is not a viable option. As an alternative to this, we find a region where the mixed-event correlations are maximal, and normalize such that the correlations at that point are valued at 1. One net effect of this is that division by mixed-event correlations will correct for the relative inefficiency near $\Delta\phi = 0$.

The algorithm for finding the region to normalize to is also shown in Figure 3.41. After projecting the region $-0.1 < \Delta\eta < 0.1$ onto $\Delta\varphi$, a running average is calculated at each bin, using a range of 3 bins. The maximum location is identified, and that is used as the point at which to normalize to unity.

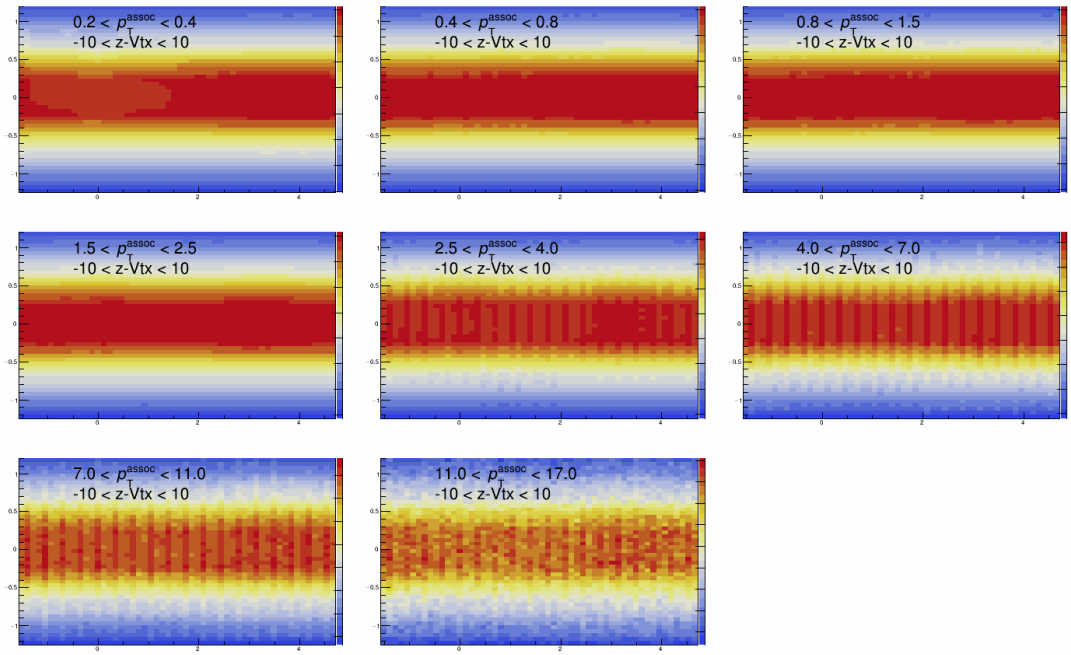

Figure 3.42: mixed-event π^0-hadron correlations for EGA-triggerd 30-50% central events with $11 \leq p_{\mathrm{T}}^{\mathrm{trigger}} < 14$ GeV/c. Starting from the top left, each plot is a bin of the associated hadron p_{T}.

3.7 Projections in $\Delta\eta, \Delta\phi$

To analyze the correlations, we project the raw (before impurity correction) correlations onto the $\Delta\eta$ and $\Delta\phi$ axes. One purpose for projecting onto the $\Delta\eta$ axis is to determine the extent of the near-side peak in pseudorapidity and identify the regions in $\Delta\phi\Delta\eta$ space that are dominated by background. While ultimately the analysis uses fixed $\Delta\eta$ cuts, a method using the width of the nearside peak is used as an alternative to investigate systematic uncertainties.

An example of the $\Delta\eta$ projection is given in Figure 3.43, showing both the nearside and awayside region, after it has been scaled to match the nearside region in $0.6 < |\eta| < 1.2$. In a following step, this scaled awayside region is subtracted from the nearside and a fit is performed using the sum of two gaussians. The fit function is defined in Equation 3.14 and shown in Figure 3.44.

$$f(\Delta\eta) = Y_1 \left(e^{-\frac{1}{2}(\Delta\eta/\sigma_1)^2} + Y_2 e^{-\frac{1}{2}(\Delta\eta/(\sigma_1 * \sigma_2))^2} \right) \tag{3.14}$$

The purpose of the subtraction is to correct for a "skew" that occurs in some low p_{T} bins. This skew is discussed in more detail in Section 3.7.1. The awayside subtraction is valid in this case as the awayside peak is roughly flat in $\Delta\eta$ due to the range of net

longitudinal momentum of the hard scatter. The width that is extrapolated from the fit and used for an alternative determination of the $\Delta\eta$ regions is determined by the σ_1 parameter, the width of the central peak.

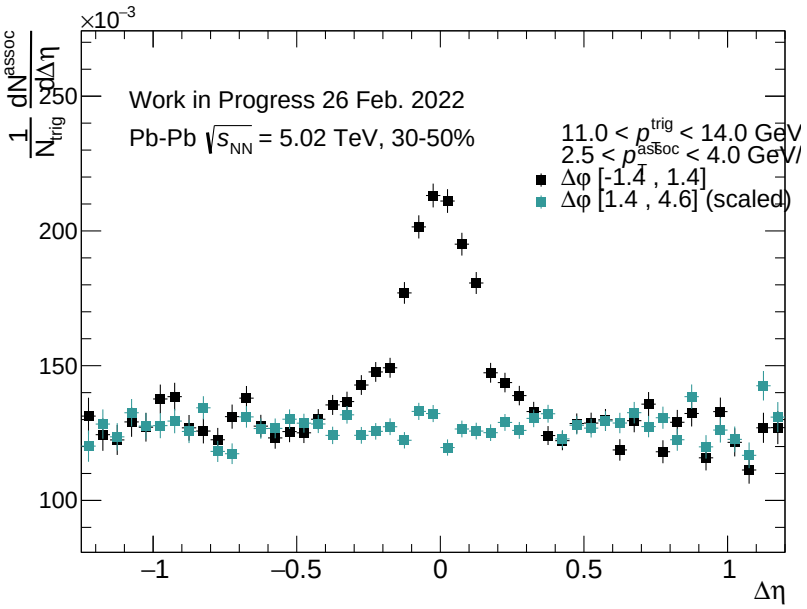

Figure 3.43: Raw π^0-hadron correlations projected onto the $\Delta\eta$ axis for 2.5-4 GeV/c associated particles. The nearside $\Delta\phi$ region is plotted in black points, and the awayside region is scaled to match the nearside region using the $0.6 < |\Delta\eta| < 1.2$ region. These are from EGA Triggered events, 30-50% centrality range, 11-14 GeV/c $p_{\mathrm{T}}^{\mathrm{trig}}$.

3.7.1 Mixed-Event Correction Skew

One significant challenge in the analysis is that the current mixed-event correction leads to a skew in $\Delta\eta$ at low $p_{\mathrm{T}}^{\mathrm{assoc}}$, as can be seen in Figure 3.45. This is particularly problematic because this skew results in changes between different event plane angles relative to the trigger. Examples of this are shown in Figure 3.46. This is highly problematic, as the RPF method used for subtracting the flowing background assumes that the background in the far $\Delta\eta$ region is the same as in the near $\Delta\eta$ region. However, with the skew, the far $\Delta\eta$ region may be raised above or below the signal region.

This problem motivated including the angle of the event plane as a parameter in the event mixing for the correlations. However this had a negligible effect. It remains possible that a data-driven correction could be derived, but the low signal to background in the region hinders this approach. As a fix for the skew has not been found, this effect sets the lower bound of the p_{T}^{assoc} of this analysis, at 0.8 GeV/c for the 30-50% central EGA-triggered data.

The next step is projecting the correlations onto $\Delta\varphi$, in three regions of $\Delta\eta$:

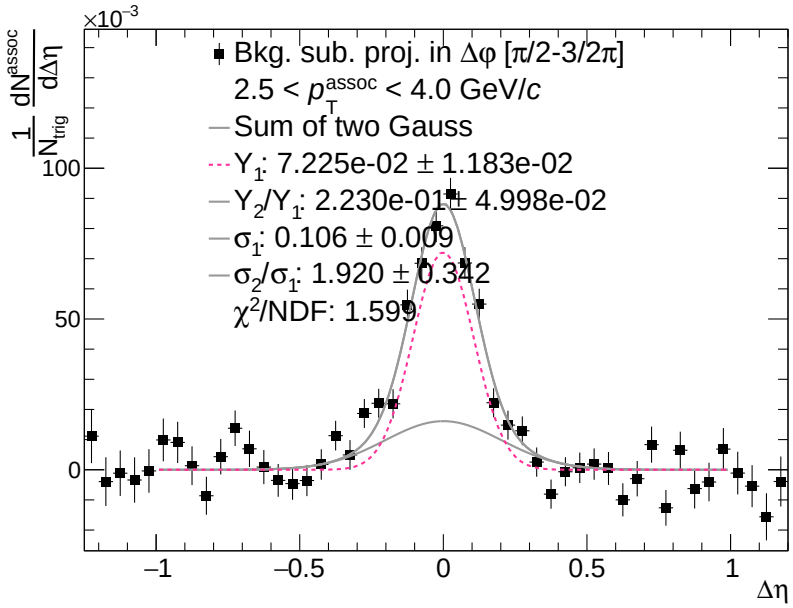

Figure 3.44: Raw π^0-hadron correlations projected onto the $\Delta\eta$ axis with the scaled away-side correlations subtracted from the nearside for 2.5-4 GeV/c. These are from EGA Triggered events, 30-50% centrality range, 11-14 GeV/c $p_{\mathrm{T}}^{\mathrm{trig}}$s. A fit using the sum of two gaussians is performed.

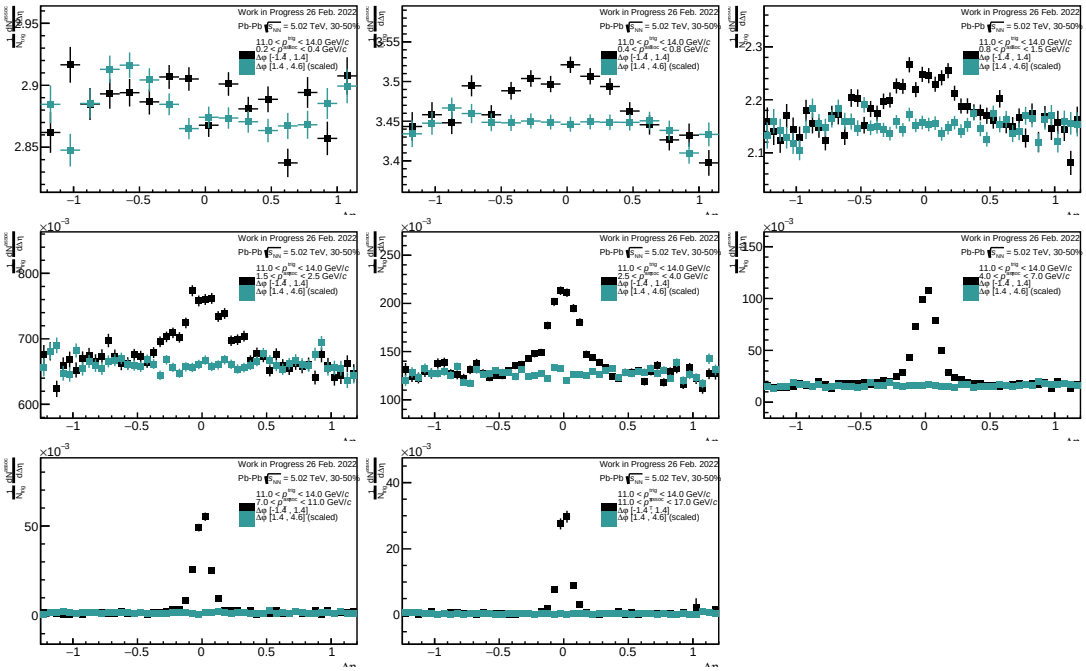

Figure 3.45: Projected correlations onto the $\Delta\eta$ axis. From left to right and top to bottom, the p_{T} range of the associated particles is changed.

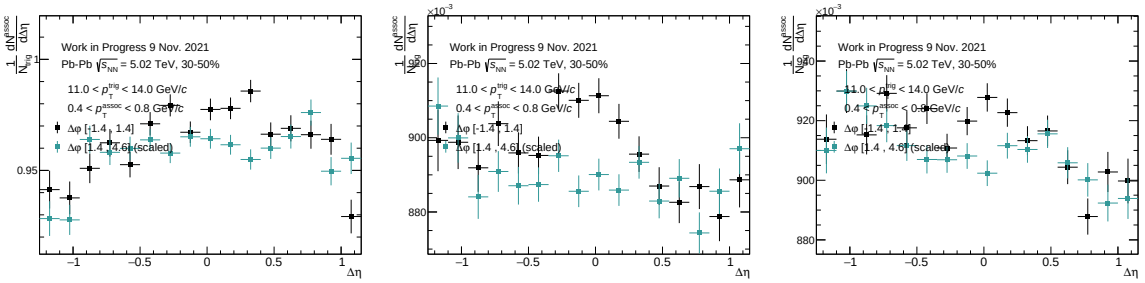

(a) In-plane (b) Mid-plane (c) Out-of-plane

Figure 3.46: Correlations projected onto the $\Delta\eta$ axis for 30-50% EGA-triggered events, 11-14 GeV/c $p_{\mathrm{T}}^{\mathrm{trig}}$, 0.4-0.8 GeV/c hadrons. The event-plane dependent skew in $\Delta\eta$ is significant at low p_T^a, and is the analysis' limiting factor in reaching lower p_T^a

- Full region: $|\eta| < 1.35$
- Near $\Delta\eta$ region: $|\eta| < 0.8$
- Far $\Delta\eta$ region: $0.8 < |\eta| < 1.35$

These defined regions are shown visually in Figure 3.47, which also emphasizes the regions that will be used for the background fitting (far $\Delta\eta$, nearside $|\Delta\varphi| < \pi/2$), and for the analysis of the awayside (the full $\Delta\eta$ region).

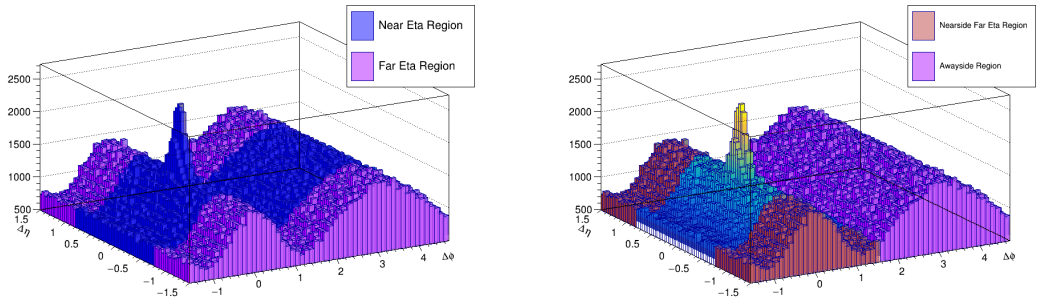

Figure 3.47: Pseudo-data plots shaded to display the definition of the near $\Delta\eta$ and far $\Delta\eta$ regions (shown on the left) the nearside far $\Delta\eta$ region and awayside region (right).

Raw π^0-hadron correlations for the 11-14 GeV/c trigger p_{T} bin, projected onto $\Delta\varphi$ in the near and far $\Delta\eta$ regions are shown in Figure 3.48. More correlation plots, including those for different event planes and centralities in appendix E.

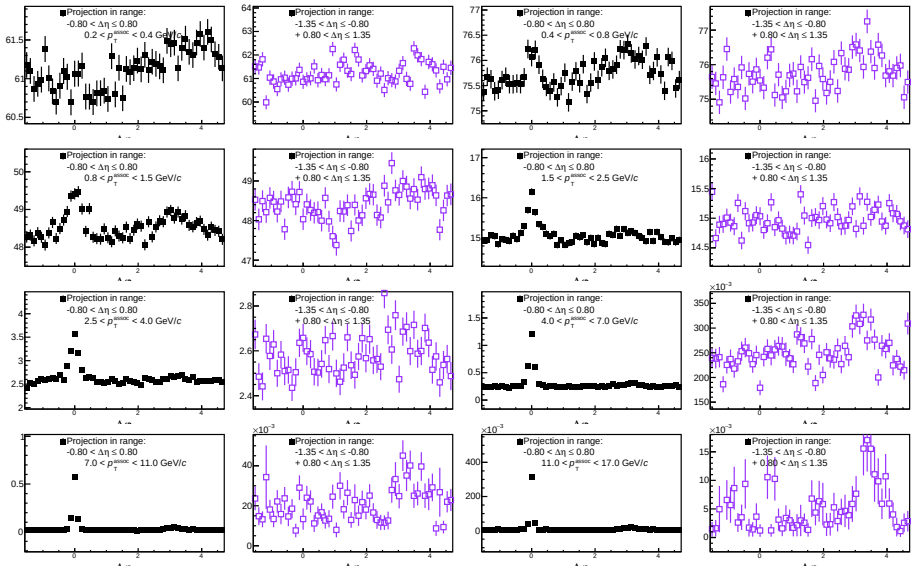

Figure 3.48: Projected π^0_{Cand}-hadron correlations, projected on to $\Delta\varphi$ for π^0_{Cand} in the 11-14 GeV/c p_{T} range. The near $\Delta\eta$ regions are in black full markers, while the far $\Delta\eta$ region is show in empty violet markers.

3.8 π^0 Impurity Correction

As the purity of the sample of π^0 candidates used as triggers for the correlations is not 100%, some of the correlation signal will be built from charged hadrons in the same event as a background cluster pair, defined as any pair of clusters that do not correspond to a $\pi^0 \rightarrow \gamma\gamma$ decay. As described in detail in Section 3.4.7, these background pairs come from a mix of higher decays (e.g. $\eta \rightarrow 3\pi^0 \rightarrow 6\gamma$), jets, and uncorrelated combinatorial background.

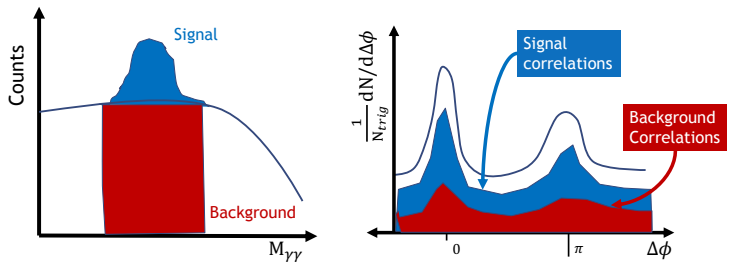

Figure 3.49: Cartoon of general sideband method.

As such, the measured per-trigger correlations will be a sum of signal correlations and background correlations, as described by Equation 3.15 and expressed in Figure 3.49.

$$\begin{aligned} C_{Cand} &= C_{Sig} + C_{Bkg} \\ \frac{1}{N_{Cand}} C_{Cand} &= \frac{1}{N_{\pi^0} + N_{Bkg}} \left(C_{Sig} + C_{Bkg} \right) \end{aligned} \tag{3.15}$$

Here, $\frac{1}{N_{\pi^0}} C_{Sig}$ is the real per-trigger yield we wish to measure, $\frac{1}{N_{Bkg}} C_{Bkg}$ is the correlation per-trigger yield of the background cluster pairs, and $\frac{1}{N_{Cand}} C_{Cand}$ is the actual measured per-trigger yield.

By introducting the purity of the identified π^0s, $P = \frac{N_{\pi^0}}{N_{Cand}}$, we can rewrite this as Equation 3.16.

$$\frac{1}{N_{Cand}} C_{Cand} = P \frac{1}{N_{\pi^0}} C_{Sig} + (1 - P) \frac{1}{N_{Bkg}} C_{Bkg} \tag{3.16}$$

Solving for the signal correlations yields Equation 3.17:

$$\frac{1}{N_{\pi^0}} C_{Sig} = \frac{1}{P} \left[\frac{1}{N_{Cand}} C_{Cand} - (1 - P) \frac{1}{N_{Bkg}} C_{Bkg} \right] \tag{3.17}$$

This outlines how we can extract the signal correlations if we have two components: the purity (P) and the background correlations ($\frac{1}{N_{Bkg}} C_{Bkg}$). As the purity is determined in Section 3.4.7, it only remains to determine the background correlations.

In typical analyses using particles identified via invariant mass, the background is studied by using the "sidebands" at slightly lower and slightly higher mass ranges than the mass peak of the signal particle. Then the behavior of the background under the peak is determined by averaging the lower and upper sidebands. This method assumes that the background is sufficiently similar as a function of mass in the region of the target peak. The step of averaging sidebands on both sides of the peak should cancel any first order (as a function of mass) effects.

A particular challenge in this analysis is that the lower sideband is unavailable for these high momentum π^0s. This is due to two factors: EMCal cluster energy thresholds and cluster merging. To address this problem, we take several steps to determine what impact this has on applying a sideband correction to the correlations and if this impact can be corrected.

3.8.1 Tools for Validation in ALICE Monte Carlo

To test and validate impurity-correction methods and estimate the systematic uncertainty that is introduced, the correlation analysis code was run over Monte Carlo simulations done for ALICE. When running over the simulations, the correlation code runs almost

identically to how it runs in data, except that it associates Monte Carlo information about the trigger (whether or not the cluster pair comes from a true $\pi^0 \to \gamma\gamma$ decay) with the correlations. This allows one to split the recorded correlations into those corresponding to true π^0 triggers and those from background. The primary usage of this is to study the sideband subtraction.

The correlations are saved into 4 different MC modes:

Table 3.20: Monte Carlo Modes for Correlations

Mode number	MC Mode
0	All triggers
1	Background only
2	True π^0 only
3	True η only

Subtracting Background from Background

To test, optimize, and validate the sideband subtraction, we apply it to purely background-hadron correlations. These correlations are built using triggers that are pairs of clusters that do not have a common ancestor that is a π^0 or η.

The sideband correlation is then applied assuming purity = 0, which is true by construction.

3.8.2 Sideband Selection

With three defined sidebands, we have the option to vary which will be included in the subtraction. By choosing the sidebands closer to the π^0 mass peak, we can minimize any effect of the difference between the sideband mass and the mass of the true background under the π^0 peak. On the other hand, we can include more sidebands to improve our statistics. It may also be of interest to use the farthest mass peaks to study the mass effect, and see if any extrapolation can be done, which is investigated in Section 3.8.5.

In the final version of this analysis, we define 3 sideband regions evenly within the range $(m_{\pi^0} + 5\sigma_{\pi^0}, 500\ \text{MeV}/c^2)$. An example is shown in Figure 3.50.

3.8.3 First Test

A first attempt with the sideband selction is to simply use the sideband correlations, after scaling for the purity and without further correction, to subtract a background. To avoid possible impact from the η peak, only the sidebands 1 and 2 are used in this test, shown in Figure 3.51.

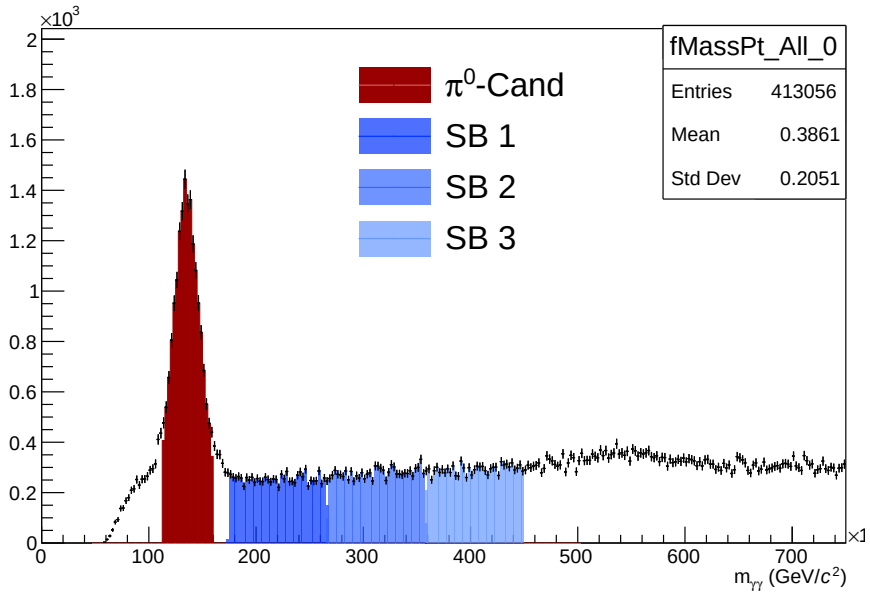

Figure 3.50: π^0-Candidate peak and 3 sidebands for $5 \leq p_T < 7$ GeV$/c$, 10-30% central MB event.

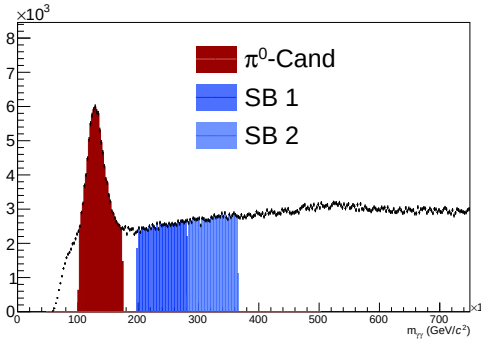

Figure 3.51: Sidebands used in the first test of the sideband subtraction, with simulated events in MC production LHC16h2, 0-10% central events.

This test is done in MCMode 1, so we are subtracting the background estimate from the real background. The real background is shown for a range of $p_{\mathrm{T}}^{\mathrm{assoc}}$ are shown in Figure 3.52. At low $p_{\mathrm{T}}^{\mathrm{assoc}}$, there may be a pedestal offset between the estimated background and the real background. Of more concern is the difference visible in the nearside peak, where the background estimated with the sideband underestimates the center of the nearside peak. This will result in a change in the shape of the nearside peak, and is a sign of an underlying issue in the method.

Other selections of the sideband region yield similar results. This evident failure motivates the analysis described in the next section.

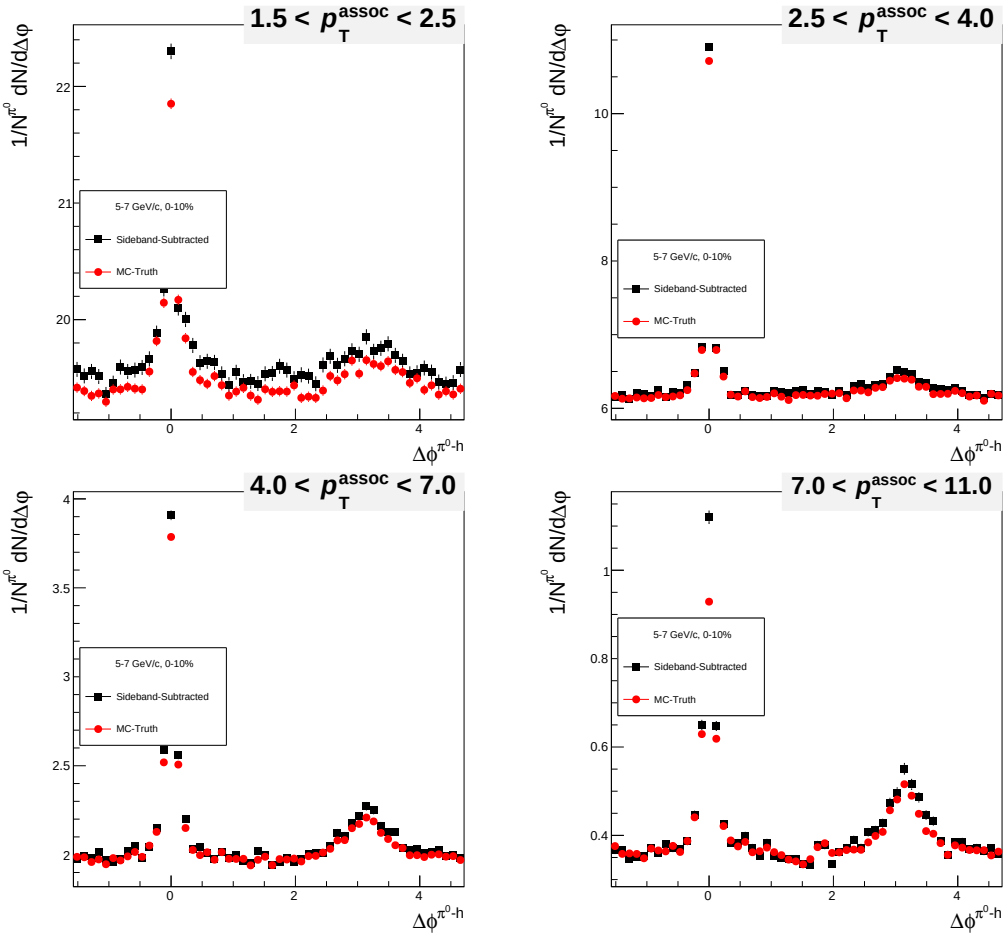

Figure 3.52: Comparison of sideband-subtracted correlations in MC with the MC true π^0-hadron correlations. This is using the closest two sidebands to the π^0 peak, without any extrapolation applied. These correlations for triggers in the p_{T} range 5-7 GeV/c.

3.8.4 Sideband Theory: Why the First Test Failed

MC Simulations suggest that the sideband correlations can be broken down into two contributions: correlated C_c and uncorrelated C_u cluster pairs:

$$\frac{1}{N_{trig}}C = \frac{1}{N_{trig}}(C_c + C_u)$$

Correlated cluster pairs come from the same jet, but don't share the same mother particle. Uncorrelated background do not share a common ancestor. These two populations can be expected to have different properties and correlations. For example, since correlated cluster pairs come from jets, they should have an azimuthal distribution representing the flow of jets of higher p_T. Uncorrelated pairs should have flow corresponding to the flow of the two individual particles, which are of much lower p_T than the jets.

This can be investigated with real data, by comparing the correlations of the π^0-

candidates and the sideband triggers, as seen from MB data (see Figure 3.53). The sideband triggers have a significantly different elliptical flow from the π^0-candidates, and the flow changes with the same order as the sidebands.

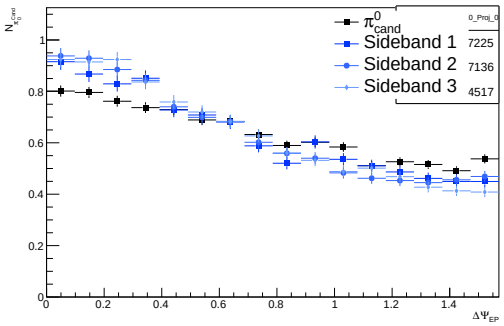

Figure 3.53: Correlation with the event plane of π^0-candidates and sideband triggers, from the $5-7$ GeV$/c$, 30-50% central MB events.

Our hypothesis is that the key variable that changes with the sidebands is the relative contribution of correlated and uncorrelated pairs. To develop a mathematical description of this, define F as the ratio of uncorrelated background to all background:

$$F \equiv \frac{N_c}{N_c + N_u} = \frac{N_c}{N_{trig}}$$

Where $N_{trig} = N_c + N_u$ is the total number of triggers

Then define functions f, g, h

$$f = \frac{1}{N_{trig}} C, g = \frac{1}{N_c} C_c, h = \frac{1}{N_u} C_u$$

Here f is the observed correlation function, g is the correlation function for correlated background, and h is the correlation function of the uncorrelated background. Note that g corresponds to a correlation function for jets, and should be dominated by the nearside and awayside peaks. h corresponds to the correlation function between two independent (from separate partons) particles and other particles in the event. This function is anticipated to be dominated by flow.

Note that these could be replaced with other observables, like the distribution with respect to event planes.

Then our observed correlations can be described by:

$$\frac{1}{N_{trig}} C = f = \frac{1}{N_c} \frac{N_c}{N_{trig}} C_c + \frac{1}{N_u} \frac{N_u}{N_{trig}} C_u$$

$$f = \frac{1}{N_c} F C_c + \frac{1}{N_u} (1 - F) C_u$$

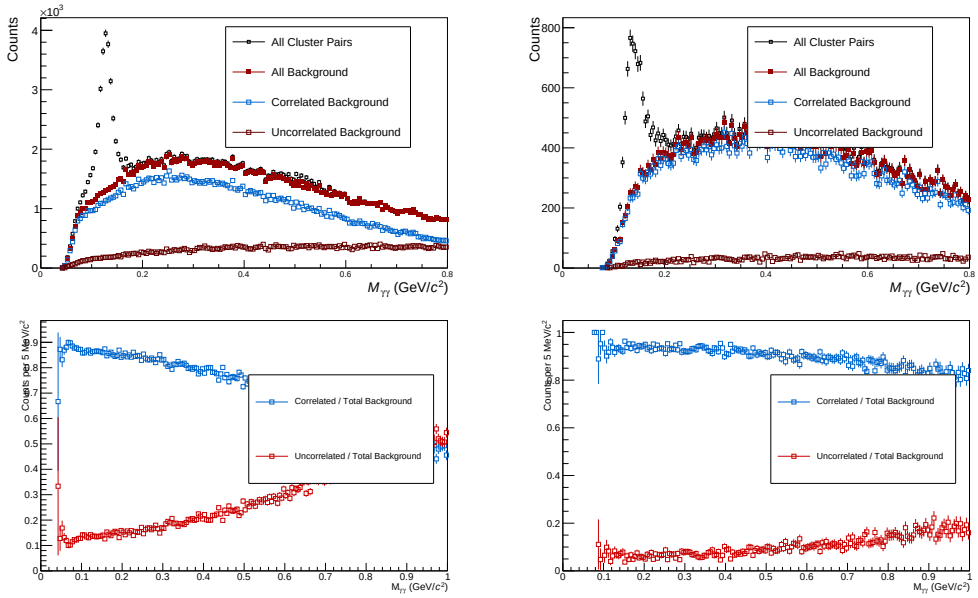

Figure 3.54: Invariant mass distribution for cluster pairs in the LHC16h2 MC production in the 5-7 (upper left) and 11-14 (upper right) GeV/cwindows. The background is broken up into the correlated background (cluster pairs that share a common ancestor) and the uncorrelated background (cluster pairs with no common ancestor). The relative fractions of the correlated and uncorrelated fractions are shown in the lower plots.

$$f = Fg + (1 - F)h$$

For azimuthal correlations, this can be written as

$$f(\Delta\varphi) = Fg(\Delta\varphi) + (1 - F)h(\Delta\varphi)$$

If we apply the same logic to to the distribution with respect to the nth order event plane:

$$f(\Delta\Psi_{EP,n}) = Fg(\Delta\Psi_{EP,n}) + (1 - F)h(\Delta\Psi_{EP,n})$$

Hypothesis: F changes linearly with mass.

$$F = \alpha(m - M) + x \tag{3.18}$$

Here, m is the invariant mass, M is the π^0 peak mass, and α and x are constants. Note that x is the value of F for the true background under the π^0 peak. We can investigate this in MC, but we cannot trust that the correlated background has the same shape in MC as in data. This is done in Figure 3.54, wherein we can observe that the fraction F (Correlated / Total Background) is approximately linear in the region under the π^0 peak and to the right.

Working with this hypothesis:

$$f = (\alpha(m - M) + x)g + (1 - \alpha(m - M) - x)h \tag{3.19}$$

We can also calculate $\frac{df}{dm}$ from Equation 3.19:

$$\frac{df}{dm} = \alpha g - \alpha h = \alpha(g - h) \tag{3.20}$$

Equation 3.20 is useful for interpreting the slopes for different $f(\Delta\varphi)$ and $f(\Delta\Psi_{EP,n})$ values. If we could experimentally determine α and x or g and h, this would be extremely useful for determining the background correlation functions at the π^0 peak. However, doing so is not trivial.

In principle, the ratio $F(m)$ could be determined by fitting the invariant mass spectrum to a linear combination of the π^0 and η peaks, the uncorrelated background and the correlated background. The shape of the uncorrelated background can be determined with some accuracy via mixed event and similar methods. However the shape of the correlated background is not known a priori and is a function of the jet spectrum and distribution of particles within the jet.

In practice, it was found that this linear extrapolation did not always yield the correct correlations. This could be explained by non-linearity of the fraction F as a function of mass. To account for this, the sideband subtraction was done with a wide range of fit functions and subsets of the 3 sidebands (as described in Table 3.21). It was found that the linear fit and the constant term with only the nearest sideband consistently produced results near the true value, but on opposite sides (where one overestimated, the other underestimated). This lead to the creation of function 4, which uses the average of these two, and is the default sideband extrapolation used. The choice of function 4 is the only part of this procedure that is dependent on Monte Carlo.

Index	Function	Formula	Valid subsets
0	Constant	A	all
1	Linear	$A + B(x - m_{peak})$	111,110,101,011
2	Quadratic	$A + B(x - m_{peak})(x - C)$	111
3	Rational	$(A + B(x - m_{peak}))/(1 + C(x - m_{peak}))$	111
4	Semi-linear	Average(linear, constant with 100)	111,110,101,011

Table 3.21: Sideband extrapolation functions. Functions are defined such that the parameter A is the value for $x = m_{peak}$, which is fixed to the location of the π^0 peak found in this analysis. Subsets are the list of masks determining which sidebands are included (e.g. 101 denotes sidebands 1 and 3)

3.8.5 Extrapolation

One concern in this analysis is how much the sideband subtraction is impaired having a sideband on only one side of the target particle's mass peak. We study whether any effect from this is significant and, if so, whether we can correct for it by comparing the different correlations for the different sidebands.

Exploring the possibility that the effect of the mass range on the background is just a scaling, we compare the integrals of the correlation functions between different sidebands for the same p_T range.

Comparing to MC Truth Correlations

The final step for validating the sideband correction is to apply the sideband correction to MC Mode 0 (all triggers, as in data), and compare to the correlations found with MCMode 2 (True π^0s only). This is done for the 11-14 GeV/c range in 0-10% central MC events in Figure 3.55, using sideband extrapolation function and sideband selection 111. For low p_{T} associated particles, there appears to be vertical shift between the sideband-corrected correlations and the MC true correlations. This is not a concern, as any flat background component will be removed during the flow subtraction procedure. For higher p_{T} associated particles, the agreement between the sideband-subtracted correlations is very good. Similar comparisons for 5-7 GeV/c triggers are provided in appendix F.

Note that extrapolation function 4 was devised as it was found to produce the best agreement in MC. It likely performs well because it is a good approximation to the fraction of correlated to total background in the simulation, something that is not guaranteed to be true in real data. For this reason, it is necessary to use all the functions that are reasonable to estimate the systematic uncertainty.

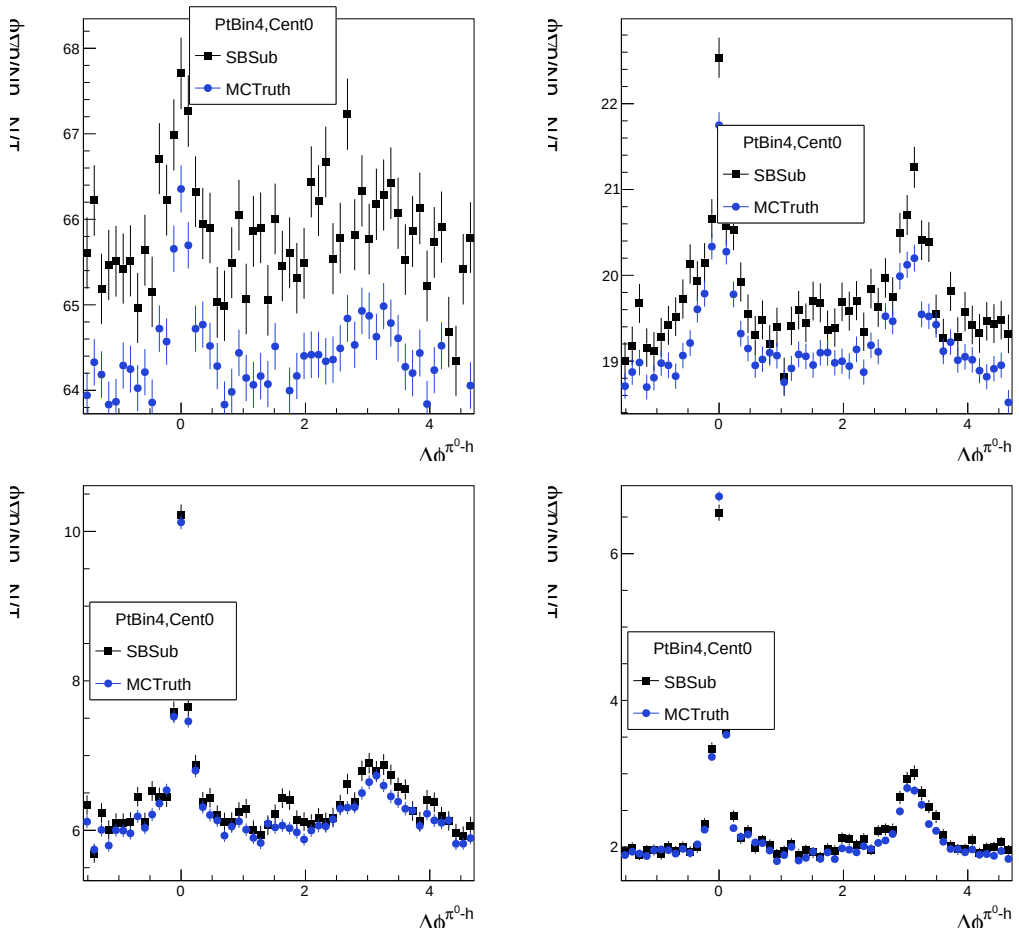

Figure 3.55: Comparison of sideband-subtracted correlations in MC with the MC true π^0-hadron correlations. This is using extrapolation function 4, with all three sidebands. These correlations for triggers in the p_{T} range 11-14 GeV/c.

3.9 Flow Subtraction

A significant challenge in extracting jet physics results from these correlations is the fact that a significant background comes from the flow of trigger and associated particles. In this case, both the $\pi^0 s$ measured here and the associated charged hadrons have correlations with respect to the event planes of the event, especially the 2nd order event plane. The flow parameters are labelled as v_n^t for the trigger π^0s and v_n^a for the associated hadrons, as listed

in Equation 3.21.

$$
\begin{aligned}
f^{\text{trigger}}(\varphi) &= 1 + \sum_{n=1}^{\infty} 2v_n^t \cos[n(\varphi - \Psi_n)] \\
f^{\text{assoc}}(\varphi) &= 1 + \sum_{n=1}^{\infty} 2v_n^a \cos[n(\varphi - \Psi_n)]
\end{aligned}
\tag{3.21}
$$

3.9.1 Reaction Plane Fit

One method that has been used in similar studies is to split the correlations by the angle of the trigger particle with respect to the event plane. This method is known as the Reaction Plane Fit (RPF) method, and has been used in [49] to fit and subtract the background due to flow in jet-hadron correlations.

When restricting the triggers to different angles with respect to the event plane, background contribution from flow changes dramatically. This can be understood intuitively from the fact that requiring the trigger to be out-of-plane causes it to be anti-aligned with the elliptical flow. In the reaction plane method, this is derived analytically to find the effective flow terms in each event plane as a function of the flow parameters of the trigger and associated particles. The full formula for the effective background flow and the effective flow parameters are given in Equations 3.22 and 3.24, respectively.

$$
\frac{dN}{d\Delta\phi} \propto \tilde{\beta} \left(1 + \sum_{n=1}^{\infty} 2\tilde{v}_n^t \tilde{v}_n^a \cos(n\Delta\phi) \right) \tag{3.22}
$$

Where $\tilde{\beta}$ is given by:

$$
\tilde{\beta} = 1 + \sum_{n=2,4,\ldots}^{\infty} 2v_k \cos(k\phi_s) \frac{sin(kc)}{kc} R_k \tag{3.23}
$$

The effective trigger v_n terms are given by:

$$
\tilde{v}_n^t = \frac{v_n + \cos(n\phi_S)\frac{\sin(nc)}{nc} + \sum_{k=2,4,6,\ldots}(v_{k+n} + v_{|k-n|})\cos(k\phi_s)\frac{kc}{kc}R_k}{1 + \sum_{k=2,4,6,\ldots} 2v_k \cos(k\phi_S)\frac{\sin(kc)}{kc}R_k} \tag{3.24}
$$

Here, R_k is the $(n = k)$ event plane resolution, with respect to the second order event plane, which will be detailed in Section 3.9.2.

With this formula, one can fit the background correlations in each event plane bin simultaneously, and extract more information than would be gained by simply fitting the background to flow terms without splitting up by event plane.

The flow parameters for the trigger and associated particles that can be extracted with this fit may have some deviation from the flow parameters that would be found in a standard flow analysis, as the flow in these correlations is only being sampled from a biased event sample required to contain a high p_{T} particle [42].

In this and most analyses with the method so far, three bins of the event plane angle are used as defined visually in Figure 3.56. A benefit of using this background technique is that one can easily perform the flow subtraction in each event plane bin, allowing one to study event plane dependent observables.

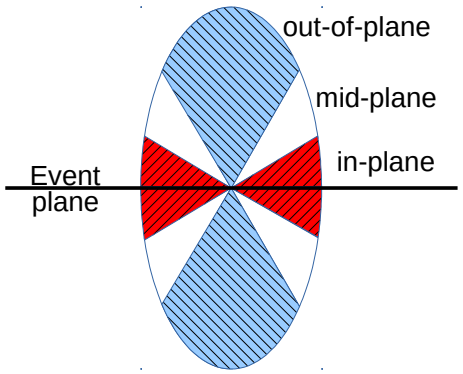

In-plane	$0 \leq \lvert\varphi - \Psi_2\rvert < \pi/6$
Mid-plane	$\pi/6 \leq \lvert\varphi - \Psi_2\rvert < \pi/3$
Out-of-plane	$\pi/3 \leq \lvert\varphi - \Psi_2\rvert < \pi/2$

Figure 3.56: Diagram of in-plane, mid-plane, and out-of-plane regions used in this analysis, alongside the mathematical description. Figure from the ALICE jet-hadron analysis [14]

.

3.9.2 Event Plane Resolution

One key set of ingredients to the reaction plane fit are the event-plane resolutions (R_n) for the detector used to determine the event-plane. The R_n characterizes the accuracy of the event-plane determination, and is 1 for perfect resolution and near zero for poor resolution, and is defined in Equation 3.25.

$$R_n \equiv \langle \cos(n[\Psi_{2,\text{Measured}} - \Psi_{2,\text{Truth}}]) \rangle \tag{3.25}$$

This leads to the useful general equation $v_n^{measured} = R_n v_n^{true}$. Thus, lower event-plane resolution values will lower the observed v_n, but this can be accounted for if R_n is known.

While, in principle, the event-plane resolutions could be estimated using a realistic Monte Carlo simulation, a practical, data-driven, approach is to use a subevent method. When we calculate the event-plane angles using two different detectors or parts of a detector (forming subevents), the event-plane angles from each subevent are affected by the

subdetector's individual resolution. When we use three subdetectors, we can use Equation 3.26 to determine the EPR for any one of the subdetectors.

$$R_n = \sqrt{\frac{\langle \cos(n[\Delta\Psi_1])\rangle \langle \cos(n[\Delta\Psi_2])\rangle}{\langle \cos(n[\Delta\Psi_3])\rangle}} \tag{3.26}$$

$$\Delta\Psi_1 \equiv \psi_2^{V0} - \psi_2^{TPCA} \tag{3.27}$$

$$\Delta\Psi_2 \equiv \psi_2^{V0} - \psi_2^{TPCC} \tag{3.28}$$

$$\Delta\Psi_3 \equiv \psi_2^{TPCA} - \psi_2^{TPCC} \tag{3.29}$$

Impurity Correction in Different Event Plane Angles

As the impurity of the π^0 selection varies as a function of the angle relative to the event plane, it is critical to do the sideband subtraction of correlations in different event plane bins separately.

3.9.3 Reaction Plane Fit Parameters

Included Parameters

The parameters that can be included in the RPF are the overall normalization parameter B, the even flow terms:

$$v_2^t, v_2^a, v_4^t, v_4^a, v_6^t, v_6^a, ...$$

And the odd flow terms:

$$v_1^t v_1^a, v_3^t v_3^a, v_5^t v_5^a, ...$$

The odd terms for trigger and associated particles do not factorize in the Reaction Plane Fit formula, as the odd-ordered event planes are assumed to be uncorrelated with the reaction plane. As such, their product must be considered as a single parameter.

Higher Order Terms

We have also tested the results of the reaction plane fit when including additional flow terms. Specifically, including terms up to v_5 and v_6, as well as including a v_1 directed flow term.

Calculating Parameters Directly

If any of the parameters can be determined separately, then it will not be necessary to leave those parameters free.

The simplest term to determine is v_2^a, which corresponds to the v_2 of charged hadrons. As this can be different in events including the trigger particle, using the published values for flow measurements may not be correct, although they may be useful for comparison. Another option is to calculate the parameters directly using the same data sets. This is done in this analysis for the v_2 and v_3 terms for charged hadrons. That is done by measuring the correlations between the particles and the 2nd and 3rd order event planes as measured with the V0 detector, and correcting for the event plane resolution. The fitting procedure is shown in Figure 3.57.

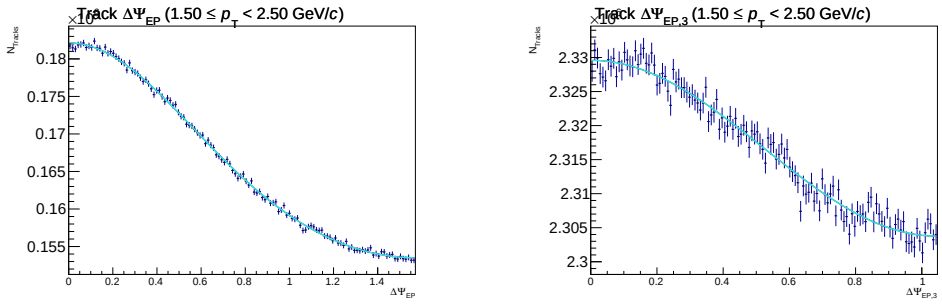

Figure 3.57: Fits of tracks to v_2 (left) and v_3 (right) in EGA-triggered 30-50% central events.

An interesting finding resulting from this is that the flow parameters measured in EGA-triggered events are significantly lower than those in MB events. As can be seen in Figure 3.58, this difference appears both for v_2 and v_3. This finding may support the idea that the particle flow is different in events having a high p_{T} trigger.

Free RPF Parameters vs Calculated Values.

In this section we run the RPF with all parameters up to order 4 free, and compare the results to what direct calculations of those parameters yields, as well as published v_n values, when available. Additionally, it should be noted that two independent implementations of the RPF were also used (one implemented by the author (labelled 1 in plots), and one implemented by Raymond Ehlers (labelled 2 in plots), available at [23]).

In Figure 3.59, the v_2^a parameter from the free RPF is significantly lower than the published v_2 for charged particles at this energy, but it is consistent with the v_2 found by measuring v_2 in these same events. Due to this, it is reasonable to fix the v_2^a to that found through fitting, to reduce this uncertainty in the RPF fit. In Figure 3.60, the v_2^t parameter is found to be consistent across p_T^a bins, which is to be expected as the π^0 v_2 does not

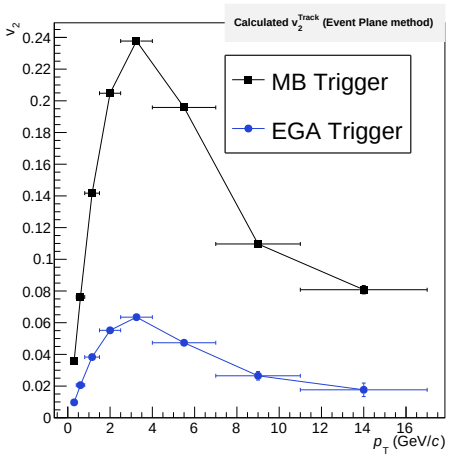

(a) Charged track v_2.

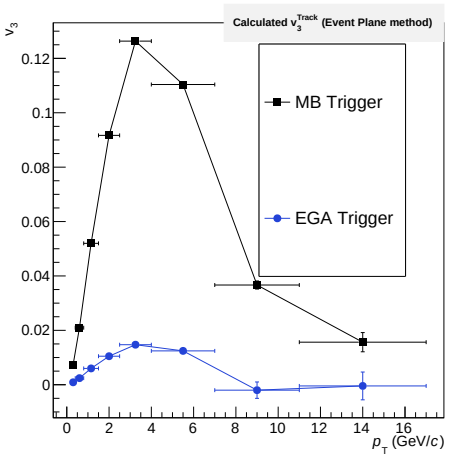

(b) Charged track v_3.

Figure 3.58: Comparison of flow parameters for charged calculated directly in this analysis between MB and EGA-triggered events, for 30-50% central events.

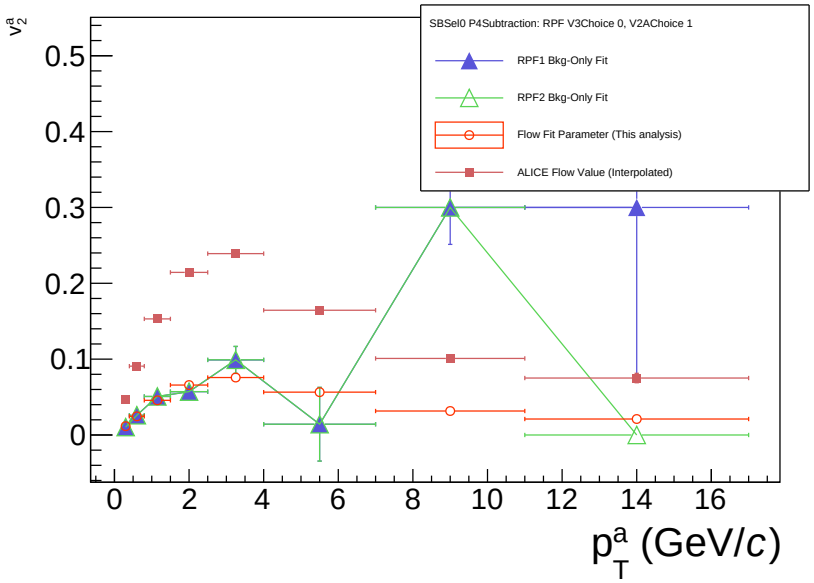

Figure 3.59: Comparison (for 11-14 GeV/c, 30-50% central EGA-triggered events) of parameter v_2^a from the RPF method with no fixed parameters, from fitting the tracks vs the event plane in the same events, and the ALICE published data with a cumulant method in MB events.

change with the p_{T}^a. This is used to justify using the lower p_{T}^a points, which have lower uncertainty, to fix the v_T parameters.

For the $v_3^t v_3^a$ parameter, the RPF fit at low p_{T} can be influenced by contamination of the near-side peak spreading into the far $\Delta\eta$ region. The wide part of the near-side peak

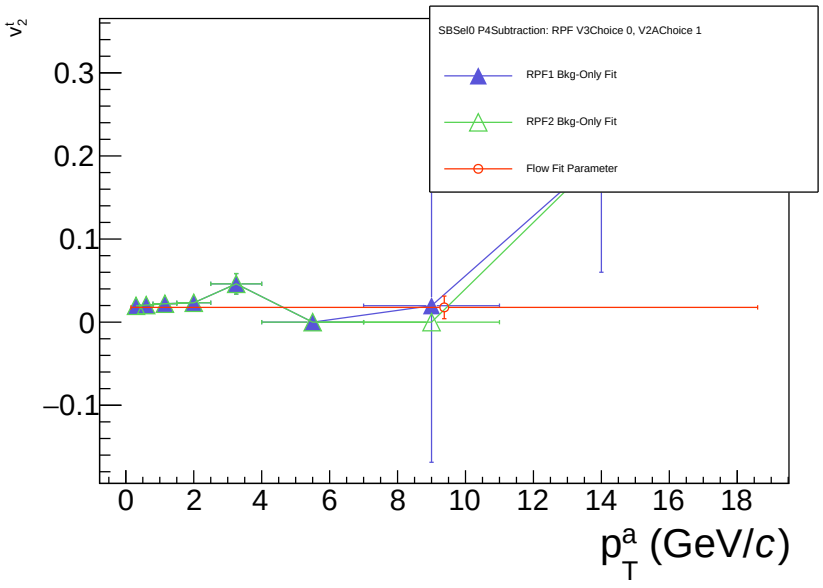

Figure 3.60: Comparison (for 11-14 GeV/c, 30-50% central EGA-triggered events) of parameter v_2^t from the RPF method with no fixed parameters and from fitting the π^0 vs the event plane (after applying a sideband subtraction) in the same events.

is similar in shape to the $\cos(3\Delta\varphi)$ term, and can lead to a "fake" v_3 signal in the fit, particularly when, as is done in this analysis, the RPF fit is performed only in the near-side region. For this reason, the $v_3^t v_3^a$ parameter is estimated from the product of the v_3 of tracks evaluated at the p_T of the associated particle and at the p_T of the π^0. The result of this, and a comparison to the values found with free parameters, is shown in Figure 3.61. This uses an approximation that the v_3 of π^0s will be the same as those of all tracks, which is not expected to be exactly true. However, the uncertainty in v_3 at the π^0 p_T in this analysis (for π^0s in the 11-14 GeV/c range) is so large that it cannot be distinguished from zero. Thus, it will be particularly important to vary the value used as the fixed $v_3^t v_3^a$ value for the purpose of calculating the systematic uncertainty.

The fourth-order parameters are investigated in Figures 3.62 and 3.63. One finding from this is that, similarly to v_2^a, the RPF returns a v_4 for charged particles significantly lower than the MB v_2 recorded in ALICE published measurements. The v_4 term found from fitting tracks was found by fitting the tracks to a function $B(1+2v_2\cos(2(\varphi-\Psi_2))+2v_4\cos(4(\varphi-\Psi_2)))$, which should give the v_4 diminished by the decorrelation between the $(n=2)$ and $(n=4)$ event plane angles. As such, this v_4 will not be used to fix the v_4 in the fit, leaving v_4 as a free parameter. The v_4^t can be treated with the same procedure of fixing the parameter from free low p_T fits.

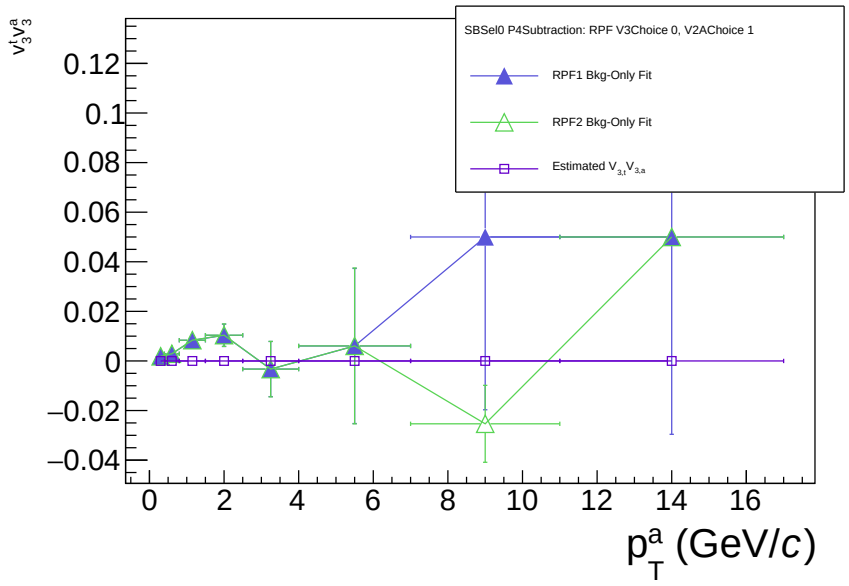

Figure 3.61: Comparison (for 11-14 GeV/c, 30-50% central EGA-triggered events) of parameter $v_3^t v_3^a$ from the RPF method and from fitting the tracks vs the event plane in the same events.

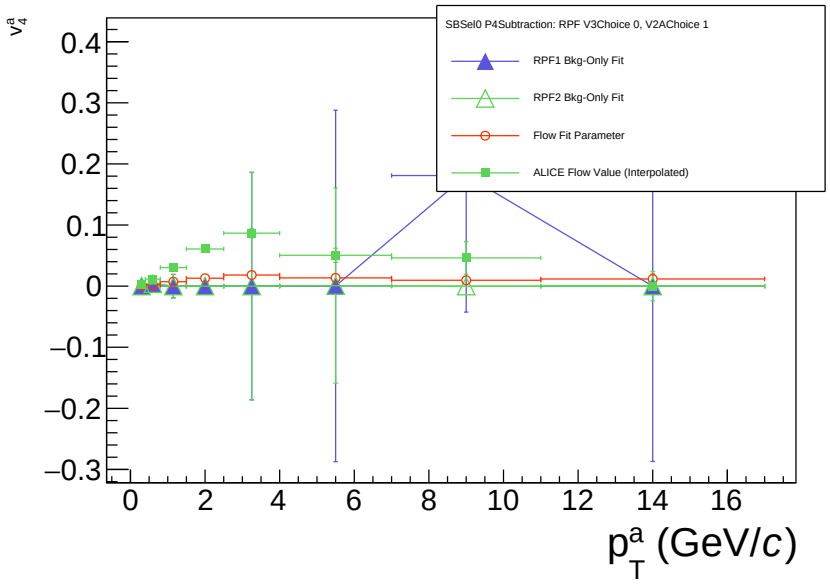

Figure 3.62: Comparison (for 11-14 GeV/c, 30-50% central EGA-triggered events) of parameter v_4^a from the RPF method, from fitting the tracks vs the event plane in the same events, and the ALICE published data with a cumulant method in MB events.

3.9.4 Results of Flow Subtraction

The full process of the RPF subtraction is presented in plots such as Figure 3.64. More of such Figures (for different associated p_{T} ranges) are given in appendix G.

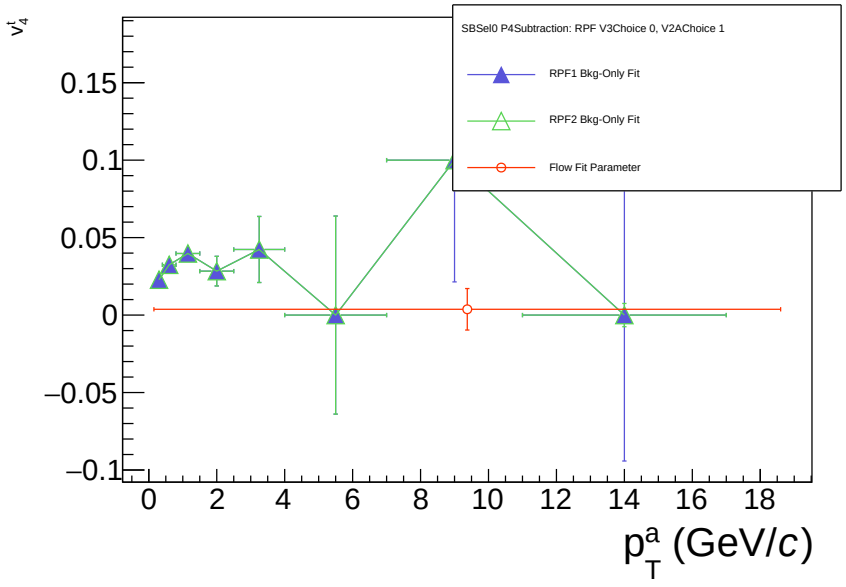

Figure 3.63: Comparison (for 11-14 GeV/c, 30-50% central EGA-triggered events) of parameter v_4^t from the RPF method and from fitting the tracks vs the event plane in the same events.

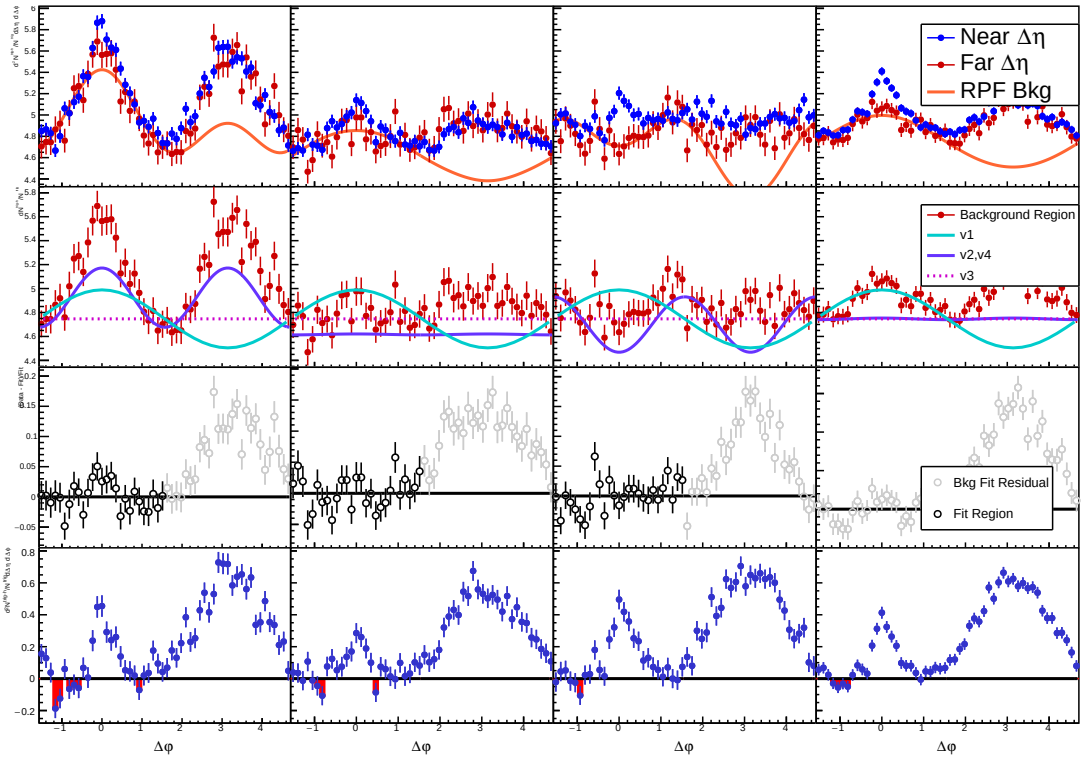

Figure 3.64: Plots of the reaction plane fit process. In the top row, the π^0-hadron correlations in the near-$\Delta\eta$ (signal dominated) and far-$\Delta\eta$ (background dominated) regions are plotted for triggers in-plane, mid-plane, and out-of-plane and finally all triggers. In the second row, the far-$\Delta\eta$ region is plotted along with individual components of the RPF. In the third row, the residuals of the far $\Delta\eta$ region vs the RPF. The darkened points in the nearside region are those used for the fit. In the final row, the subtracted near-$\Delta\eta$ correlations are shown, with any over-subtraction highlighted.

3.10 Systematic Uncertainties

In this section, we study the various systematic uncertainties affecting the results of this analysis.

The general method used to analyze these uncertainties is to take a parameter of a correction step and vary the value used and complete the full analysis. In cases of calculated parameters, such as for the $v_{2,a}$ and $v_{3,t}v_{3,a}$ parameters, the variations are defined by adding and subtracting the uncertainty in the calculated parameter. After the varied analyses have been carried out to the point of calculating the final observables, the variance of the distribution of observables with respect to each variable is used to calculate the systematic uncertainty.

The systematic uncertainty is calculated separately (when possible) for each point (in associated particle p_{T}). This includes calculating the total systematic uncertainty by adding the sources in quadrature. To prevent fluctuations from leading to underestimates of systematic uncertainty, the uncertainties from different sources are fitted as a constant function of p_{T}, with these fits added in quadrature to produce a alternative minimum uncertainty. The final uncertainty that is reported is the maximum of the individually calculated total uncertainties and the alternative minimum from fitting the systematic uncertainties.

3.10.1 Pseudorapidity Cut Uncertainty

One analysis choice to vary is the $\Delta\eta$ cut used to define the near-eta and far-eta regions. The primary purpose of this cut is to cut out the near-side peak. The cut needs to balance cutting out the near-side peak while leaving enough statistics in the far eta region to use for the background fit.

1. $\Delta\eta = 0.8$
2. $\Delta\eta = 0.7$
3. $\Delta\eta \approx n\sigma_{NS}$

In the $n\sigma_{NS}$ option, the cut is determined algorithmically, by fitting the nearside peak in $\Delta\eta$ and applying an $n * \sigma$ cut that is bounded between 0.5 and 0.8 (i.e. if the $n * \sigma$ cut would be outside that range it is limited to 0.5 or 0.8). The n_σ is 5 by default. The upper bound ensures the far η region has sufficient statistics, while the lower bound provides extra protection against contamination of the nearside peak into the far η region. The out/in away-side ratio is shown for different $\Delta\eta$ values in Figure 3.65.

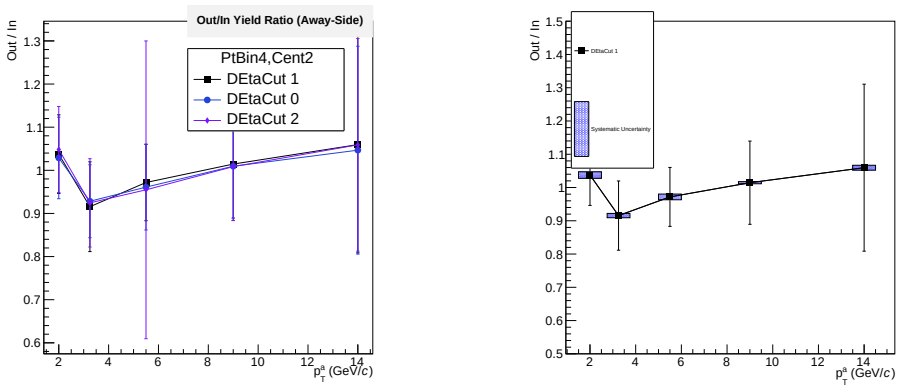

Figure 3.65: Awayside yield out/in event plane ratio with different $\Delta\eta$ cut options are shown on the left. On the right, variance in the points on the right are used to calculate the systematic uncertainty thhat is shown on the right.

3.10.2 Mixed Event Correction Uncertainty

In the mixed event correction, the method of scaling the mixed events to an algorithmically determined region introduces a potential systematic uncertainty. To address this, we vary some parameters of the algorithm determining the region that is scaled to unity. One parameter to vary is the size in $\Delta\eta$ of the region projected onto $\Delta\varphi$ for the determination, which has the default value of 0.1. Another parameter to vary is the number of bins included in the normalization region. By default three bins are used to evaluate the running average.

The following variations were tested for the $11 - 14$ GeV$/c$, 30-50% central, EGA-triggered π^0 candidate correlations:

Table 3.22: Mixed Event correction parameter variations tested.

index	$\Delta\eta$ region size	Averaging window bins
0 (default)	0.1	3
1	0.1	5
2	0.15	3
3	0.15	5
4	0.05	3
5	0.05	5
6	0.25	3
7	0.25	5
8	0.2	1
9	0.1	1

The results of applying the mixed event correction are shown in Figure 3.66. It can be concluded that the choice of mixed event correction parameters has no impact on the shape.

Additionally, the effect is negligible at low $p_{\mathrm{T}}^{\mathrm{assoc}}$, and approximately 0.5% at high $p_{\mathrm{T}}^{\mathrm{assoc}}$. As this is dominated by the 4% scale uncertainty from the tracking efficiency uncertainty, it can be included in that scale uncertainty.

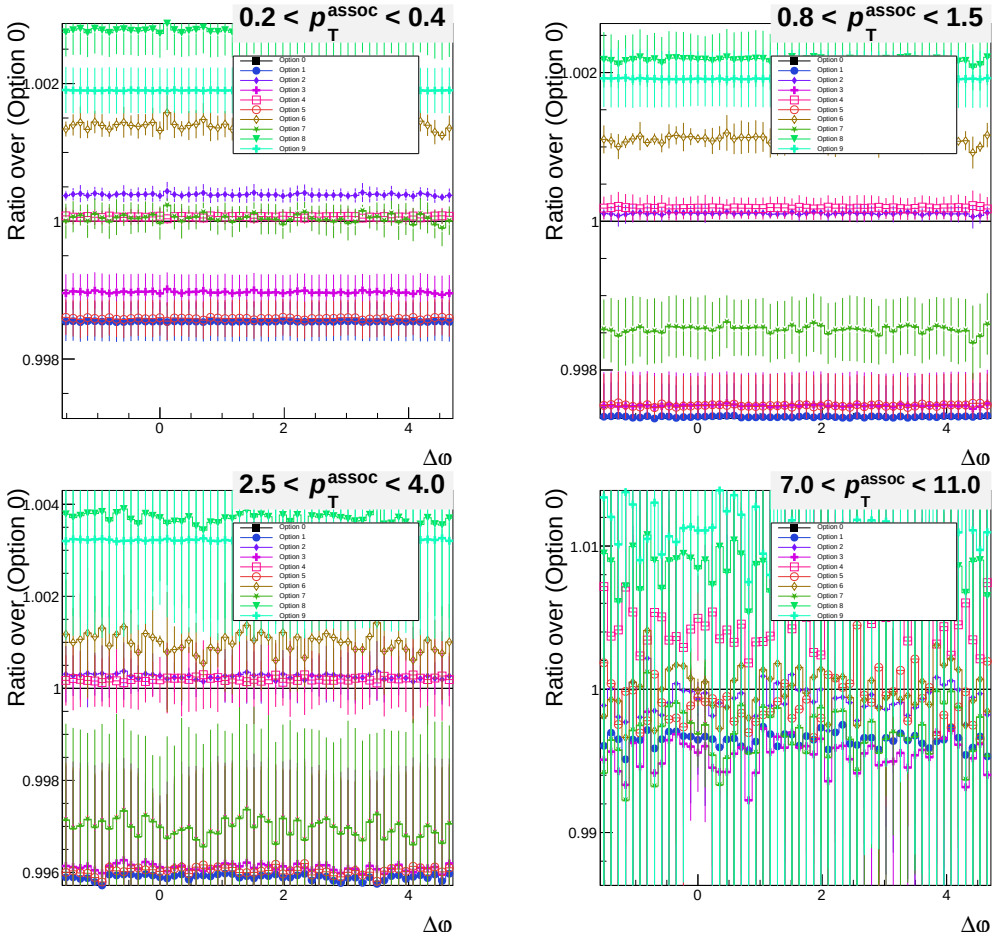

Figure 3.66: Ratio of different mixed event correlation correction options to the default value. Four $p_{\mathrm{T}}^{\mathrm{assoc}}$ bins are shown. The data is for raw π^0-hadron correlations in the $11-14$ GeV/c bin, 30-50% central EGA-triggered events.

Note that the mixed event correlations used in the denominator of the correction is the same for each event plane bin, so this scale uncertainty is correlated between event plane bins.

3.10.3 π^0 Purity

The calculation of the uncertainty in the π^0 purity itself is discussed in Section 3.4.7. Here we discuss the propagation of this uncertainty to the final observables. As previously mentioned, the purity is an important variable to study, as an error in the purity will cause the background correlations to be over or under-subtracted.

The purity uncertainty is propagated to the final observables by varying the used purity up and down by its uncertainty (the quadratic sum of the statistical and systematic uncertainties calculated in Section 3.4.7).

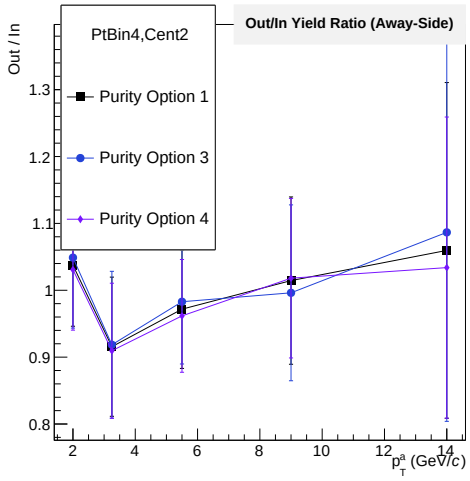

Figure 3.67: Final results with varying of the purity value used in the sideband subtraction by $\pm$ the uncertainty in the purity.

3.10.4 Impurity Correction

The π^0 impurity correction via sideband subtractions entails significant uncertainty, particularly due to the need to extrapolate the background correlations from sidebands on only one side. As discussed in section 3.8.4, a wide range of functions and selections of sideband regions are used to quantify this uncertainty. For the final observables in this analysis, all usable functions and sideband selections listed in Table 3.21 are used to produce a range of results, whose variance is used to calculate the systematic uncertainty from the impurity correction.

3.10.5 Tracking Efficiency

The efficiency for finding real particles in ALICE's ITS and TPC directly impacts this analysis in the yields of correlated particles. As described in Section 3.2.1, we apply a correction factor for the efficiency that accounts for changes in p_{T} and η.

Global Tracking Efficiency Uncertainty

The global uncertainty on the tracking efficiency of 4% applies as a scale uncertainty on the correlations, contributing to the uncertainty on yields, but not to any width measurements.

The tracking efficiency uncertainty in ALICE has been estimated at 4%, using variations of the cuts and parameters used in matching tracks between the ITS and TPC [50].

Event-Plane Dependence

While the tracking efficiency and its overall uncertainty cancel out in the ratios between observables out-of-plane vs in-plane, if the efficiency varies with the event plane, it would effect the ratios. Of particular concern is that if the tracking efficiency is lower in-plane (due to higher track multiplicity in-plane) then that would create an apparent suppression of tracks in-plane and obscure any real event-plane dependent signal.

As early simulations may not have accurate event plane determination and flow simulation, it is preferable to find an indirect method to investigate event plane dependence in the tracking efficiency. If the efficiency changes due to the event plane, it is because of the local track multiplicity out-of-plane vs in-plane. We can estimate the event plane dependence by using the centrality-dependence (which we already know) as a proxy for the local multiplicity dependence, and then use flow coefficients to estimate how different the multiplicity in-plane and out-of-plane.

For the multiplicity as a function of centrality, we must use the multiplicity in the MC events, which can be determined from the average number of MC charged particles in the range $(-\eta, \eta)$.

Once the multiplicity dependence is determined in MC, we will need to use the ALICE publication of measured and captured $dN/d\eta$ in the [25].

To simplify the calculation, we convert the multiplicity to a variable $\rho_M = \langle \frac{d^2N}{d\eta d\varphi} \rangle = \frac{1}{2\pi}\frac{dN}{d\eta}$, the particle density per unit in $\phi - \eta$ space, shown for both MC and data in Table 3.23.

Centrality	$\langle dN/d\eta \rangle$ (MC)	ρ_M (MC)	$\langle dN/d\eta \rangle$ (Data)	ρ_M (Data)
0-10%	1925.81 ± 0.13	306.502 ± 0.020	1764 ± 25	281 ± 4
10-30%	1020.073 ± 0.074	162.350 ± 0.012	983 ± 9	156.4 ± 1.4
30-50%	441.690 ± 0.049	70.2971 ± 0.0078	415 ± 10	66.0 ± 1.6
50-80%	90.644 ± 0.015	14.4264 ± 0.0024	108 ± 4	17.2 ± 0.6

Table 3.23: Average $dN/d\eta$ and ρ_M per centrality bin, as produced in the LHC16g1 MC production, and as measured by ALICE in $\sqrt{s_{\rm NN}}$=5.02 TeV PbPb collisions[25]. MC uncertainties are only statistical, while the data uncertainties included systematic uncertainties.

Then we use the tracking efficiency as a function of track $p_{\rm T}$ in different centrality bins, using the same train as used in Section 3.2.1. This is shown in Figure 3.68.

The next step is to use the ρ_M value in Table 3.23 to fit the efficiency as a function of ρ_M in different $p_{\rm T}$ bins. Two examples are shown in Figure 3.69. The slope of these

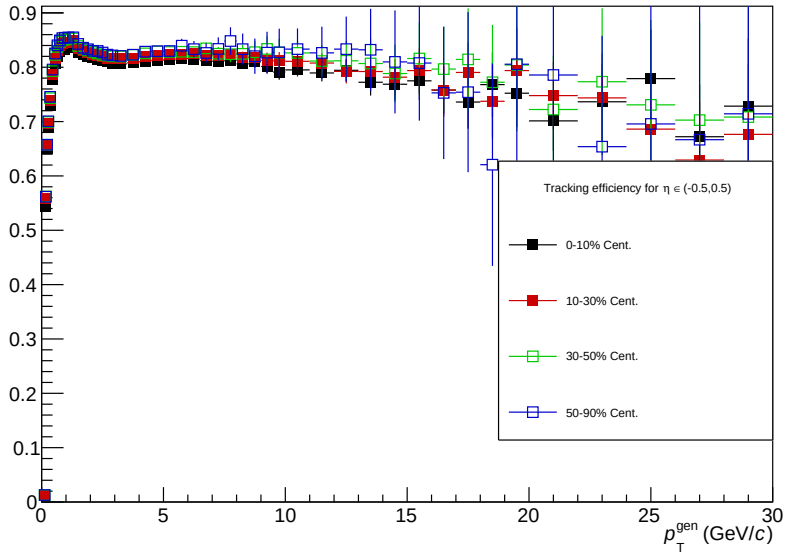

Figure 3.68: Tracking efficiency in different centrality bins.

efficiency plots (S) is the change in efficiency per change in particle density rho, shown in Figure 3.69.

$$S = \frac{d(Efficiency)}{d(\rho_M)}$$

The slopes for each p_{T} value is shown in Figure 3.70.

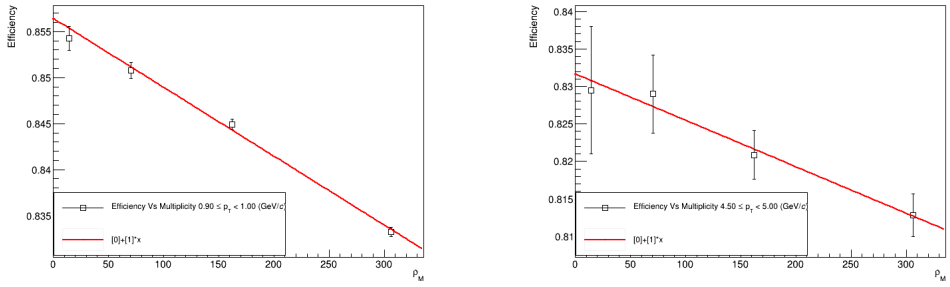

Figure 3.69: Example plots of the efficiency vs ρ_M.

To set an upper limit on the effect on the efficiency in different angles with respect to the event plane, we take the bound on the magnitude of S, around -0.8×10^{-4}. The change in efficiency between event planes ($\Delta\epsilon$) can be approximated using S.

$$\Delta\epsilon = S * (\rho_{M,out-of-plane} - \rho_{M,in-plane}) \tag{3.30}$$

To estimate the difference in particle density between the in-plane and out-of-plane

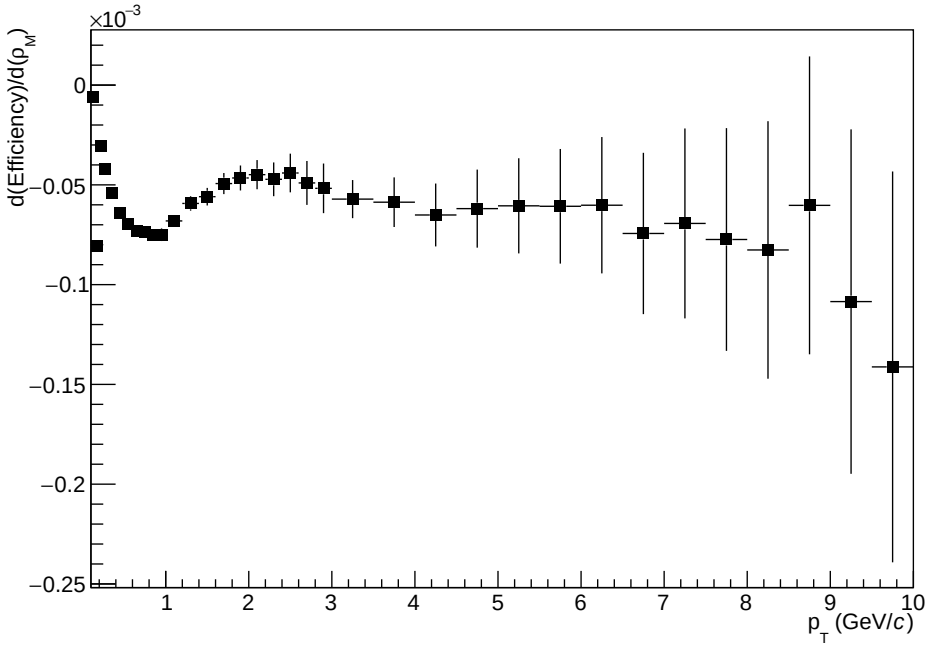

Figure 3.70: Slopes ($d\epsilon/d\rho_M$) of the efficiency vs particle density plots.

regions, we use the flow decomposition, as in 3.31.

$$\frac{d^2N}{d\eta d\varphi} = \frac{1}{2\pi}\frac{dN}{d\eta}\left(1 + \sum_{n=1}^{\infty} 2v_n \cos(n\varphi))\right) \tag{3.31}$$

$$\frac{d^2N}{d\eta d\varphi} = \rho_M(1 + \sum_{n=1}^{\infty} 2v_n \cos(n\varphi))) \tag{3.32}$$

Next, we want to calculate the particle density in the in-plane region ($-\pi/3 < \varphi < \pi/3$). To get the average particle density in plane, we integrate the series in 3.32 over the 2 in-plane regions (while also dividing by the size of the region). By noting that the odd terms will cancel over the 2 in-plane regions, we get Equation 3.33.

$$\rho_{M,in} = 2\rho_M \frac{1}{2(\pi/6 - (-\pi/6))}\left[\int_{-\pi/6}^{\pi/6} d\varphi \left(1 + \sum_{n=2,4,\ldots}^{\infty} 2v_n \cos(n\varphi)\right)\right] \tag{3.33}$$

$$\rho_{M,in} = \frac{3}{\pi}\rho_M \left[\frac{\pi}{3} + \sum_{n=2,4,\ldots}^{\infty} \frac{2v_n}{n}\left[\sin(n\varphi)\right]_{-\pi/6}^{\pi/6}\right]$$

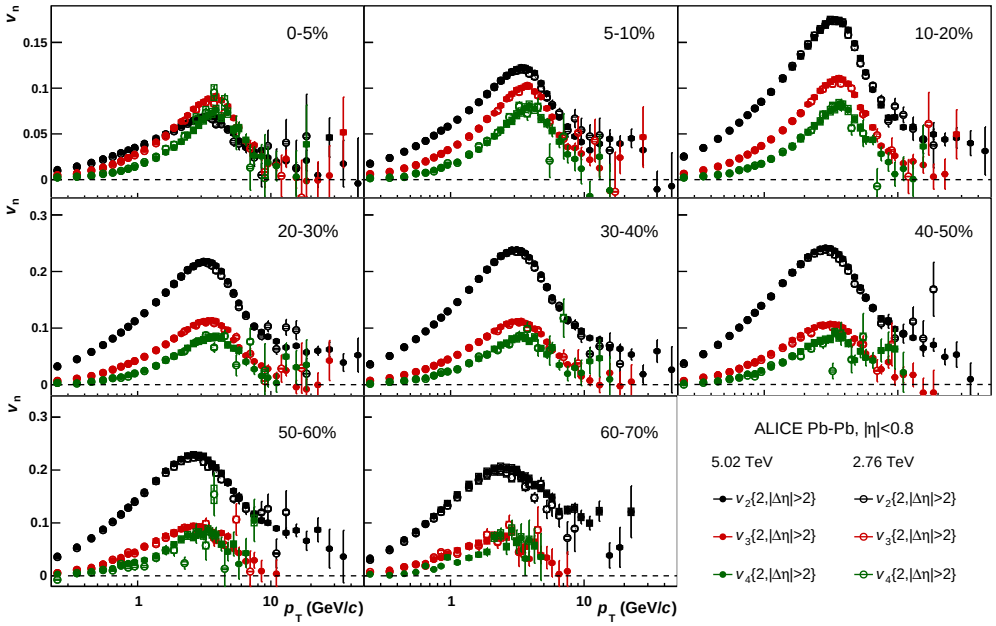

Figure 3.71: Flow values as found by ALICE [22].

$$\rho_{M,in} = \frac{3}{\pi}\rho_M \left[\frac{\pi}{3} + \sqrt{3}v_2 + \frac{\sqrt{3}}{2}v_4 + \dots\right]$$

Similarly, we have Equation 3.34 for the out-of-plane multiplicity.

$$\rho_{M,out} = 2\rho_M \frac{1}{2(\pi/6 - (-\pi/6))}\left[\int_{\pi/3}^{4\pi/3} d\phi \left(1 + \sum_{n=2,4,\dots}^{\infty} 2v_n \cos(n\phi)\right)\right] \tag{3.34}$$

$$\rho_{M,out} = \frac{3}{\pi}\rho_M \left[\frac{\pi}{3} + \sum_{n=2,4,\dots}^{\infty} \frac{2v_n}{n}\left[\sin(n\varphi)\right]_{\pi/3}^{2\pi/3}\right]$$

$$\rho_{M,out} = \frac{3}{\pi}\rho_M \left[\frac{\pi}{3} - \sqrt{3}v_2 + \frac{\sqrt{3}}{2}v_4 + \dots\right]$$

$$\Delta\epsilon = S\left[\frac{3}{\pi}\rho_M\left(\frac{\pi}{3} - \sqrt{3}v_2 + \frac{\sqrt{3}}{2}v_4\right) - \frac{3}{\pi}\rho_M\left(\frac{\pi}{3} + \sqrt{3}v_2 + \frac{\sqrt{3}}{2}v_4\right)\right] \tag{3.35}$$

$$\Delta\epsilon = -S\frac{6}{\pi}\rho_M\left[\sqrt{3}v_2\right] \tag{3.36}$$

Equation 3.30 approximates the change in tracking efficiency between the in-plane

and out-of-plane regions. To properly calculate the local particle density in each event plane bin, it is necessary to convolve the $v_2(p_{\mathrm{T}})$ with dN/dp_{T}. To set an upper bound for the effect, we can use the maximum value for v_2 in the 30-50% centrality range is approximately 0.24, as can be read from Figure 3.71.

$$\Delta\epsilon_{\text{max}} = -(-0.8 \times 10^{-4}(6/\pi)(66.0)\left[\sqrt{3}(0.24)\right] = 0.0042 \tag{3.37}$$

Note that because the upper bounds of the $v_2(p_{\mathrm{T}})$ and the magnitude of the slope $(d(\epsilon)/d(\rho_M))$, this value of $\Delta\epsilon_{\text{max}}$ is an upper bound on the effect. A more precise value could be calculated by using Equation 3.30 and convolving the v_2, ρ_M, and S parameters as functions of p_{T}. This could then be applied as a correction factor. Given the scale of the maximum bound on this effect found here, it suffices to leave this as a systematic uncertainty in the yield event plane ratios.

3.10.6 Flow Subtraction Uncertainty

One major part of the uncertainty introduced by the flow subtraction is the uncertainty in the RPF fit, which should be propagated to the final observables.

Whenever we fix a parameter of the Reaction Plane Fit (e.g. $v_t^a, v_3^a v_3^t$), we introduce a new systematic uncertainty from that parameter.

RPF Fit Uncertainty

The reaction plane fit entails some uncertainty that must be propagated to any final observables. For example, the implementation shown in Figure 3.72 shows the large error bars in the fits away-side region.

It is feasible to calculate error bands for the function and use these to calculate uncertainties in the fit subtracted integrals in each event plane angle and then propagate those errors to the ratio. However, that will not capture important correlations between the parameters and the event planes in the RPF subtraction, as well as uncertainties that cancel out. For example, if a v_2 parameter is too large, it will over-subtract in-plane, and under-subtract out-of-plane, significantly affecting out/in ratios. On the other hand, parameters such as B, v_1, v_3 affect each event plane equally, so errors in those parameters should largely cancel out in the ratios. Importantly, there is a large anti-correlation between the B and v_1 parameters (a consequence of only fitting the near-side).

To ensure that the calculated uncertainties from flow subtraction in the final ratios reflect these correlations, a Monte Carlo approach is used for error propagation. In this method, a large number (500) of RPF variants are produced from the uncertainties in the final fit parameters. To account for the correlations between parameters, the variant parameters are sampled according to the fit's covariance matrix. This is done using the Foam distribution sampler available in ROOT's math library (A helpful guide is found at

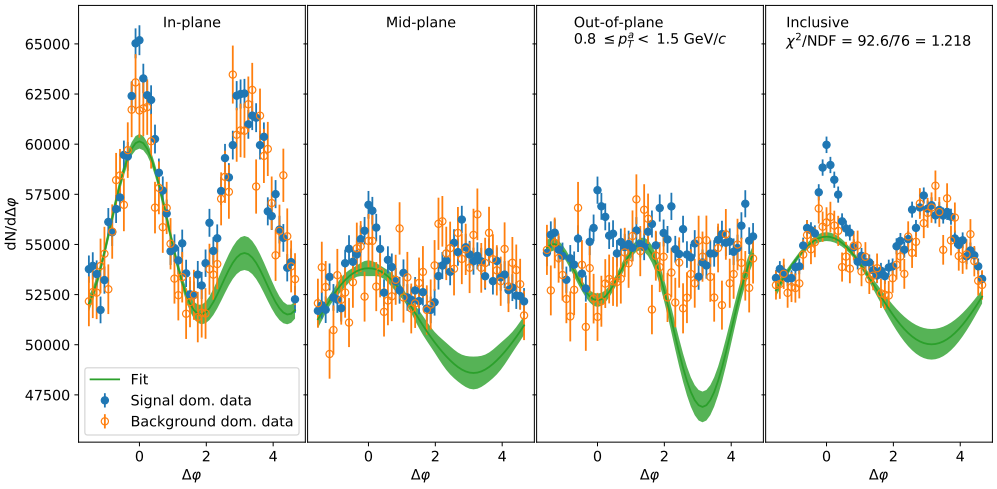

Figure 3.72: Reaction Plane Fit of 30-50% Central, EGA-Triggered events, 11-14 GeV/c π^0s using reactionPlaneFit python implementation by [23]

`https://root.cern/doc/master/multidimSampling_8C.html`). An example of the varied parameters for a set of RPF variants is shown in Figure 3.73. This parameter sampling is done with all free parameters in the RPF, so it will not include parameters that we fix, such as $v_3^t v_3^a$. As a result, the uncertainty in those parameters needs to be studied separately, by varying the fixed value and repeating the analysis.

The uncertainties found from variation of the RPF parameters will ultimately be treated as statistical uncertainties, as they derive from the uncertainty in the fit parameters.

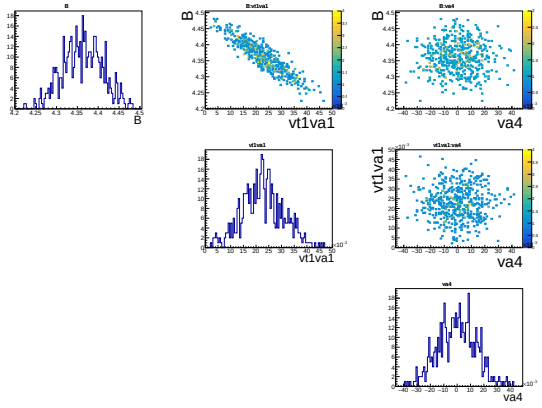

Figure 3.73: Covariance matrix sampling for the RPF with 11-14 GeV/c π^0s, 1.5-2.5 GeV/c associated particles. The diagonal plots show the 1-D distribution of each parameter, while the off-diagonal plots show the correlations between parameters.

Parameter $v_3^t v_3^a$ Uncertainty

As we fix the $v_3^t v_3^a$ value to a calculated value (as opposed to leaving it as a free parameter in the RPF), we must vary the value used according to its uncertainty. The varying of the $v_3^t v_3^a$ value is shown in Figure 3.74 and its effect is shown in Figure 3.75.

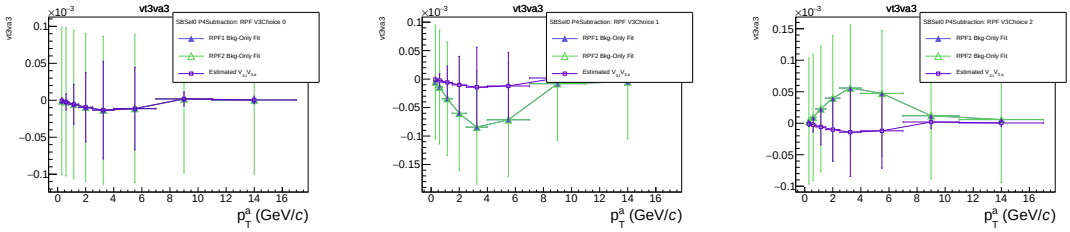

Figure 3.74: Variations of the $v_3^t v_3^a$ parameter in EGA-triggered 30-50% central events. The parameters used for each fit are labeled in green and blue, while the calculated $v_3^t v_3^a$ values are shown in purple.

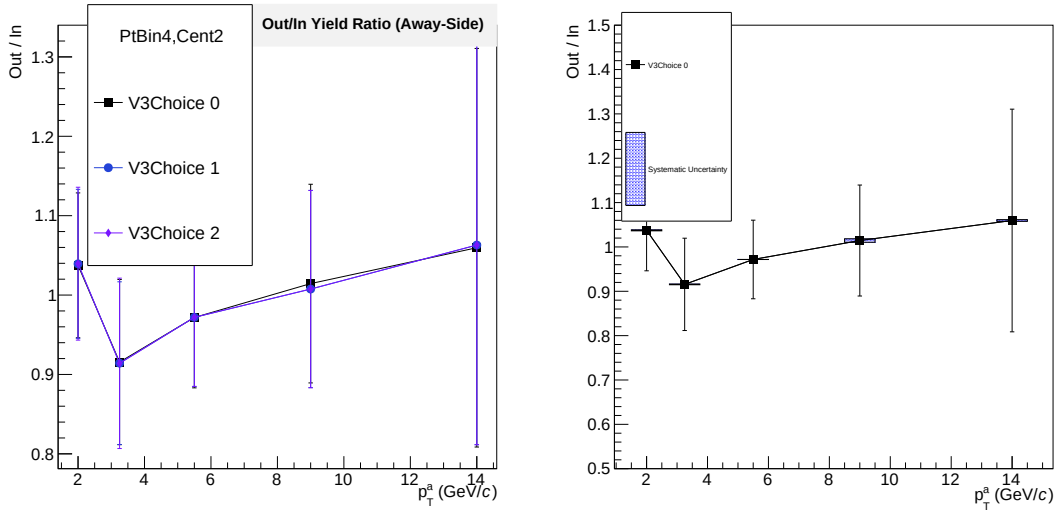

Figure 3.75: Effect of the $v_3^t v_3^a$ variation on the out/in awayside yield ratio.

Parameters $v_{2,t}$, $v_{4,t}$ Uncertainty

In the procedure of fixing the $v_{2,t}$ and $v_{4,t}$ parameters in the RPF to what are found with the low $p_{T,assoc}$, the choice of how many low $p_{T,assoc}$ are used is an arbitrary choice, and thus must be varied as a source of systematic uncertainty. The $v_{2,t}$ fixing with different numbers of points is shown in Figure 3.76. The effect of varying this is shown in Figure 3.77.

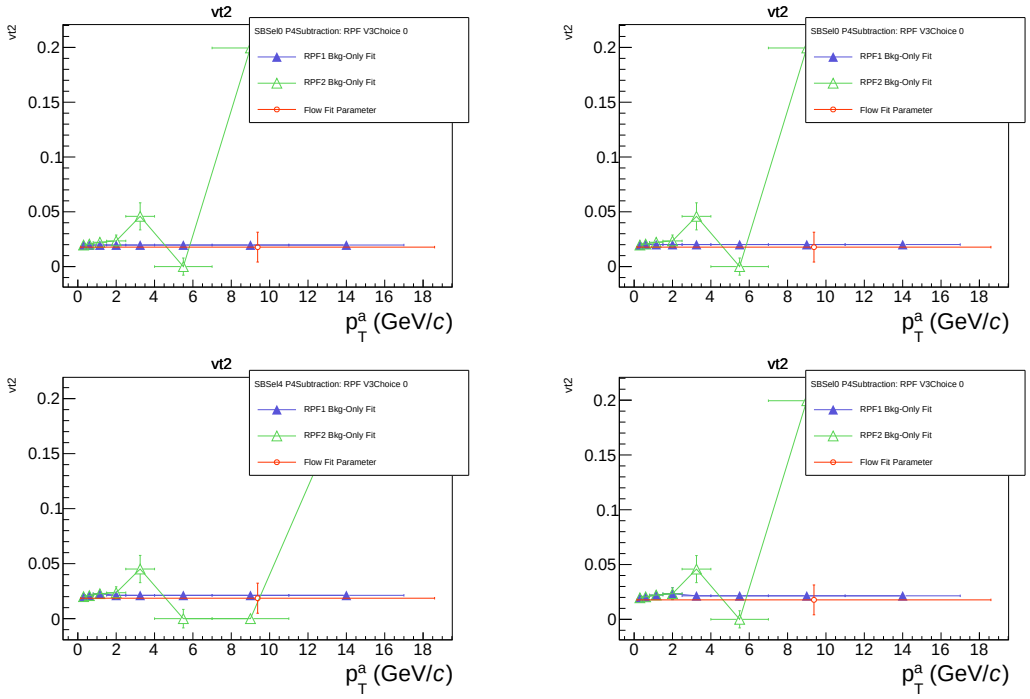

Figure 3.76: Variation of the choice of how many low assoc. p_{T} bins are used to fit the $v_{2,t}$ and $v_{4,t}$ parameters via the RPF. The fixing is not implemented in RPF Method 2, leaving the $v_{2,t}$ and $v_{4,t}$ parameters free.

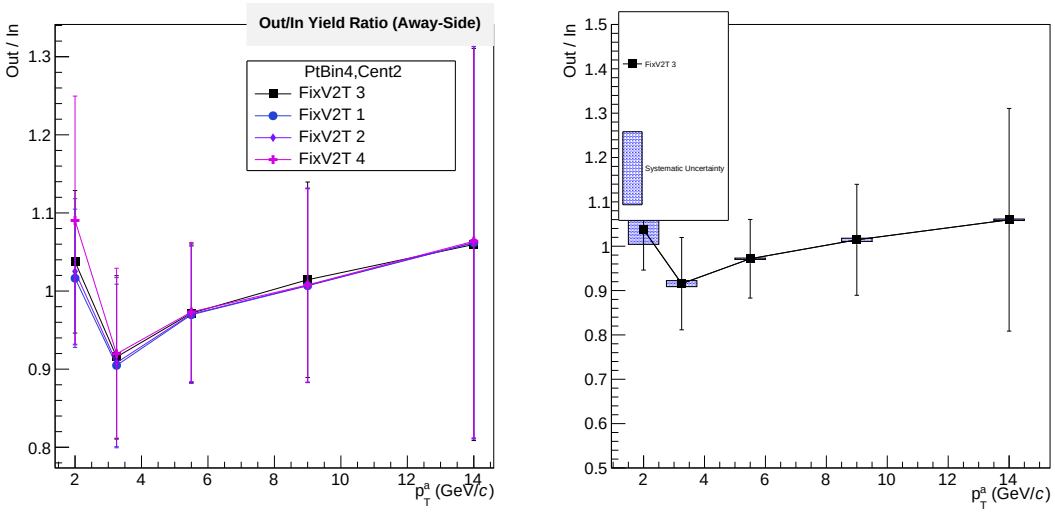

Figure 3.77: Effect of the FixV2 variation on the out/in awayside yield ratio.

3.10.7 $\Delta\phi$ Integration Window.

As the choice of the integration and fitting regions in $\Delta\varphi$ is somewhat arbitrary, it should also be varied for some measurements. The yields and the widths found through the trun-

cated RMS are defined in part by these cuts, so varying the $\Delta\varphi$ regions should not be used as a systematic for the raw values. However, this variation is important for the uncertainty on ratios between observables, such as the event plane ratios, and would also be appropriate for ratios to values for models.

This variation is implemented by increasing or decreasing the integration and fitting windows in $\Delta\varphi$ by one or two bins. The results for these variations are shown in Figures 3.78 (away-side out/in yield ratio) and 3.79 (away-side out/in σ ratio).

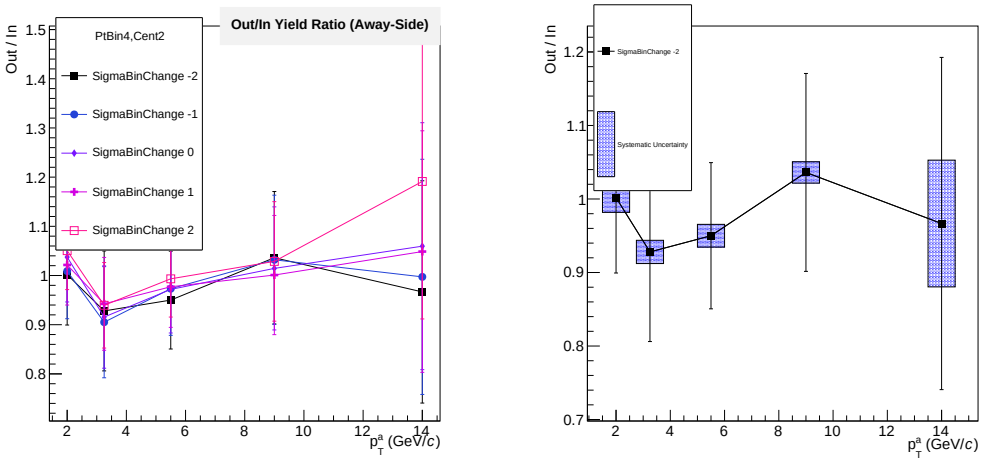

Figure 3.78: Out/In yield ratios with different integration windows for fitting.

3.10.8 Summary of Systematic Uncertainties

To summarize the results of these studies of systematic uncertainty in this analysis, plots were produced of the systematic uncertainty in each of the final observables and from each source, with the total systematic uncertainty also included.

Event Plane Ratios

The systematic uncertainty contributions for the event plane ratios are provided in Figures 3.80, 3.81, 3.82.

Raw Observables

The systematic uncertainties inclusive yields are given in Figures 3.83 (away-side) and Figures 3.84 (near-side). Unlike in the yield ratios, the tracking efficiency has a significant contribution from the uncertainty in the tracking efficiency. The contributions to the yields per event plane are given in appendix G.1.

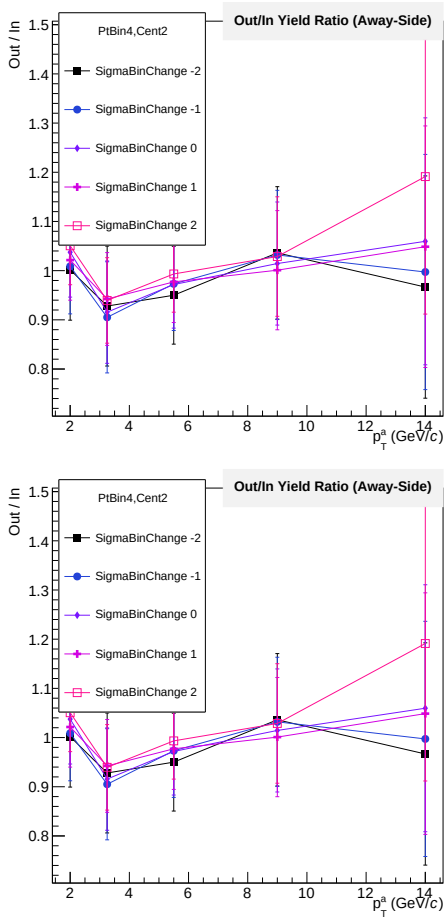

Figure 3.79: Out/In σ ratios with different integration windows for fitting.

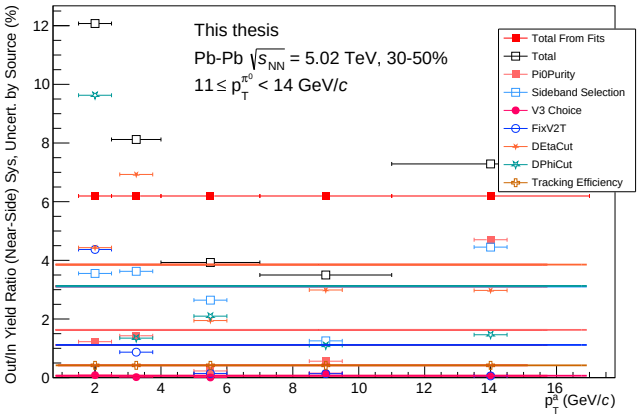

Figure 3.80: Systematic uncertainty in the nearside out/in yield ratio by contribution.

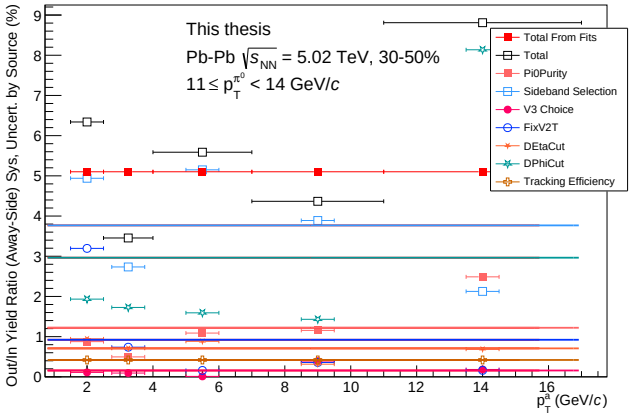

Figure 3.81: Systematic uncertainty in the awayside out/in yield ratio by contribution.

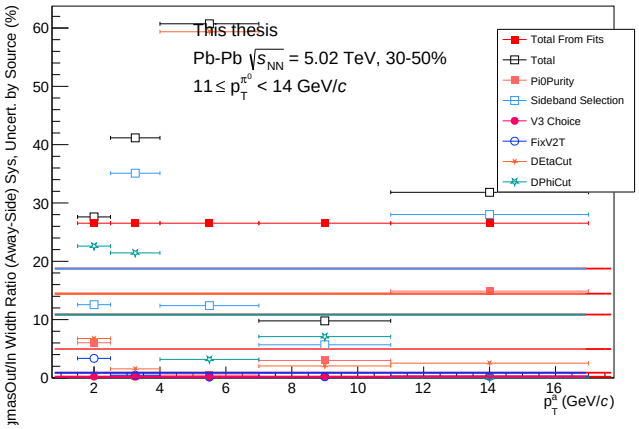

Figure 3.82: Systematic uncertainty in out/in width (sigma) ratio by contribution.

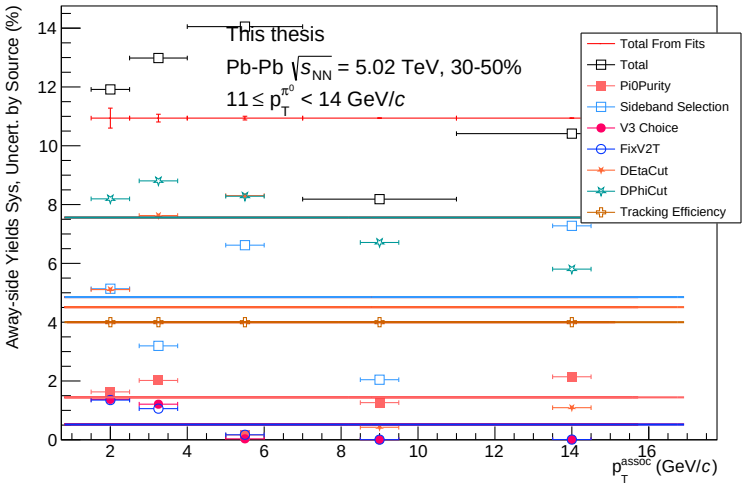

Figure 3.83: Systematic uncertainties by source for away-side yields (inclusive).

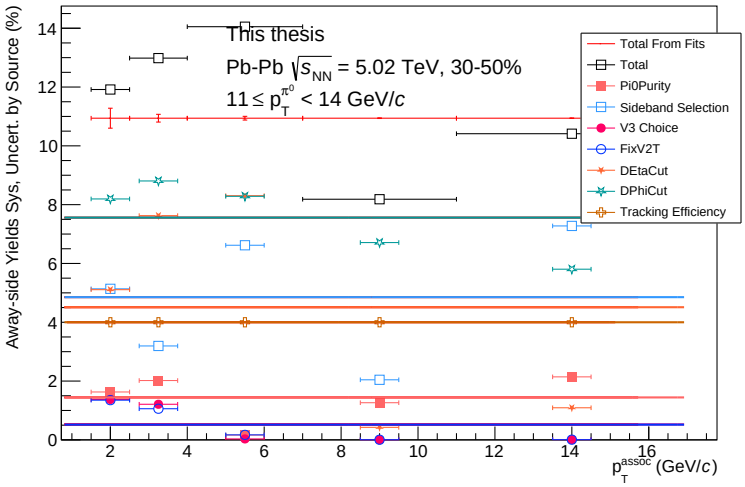

Figure 3.84: Systematic uncertainties by source for near-side yields (inclusive).

3.11 Results

3.11.1 Observable Definitions

The primary observables to calculate from the correlations are the magnitudes and widths of the jet peaks. Of particular interest are the characteristics of the peak of the away-side jet, which typically traverses more of the medium.

It is commonly assumed that the near-side jet traverses less of the medium due to the surface bias of surviving jets imposed by path-length dependent energy loss.

Yields

The first observable we look at is the yield of associated particles, defined as the integral of the flow subtracted correlations in a range around the nearside and awayside region, expressed in Equation3.38.

$$Y_X = \int_X f(\Delta\varphi) d\Delta\varphi \tag{3.38}$$

The default integration regions are $-\pi/3 < \Delta\varphi < \pi/3$ for the nearside and $2\pi/3 < \Delta\varphi < 4\pi/3$, but these regions can be expanded or contracted for studying the systematic uncertainty on event plane ratios using these yields.

Widths: RMS

One option for characterizing the widths of the peak is to calculate the truncated root-mean-square (RMS). Specifically, the RMS is calculated within a range, expressed mathematically in Equation 3.39. The range used here is $|\Delta\varphi - \mu| < \pi/3$, where $\mu = 0$ for the nearside peak and $\mu = \pi$ for the awayside peak.

$$RMS_X = \sqrt{\frac{\int_X f(\Delta\varphi)(\Delta\varphi)^2 d\Delta\varphi - (\int_X f(\Delta\varphi) d\Delta\varphi)^2}{\int_X f(\Delta\varphi) d\Delta\varphi}} \tag{3.39}$$

Widths: Sigma

The second option for characterizing the width of the peaks is to use a fit function. The approach here is to use a generalized gaussian: defined as such:

$$y(\Delta\varphi) = \frac{Y\beta}{2\alpha\Gamma(1/\beta)} \exp\left\{-(|x-\mu|/\alpha)^\beta\right\} \tag{3.40}$$

The function is reparametrized such that the standard deviation σ is a parameter:

$$y(\Delta\varphi) = Y\frac{\beta(\Gamma(3/\beta))^{1/2}}{\sigma\Gamma(1/\beta)^{3/2}}\exp\left\{-\left(\frac{|x-\mu|}{\sigma(\Gamma(1./\beta)/\Gamma(3./\beta))^{1/2})}\right)^{\beta}\right\} \tag{3.41}$$

Event Plane Ratios

One way to investigate path-length dependence of modification of jets is to compute the ratios of the yields and widths between different angles with respect to the event plane. On average, in-plane jets traverse less of the medium than out-of-plane jets. This is especially true for the away-side jet which is expected to traverse more of the medium if there is any surface bias for the hard scatters selected by our triggers.

A critical advantage of this observable is that some uncertainties, especially corresponding to parameters in the flow subtraction that are common to all event plane angles (B, $v_{t,1}v_{a,1}$, and $v_{t,3}v_{a,3}$) cancel out. For example, we may have large uncertainty from the $v_{t,1}v_{a,1}$ parameter affecting the yields, as long as the 1st order event plane is not correlated with the 2nd order event plane, the effect on the yields will be identical between event plane bins.

3.11.2 Gamma Triggered Results

Yields

The near-side yields with the final statistical uncertainties are provided for all angles in Figure 3.85 and individually in appendix G.1.

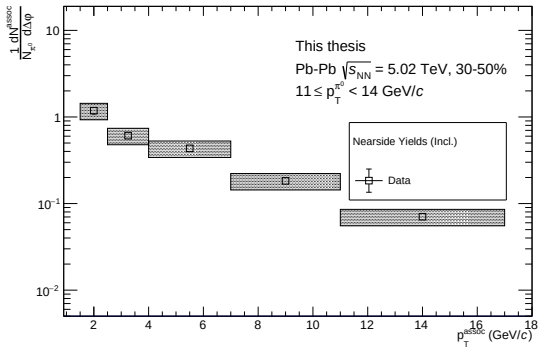

Figure 3.85: Near-side yields (all-angles) for π^0 range 11-14 GeV/c in 30-50% central EGA-trigger events.

Similarly, the away-side yields with the final statistical uncertainties are provided for all angles in Figure 3.86 and individually by event plane in Appendix G.1.

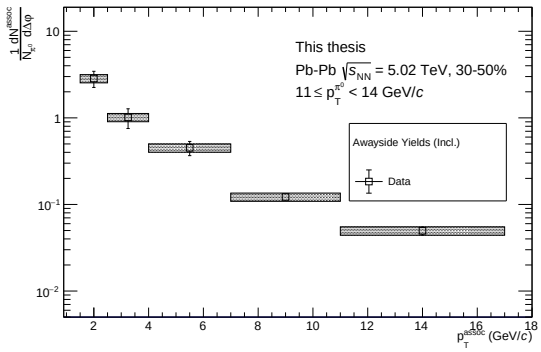

Figure 3.86: Away-side yields (all-angles) for π^0 range 11-14 GeV/c in 30-50% central EGA-trigger events.

Widths

The near-side widths determined with the standard deviation parameter from fitting with a peak function are shown in Figures 3.87 (all event angles) and individually by event plane in appendix G.1.

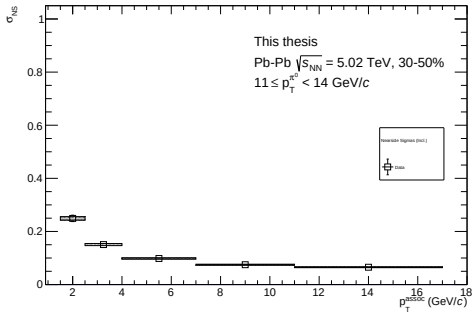

Figure 3.87: Near-side widths with σ parameter (all-angles) for π^0 range 11-14 GeV/c in 30-50% central EGA-trigger events.

Similarly, the away-side widths determined with the standard deviation parameter from fitting with a peak function are shown in Figure 3.88.

Event Plane Ratios

The final event plane ratios (out-of-plane / in-plane) are provided for the yields in Figure 3.89.

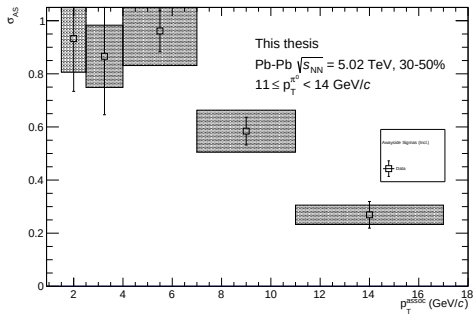

Figure 3.88: Away-side widths with σ parameter (all-angles) for π^0 range 11-14 GeV/c in 30-50% central EGA-trigger events..

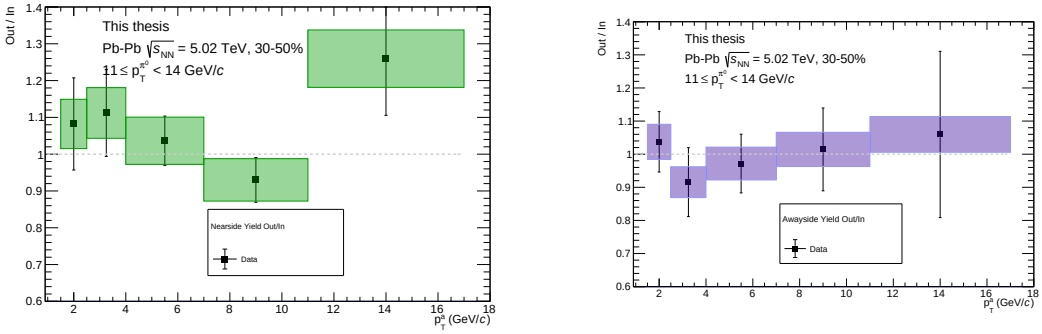

Figure 3.89: Near-side (left) and away-side (right) Yield Ratios 30-50%, EGA-triggered events.

3.11.3 Comparison to Theory

In Figures 3.90 and 3.91, the nearside and awayside yields are compared to results from the JEWEL model. On both sides, the experimental yields exceed the JEWEL results (see figures 3.90 and 3.91), although the discrepancy is lower for the near-side yields than the away-side yields.

Event Plane Ratios

The yield out/in ratio are compared to the predictions with the JEWEL model, with and without recoils are shown in Figure 3.92. As noted previously, many sources of uncertainty cancel when we take the ratio between event plane angles. The yield ratios are generally consistent with unity, indicating no observation of path-length dependence via the event plane. This is consistent with the prediction with JEWEL. More discussion of these results is included in chapter 5.

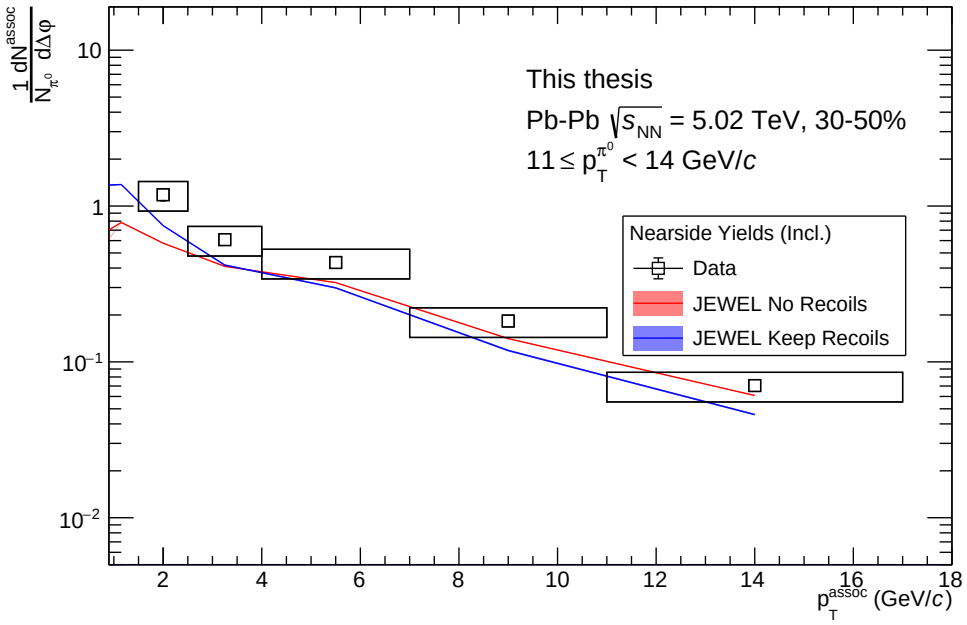

Figure 3.90: Nearside yields (all angles) with JEWEL model comparisons.

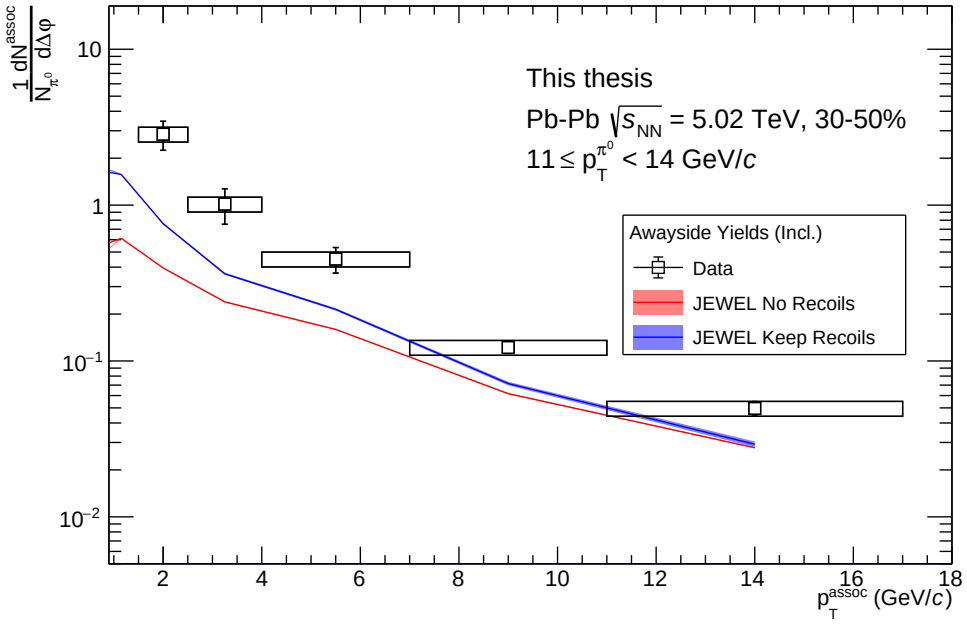

Figure 3.91: Awayside yields (all angles) with JEWEL model comparisons.

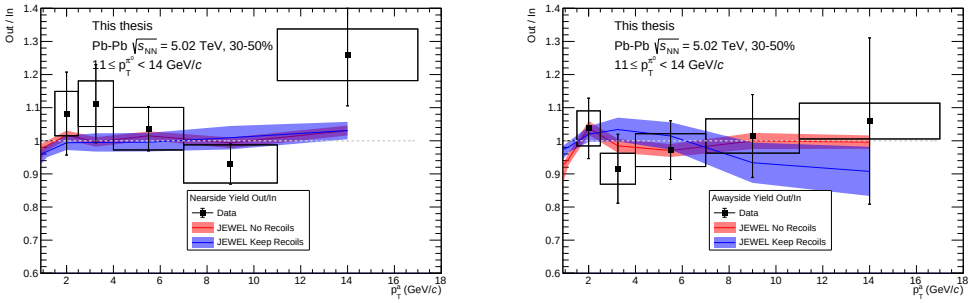

Figure 3.92: Near-side (left) and away-side (right) Yield Ratios 30-50%, EGA-triggered events.

Chapter 4

Jet Energy Loss Models

A portion of this thesis research was spent in producing theoretical predictions for a number of observables related to the path-length dependence of jet energy loss. These predictions are made with the popular JEWEL (Jet Evolution With Energy Loss) model, which simulates QCD jets traversing a simple QGP medium in a perturbative framework that implements both collisional and radiative energy loss [51],[52]. The primary impetus for this work was an analysis underway in ALICE on jet-hadron correlations in Pb–Pb collisions at $\sqrt{s_{\rm NN}} = 2.76$ TeV that sought theory comparisons. That analysis is now a published ALICE paper (see [14]). The framework for running and analyzing the model was then updated and reused for producing model predictions for jet-hadron correlations in Pb–Pb collisions at $\sqrt{s_{\rm NN}} = 5.02$ TeV for Raymond Ehlers Ph.D Thesis ([53]) and π^0-hadron correlations for this thesis.

This chapter starts with a description of the JEWEL model and the configuration used to run it for this work (Section 4.1).

4.1 JEWEL

JEWEL is a model of jet energy loss that is popular in the heavy ion community as it is consistent with a wide range of jet and single particle quenching measurements. The model includes collisional and radiative energy loss implemented with $2 \rightarrow 2$ scatters with partons sampled from an evolving medium with a realistic geometry starting from an optical glauber model.

A key goal of the model is to implement the Landau-Pomeranchuk-Migdal effect in which bremsstrahlung radiation (gluons in the case of QCD jets) is suppressed by interference between multiple emissions. This is implemented by combining multiple generated gluon emissions if the next scattering center is generated within the formation time $t = 2\omega/k_{\rm T}^2$ (ω is the gluon energy and $k_{\rm T}$ is the transverse momentum of the emission relative to the initial parton) of the previous emission with the probability of the combined

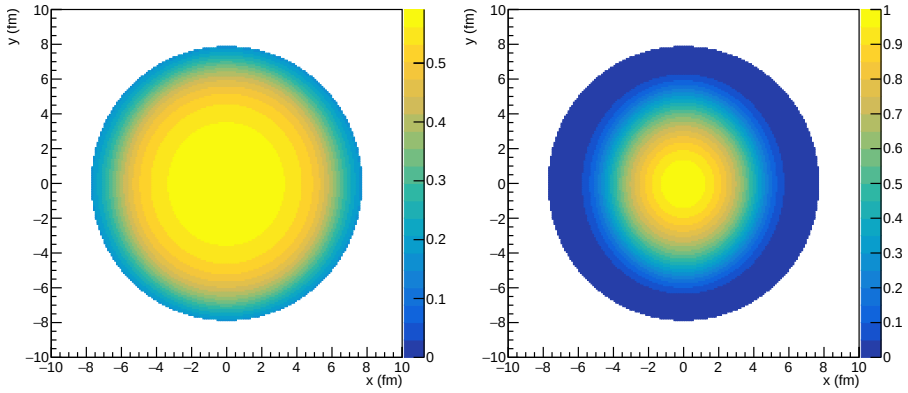

Figure 4.1: JEWEL temperature distribution at $t = 0.95$ fm/c in Pb–Pb event at $\sqrt{s_{\mathrm{NN}}} = 5.02$ TeV, in units of GeV (left) and hard-scatter vertex distribution (right), for an event in the 5% centrality percentile. The x and y axes are the positions within the x-y plane in units of fm.

emission scaled down by the number of emissions being combined.

JEWEL uses PYTHIA 6 to generate the initial partons emerging from a hard-scatter in a nucleon-nucleon interaction. These hard-scatters are generated using the CTEQL1 Parton Distribution Function (PDF) and the EPS09LO nuclear PDF parametrizations. The jets start at a vertex in the $x - y$ plane with a distribution determined by product of the overlapping nuclear thickness functions as visible in the right plot of Figure 4.1. JEWEL then simulated the parton shower and its interaction with the medium, before passing final state partons back to PYTHIA to hadronize with the Lund string fragmentation model.

The medium in JEWEL is simulated as an ideal gas of quarks and gluons undergoing longitudinal expansion after starting with an initial density. The beginning of the event starts with 0 energy density and temperature and linearly increases for a thermalization time τ_i, after which the temperature decreases by a factor $(\tau/\tau_i)^{-1/3}$. When the medium falls below the critical temperature of 165 MeV, the medium is treated as absent. This is visualized in Figure 4.2, produced with the medium code in JEWEL. More detailed descriptions of JEWEL are given in [52] and [51].

4.1.1 JEWEL Configuration

For these studies, the JEWEL simulations were run on high-performance computing clusters available at Yale, primarily the Grace cluster, in addition to the now defunct Omega cluster.

To configure JEWEL to simulate jets in heavy ion events, a few parameters must be provided. The simplest is the value for σ_{NN}, the inelastic nuclear cross section. This parameter is used for JEWEL's simple Glauber model. The default values to use for JEWEL

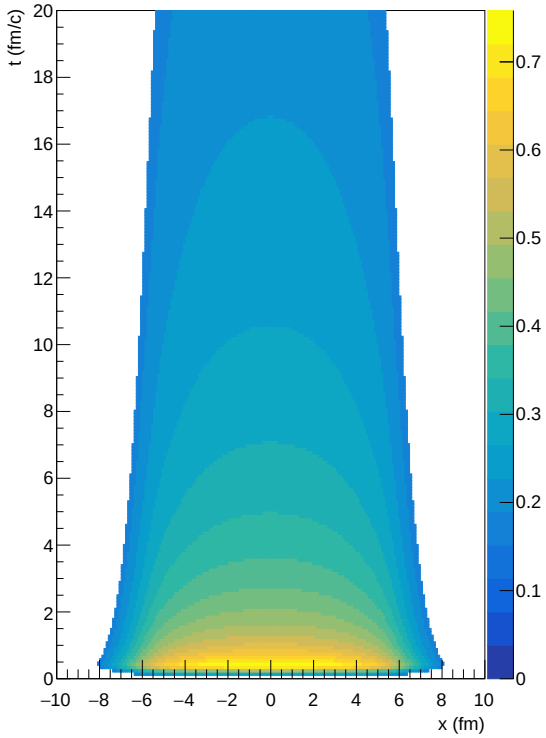

Figure 4.2: Temperature distribution in the $y = 0$ plane of an event in units of fm vs time in the longitudinally expanding medium model used by JEWEL, for a Pb–Pb event at $\sqrt{s_{\mathrm{NN}}} = 5.02$ TeV in the 5% centrality percentile. The z-axis gives the temperature in GeV.

for Au–Au at $\sqrt{s} = 200$ GeV and Pb–Pb at $\sqrt{s_{\mathrm{NN}}} = 2.76$ TeV are already established at 4.2 and 6.2 fm^2, respectively. Similarly, it is necessary to provide a parameter for the initial temperature of the medium. The established default values for use in JEWEL are 360 MeV for Au–Au collisions at $\sqrt{s} = 200$ GeV and 485 MeV and 590 MeV for Pb–Pb collisions at $\sqrt{s_{\mathrm{NN}}} = 2.76$ TeV and $\sqrt{s_{\mathrm{NN}}} = 5.02$ TeV, respectively [54].

For simulating jets in Pb–Pb collisions at $\sqrt{s_{\mathrm{NN}}} = 5.02$ TeV, it was necessary to provide a value for σ_{NN} at $\sqrt{s_{\mathrm{NN}}} = 5.02$ TeV. This was estimated using the Particle Data Group's ([1]) proton-proton cross section plot, as shown in Figure 4.3.

We set JEWEL to include some information in addition to the final state particles.

Extracting Hard-Scatter Information

To extract information on the hard scatter partons, a common block was added to our version of the JEWEL code to start the four-momenta and particle identification of the leading two partons from the hard-scatter. In the analysis, one of the first steps is to take

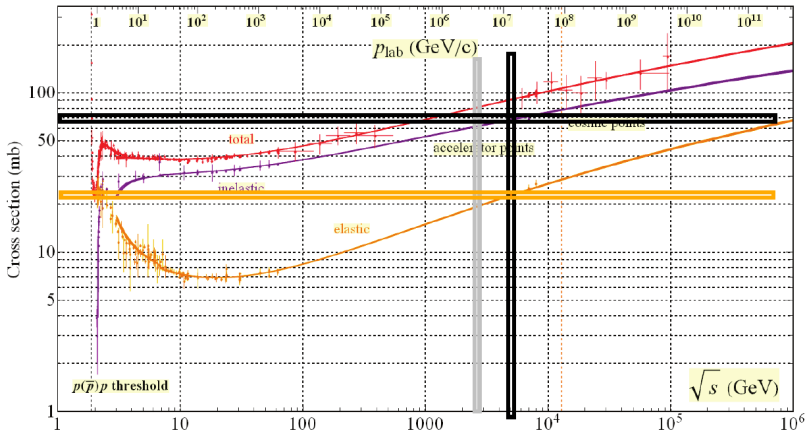

Figure 4.3: Estimation of inelastic nuclear cross section σ_{NN} at 5.02 TeV, using proton-proton cross section plot from [1].

the leading trigger (jet, π^0, or hard scatter γ) and compare it to the nearer of the two hard scatters. The correlations angular correlations between the leading trigger and nearest hard scatter are shown in Figures 4.4 (pp) and 4.5 (Pb–Pb). In the Pb–Pb plots is included the case where the hard scatter photon is used as the trigger, placing correlations trivially at the origin. From these figures it can be observed that the high p_{T} π^0 is more strongly correlated with the angle of the parton than the R = 0.2 anti-k_{T} jets. In Figure 4.6, the p_{T} correlation between the hard-scatter parton and the trigger particles are shown. As can be expected, jets and π^0s measured at a given p_{T} originate from hard-scatter partons with a wide range of initial p_{T}, whereas the direct photons have a one-to-one correlation trivially.

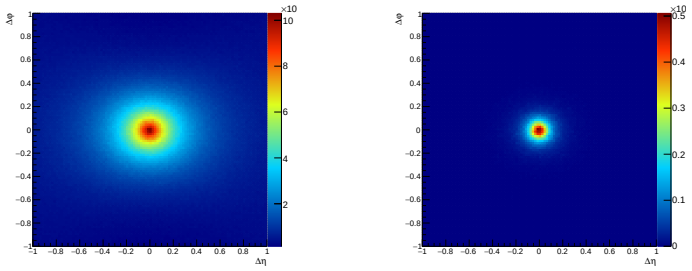

Figure 4.4: Hard scatter angular correlation in $(\Delta\eta, \Delta\phi)$ with different triggers in JEWEL's proton-proton mode. Left: R=0.2 full (tracks + clusters) jets , right: π^0s.

Extracting Vertex Information

To ensure that the information on the vertex of the hard scatter in x, y coordinates is saved to the output HepMC file, a common block is added to the modified version of JEWEL. The vertex x and y are added to the "V" (vertex) line of HepMC output for the vertex that

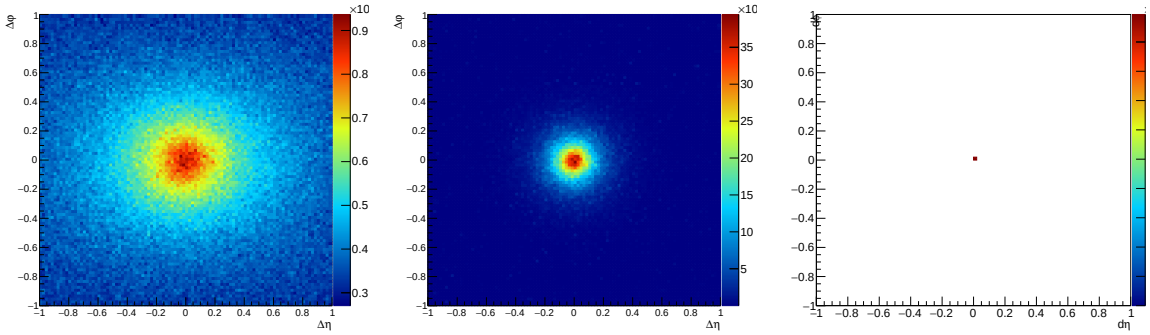

Figure 4.5: Hard scatter angular correlation in $(\Delta\eta, \Delta\phi)$ with different triggers in Pb–Pb, 30-50% Central events, JEWEL without recoils. Left: R=0.2 full (tracks + clusters) jets, middle: π^0s, right: direct photons.

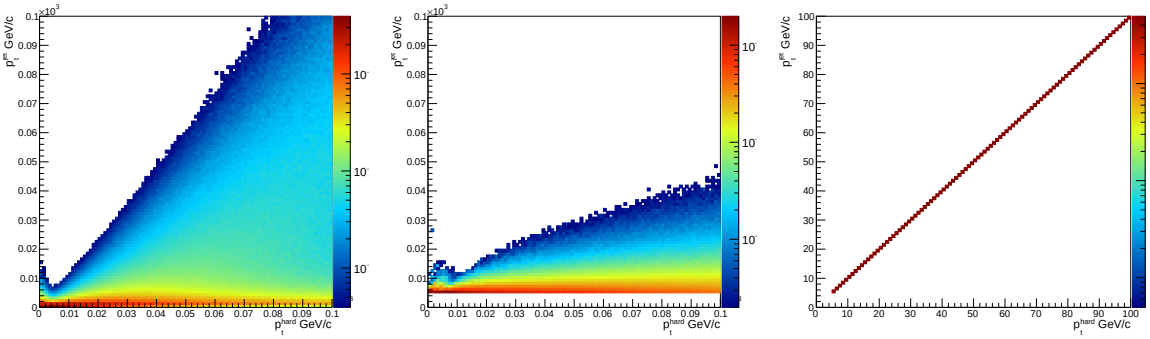

Figure 4.6: Hard scatter p_{T} correlation with different triggers in Pb–Pb, 30-50% Central events, JEWEL without recoils. The correlations are normalized per column (p_T^{parton}). Left: R=0.2 full (tracks + clusters) jets, middle: π^0s, right: direct photons.

has the hard scattering nucleons as incoming particles.

Temperature Distributions

To help interpret results from JEWEL simulations, an additional code was written to save the medium temperature used by JEWEL as a function of space and time.

4.2 JEWEL Parameters

4.2.1 Monte Carlo Configuration

The JEWEL model, version 2.2.0 was used. The configuration parameters chosen are given in Tables 4.1 (JEWEL parameters) and 4.2 (medium parameters)[1].

[1]These two sets of parameters correspond to the two configuration files that JEWEL uses.

Table 4.1: JEWEL Parameters.

Parameter	Note	Value(s)
SQRTS	$\sqrt{s_{\mathrm{NN}}}$	5023.0 (GeV)
PTMIN	Minimum $\hat{p}_{\mathrm{T}}$	5.0 (GeV/c)
PTMAX	Maximum $\hat{p}_{\mathrm{T}}$	250.0 (GeV/c)
WEIGHTED	Enable weightings towards events with higher $\hat{p}_{\mathrm{T}}$	T
WEXPO	$\hat{p}_{\mathrm{T}}$ over-weighting exponent	3.5
KEEPRECOILS	Save recoil partons in hadronization and final state	F,T
ETAMAX	η-range of the medium simulation	2.5
NSET	Nuclear PDF setting	1
MASS	Nucleon number	208
SHORTHEPMC	Shorten output by only including final state particles	F

Table 4.2: JEWEL Medium Parameters.

Parameter	Note	Value(s)
TAUI	Medium thermalization time	0.4 (fm/c)
TI	Initial temperature	0.590 (GeV)
A	Nucleon number	208
SIGMANN	Nucleon-nucleon cross section	6.9 fm^2
CENTRMIN	Minimum Cent. (%)	0,10,30,50
CENTRMAX	Maximum Cent. (%)	10,30,50,90

Production	Num. of Events	Num. of π^0s in 11-14 GeV/c
No-Recoils (30-50% Cent)	1.61×10^8	1826266
Keep-Recoils (30-50% Cent)	2.22×10^8	2430261

Table 4.3: JEWEL Production Statistics

4.2.2 Longitudinal Asymmetry Bug

One challenge for these analyses that had to be overcome to make use of JEWEL in the "Keep-Recoil" mode was a bug introducing a significant pseudorapidity bias within the system, which can be seen in the "before" plot of Figure 4.7. After some investigation, the error was determined to be caused by recoil particles remaining rotated in the coordinates in which the scatter with the medium parton was calculated, and not rotated back into the lab frame coordinates. The bug and proposed fix were sent to the JEWEL developers.

The bug is present in JEWEL versions 2.0.0,2.0.1,2.0.2, but is fixed in the more recent 2.1.0 and 2.2.0 versions.

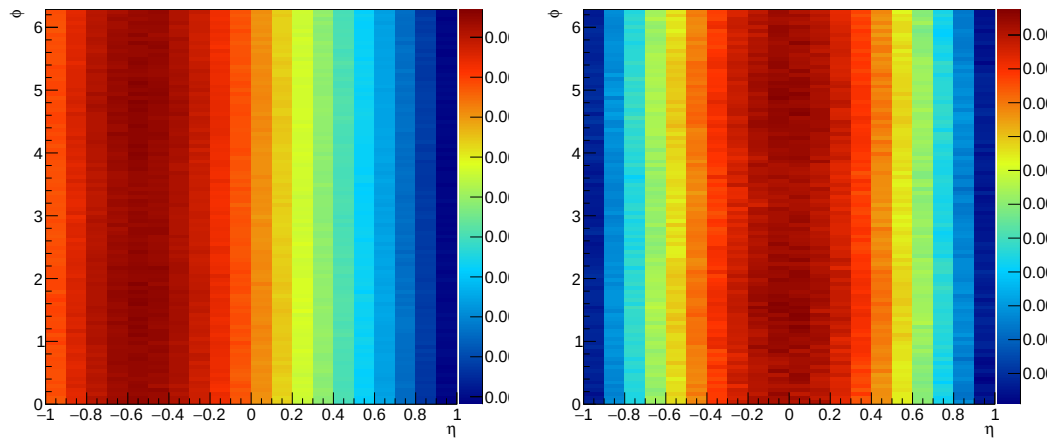

Figure 4.7: Distribution of final state particles in η and φ in JEWEL with recoils enabled. On the left is the distribution before the longitudinal bug fix, where a significant skew is present. On the right is the distribution after the fix has been applied, and no apparent bias or skew is observable.

4.2.3 Validation of Configuration

To verify that the JEWEL simulations used here are properly configured, we compute some benchmark measurements.

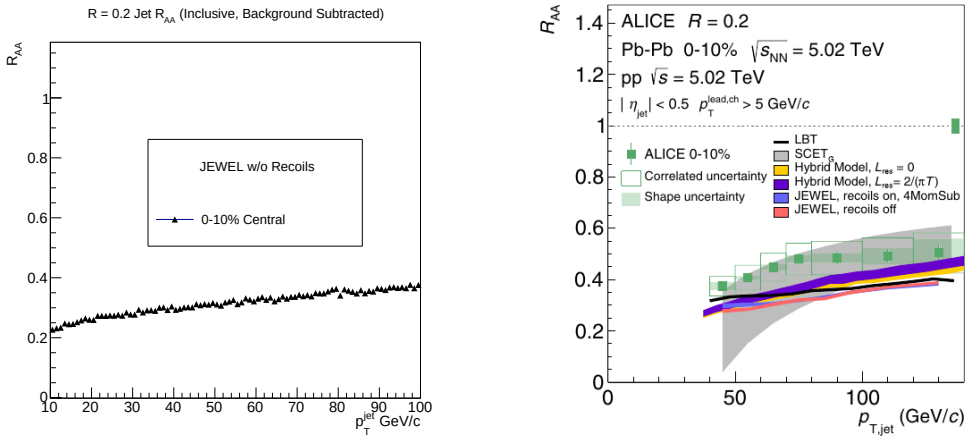

(a) R_{AA} for R = 0.2 anti-k_T jets.

(b) Published ALICE Jet R_{AA} in Pb–Pb collisions with model comparisons (including JEWEL)

Figure 4.8: Validation of JEWEL configuration by comparing jet R_{AA} to independently produced JEWEL predictions.

As is demonstrated in Figure 4.8, the jet R_{AA} for R = 0.2 jets as produced with this JEWEL configuration is consistent with independently produced for comparison to ALICE

R_{AA} data.

4.3 Monte Carlo Analysis with JEWEL

4.3.1 MC Event Generator Analysis

To analyze the results of JEWEL simulations for different types of correlations, a single set of analysis programs was written. This event generator analysis code can analyze correlations for simulated events for jet-hadron, π^0-hadron, and γ-hadron correlations. In addition, modes are available where the hard-scatter partons are used directly as the jet triggers and where the photon trigger is required to be a direct photon from a hard-scatter.

For π^0 and γ correlations, the particles are identified by their particle ID codes.

Jet Reconstruction in Event Generator Analysis

To reconstruct jets in this analysis of JEWEL output, an array of final (after decay) state particles is created. The following cuts are applied to these particles:

- $|\eta| < 3$
- $p_T > 0.150$ GeV/c
- No neutrons, neutrinos, or K^0_L are included

Additionally, a minimum energy constituent cut of 2 or 3 GeV/c may be applied above $0.150\mathrm{GeV}/c$ to mimic a constituent cut that is applied in analyses, such as the ALICE jet-hadron analysis in Pb–Pb collisions at $\sqrt{s_{\mathrm{NN}}} = 2.76$ TeV, which used a cut of 3 GeV/c.

Then the array of accepted particles is passed to the fastjet cluster sequencer to reconstruct jets. This is done with the active jet area calculation with ghost particles of area 0.01 and a production range in η of 1.5. This area calculation allows a jet area based p_{T} correction to be applied if needed, although that has not been used in these studies. The jet algorithm is the anti-k_T algorithm ([55]), with a jet resolution parameter of 0.2. Then, the analysis rejects jets outside of a range in $\eta \in (-0.5, 0.5)$, to match the range in which ALICE measures full R=0.2 jets.

Finally a "hard core cut" is optionally applied, requiring the jet to have at least one particle above a p_{T} threshold of 5 or 6 GeV/c. This requirement is often applied in data to reduce the contribution of combinatorial background jets. Since this cut may bias measured jets based on their fragmentation, it is important to match it in these simulations.

Correlations and Projections

The correlations are recorded between the trigger particle and final state charged particles. No η cut is applied to these associated particles, but a cut on $\Delta\eta_{\text{Trigger}-h}$ will be applied. Not applying the η cut avoids the necessity to apply an acceptance correction, as well as increasing the available statistics in far $\Delta\eta$ region.

These correlations are saved in the same trigger and associated particle p_{T} bins as the data analysis. Similarly to the data, the $\Delta\eta - \Delta\varphi$ correlations are projected onto $\Delta\varphi$ in three $\Delta\eta$ ranges:

- Full $\Delta\eta$: $|\Delta\eta| < 1.8$
- Near $\Delta\eta$: $|\Delta\eta| < 0.8$
- Far $\Delta\eta$: $0.8 < |\Delta\eta| < 1.8$

Pedestal Correction for JEWEL with Recoils

In JEWEL's "keep recoils" mode, the recoiling medium partons hit by the jet partons are included in the hadronization and the final event. This has the benefit of modelling the "medium response" in a physically motivated way, as well as ensuring momentum conservation in the event. The downside is that the recoil partons have thermal energy from the simple medium simulation, which results in a partial background in the event. As only partons that interacted with the jet are saved and included in the event, this background has a significant correlation with the jets and is not a realistic underlying event. Importantly this thermal background is correlated with the jets in η (possibly due to the longitudinal boost of medium particles by JEWEL), resulting in a "tent" structure not unlike an acceptance effect, which can be seen in Figure 4.9.

As this analysis relies on the background to π^0-hadron correlations to be constant with respect to $\Delta\eta$, this is a significant problem for using the same analysis code on these MC simulations.

The solution we used is to assume that this background simply adds a flat (in $\Delta\varphi$) pedestal that varies in different $\Delta\eta$ ranges. An additional assumption is that the real away-side signal does not vary significantly with $\Delta\eta$. The solution is then to integrate the away-side region ($\pi/2 < \Delta\eta < 3\pi/2$) in the near $\Delta\eta$ and far $\Delta\eta$ regions. Then the difference is divided by the $\Delta\varphi$ range and subtracted from the near $\Delta\eta$ region as a flat pedestal, such that the near $\Delta\eta$ and far $\Delta\eta$ regions have the same pedestal. The same is also applied to the full $\Delta\eta$ region such that it also matches the pedestal in the far $\Delta\eta$ region. $\Delta\varphi$ correlations in the three different $\Delta\eta$ regions (and event planes) are shown before and after the pedestal correction in Figures 4.10 and 4.11, respectively.

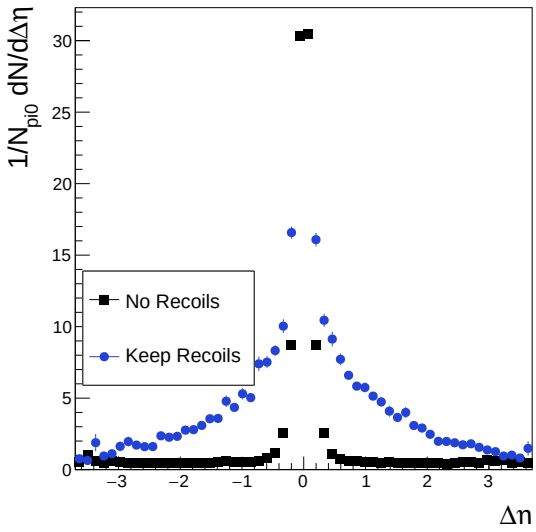

Figure 4.9: $\Delta\eta$ correlations in π^0-hadron correlations with and without recoils, for π^0s in the $11 - 14$ GeV/c range, associated hadrons in the $2.5 - 4$ GeV/c range in 30-50% central events.

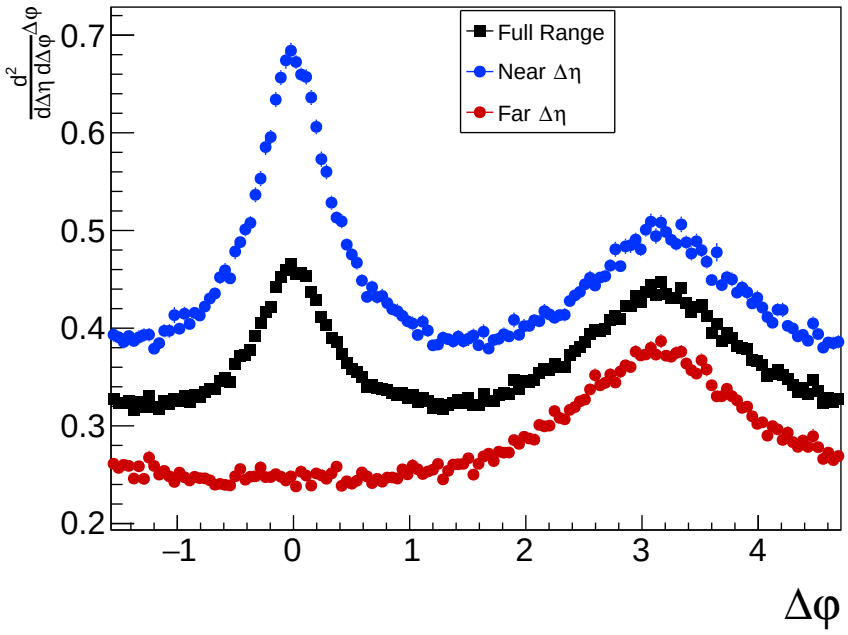

Figure 4.10: $\Delta\varphi$ correlations in different $\Delta\eta$ regions with JEWEL (with recoils) 30-50% cent. events. No pedestal correction is applied here.

Correlation Fitting

In analyzing $\Delta\phi$ correlations, one early method has been the Zero-Yield-At-Maximum (ZYAM) method, in which one finds the lowest bin in the correlations (typically between

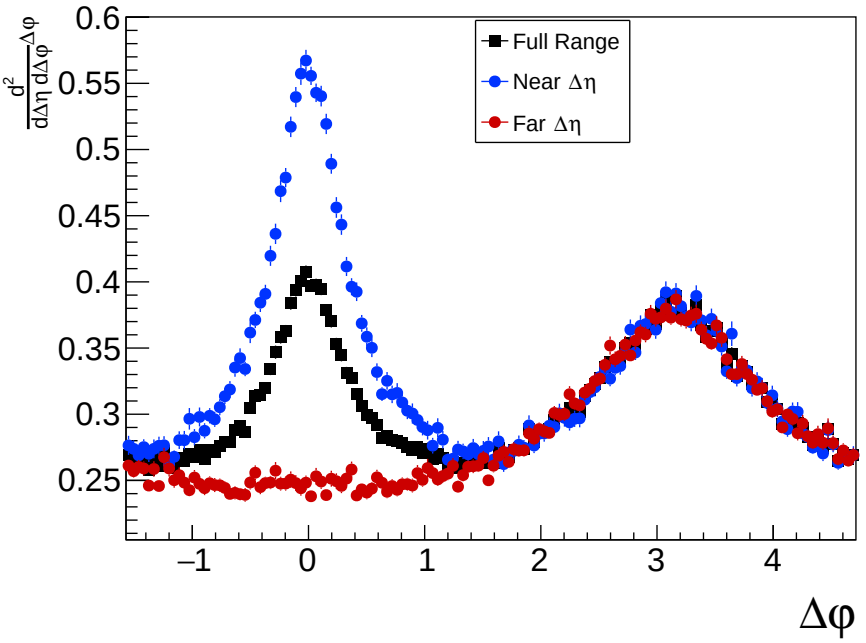

Figure 4.11: $\Delta\varphi$ correlations in different $\Delta\eta$ regions with JEWEL (with recoils) 30-50% cent. events. The pedestal correction is applied here.

$\pi/3$ and $\pi/2$ away from the nearside peak) and assume that there is zero yield from the signal peaks there. Then the correlations there consist only of background, which is assumed to be a flat pedestal in $\Delta\phi$.

It has been repeatedly demonstrated that this method performs poorly at low p_{T}^{assoc} due to overestimating the background when the jet peaks are relatively wide [56],[26]. This fact, along with an interest in characterizing the shape of the peaks, lead to an investigation of a range of fit functions for the nearside and awayside peaks. If a fit function reliably characterizes the peak, this allows an alternate method of determining the background, by fitting the azimuthal correlations to the peak functions plus a free parameter constant background.

The full list of peak functions tried is given in Table 4.4. In the implementation, the nearside and awayside peak functions are repeated at $\Delta\phi = 2\pi$ and $\Delta\phi = -\pi$, respectively, to properly account for how the peaks wrap around in azimuth.

The peak functions are each used with two different parametrizations: one with a width parameter σ corresponding to the standard variance, and one a Full-Width-at-Half-Maximum (FWHM) variable σ. This allows both the width and FWHM to be extracted from the fits with easily accessible uncertainties.

Table 4.4: Dijet fit functions tried for event generator analysis.

Label	Nearside	Awayside
1G1G	1 Gaus.	1Gaus.
1M1M	1 Mod. Gaus.	1 Mod. Gaus.
2G1M	2 Gaus.	1 Mod. Gaus.
2G1GG	2 Gaus.	1 Gen. Gaus.
1GG1GG	1 Gen. Gaus.	1 Gen Gaus
2G2G	2 Gaus.	2 Gaus.

Table 4.5: Details of individual fit functions for the σ width parametrization. The modified gaussian formula is described in [26]. The exact implementations of the fits are given in Appendix C.

Fit	Formula
Gaussian	$\frac{Y}{\sqrt{2\pi\sigma^2}} \exp\left\{-(x-\mu)^2/(2\sigma^2)\right\}$
Generalized Gaussian	$\frac{Y\beta}{2\alpha\Gamma(1/\beta)} \exp\left\{-(\lvert x-\mu\rvert/\alpha)^\beta\right\}$
Modified Gaussian	$Y/\left\{1+\frac{1}{2n}\left(\frac{x-\mu}{\sigma}\right)\right\}^n$

4.3.2 Flow Toy Model

To test and explore the applicability of the Reaction Plane Fit and other methods for estimating the flow background correlations a "toy model" of the flowing soft particle background was implemented in the event generator analysis. The purpose of the toy model is not to perfectly emulate the background, but to have background with scale and flow within an order of magnitude of the real background for testing the Reaction Plane Fit.

The toy particles are sampled from a distribution that is flat in η, and an exponential p_{T} distribution starting at $p_{\mathrm{T}}^{\mathrm{min}}$ = 0.150 GeV/c. Then the azimuthal angle is sampled from a fourier series with terms v_2, v_3, and v_4, which vary as a function of p_T. The angle for the v_2 distribution is set to be the reaction plane, which is 0 by default in JEWEL. The v_3 and v_4 terms have angles which are distributed evenly in azimuth, defined once per event.

The v_n flow parameters in the toy parameters are taken from a parametrization to v_n values measured in the π^0-hadron correlation analysis. Those values were found by fitting the angles of charged tracks in Minimum Bias events with respect to the 2nd and 3rd order event planes. Specifically, v_2 and v_4 were found by fitting the charged tracks vs Ψ_2 to a form $B(1 + 2v_2\cos(2(\varphi - \Psi_2) + 2v_4\cos(4(\varphi - \Psi_2))$ and charged tracks vs Ψ_3 to a form $B(1 + 2v_3\cos(3(\varphi - \Psi_3))$. Here, the v_4 is not a "true" v_4, which is defined in terms of Ψ_4, but v_4 with respect to the 2nd event plane, which is diminished by the decorrelation of the 4th order event plane with the 2nd. This technicality is not expected to impact the usefulness of the toy model.

The v_n flow parameters are fit as a function of p_{T} to a Landau function, which is not physically motivated but serves well.

To give the toy model a realistic multiplicity and distribution for toy particles, fits to the raw charged particles distributions in the Minimum Bias analysis were used. Specifically, the average number of charged particles per unit pseudorapidity ($\langle \frac{dN_{ch}}{d\eta} \rangle$) and a fit to the exponential component of the track p_{T} distribution were extracted from the per-event track p_{T} spectra, as shown in Figure 4.12.

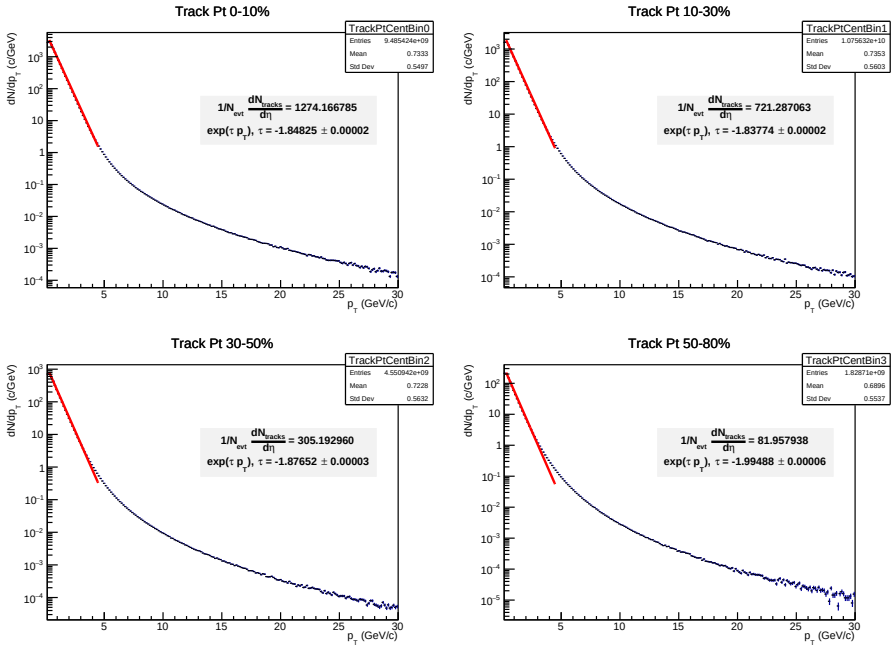

Figure 4.12: Measured Track transverse momentum spectra for Minimum Bias Events.

Table 4.6: Toy Model Particle Distribution. Landau(x, μ, c) is the unnormalized Landau distribution available in ROOT's TMath Library.

Variable	Distribution
p_{T}	Exp(-τp_{T})
η	$\frac{dN_{ch}}{d\eta}$ in [-5,5]
φ	$1 + 2v_2\cos(\varphi) + 2v_3\cos(3(\varphi - \Psi_3)) + 2v_4\cos(4(\varphi - \Psi_4))$
v_2	$P_{0,v_2} * \mathrm{Landau}(p_{\mathrm{T}}, P_{1,v_2}, P_{2,v_2})$
v_3	$P_{0,v_3} * \mathrm{Landau}(p_{\mathrm{T}}, P_{1,v_3}, P_{2,v_3})$
v_4	$P_{0,v_4} * \mathrm{Landau}(p_{\mathrm{T}}, P_{1,v_4}, P_{2,v_4})$

Table 4.7: Toy Model Parameters

	0-10%	10-30%	30-50%	50-80%
$\frac{dN_{ch}}{d\eta}$	1274	721	305	82
τ	1.84825	1.83774	1.87652	1.99488

Par.	0-10%	10-30%	30-50%	50-80%
$p_{2,0}$	$5.41e-01 \pm 3.7e-02$	$1.06 \pm 7.1e-02$	$1.357 \pm 7.8e-02$	$1.485 \pm 9.8e-02$
$p_{2,1}$	$4.46 \pm 3.9e-01$	$1.055 \pm 7.1e-02$	$4.28 \pm 3.4e-01$	$4.53 \pm 2.6e-01$
$p_{2,2}$	$2.04 \pm 2.2e-01$	$4.43 \pm 3.7e-01$	$2.00 \pm 1.9e-01$	$2.19 \pm 1.7e-01$
$p_{3,0}$	$4.72e-01 \pm 1.3e-02$	$2.027 \pm 2.1e-01$	$6.983e-01 \pm 1.9e-02$	$2.110 \pm 5.8e-02$
$p_{3,1}$	$3.71 \pm 4.5e-01$	$4.980e-01 \pm 1.4e-02$	$3.71 \pm 4.5e-01$	$3.71 \pm 4.5e-01$
$p_{3,2}$	$1.45 \pm 2.2e-01$	$1.45 \pm 2e-01$	$1.45 \pm 2.2e-01$	$1.459 \pm 2.2e-01$
$p_{4,0}$	$9.2e-02 \pm 1.2e-02$	$2.08e-01 \pm 2.3e-02$	$3.393e-01 \pm 3.3e-02$	$3.974e-01 \pm 4.4e-02$
$p_{4,1}$	$4.50 \pm 6.4e-01$	$4.361 \pm 4.5e-01$	$4.26 \pm 3.9e-01$	$4.34 \pm 4.2e-01$
$p_{4,2}$	$1.66 \pm 2.9e-01$	$1.63 \pm 2.1e-01$	$1.636 \pm 1.8e-01$	$1.70 \pm 2.0e-01$

Table 4.8: Table of parameters for the v_n used in the toy model.

4.4 Surface Bias in JEWEL

A commonly discussed idea in the field of relativistic heavy ion collisions is that of the surface bias of measured jets. The logic is high p_{T} jets starting at the edge of the nuclear overlap region will traverse less of the medium, losing less energy. Then the population of measured jets in a given p_{T} range will be biased towards jets produced near the surface. The same logic holds for any variable, such as the width of the jet, that is thought to be correlated with the amount of energy loss. The geometric bias is especially interesting to the type of analysis studied in this thesis, as it is expected to magnify path-length dependent effects, under the logic that the recoiling jet opposite the trigger jet is likely to traverse the bulk of the medium, as presented in Figure 4.13a, enhancing the observable suppression on the awayside.

The surface bias effect also raises interest in measurements of jets tagged with direct photons or leptonically decaying Z-bosons. As photons and leptons leading interaction with the QGP is electromagnetic, their expected energy loss is negligible. Thus, the starting location of measured direct photons and Z-bosons will be unbiased (described visually in Figure 4.13b), making measurements of their recoiling jets an interesting measurement to compare to dijet measurements. This can equivalently be described by noting that the direct bosons give an accurate determination of the initial energy of the recoil parton before it traverses the medium.

(a) Dijet events (b) Gamma-Jet events

Figure 4.13: Cartoon diagrams of geometric bias in dijet and gamma-jet events.

One line of inquiry that arose in the modelling studies was what we could learn from

the JEWEL model about the surface bias of jets used in analyses such as the ALICE Jet-hadron correlations analysis.

A simple means to investigate the surface bias effect is to study the distribution of hard -scatter vertices under different requirements, such as the presence of a jet in given p_{T} range. In central events, where the medium and distribution of vertices is nearly circular in the $x-y$ plane, it suffices to examine the radius $R = \sqrt{x^2+y^2}$ from the center of the collision system, which is shown in Figure 4.14 for Pb–Pb events in JEWEL w/o recoils at $\sqrt{s_{\mathrm{NN}}} = 5.02$ TeV. Compared to distribution of all vertices, those that produce a jet in any of the given p_{T} ranges are biased towards larger radii, confirming the presence of the surface bias effect in the JEWEL model.

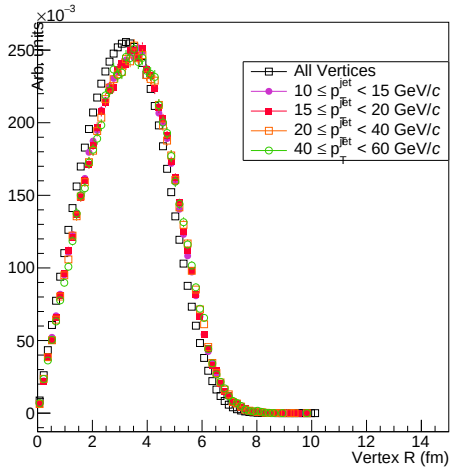

Figure 4.14: Normalized vertex radius distribution under different requirements in Pb–Pb JEWEL w/o recoils in the 0-10% centrality range.

We can also use the vertex R by examining its correlation with energy loss, as quantified by the difference between the parton and leading reconstructed jet p_{T}, as done in Figure 4.15, where a correlation between lower momentum loss and radial distance is observed.

It is also useful to characterize the geometric bias in coordinates relative to the direction of jet. We do this by defining a rotated coordinate system where the $-x$ axis is in the direction of the trigger particle or jet, while the origin remains at the center of the collision. (see Figure 4.16. Then, if energy loss effects bias towards events where a jet took a shorter path out of the medium. This also allows for the examination of transverse bias in the y_{jet} coordinate, as may be expected for highly symmetric dijets.

To quantify surface bias, we can use the ratio of vertices on the same side as the trigger jet to those opposite:

$$S = \frac{N_{x_{\mathrm{jet}}<0}}{N_{x_{\mathrm{jet}}>0}} \tag{4.1}$$

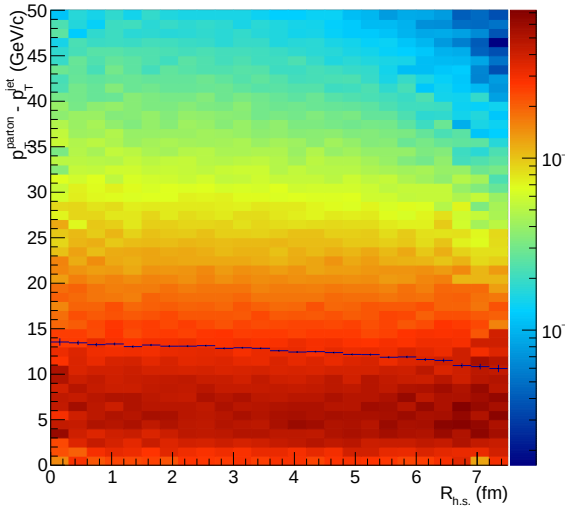

Figure 4.15: Difference in p_{T} between leading jet and matched hard scatter parton, correlated with the radius R of the hard scatter in Pb–Pb 0-10% central events in JEWEL w/o recoils. A profile is overlaid with the uncertainty in the mean as the error bars.

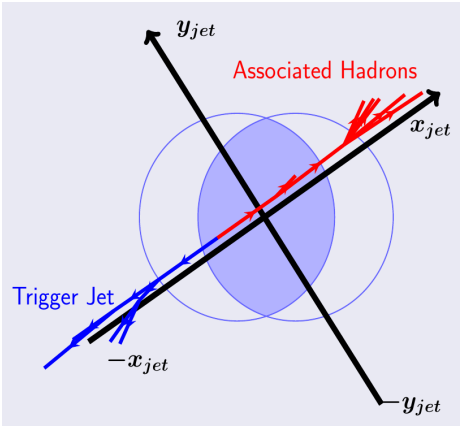

Figure 4.16: Diagram of rotated jet vertex coordinates.

When S is near 1, the surface bias is negligible, while large S indicates significant surface bias. Two examples are given in Figures 4.17 (Pb–Pb at $\sqrt{s_{\mathrm{NN}}} = 5.02$ TeV, 0-10% central) and 4.18 (Au–Au at $\sqrt{s_{\mathrm{NN}}} = 200$ GeV, 0-10%). A moderate surface bias appears in JEWEL at LHC energies, while the surface bias is significant for the energies at RHIC.

This difference can be understood as an effect of the different jet p_{T} spectra at different collision energies. To an approximation, at high p_{T} the jet spectra fit a power law $d\sigma/dp_{\mathrm{T}} \propto p_{\mathrm{T}}^{-n}$ with the exponent n depending on $\sqrt{s}$. At low $\sqrt{s}$, such as 200 GeV as in collisions at RHIC, n is higher, indicating a more steeply falling spectrum. This is relevant to the surface bias, as the harder spectrum at the LHC energies means that for a each jet

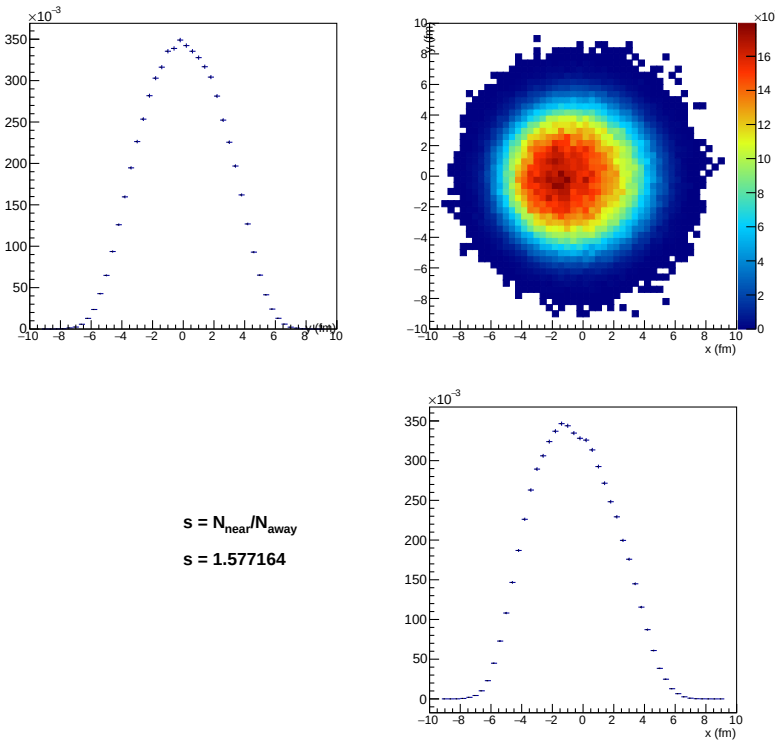

Figure 4.17: Hard-scatter vertex distribution for PbPb ($\sqrt{s_{\mathrm{NN}}} = 5.02$ TeV) 0-10% JEWEL w/o recoils in the rotated jet vertex coordinates with projections onto the x_{jet} and y_{jet} axes. The surface bias parameter S is calculated from the x_{jet} projection.

that loses no energy from starting at the surface, there is a larger population of jets that can start inside the medium, lose a significant amount of energy, and exit with the same p_{T} as the surface jet. In contrast, at RHIC energies, any high p_{T} jet is more likely be an unquenched jet. This is explained visually in Figure 4.19.

From this it can be concluded that the surface bias effect is indeed significant at the center-of-mass energies explored at RHIC, it is significantly weaker at the LHC. Of course, this conclusion relies on the JEWEL model, but the same argument from the spectra should hold for any similar model.

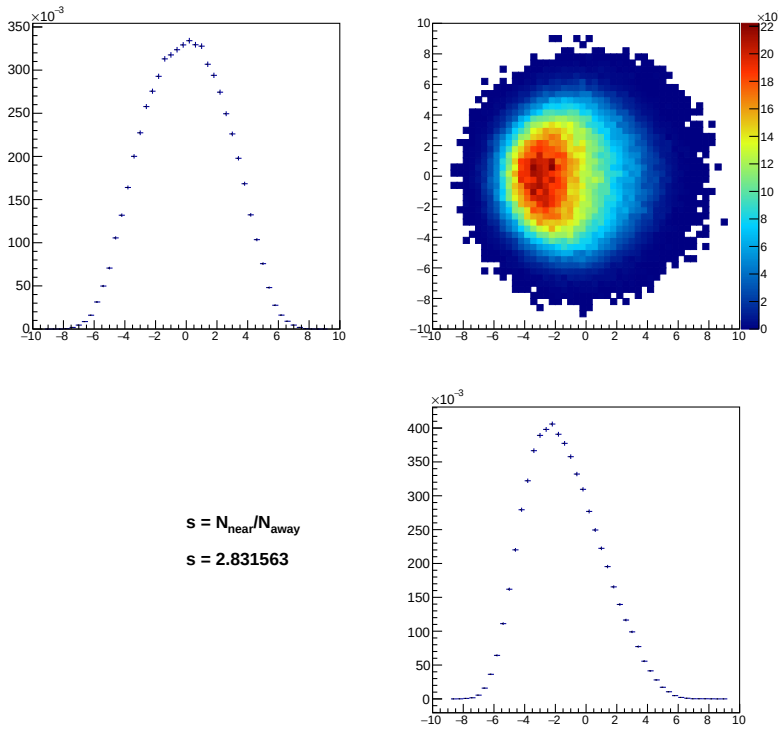

Figure 4.18: Hard-scatter vertex distribution for Au–Au ($\sqrt{s_{\mathrm{NN}}} = 200$ GeV) 0-10% JEWEL w/o recoils in the rotated jet vertex coordinates with projections onto the x_{jet} and y_{jet} axes. The surface bias parameter S is calculated from the x_{jet} projection.

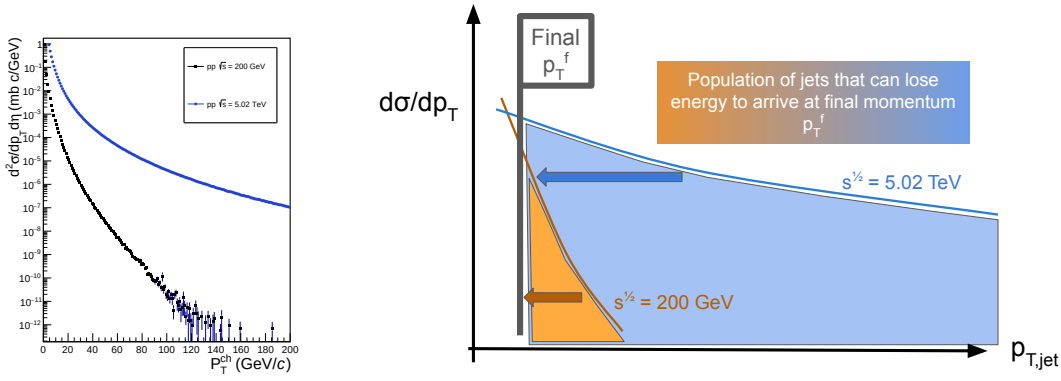

Figure 4.19: Comparison of the R = 0.2 jet cross sections in pp collisions at RHIC and LHC energies calculated with PYTHIA 6 (left) and a diagram explaining how the hardness of the jet p_{T} spectrum affects the number of jets that can start inside the medium and lose energy to arrive at the same $p_{\mathrm{T}}^{\mathrm{final}}$ of a jet starting at the surface.

4.5 JEWEL Predictions

4.5.1 Jet-Hadron Correlations at 2.76 TeV

As previously mentioned, the modelling of jet-hadron correlations covered in this section was done to provide a theory comparison for the ALICE measurement of jet hadron correlations with respect to the event plane. The jet details and binning of this analysis are listed in Table 4.9.

Table 4.9: Settings and bins for the JEWEL jet-hadron correlations analysis.

Jet type	anti-k_{T}, R = 0.2, $p_{\mathrm{T}}^{const.} > 3$ GeV/c
η_{jet}	[-0.5,0.5]
p_{T}^{jet} bins	$[10, 15, 20, 40, 60]$
p_{T}^{assoc} bins	$[0, 0.25, 0.5, 1, 1.5, 2, 3, 4, 5, 6, 10, 15]$
$\lvert\phi^{jet} - \Psi_{EP,2}\rvert$	$[0, \pi/6, \pi/3, \pi/2]$

Detector Jet Resolution Folding

One issue present for all jet analyses is that the background from the underlying event can alter the jet that is reconstructed vs the true jet.

This is particularly concerning when examining event plane dependent observables, as the preferential flow of background particles with respect to the event plane can lead to different jet modifications in different event plane angles. For example, jets angled along the 2nd order event plane will have more background particles than the out-of-plane jets, and thus they may have a larger shift in p_T.

In this case, instead of unfolding the final experimental results, we "folded" the theoretical predictions by the experimental jet resolution using the response matrix. A response matrix, such as that shown in Figure 4.20, is filled by embedding PYTHIA jets in real, reconstructed, Minimum Bias events, and reconstructing the jets exactly as is done in data. The reconstructed jet corresponding to the embedded jet is found by a matching algorithm ensuring that the reconstructed and embedded jet share a minimum amount of momentum from shared particles. Then each row in the matrix is normalized to unity. The "truth" p_{T} distribution of jets can then be treated as a vector, with the response matrix acting on it to produce the distribution that will be reconstructed in the detector. At this point, the unfolding approach would be to invert this matrix and apply it to the real reconstructed distribution to calculate the real particle level p_{T} distribution. These response matrices were also produced separately for jets three different bins of the angle relative to the event plane.

In this analysis, we simply used the response matrix to efficiently simulate detector effects on the models, and make the comparison at the level of reconstructed jets.

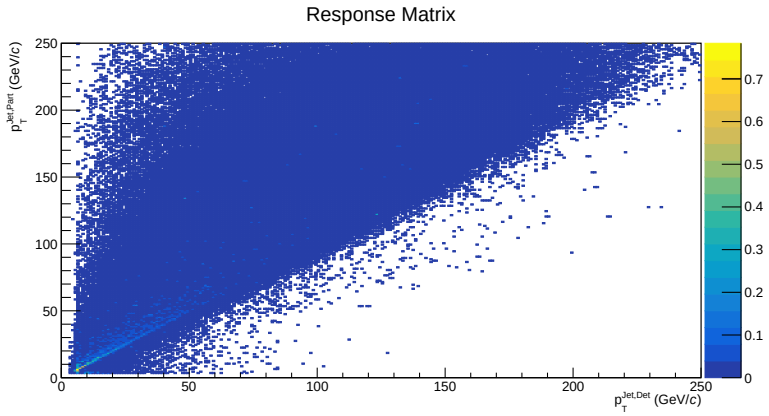

Figure 4.20: Jet Response matrix for R=0.2 anti-k_{T} jets in the 2.76 TeV jet-hadron correlations analysis, for jets at all angles relative to the event plane.

This was implemented in the analysis of JEWEL events by the following prescription: for each jet with transverse momentum p_{T}^{i} found in a JEWEL event:

- Pick the response matrix row for p_{T}^{i}, and integrate within each of the four detector-level p_{T}^{j} bins, to get weights (w^1, w^2, w^3, w^4)
- For each detector level p_{T} bin, fill the corresponding trigger and correlation histograms with the weight w^j
  - Note that the correlations are normalized by the integrals of the trigger p_{T} histograms, so the overall scale of the weighting cancels out.

Systematic Uncertainties

The primary systematic uncertainty in these calculations is the determination of the effective "background" in the correlations. To reflect this in final results, four approaches were used to estimate the background, with the variance in the final results used as the systematic from background determination. In the first approach, the standard ZYAM method is used, while in the other three methods the correlations are fit to a free background parameter plus different functions for the nearside and awayside peaks. To summarize:

1. ZYAM
2. Free background parameter
   (a) Fit 2: 2 Gaussians (nearside) + 1 Modified Gaussian (awayside)
   (b) Fit 3: 2 Gaussians (nearside) + 1 Generalized Gaussian (awayside)
   (c) Fit 4: 1 Generalized Gaussian (nearside) + 1 Generalized Gaussian (awayside)

An example of the resulting fit function is shown in Figure 4.21. The variance in the final results (event plane yield ratios) is used to calculate a systematic uncertainty from background subtraction. This uncertainty is added in quadrature to the statistical uncertainty in the ratio of the integrals used to calculate yields.

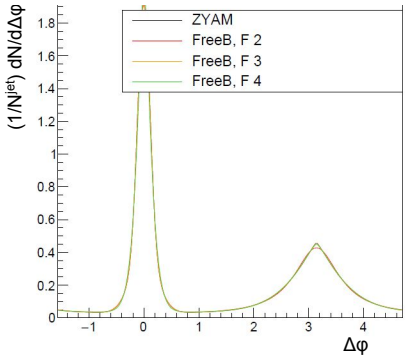

Figure 4.21: Comparison of fit functions used for 2-3 GeV/c associated hadrons and 20-40 GeV/c jets, in JEWEL w/o recoils, 30-50% centrality.

Results

The final results for yield out/in ratios for jet p_{T} ranges 20-40 GeV/c and 40-60 GeV/c in Figures 4.22 (JEWEL without recoils) and 4.23 (JEWEL with recoils). The primary observable difference with and without recoils is that JEWEL without recoils predicts suppression relative to in-plane at all p_{T}^{assoc}, whereas keeping the recoils predicts enhancement at low p_{T}^{assoc}, consistent with momentum conservation.

As noted in Section 1.5.5, the measured event plane dependence of correlations were statistically consistent with unity and with these JEWEL productions. According to two studies in Raymond Ehler's thesis ([53]), the path-length ratio between out-of-plane and in-plane jets should be between 0.72 and 0.78. Given that the energy loss is expected to scale with path-length as a mix of L and L^2, it may be considered surprising to see at most a 10% effect. Some possible explanations are that the impact of energy loss on the awayside yields may be small enough that a change in energy loss of 30% only results in a 10% change between the two path-lengths. Another possibility is that while the mean energy loss may be different between event plane angles, the large fluctuations in energy loss smear the effect in the final observable. This latter possibility is investigated in Section 4.7.

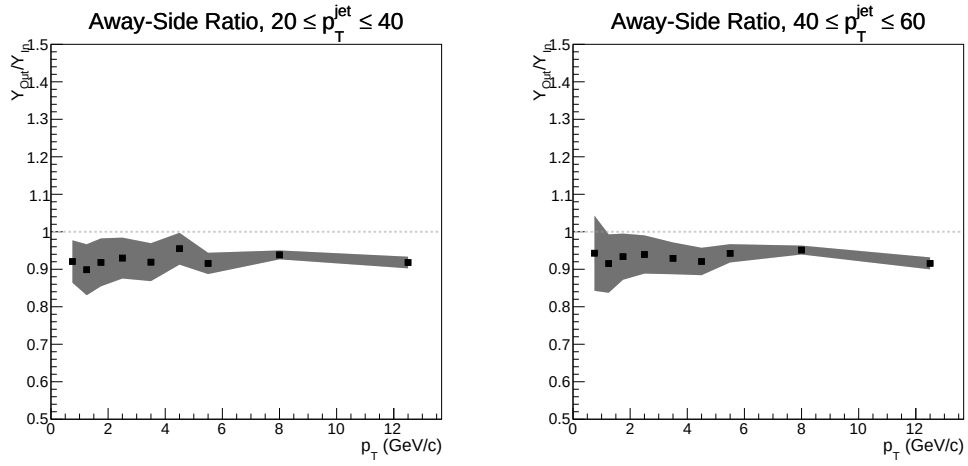

Figure 4.22: JEWEL w/o recoils model predictions for awayside yield out/in ratio in jet-hadron correlations for Pb–Pb at $\sqrt{s_{\mathrm{NN}}} = 2.76$ TeV in 30-50% centrality events.

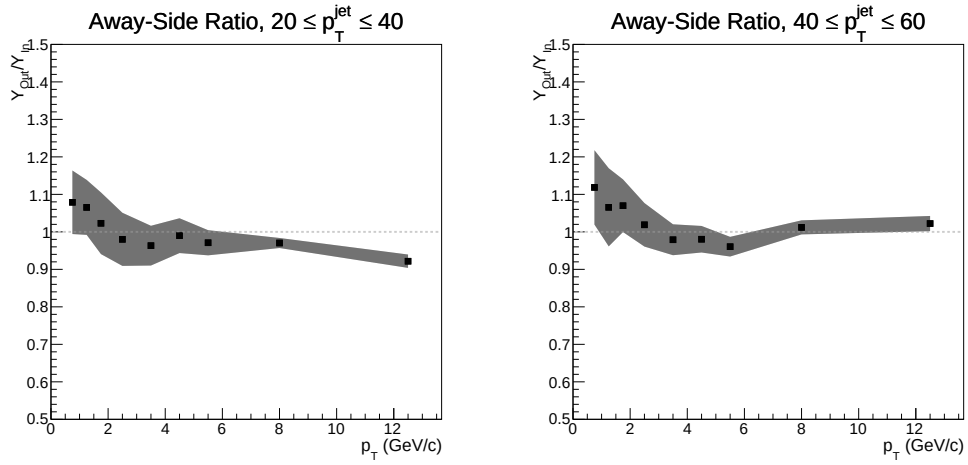

Figure 4.23: JEWEL with recoils model predictions for awayside yield out/in ratio in jet-hadron correlations for Pb–Pb at $\sqrt{s_{\mathrm{NN}}} = 2.76$ TeV in 30-50% centrality events.

4.5.2 Jet-Hadron Correlations at 5.02 TeV

Detector Jet Resolution Folding

To account for the effect of background on reconstructed jets in data, the same approach as in Section 4.5.1 was used, with the following response matrices.

Systematic Uncertainties

The same approach (described in Section 4.5.1) as in the 2.76 TeV jet-hadron modelling analysis is used for this 5.02 TeV jet-hadron modelling study.

Results

The results for awayside out/in yield ratios 30-50% jet-hadron correlations in Pb–Pb collisions at $\sqrt{s_{\rm NN}} = 5.02$ TeV are shown in Figure 4.24. As with the 2.76 TeV prediction, JEWEL w/o recoils predicts some event suppression in plane, at most a 10% effect. In JEWEL with recoils, the more realistic model, JEWEL predicts enhancement at low $p_{\rm T}^{\rm assoc}$, but no significant effect at high $p_{\rm T}^{assoc}$.

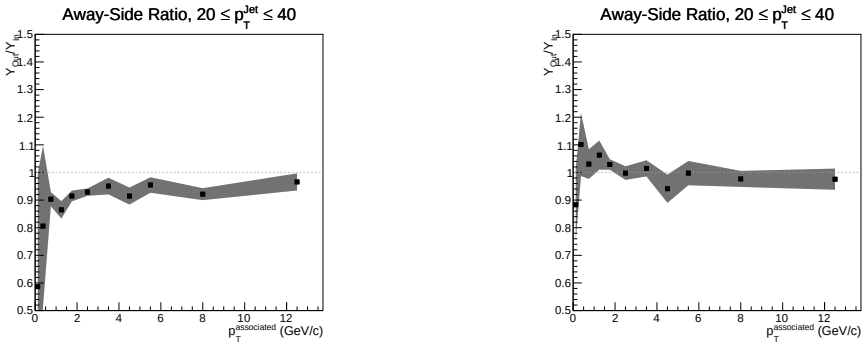

Figure 4.24: JEWEL model (w/o recoils on the left, with recoils on the right) predictions for awayside yield out/in ratio in jet-hadron correlations for Pb–Pb at $\sqrt{s_{\rm NN}} = 5.02$ TeV in 30-50% centrality events.

The results in 0-10% central Pb–Pb events at $\sqrt{s_{\rm NN}} = 5.02$ TeV are shown in Figure 4.25. No effect is observed for JEWEL with recoils, while some event plane dependence, particularly an enhancement out-of-plane over in-plane, at low $p_{\rm T}^{assoc}$.

4.5.3 π^0-Hadron Correlations at 5.02 TeV

In the analysis of these results, the projected π^0-hadron correlations were passed to the same code used in the chapter 3 at the point of applying the flow subtraction[2], to ensure

[2]"phase4" in the local π^0 analysis code, see π^0 Analysis Specific Software in A

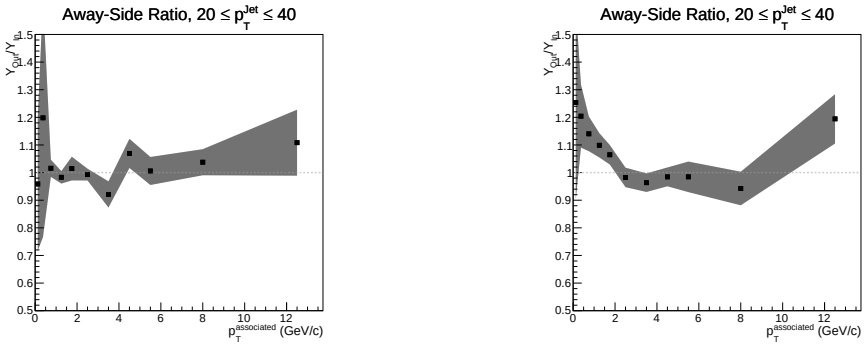

Figure 4.25: JEWEL model (w/o recoils on the left, with recoils on the right) predictions for awayside yield out/in ratio in jet-hadron correlations for Pb–Pb at $\sqrt{s_{\mathrm{NN}}} = 5.02$ TeV in 0-10% centrality events.

that the data-theory comparison was as close as possible. The same fitting procedure as used with the reaction plane fit is used, but with all flow terms fixed to zero. The result is then a pedestal fit to the far $\Delta\eta$, nearside region. The same parameter-varying uncertainty propagator (see 3.10.6) is applied, but only for the background scale parameter. This serves to accurately propagate the uncertainty in the pedestal to the final observables.

JEWEL Without Recoils

The event plane ratios for π^0-hadron correlations for JEWEL without recoils are shown for yields in Figure 4.26, which are consistent with unity.

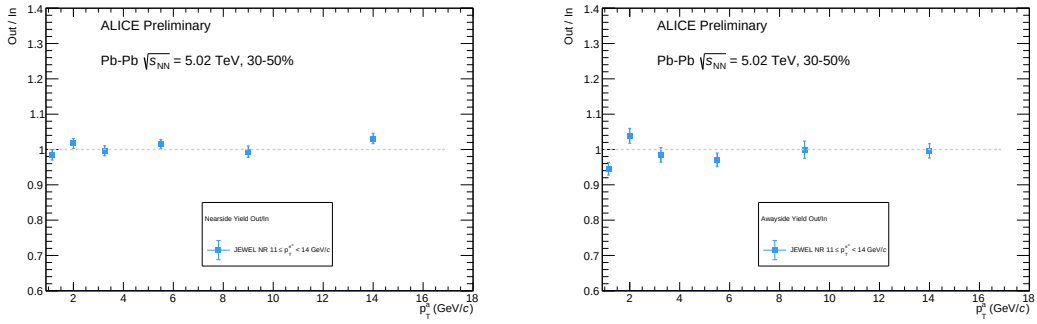

Figure 4.26: Nearside (left) and awayside (right) out/in yield ratios for π^0-hadron correlations in Pb–Pb at $\sqrt{s_{\mathrm{NN}}} = 5.02$ TeV, 30-50% central events, JEWEL without recoils.

In Figure 4.27, the out/in ratios for the widths found with a fit are shown. No event plane dependence is seen on the awayside, consistent with the lack of dependence in the yields. On the nearside, there are two significant deviations from unity. However, the widths on the nearside at high p_{T} are close to the size of the binning in $\Delta\phi$, so the point at 7-11 GeV/c is likely a fluctuation, with the uncertainty calculation failing due to the

binning.

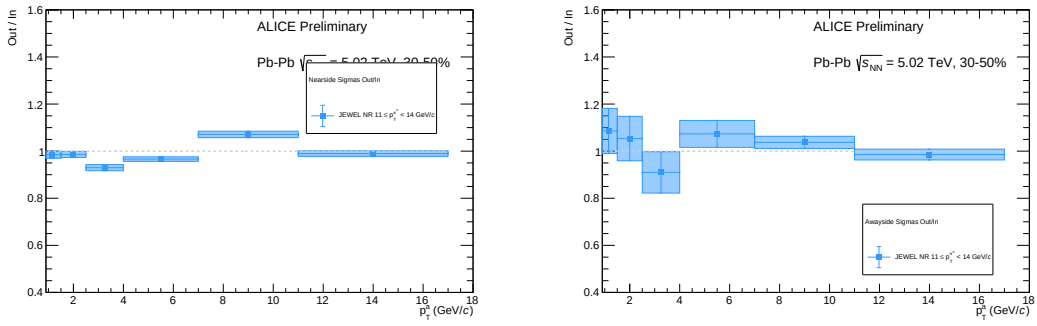

Figure 4.27: Nearside (left) and awayside (right) out/in width (sigma) ratios, JEWEL without recoils.

JEWEL with Recoils

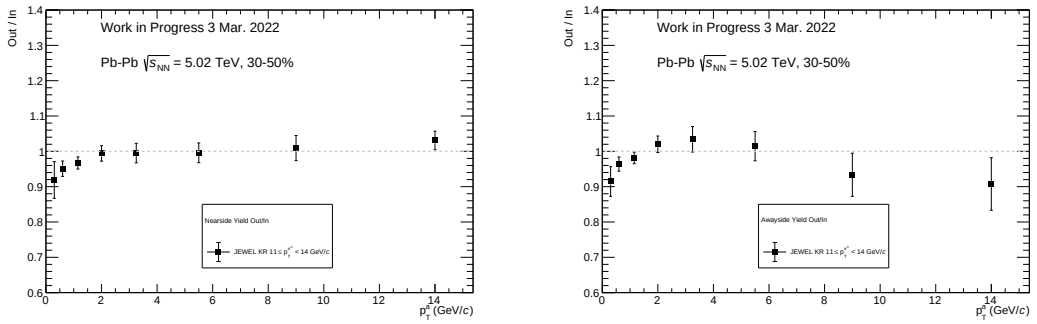

Figure 4.28: Nearside (left) and awayside (right) out/in yield ratios for π^0-hadron correlations in Pb–Pb at $\sqrt{s_{\mathrm{NN}}} = 5.02$ TeV, 30-50% central events, JEWEL with recoils.

4.5.4 Direct γ-Hadron Correlations

In this research, the study of direct γ-hadron correlations was started to simplify a study of the fluctuations in the internal jet-medium interactions in JEWEL. That study is detailed in Section 4.7.2. However, it was found that the results of analyzing the direct γ-hadron correlations in JEWEL's γ-jet events was compelling on its own.

As of the JEWEL's 2.2.0 version, more options for the hard process are available, including events that produce a vector boson and a hard parton back-to-back. The Feynmann diagrams contributing to these hard processes are displayed in Figure 4.30.

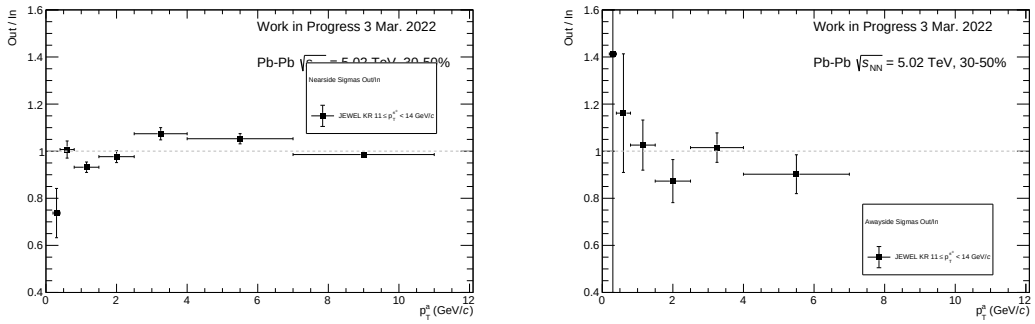

Figure 4.29: Nearside (left) and awayside (right) out/in width (sigma) for π^0-hadron correlations in Pb–Pb at $\sqrt{s_{\mathrm{NN}}} = 5.02\ \mathrm{TeV}$, 30-50% central events, JEWEL with recoils.

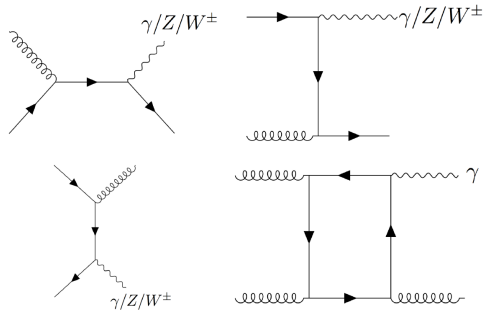

Figure 4.30: Feynmann diagrams for the hard scattering processes included in JEWEL's boson-jet hard scatter processes, sourced from [24].

The γ-jet events were analyzed with the same code as the jet-hadron and π^0-hadron model analyse, with the hard scatter photon taking the place of the trigger. As expected, there is only an awayside peak, as can be seen in the $\Delta\eta - \Delta\varphi$ plots in Figure 4.31.

One striking, but not necessarily unsurprising, finding is the scale of event plane dependence that is visible in this analysis, especially in comparison to π^0-hadron correlations with similar statistics, as visible in Figure 4.32.

The next step is to quantify this event plane dependence with event plane observables, as we have with jets and π^0s. This is done with the awayside yield event plane ratio in Figure 4.33 for JEWEL without recoils. In contrast to the jet-hadron and π^0-hadron results seen so far, a clear event plane dependence is visible, with significant suppression out-of-plane relative to in-plane at all associated hadron p_{T}.

Since this is with JEWEL without recoils, in which momentum lost by the jet is not realistically conserved within the event, we can expect that this model does not reflect reality at low assoc p_{T}.

Next, a production was done with and without JEWEL with recoils, focusing on the high p_{T} γ trigger region. In Figure 4.34, the event plane yield ratio is shown for the awayside from 40-50 GeV/c, in which statistically significant event plane dependence

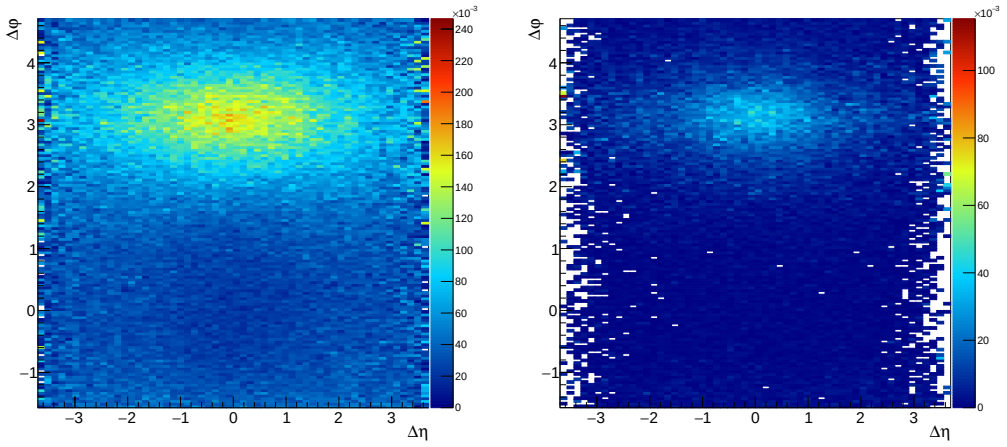

(a) $0.8 < p_T^{assoc} < 1.5\mathrm{GeV}/c$ (b) $2.5 < p_T^{assoc} < 4\mathrm{GeV}/c$

Figure 4.31: Direct γ-hadron correlations in JEWEL PbPb collisions w/o recoils at $\sqrt{s_{\mathrm{NN}}} = 5.02$ TeV, 30-50% central, with trigger direct photons in $11 < p_T < 14\mathrm{GeV}/c$.

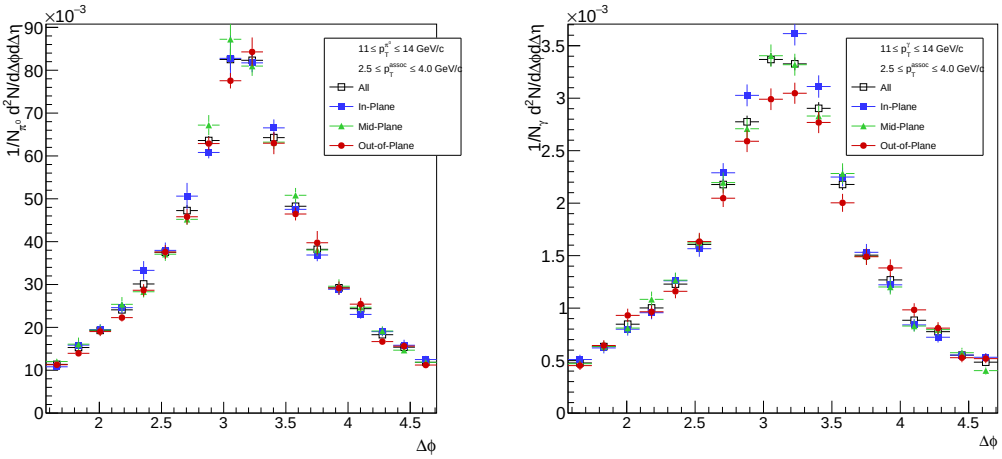

Figure 4.32: Awayside peak for π^0-hadron (left) and direct γ-hadron (right) correlations in PbPb correlations simulated with JEWEL w/o recoils, 30-50% centrality with trigger particles in the range $11 < p_T < 14$ GeV$/c$.

can be observed. In JEWEL with recoils, enhancement appears at at low p_{T}^{assoc}, as should be expected from momentum conservation.

To further emphasize the potential of γ-hadron correlations to study energy loss, we calculate the D_{RP} variable, as defined in 4.2 and compare it to the original inspiration for D_{RP}, the D_{AA} variable measured in jet-hadron correlations. Like the D_{AA}, the D_{RP} observable is designed to investigate if we can track the full conservation of the original

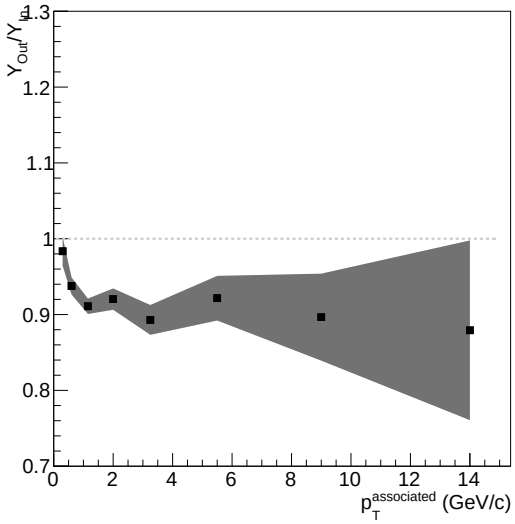

Figure 4.33: Awayside Out/In yield ratio for direct γ-hadron correlations in Pb–Pb JEWEL events w/o recoils at $\sqrt{s_{\rm NN}} = 5.02$ TeV in 30-50% centrality, $11 \leq p_{\rm T}^{\gamma} < 14$ GeV/c.

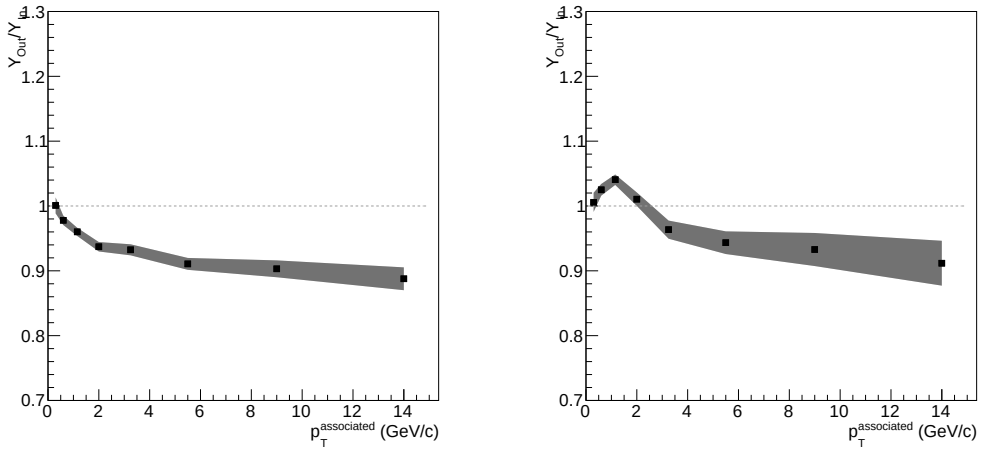

Figure 4.34: Awayside Out/In yield ratio for direct γ-hadron correlations in Pb–Pb JEWEL events without recoils (left) and with recoils (right) at $\sqrt{s_{\rm NN}} = 5.02$ TeV in 30-50% centrality, $40 \leq p_{\rm T}^{\gamma} < 50$ GeV/c.

momentum of the recoil parton.

$$D_{\rm RP}^{\rm Out} = Y_{\rm Out}(p_{\rm T}^{\rm assoc}) * \langle p_{\rm T}^{\rm assoc,Out} \rangle - Y_{\rm In}(p_{\rm T}^{\rm assoc}) * \langle p_{\rm T}^{\rm assoc,In} \rangle \tag{4.2}$$

In Figure 4.35, we compare the D_{AA} measured by STAR showing the momentum shifting towards low $p_{\rm T}$ associated particles between Au–Au and pp collisions to the D_{RP}, which can show the same effect but from varying the path-length using the event plane angle.

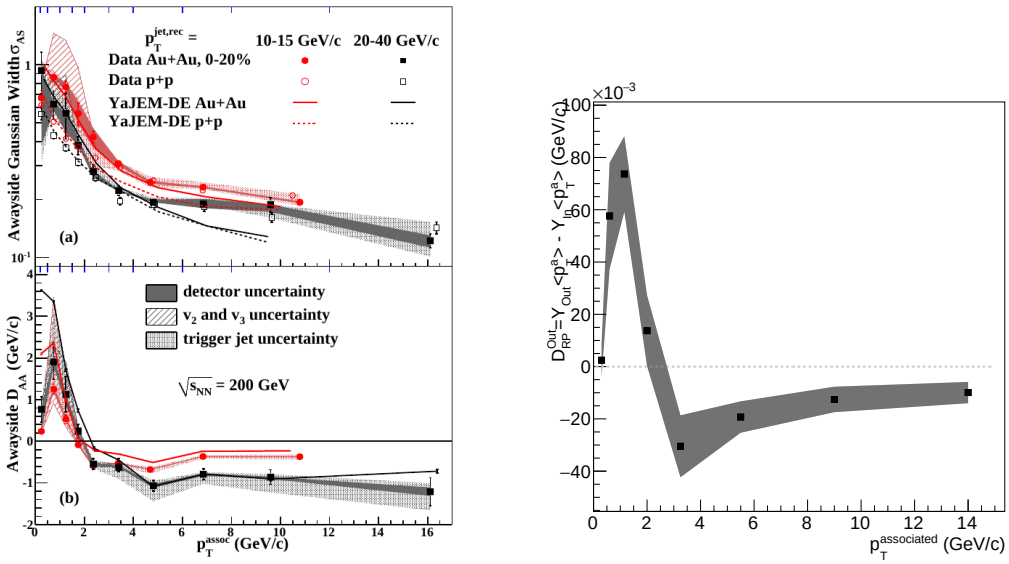

Figure 4.35: D_{AA} in jet-hadron measurements by STAR ([11]) and D_{RP}.

Additionally, we show the direct γ-hadron correlations D_{RP} for JEWEL without recoils in , which shows only suppression for out-of-plane, consistent with the non-conservation of momentum within the event in JEWEL without recoils.

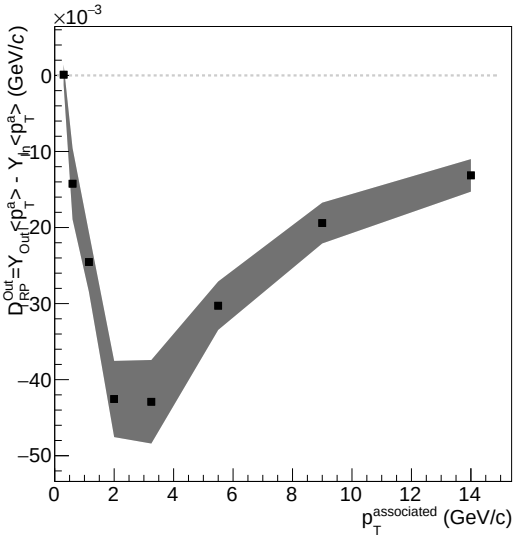

Figure 4.36: D_{RP} in direct γ-hadron correlations in Pb–Pb at $\sqrt{s_{\mathrm{NN}}} = 5.02$ TeV for 30-50% central events in JEWEL without recoils.

4.6 Discussion and Analysis

In order to understand the surprisingly small effects predicted by JEWEL for correlations observables relative to the event plane with π^0 and jet triggers, it would be useful to study not only the average path-length and energy-loss jets travel and undergo, but the full distribution of these variables. The primary motivation for this is to understand the scale of fluctuations in path-length and energy-loss, and how these fluctuations act to smear out the event plane angle dependence of these and similar observables.

4.7 Jet-Medium Interactions in JEWEL

After observing little path-length dependence in experiment (the ALICE jet-hadron in Pb–Pb at $\sqrt{s_{\mathrm{NN}}} = 2.76\ \mathrm{TeV}$ analysis, Raymond Ehler's jet-hadron analysis in Pb–Pb at $\sqrt{s_{\mathrm{NN}}} = 5.02\ \mathrm{TeV}$, and the π^0-hadron correlations analysis in this thesis) and in theory (the JEWEL model predictions for each of these analyses), the question of why the intuitive expectation of path-length dependence appearing in two-particle correlations was not working out.

In the ALICE publication of jet-hadron correlations, the lack of significant observable dependence was attributed to smearing of the path-length dependence by jet-by-jet fluctuations in energy loss, with fluctuations in medium energy density potentially contributing as well [14]. This conclusion was inspired primarily by the JEWEL dijet asymmetry study by Milhano and Zapp ([10]), which showed that jet-by-jet fluctuations could entirely explain dijet asymmetry effects in the absence of geometric effects.

In this study, the goal was to quantify the fluctuations in jet-by-jet interactions with the medium. A few tools are used here to study the internal features of jet energy loss by event in JEWEL. One is to directly compute the differences between the hard-scatter partons and final-state jets, while the other is to study the number of medium particles with which the simulated jets interact.

4.7.1 Energy Loss

The simplest way to investigate the energy loss in jets in JEWEL is to simply compare the hard-scatter partons with the reconstructed jets in the final state. In this analysis, this is done by using the leading jet in the event and matching it with the nearest of the two hard-scatter partons.

While this means that this does not reflect the true jet energy loss, it does mean that this does mean that it reflects the the scale of changes that will be observable in experimental measurements.

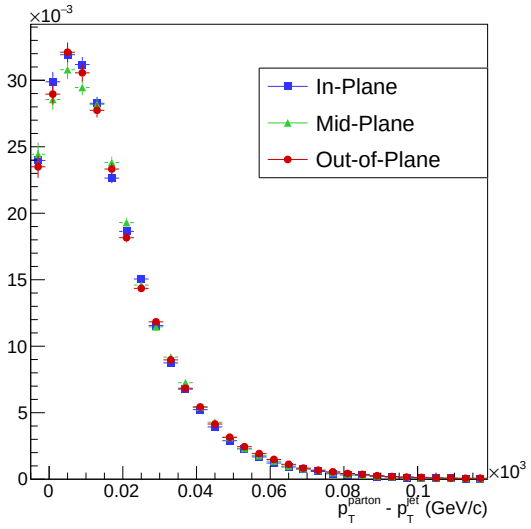

Figure 4.37: Momentum difference between reconstructed jets ($20 < p_{\mathrm{T}} < 40$ GeV/c) and the matched hard scatter parton, in Pb–Pb events $\sqrt{s_{\mathrm{NN}}} = 5.02$ TeV in JEWEL w/o recoils in 30-50% centrality.

4.7.2 Scattering Centers

In JEWEL's implementation of the jet-medium interaction, there is never any explicit calculation of a path length for a given jet. Instead, the parton shower is simulated traversing the medium while showering and interacting with the medium.

One way to study the underlying physics that should determine the geometric dependence of energy loss is to use a quantity that is directly calculated in JEWEL: the number of scattering centers. Since JEWEL's parton-medium interaction is based on sampling medium particles to interact with when the temperature at a parton's location is above a threshold, the number of individual medium scattering events is a good proxy for the path length.

In JEWEL's default mode, a QCD hard-scatter produces two partons, in addition to initial- and final-state radiation. Since it is nontrivial to modify JEWEL to monitor the number of scattering centers for each jet individually, an alternative approach is used here.

As noted in Section 4.5.4, JEWEL's 2.1.0 version allows for the simulation of hard-scatters involving a single jet and an electroweak boson.

In these γ+jet events, there is only one primary QCD jet formed, though there may be contributions from the initial- and final-state radiation. Thus, it can be assumed that the number of scattering centers that JEWEL produces in the event will correspond closely to those encountered by the primary jet.

Two quantities to track are the average and variance of the number of scattering centers under different conditions, especially changes with the angle relative to the event plane.

4.7.3 Event Plane Dependence

The event plane dependence of the number of scattering centers can be investigated by varying the angle of the trigger direct γ with respect to the event plane, as shown for Pb–Pb semicentral events in Figure 4.38. It should be recalled that since the direct photon does not interact with the medium, there is certainly no geometric bias in the distribution of the origins of the jets. One notable feature is that the differences in scattering center distributions between event-plane angle are significant only in the range of very few scattering centers. This suggests that the event plane dependence between jets is mainly in the probability to have almost no interactions with the medium.

Another observation that can be drawn from this is the large variance in the number of scattering centers, approximately $5/6$ of the mean number, which is much larger than the differences in the mean number of scatterers between event planes.

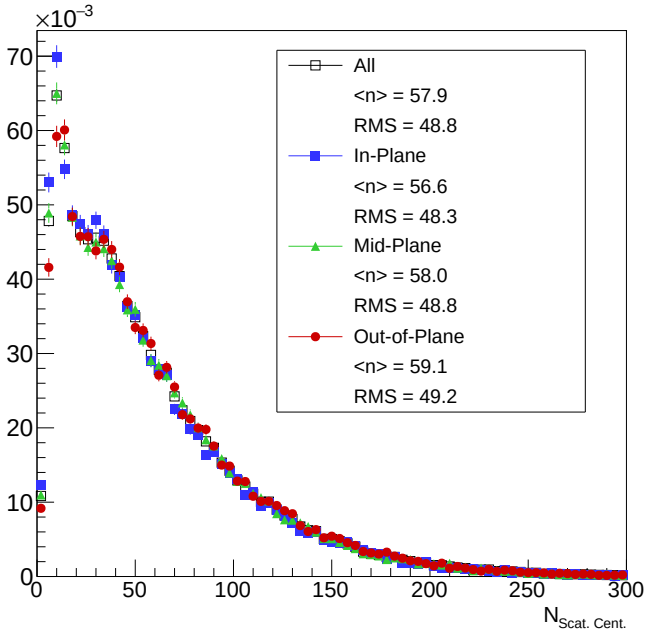

Figure 4.38: Number of scattering centers in different event plane angles encountered by jets tagged by direct photons in the p_{T} range 20-40 GeV/c in JEWEL Pb–Pb events at $\sqrt{s_{\mathrm{NN}}} = 5.02$ TeV in the 30-50% centrality range.

4.7.4 Centrality Dependence

Examining this mean number of scattering centers variable as a function of centrality and γ p_{T} ($\approx p_{\mathrm{T}}^{\mathrm{parton}}$) helps to interpret its meaning. In Figure 4.39, we can see that $\langle N_{scat} \rangle$ increases with more central events as expected. As the initial parton p_{T} increases, $\langle N_{scat} \rangle$

increases, which can be understood from higher p_{T} partons producing greater multiplicities of fragmenting partons.

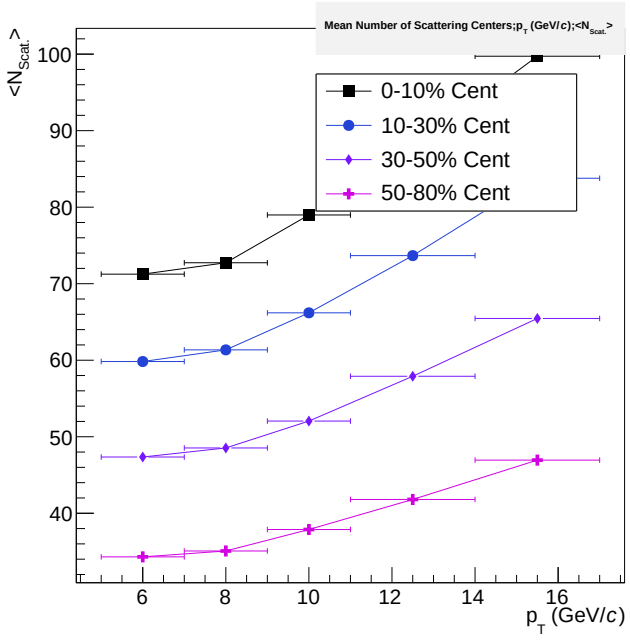

Figure 4.39: Average number of scattering centers direct photon-tagged jets interact with in Pb–Pb events at $\sqrt{s_{\mathrm{NN}}} = 5.02$ TeV in different centrality ranges.

4.7.5 System Dependence

Finally, we can compare event-plane dependence of $\langle N_{scat} \rangle$ between the collision systems available at RHIC and the LHC. This yields the surprising result that the number of scattering centers used by JEWEL has more significant event-plane dependence in the collision system at RHIC than at the LHC, as visible in Figure 4.40.

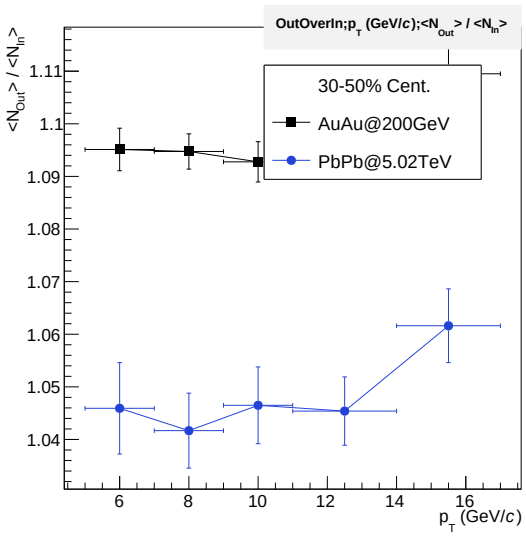

Figure 4.40: Ratio of the number of scattering centers sampled by jets in JEWEL out-of-plane relative to in-plane

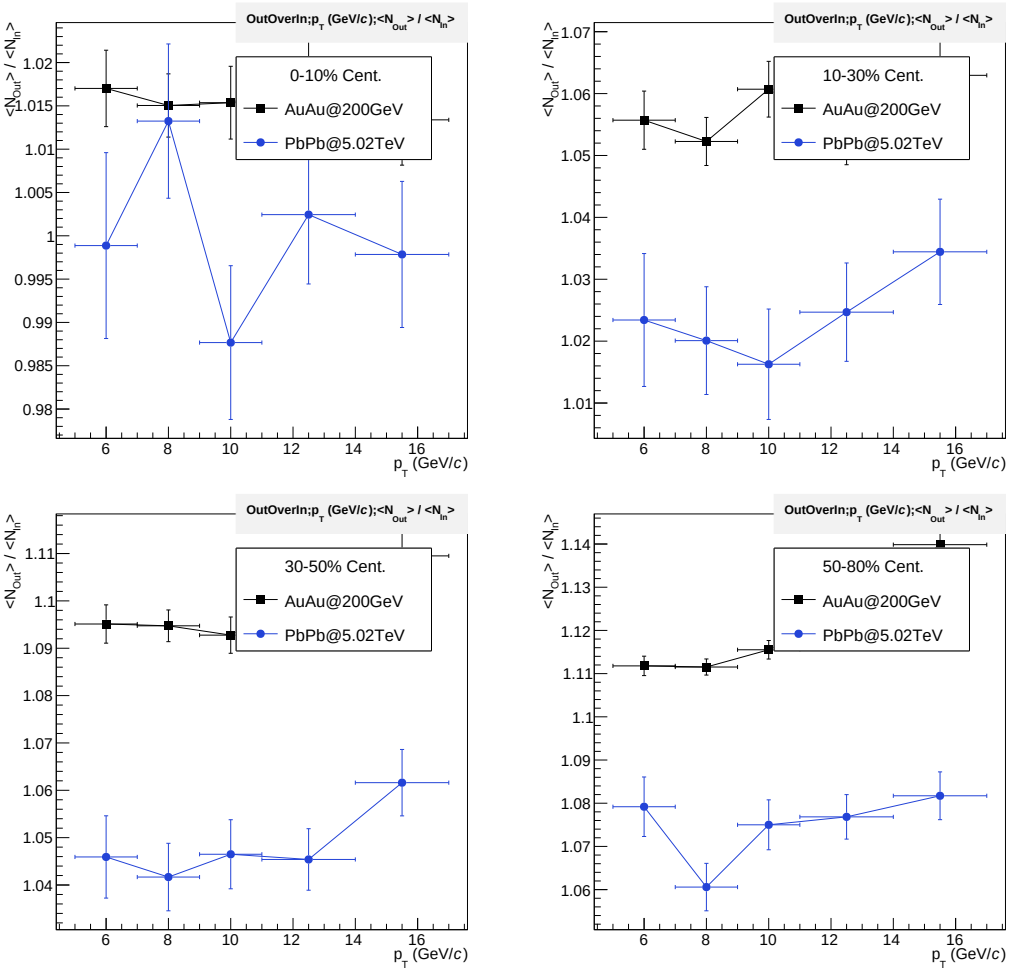

Figure 4.41: Out/In ratios for the average number of scattering centers with which jets interact in JEWEL in different centrality bins, with a comparison between the Pb–Pb collisions at $\sqrt{s_{\mathrm{NN}}} = 5.02$ TeV and Au–Au collisions at $\sqrt{s_{\mathrm{NN}}} = 200$ GeV.

4.8 Concluding Notes

In addition to providing theory comparisons for a number of measurements these modelling studies have proven useful in interpreting results and in providing a qualitative understanding of how surface bias changes between different collision energies. Some limitations of these studies to consider is that the JEWEL model does not include effects such as fluctuations in the initial-state density, which are already known to have significant impact on the final state. In addition, the hydrodynamic model in JEWEL is a simple analytic longitudinal expansion, which neglects radial and elliptical flow. While the sampled partons from the medium are boosted in the longitudinal direction as a function of position and time, the boosts from radial and elliptical flow are missing. Thus, JEWEL may not be properly modelling effects arising from the relative angle between the jet and the local medium velocity.

Additionally, the assumption that JEWEL uses of a medium that linearly increases in time from temperature 0 at time 0 to the initial temperature parameter at time τ_i (visible in Figure 4.2 may be an oversimplification. This is important because the time before the medium "turns on" provides a window in which some jets may escape the event with out ever interacting with the medium. While this is plausible, it merits further investigation.

While using JEWEL with recoils provides some modelling of the medium's response to the jet, there are ambiguities in how to treat the added thermal energy to the event. Some possibilities for future modelling investigations are given in Section 5.1.3.

Chapter 5

Results and Discussion

In Chapter 1, we sought to motivate why we should expect to see event plane dependence of jet observables as a result of path-length dependence. However, as seen here in Figure 5.1, the analysis using π^0 triggers and analyzing the correlated hadrons with respect to the event plane did not find significant event plane dependence.

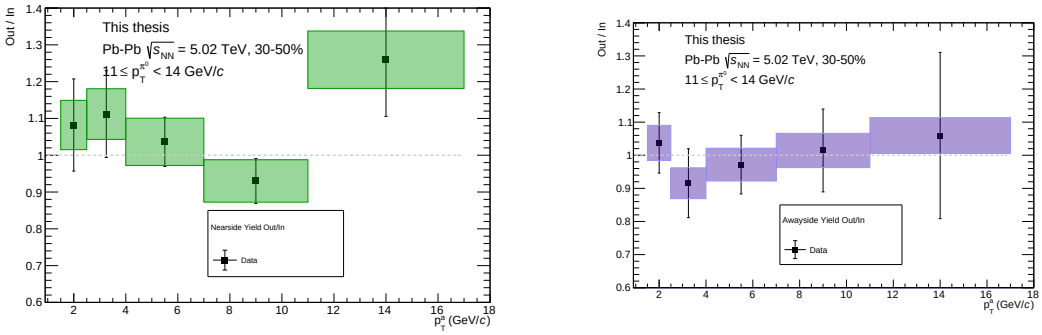

Figure 5.1: Near-side (left) and away-side (right) yield ratios in 30-50% centrality, EGA-triggered events.

In Figure 5.2, we compare the three similar results of jet- and π^0-hadron correlations with respect to the event plane. These are all generally consistent with unity and the non-observation of event-plane dependence, which is consistent with the JEWEL model. A possible "hint" of an effect is noticeable around 3 GeV/c in the away-side in all three, most significant in the jet-hadron results at $\sqrt{s_{\mathrm{NN}}} = 5.02$ TeV. The coincidence of this in all three measurements may not be as scientifically significant as it appears though, as the 5.02 TeV results use the same data set, and all three use the same methods for flow subtraction.

This non-observation is qualitatively surprising, considering that radiative energy loss is theorized to scale with the square of the path-length through the medium, which should enhance the effect of any modest difference in path-length. It is also surprising when we

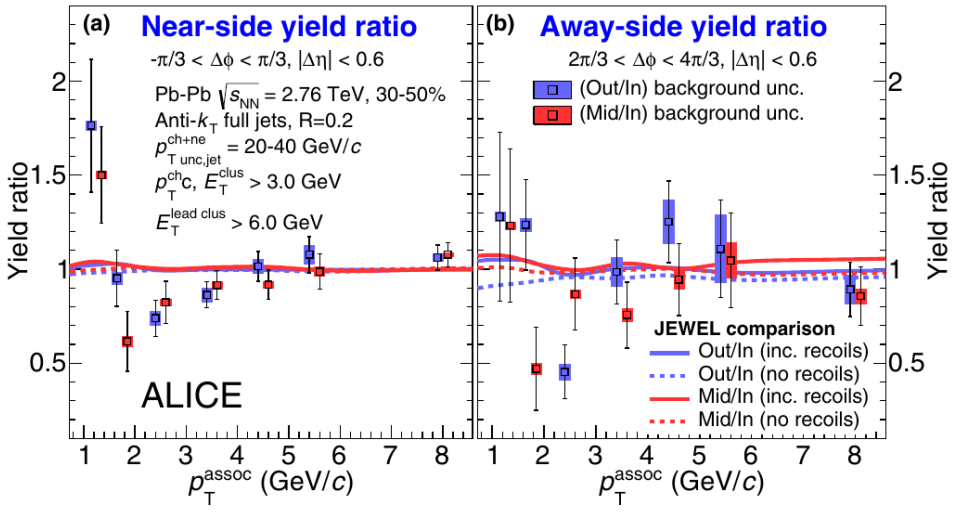

(a) ALICE jet-hadron correlations at $\sqrt{s_{\mathrm{NN}}} = 2.76$ TeV [14]

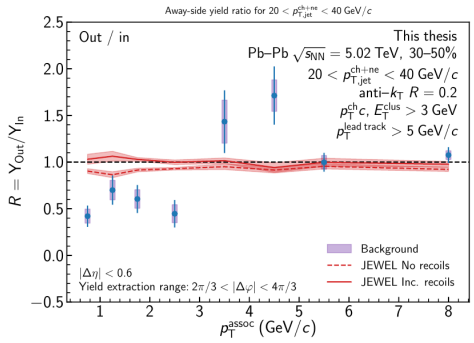

(b) ALICE jet-hadron at $\sqrt{s_{\mathrm{NN}}} = 5.02$ TeV [23]

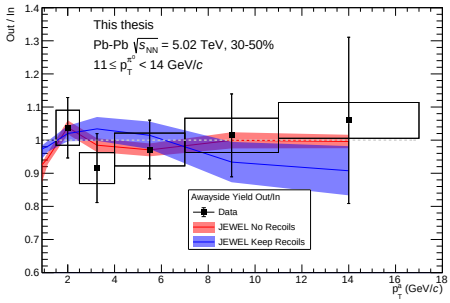

(c) ALICE π^0-hadron at $\sqrt{s_{\mathrm{NN}}} = 5.02$ TeV (this thesis)

Figure 5.2: Out/In yield ratios in three experimental measurements.

consider the likely parton configuration (whether the π^0-producing and recoil jets originate from quarks or gluons) of the hard scatter producing the trigger π^0. In MC simulations, we can make a model-dependent analysis to examinate of this using JEWEL, which is shown in Figure 5.3 for pp collisions. In this figures, we plot the p_{T} distributions for hard scatters associated with π^0 triggers, sorted by parton configuration. The primary finding from this is that the main source of the π^0 triggers is from quark-gluon dijets, meaning that the recoiling jet is most often a gluon jet. Gluon jets are expected to lose more energy, which should make path-length dependence easier to measure.

As we found in Chapter 4, the predictions of the JEWEL model are also consistent with the non-observation of event plane dependence in this observable. A possible interpretation of the JEWEL model result is that the fluctuations in energy loss smear out path-length dependence too much to be seen with this observable.

In the JEWEL dijet asymmetry paper by Milhano and Zapp, it was found that asym-

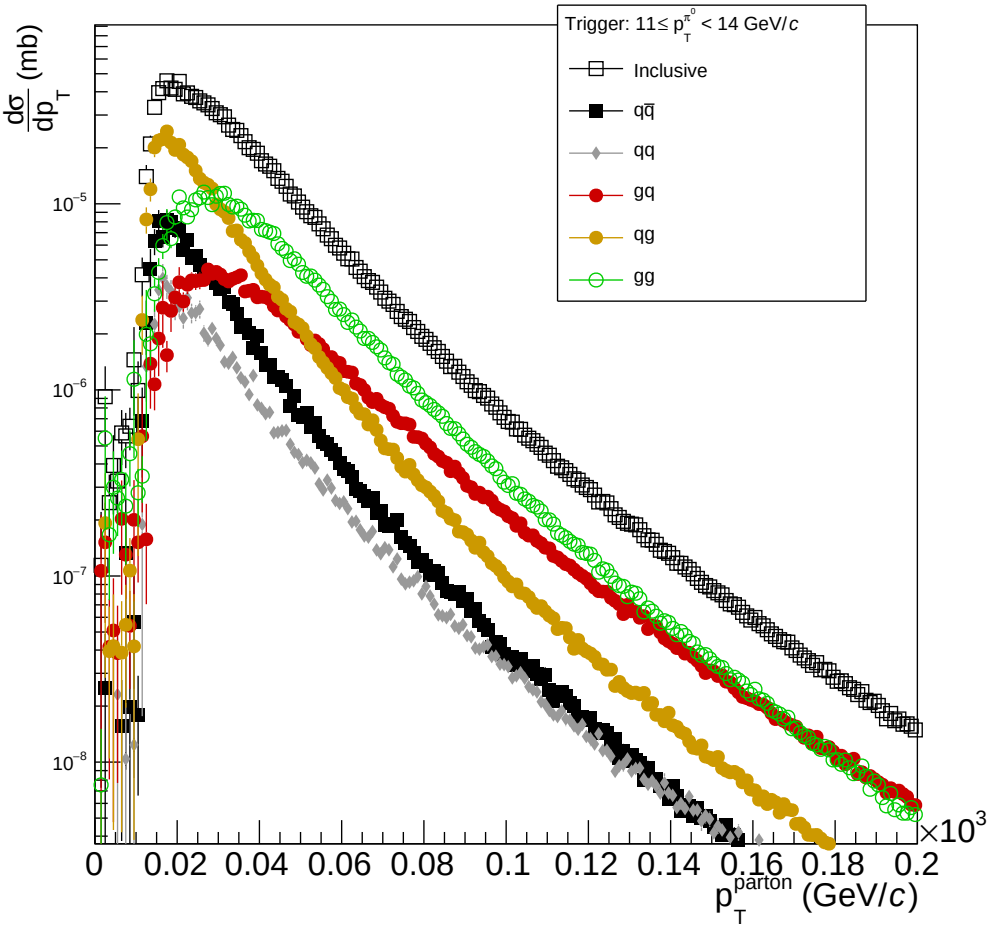

Figure 5.3: Distribution of hard-scatter parton p_{T} producing π^0 triggers in the p_{T} range 11-14 GeV/c in pp collisions at $\sqrt{s} = 5.02$ TeV, produced with JEWEL's vacuum mode (equivalent to PYTHIA6). The distributions are divided by parton configuration. The first entry (q or g) indicates the type of parton that produced the π^0 (with no distinction between quarks and anti-quarks).

metry in the jet m/p_{T} (related to the width of the jet) between jets in a dijet pair could create a significant dijet asymmetry without any geometric effect [10].

It is interesting to consider what the implications of measuring a significant event-plane dependence could be, especially since that is not ruled out by the uncertainties in these results. If the small size of the signal in JEWEL is due to smearing by the fluctuations in energy loss, a larger event plane dependence than JEWEL's could indicate that JEWEL's treatment of jets overestimates the fluctuations in energy loss. More specifically, it could point towards models not entirely based on perturbative QCD. However, current measurements are still consistent with JEWEL's approach.

As shown in the model comparisons in Section 3.11, there remains disagreement be-

tween the measured and JEWEL-predicted yields, with a greater disagreement on the away-side. One possible explanation is that the fragmentation of jets in JEWEL in Pb–Pb does not reflect reality, with real π^0 triggers more likely to come from higher p_{T} jets, resulting in higher yields in the data.

5.1 Future Possibilities

5.1.1 Flow in Events With High p_{T} Triggers

One finding in this analysis that merits further research is the large difference between flow observed in EMCal Gamma-triggered events compared to MB events, described in Section 3.9.3. This could be studied further by measuring flow in events requiring a cluster or track of a given p_{T} threshold. The events would be selected from MB events, as the EGA triggered events already have a form of this requirement.

5.1.2 New Data and Reconstruction

Work that is planned for the future is to include the 2018 Pb–Pb data set taken by ALICE and a new reconstruction of the data done on both the 2015 and 2018 Pb–Pb datasets. The primary reason this is not already included is a current lack of calibrations for the event plane angle determination.

The new reconstructions improve the tracking efficiency with the TPC significantly. This improvement also reduces the irregularities in ϕ. The mixed event skew problem affecting low $p_{\mathrm{T}}^{\mathrm{assoc}}$ bins (see Section 3.7.1) is likely to be alleviated by a more isotropic efficiency. Also, with more data, a data-driven correction for any skew could be created.

Another possible extension to this analysis would be to use merged clusters as π^0 triggers, perhaps using the V1+unfolding clusterization method, or using a shower shape variable. Two challenges for this are the determination of the π^0 purity (for which techniques already exist) and for subtracting background correlations.

5.1.3 Additional Model Comparison

Another continuation of this research would be to compare to a wider range of models. One model framework that would be exciting for comparisons is called JETSCAPE. It is designed to integrate models for different parts of the collision (initial events, jet-medium interaction, hydrodynamics, hadronization, etc.) in a modular manner. For example one can swap out different energy loss models, while keeping all other parts of the simulation the same. Another exciting planned feature is the treatment of energy lost by the jets to be included as energy and momentum source terms in the hydrodynamics model, to better model the medium interaction [57]. One model that is included with JETSCAPE is the

hybrid strong/weak coupling model. For high energy scales, pQCD calculations are used, similar to JEWEL, but for energy loss at lower energy scales where the coupling becomes strong the model uses calculations based on AdS/CFT correspondence [58].

5.1.4 Correlations with Direct Photons

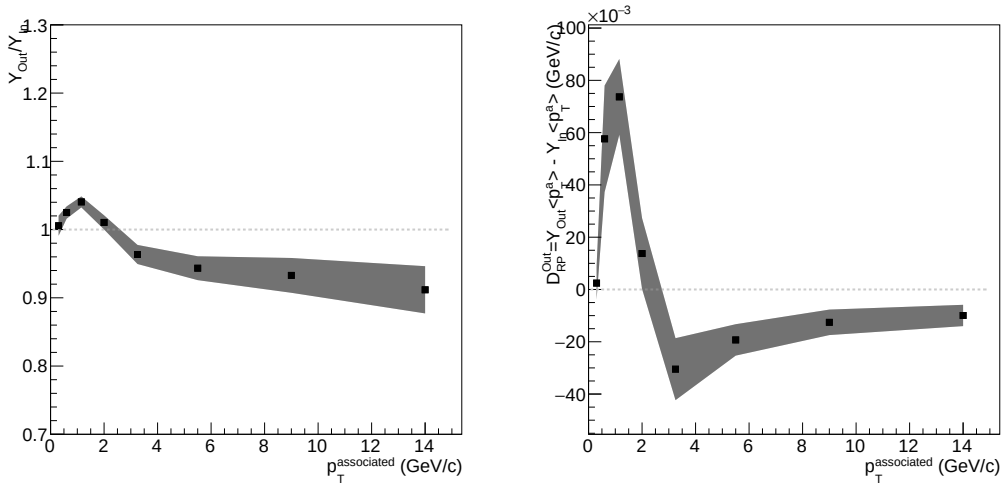

Figure 5.4: Out/in yield ratio I_{RP} and p_{T}-weighted yield difference D_{RP} for direct γ-hadron correlations with 40-50 $\mathrm{GeV}/c\,\gamma$ triggers in JEWEL with recoils in 30-50% central events.

As demonstrated in Section 4.5.4 and shown here for in Figure 5.4, correlations of hadrons with direct photons give a viable measurement of path-length dependence, according to the JEWEL model. Thus, such research would be a logical continuation of this line of inquiry. Unfortunately, measurements of direct photons and their correlations entail significant difficulties. One major source is the fact that high p_{T} direct photons are produced at significantly lower rates than QCD jets. This results directly from the fact that the $2 \to 2$ scatters that produce direct photons replace one strong interaction vertex (with a coupling strength around 0.15 at a scale of 25 GeV) with an electromagnetic vertex (coupling strength $\approx$ 1/137), leading to a relative suppression factor proportional to $(\alpha_{EM}/\alpha_s)^2$.

Another challenge for direct photon measurements are the significant backgrounds. One background is from fragmentation photons, which are produced as part of a jet from a quark or gluon. This background can be mitigated with isolation requirements on the direct photon candidates, although this of course limits the available statistics.

An additional path of further research is to better understand why JEWEL predicts less observable event-plane dependence in π^0-hadron correlations than in direct γ-hadron correlations, or even jet-hadron correlations. This may be aided by more explicit calculation

of the jet energy loss, as well as examination of the relative contribution from quark and gluon jets.

Appendix A

Software

A.1 Alice Collaboration Software

https://github.com/alisw/AliPhysics
https://github.com/alisw/AliRoot

A.2 π^0 Analysis Specific Software

https://github.com/moliver813/Pi0HadronCorr

A.3 Monte Carlo Generator Analysis Software

https://github.com/moliver813/MyEventGeneratorCode

Appendix B

Configurations

B.1 EMCal Corrections Framework

The configuration used for the LHC15o pass1 data is given below.

```
period: ""
# standard yaml file is located in:
pass: ""
# AliPhysics/PWG/EMCAL/config/
CellEnergy:
    enabled: true
    createHistos: false
CellBadChannel:
    enabled: true
    createHistos: false
CellTimeCalib:
    enabled: true
    createHistos: false
Clusterizer:
    enabled: true
    clusterizer: kClusterizerv3
    # Type of clusterizer to use.
    recalDistToBadChannels: true
    # True will recalculate the distance to bad channels
    #cellTimeMin: -50e-6
    # Min cell time (s)
    #cellTimeMax: +50e-6
    # Max cell time (s)
    cellE: 0.1
    seedE: 0.5
ClusterExotics:
    enabled: true
ClusterNonLinearity:
    enabled: true
ClusterTrackMatcher:
# Cluster-track matcher component
    enabled: true
   #pt track cut in old version!
ClusterHadronicCorrection:
# use no hadronic correction for g-h correlation
```

```
    enabled: false
```

And the configuration for the Monte Carlo Productions anchored to LHC15o pass1:

```
period: ""
# standard yaml file is located in:
pass: "default"
# AliPhysics/PWG/EMCAL/config/
CellEnergy:
    enabled: false
    createHistos: false
CellBadChannel:
    enabled: true
    createHistos: false
CellTimeCalib:
    enabled: false
    createHistos: false
Clusterizer:
    enabled: true
    clusterizer: kClusterizerv2
    # Type of clusterizer to use.
    recalDistToBadChannels: true
    # True will recalculate the distance to bad channels
    #cellTimeMin: -50e-6
    # Min cell time (s)
    #cellTimeMax: +50e-6
    # Max cell time (s)
    cellE: 0.1
    seedE: 0.5
ClusterExotics:
    enabled: true
ClusterNonLinearity:
    enabled: true
ClusterTrackMatcher:
# Cluster-track matcher component
    enabled: true
   #pt track cut in old version!
ClusterHadronicCorrection:
# use no hadronic correction for g-h correlation
    enabled: false
```

Appendix C

Fit Function Implementations in ROOT

Included here are the dijet fit functions described in section 4.3.1 implemented in ROOT. Additional steps such as the limits on parameters are excluded for brevity.

```
// Simple, Two Gaussians + Constant background
TF1 * phiCorrFit_1Gaus_1Gaus(TH1D * hist, std::string name)

  TF1 * fit = new TF1(name.c_str(),"[0]*(TMath::Gaus(x, \
  -2*TMath::Pi(),[1],1) + TMath::Gaus(x,0,[1],1) +\
  TMath::Gaus(x,2*TMath::Pi(),[1],1)) + \
  [2] * (TMath::Gaus(x,-TMath::Pi(),[3],1) +\
  TMath::Gaus(x,TMath::Pi(),[3],1) +\
  TMath::Gaus(x,3*TMath::Pi(),[3],1)) + \
  [4]",-PI/2,3.0*PI/2);
  //name parameters
  fit->SetParName(0,"Y_NS");
  fit->SetParName(1,"Sigma_NS");
  fit->SetParName(2,"Y_AS");
  fit->SetParName(3,"Sigma_AS");
  fit->SetParName(4,"B");
```

```
// Simple, Two Gaussians + Constant background, using FWHM for AS width\
TF1 * phiCorrFit_1Gaus_1Gaus_Fwhm(TH1D * hist, std::string name)

  TF1 * fit = new TF1(name.c_str(),"[0]*(TMath::Gaus(x,-2*TMath::Pi(),[1],1)\
  + TMath::Gaus(x,0,[1],1) + TMath::Gaus(x,2*TMath::Pi(),[1],1)) + \
  [2] * (2./[3]) *\
  TMath::Sqrt(TMath::Log(2) / (2 * TMath::Pi() )) * (TMath::Exp(-TMath::Power(x+\
  TMath::Pi(),2)*4*TMath::Log(2)/TMath::Power([3],2)) +\
  TMath::Exp(-TMath::Power(x-TMath::Pi(),2)*\
  4*TMath::Log(2)/TMath::Power([3],2)) + TMath::Exp(-TMath::Power(x-3.*\
  }TMath::Pi(),2)*4*TMath::Log(2)/TMath::Power([3],2)) )\
  + [4]",-PI/2,3.0*PI/2);
  //name parameters
  fit->SetParName(0,"Y_NS");
  fit->SetParName(1,"Sigma_NS");
  fit->SetParName(2,"Y_AS");
  fit->SetParName(3,"Omega_AS");
  fit->SetParName(4,"B");
```

```
  TF1 * phiCorrFit_2Gaus(TH1D * hist, std::string name)
{
  TF1 * fit = new TF1(name.c_str(),"[0]*(TMath::Gaus(x,-2*TMath::Pi(),[1],1)\
  + TMath::Gaus(x,0,[1],1) + TMath::Gaus(x,2*TMath::Pi(),[1],1)) +\
  [2]*(TMath::Gaus(x,-2*TMath::Pi(),[3],1) + TMath::Gaus(x,0,[1]+[3],1) +\
  TMath::Gaus(x,2*TMath::Pi(),[1]+[3],1)) + [4] * (TMath::Gaus(x,-TMath::Pi(),[5],1) +\
  TMath::Gaus(x,TMath::Pi(),[5],1) +\ TMath::Gaus(x,3*TMath::Pi(),[5],1)) +\
  [6]",-PI/2,3.0*PI/2);
  //name parameters
  fit->SetParName(0,"Y_NS_1");
  fit->SetParName(1,"Sigma_1_NS");
  fit->SetParName(2,"Y_NS_2");
  // NOTE: sigma_2_NS is the difference between sigma_2 and sigma_1
  fit->SetParName(3,"Sigma_2_NS");
  fit->SetParName(4,"Y_AS");
  fit->SetParName(5,"Sigma_AS");
  fit->SetParName(6,"B");
```

```
/** New method: 2 gaussians for nearside, and a generalized gaussian for the
 * awayside
 *
 */
TF1 * phiCorrFit_2Gaus_1GenGaus(TH1D * hist, std::string name)
{
  TF1 * fit = new TF1(name.c_str(),"[0]*\
  (TMath::Gaus(x,-2*TMath::Pi(),[1],1) +\
  TMath::Gaus(x,0,[1],1) +\
  TMath::Gaus(x,2*TMath::Pi(),[1],1)) +\
  [2]*(TMath::Gaus(x,-2*TMath::Pi(),[1]+[3],1) +\
  TMath::Gaus(x,0,[1]+[3],1) +\
  TMath::Gaus(x,2*TMath::Pi(),[1]+[3],1)) +\
  [4] * (2.*[6] * pow(TMath::Gamma(3./[6]),0.5))/\
  (2.*[5]*pow(TMath::Gamma(1./[6]),1.5)) *\
  (TMath::Exp(-pow(abs(x-TMath::Pi())/([5]*pow(TMath::Gamma(1./[6])/\
  TMath::Gamma(3./[6]),0.5)),[6])) +\
  TMath::Exp(-pow(abs(x+TMath::Pi())/([5]*\
  pow(TMath::Gamma(1./[6])/TMath::Gamma(3./[6]),0.5)),[6])) +\
  TMath::Exp(-pow(abs(x-3*TMath::Pi())/([5]*pow(TMath::Gamma(1./[6])\
  TMath::Gamma(3./[6]),0.5)),[6]))) + [7]",-PI/2,3.0*PI/2);

  //name parameters
  fit->SetParName(0,"Y_NS_1");
  fit->SetParName(1,"Sigma_1_NS");
  fit->SetParName(2,"Y_NS_2");
  // NOTE: sigma_2_NS is the difference between sigma_2 and sigma_1
  fit->SetParName(3,"Sigma_2_NS");
  fit->SetParName(4,"Y_AS");
  fit->SetParName(5,"Sigma_AS");
  fit->SetParName(6,"Beta_AS");
  fit->SetParName(7,"B");
```

```
/**
 * Same method as above, but with the FWHM as a parameter instead of sigma
 */
TF1 * phiCorrFit_2Gaus_1GenGaus_Fwhm(TH1D * hist, std::string name)
{
   TF1 * fit = new TF1(name.c_str(),"[0]*(TMath::Gaus(x,\
   -2*TMath::Pi(),[1],1) + TMath::Gaus(x,0,[1],1) +\
```

```
    TMath::Gaus(x,2*TMath::Pi(),[1],1)) +\
    [2]*(TMath::Gaus(x,-2*TMath::Pi(),[1]+[3],1) +\
    TMath::Gaus(x,0,[1]+[3],1) +\
    TMath::Gaus(x,2*TMath::Pi(),[1]+[3],1)) +\
    [4] * (2.* [6] * pow(TMath::Log(2),1./[6]))/\
    ([5]*TMath::Gamma(1./[6])) *\
    (TMath::Exp(-TMath::Log(2) *\
    pow(2*abs(x-TMath::Pi())/([5]),[6])) +\
    TMath::Exp(-TMath::Log(2) *\
    pow(2*abs(x+TMath::Pi())/([5]),[6])) + \
    TMath::Exp(-TMath::Log(2) *\
    pow(2*abs(x-3.*TMath::Pi())/([5]),[6]))) +\
    [7]",-PI/2,3.0*PI/2);



  //name parameters
  fit->SetParName(0,"Y_NS_1");
  fit->SetParName(1,"Sigma_1_NS");
  fit->SetParName(2,"Y_NS_2");
  // NOTE: sigma_2_NS is the difference between sigma_2 and sigma_1
  fit->SetParName(3,"Sigma_2_NS");
  fit->SetParName(4,"Y_AS");
  fit->SetParName(5,"Omega_AS");
  fit->SetParName(6,"Beta_AS");
  fit->SetParName(7,"B");
```

```
/**
 * 2 Gaus for near side, 2 Gaus for Awayside
 */
TF1 * phiCorrFit_2Gaus_2Gaus(TH1D * hist, std::string name)
{
  TF1 * fit = new TF1(name.c_str(),"[0]*(TMath::Gaus(x,-2*TMath::Pi(),[1],1) + \
  TMath::Gaus(x,0,[1],1) +\
  TMath::Gaus(x,2*TMath::Pi(),[1],1)) +\
  [2]*(TMath::Gaus(x,-2*TMath::Pi(),[1]+[3],1) +\
  TMath::Gaus(x,0,[1]+[3],1) +\
  TMath::Gaus(x,2*TMath::Pi(),[1]+[3],1)) + \
  [4] * (TMath::Gaus(x,-TMath::Pi(),[5],1) +\
  TMath::Gaus(x,TMath::Pi(),[5],1) +\
  TMath::Gaus(x,3.*TMath::Pi(),[5],1)) +\
  [4]*[6]*(TMath::Gaus(x,-TMath::Pi(),[5]+[7],1) +\
  TMath::Gaus(x,TMath::Pi(),[5]+[7],1) +\
  TMath::Gaus(x,3*TMath::Pi(),[5]+[7],1))+\
  [8]",-PI/2,3.0*PI/2);

  //name parameters
  fit->SetParName(0,"Y_NS_1");
  fit->SetParName(1,"Sigma_1_NS");
  fit->SetParName(2,"Y_NS_2");
  // NOTE: sigma_2_NS is the difference between sigma_2 and sigma_1
  fit->SetParName(3,"Sigma_2_NS");

  fit->SetParName(4,"Y_AS_1");
  fit->SetParName(5,"Sigma_1_AS");

  fit->SetParName(6,"Y_AS_2");
  // NOTE: sigma_2_NS is the difference between sigma_2 and sigma_1
  fit->SetParName(7,"Sigma_2_AS");
```

```
  fit->SetParName(8,"B");
```

```
/**
 * Same method as above, but with the FWHM as a parameter instead of sigma
 */
TF1 * phiCorrFit_2Gaus_2Gaus_Fwhm(TH1D * hist, std::string name)
{
   TF1 * fit = new TF1(name.c_str(),"[0]*(TMath::Gaus(x,\
   -2*TMath::Pi(),[1],1) + \
   TMath::Gaus(x,0,[1],1) + TMath::Gaus(x,2*TMath::Pi(),[1],1)) +\
   [2]*(TMath::Gaus(x,-2*TMath::Pi(),[1]+[3],1) +\
   TMath::Gaus(x,0,[1]+[3],1) +\
   TMath::Gaus(x,2*TMath::Pi(),[1]+[3],1)) + \
   [4] * (2.* [6] * pow(TMath::Log(2),1./[6]))/\
   ([5]*TMath::Gamma(1./[6])) * (TMath::Exp(-TMath::Log(2) *\
   pow(2*abs(x-TMath::Pi())/([5]),[6])) + TMath::Exp(-TMath::Log(2) *\
   pow(2*abs(x+TMath::Pi())/([5]),[6])) +  TMath::Exp(-TMath::Log(2) *\
   pow(2*abs(x-3.*TMath::Pi())/([5]),[6]))) + [7]",-PI/2,3.0*PI/2);

  //name parameters
  fit->SetParName(0,"Y_NS_1");
  fit->SetParName(1,"Sigma_1_NS");
  fit->SetParName(2,"Y_NS_2");
  // NOTE: sigma_2_NS is the difference between sigma_2 and sigma_1
  fit->SetParName(3,"Sigma_2_NS");
  fit->SetParName(4,"Y_AS");
  fit->SetParName(5,"Omega_AS");
  fit->SetParName(6,"Beta_AS");
  fit->SetParName(7,"B");

  fit->SetParName(8,"R");
  fit->FixParameter(8,R);
```

```
/*  1 Generalized Gaussian for each peak
 *
 */

TF1 * phiCorrFit_1GenGaus_1GenGaus(TH1D * hist, std::string name)
{
  TF1 * fit = new TF1(name.c_str(),"[0] * (2.*[2] * pow(TMath::Gamma(3./[2]),0.5))/\
  (2.*[1]*pow(TMath::Gamma(1./[2]),1.5)) *\
  (TMath::Exp(-pow(abs(x+2.*TMath::Pi())/([1]*pow(TMath::Gamma(1./[2])/\
  TMath::Gamma(3./[2]),0.5)),[2])) + TMath::Exp(-pow(abs(x)/([1]*\
  pow(TMath::Gamma(1./[2])/TMath::Gamma(3./[2]),0.5)),[2])) +\
  TMath::Exp(-pow(abs(x-2.*TMath::Pi())/([1]*pow(TMath::Gamma(1./[2])/\
  TMath::Gamma(3./[2]),0.5)),[2]))) + [3] * (2.*[5] *\
  pow(TMath::Gamma(3./[5]),0.5))/ (2.*[4]*pow(TMath::Gamma(1./[5]),1.5)) *\
  (TMath::Exp(-pow(abs(x-TMath::Pi())/([4]*pow(TMath::Gamma(1./[5])/\
  TMath::Gamma(3./[5]),0.5)),[5])) + TMath::Exp(-pow(abs(x+TMath::Pi())/\
  ([4]*pow(TMath::Gamma(1./[5])/\
  TMath::Gamma(3./[5]),0.5)),[5])) +TMath::Exp(-pow(abs(x-3*TMath::Pi())/\
  ([4]*pow(TMath::Gamma(1./[5])/\
  TMath::Gamma(3./[5]),0.5)),[5]))  ) + [6]",-PI/2,3.0*PI/2);

  //name parameters
  fit->SetParName(0,"Y_NS");
  fit->SetParName(1,"Sigma_NS");
  fit->SetParName(2,"Beta_NS");

```

```
  fit->SetParName(3,"Y_AS");
  fit->SetParName(4,"Sigma_AS");
  fit->SetParName(5,"Beta_AS");
  fit->SetParName(6,"B");
```

```
/**
 * Same method as above, but with the FWHM as a parameter instead of sigma
 *
 */
TF1 * phiCorrFit_1GenGaus_1GenGaus_Fwhm(TH1D * hist, std::string name)
{
  TF1 * fit = new TF1(name.c_str(),"[0] * (2.*[2] * pow(TMath::Gamma(3./[2]),0.5))/\
  (2.*[1]*pow(TMath::Gamma(1./[2]),1.5)) *\
  (TMath::Exp(-pow(abs(x+2.*TMath::Pi())/\
  ([1]*pow(TMath::Gamma(1./[2])/TMath::Gamma(3./[2]),0.5)),[2])) +\
  TMath::Exp(-pow(abs(x)/([1]*pow(TMath::Gamma(1./[2])/TMath::Gamma(3./[2]),0.5)),[2]))\
  +TMath::Exp(-pow(abs(x-2.*TMath::Pi())/\
  ([1]*pow(TMath::Gamma(1./[2])/TMath::Gamma(3./[2]),0.5)),[2]))) + [3] * (2.* [5] *\
  pow(TMath::Log(2),1./[5]))/ ([4]*TMath::Gamma(1./[5])) *\
  (TMath::Exp(-TMath::Log(2) * pow(2*abs(x-TMath::Pi())/([4]),[5])) +\
  TMath::Exp(-TMath::Log(2) *\
  pow(2*abs(x+TMath::Pi())/([4]),[5])) +  TMath::Exp(-TMath::Log(2) *\
  pow(2*abs(x-3.*TMath::Pi())/([4]),[5]))) +\
  [6]",-PI/2,3.0*PI/2);

  //name parameters
  fit->SetParName(0,"Y_NS");
  fit->SetParName(1,"Sigma_NS");
  fit->SetParName(2,"Beta_NS");
  fit->SetParName(3,"Y_AS");
  fit->SetParName(4,"Omega_AS");
  fit->SetParName(5,"Beta_AS");
  fit->SetParName(6,"B");
```

```
  /**
  * 2 Gaussians for Nearside, 1 Modified Gaussian for awayside
  * G(X) = A(1+(1/(2n))((x/sigma)/2)^2)^(-n)
  * see https://arxiv.org/pdf/1509.04732v2.pdf
  * is that link right? https://arxiv.org/pdf/0904.1733.pdf
  * Standard deviation sigma as width parameter
  */
TF1 * phiCorrFit_2Gaus_1ModGaus(TH1D * hist, std::string name)
{

  TString functionString = "[0]*(TMath::Gaus(x,-2*TMath::Pi(),[1],1) +\
  TMath::Gaus(x,0,[1],1) + TMath::Gaus(x,2*TMath::Pi(),[1],1)) +\
  [2]*(TMath::Gaus(x,-2*TMath::Pi(),[1]+[3],1) + TMath::Gaus(x,0,[1]+[3],1) +\
  TMath::Gaus(x,2*TMath::Pi(),[1]+[3],1))";
  functionString += "+ [4] * (1. / ([5] *TMath::Sqrt(2 * TMath::Pi() * [6]))) *\
  (TMath::Gamma([6])/TMath::Gamma([6]-0.5)) * (TMath::Power(1 +\
  TMath::Power((x+TMath::Pi())/[5],2)/(2*[6]),-[6]) + TMath::Power(1 +\
  TMath::Power((x-TMath::Pi())/[5],2)/(2*[6]),-[6])";
  functionString += " + TMath::Power(1 +\
  TMath::Power((x-3*TMath::Pi())/[5],2)/(2*[6]),-[6])) + [7]";


  TF1 * fit = new TF1(name.c_str(),functionString,-PI/2,3.0*PI/2);


```

```
  //name parameters
  fit->SetParName(0,"Y_NS_1");
  fit->SetParName(1,"Sigma_1_NS");
  fit->SetParName(2,"Y_NS_2");
  // NOTE: sigma_2_NS is the difference between sigma_2 and sigma_1
  fit->SetParName(3,"Sigma_2_NS");
  fit->SetParName(4,"Y_AS");
  fit->SetParName(5,"Sigma_AS");
  fit->SetParName(6,"Beta_AS");
  fit->SetParName(7,"B");
```

```
/**
  * 2 Gaussians for Nearside, 1 Modified Gaussian for awayside
  * G(X) = A(1+(1/(2n))((x/sigma)/2)^2)^(-n)
  * see https://arxiv.org/pdf/1509.04732v2.pdf
  * FWHM omega as width parameter
  */
TF1 * phiCorrFit_2Gaus_1ModGaus_Fwhm(TH1D * hist, std::string name)
{
  TString functionString = "[0]*(TMath::Gaus(x,-2*TMath::Pi(),[1],1) +\
  TMath::Gaus(x,0,[1],1) + TMath::Gaus(x,2*TMath::Pi(),[1],1)) +\
  [2]*(TMath::Gaus(x,-2*TMath::Pi(),[1]+[3],1) + TMath::Gaus(x,0,[1]+[3],1) +\
  TMath::Gaus(x,2*TMath::Pi(),[1]+[3],1))";
  functionString += "+ [4] * (2*TMath::Sqrt(TMath::Power(2,1/[6])-1)/\
  (TMath::Sqrt(TMath::Pi())*[5]))\
  *(TMath::Gamma([6])/TMath::Gamma([6]-0.5)) * (TMath::Power(1 +\
  (TMath::Power(2,1/[6])-1)*TMath::Power(2*(x+TMath::Pi())/[5],2)/(2*[6]),-[6])\
  + TMath::Power(1 +\
  (TMath::Power(2,1/[6])-1)*TMath::Power(2*(x-TMath::Pi())/[5],2)/(2*[6]),-[6])";
  functionString += " + TMath::Power(1 + (TMath::Power(2,1/[6])-1)*\
  TMath::Power(2*(x-3*TMath::Pi())/[5],2)/(2*[6]),-[6])) + [7]";


  TF1 * fit = new TF1(name.c_str(),functionString,-PI/2,3.0*PI/2);


  //name parameters
  fit->SetParName(0,"Y_NS_1");
  fit->SetParName(1,"Sigma_1_NS");
  fit->SetParName(2,"Y_NS_2");
  // NOTE: sigma_2_NS is the difference between sigma_2 and sigma_1
  fit->SetParName(3,"Sigma_2_NS");
  fit->SetParName(4,"Y_AS");
  fit->SetParName(5,"Omega_AS");
 // fit->SetParName(6,"N_AS");
  fit->SetParName(6,"Beta_AS");
  fit->SetParName(7,"B");
```

```
/**
  * 1 Modified Gaussian for nearside, 1 Modified Gaussian for awayside
  * G(X) = A(1+(1/(2n))((x/sigma)/2)^2)^(-n)
  * see https://arxiv.org/pdf/1509.04732v2.pdf
  */
TF1 * phiCorrFit_1ModGaus_1ModGaus(TH1D * hist, std::string name)
{
  //TString functionString = "[0]*(TMath::Gaus(x,-2*TMath::Pi(),[1],1) +\
  TMath::Gaus(x,0,[1],1) + TMath::Gaus(x,2*TMath::Pi(),[1],1)) +\
  [2]*(TMath::Gaus(x,-2*TMath::Pi(),[1]+[3],1) + TMath::Gaus(x,0,[1]+[3],1) +\
  TMath::Gaus(x,2*TMath::Pi(),[1]+[3],1))";
```

```
  TString functionString = "[0] * (TMath::Gamma([2])/(TMath::Sqrt(2*TMath::Pi()*\
  ([2]-1.5))*[1]*TMath::Gamma([2]-0.5))) *(TMath::Power(1 +\
  TMath::Power((x+2.*TMath::Pi())/[1],2)/(2*([2]-1.5)),-[2]) + \
  TMath::Power(1 + TMath::Power((x)/[1],2)/(2*([2]-1.5)),-[2])";
  functionString += " + TMath::Power(1 + TMath::Power((x-2*TMath::Pi())/[1],2)/\
  (2*([2]-1.5)),-[2]))";
  functionString += "+ [3] *  (TMath::Gamma([2])/\
  (TMath::Sqrt(2*TMath::Pi()*([5]-1.5))*[4]*TMath::Gamma([5]-0.5))) *\
  (TMath::Power(1 + TMath::Power((x+TMath::Pi())/[4],2)/(2*([5]-1.5)),-[5]) + \
  TMath::Power(1 + TMath::Power((x-TMath::Pi())/[4],2)/(2*([5]-1.5)),-[5])";
  functionString += " + \
  TMath::Power(1 + TMath::Power((x-3*TMath::Pi())/[4],2)/(2*([5]-1.5)),-[5])) + [6]";

  TF1 * fit = new TF1(name.c_str(),functionString,-PI/2,3.0*PI/2);

  //name parameters
  fit->SetParName(0,"Y_NS");
  fit->SetParName(1,"Sigma_NS");
  fit->SetParName(2,"Beta_NS");
//  fit->SetParName(3,"Sigma_2_NS");
  fit->SetParName(3,"Y_AS");
  fit->SetParName(4,"Sigma_AS");
  fit->SetParName(5,"Beta_AS");
  fit->SetParName(6,"B");
```

```
/**
  * 1 Modified Gaussian for nearside, 1 Modified Gaussian for awayside
  * G(X) = A(1+(1/(2n))((x/sigma)/2)^2)^(-n)
  * see https://arxiv.org/pdf/1509.04732v2.pdf
  * FWHM as width parameter
  */

TF1 * phiCorrFit_1ModGaus_1ModGaus_Fwhm(TH1D * hist, std::string name)
{

  TString functionString = "[0] * (2*TMath::Sqrt(TMath::Power(2,1/[2])-1)/\
  (TMath::Sqrt(TMath::Pi())*[1])) * (TMath::Gamma([2])/TMath::Gamma([2]-0.5)) *\
  (TMath::Power(1 + (TMath::Power(2,1/[2])-1)*\
  TMath::Power(2*(x+2*TMath::Pi())/[1],2)/(2*[2]),\
  -[2]) + TMath::Power(1 + (TMath::Power(2,1/[2])-1)*\
  TMath::Power(2*(x)/[1],2)/(2*[2]),-[2])";
  functionString += " + TMath::Power(1 + (TMath::Power(2,1/[2])-1)*\
  TMath::Power(2*(x-2*TMath::Pi())/[1],2)/(2*[2]),-[2])) ";

  functionString += "+ [3] * (2*TMath::Sqrt(TMath::Power(2,1/[5])-1)/\
  (TMath::Sqrt(TMath::Pi())*[4])) * (TMath::Gamma([5])/TMath::Gamma([5]-0.5)) *\
  (TMath::Power(1 + (TMath::Power(2,1/[5])-1)*\
  TMath::Power(2*(x+TMath::Pi())/[4],2)/(2*[5]),-[5]) +\
  TMath::Power(1 + (TMath::Power(2,1/[5])-1)*\
  TMath::Power(2*(x-TMath::Pi())/[4],2)/(2*[5]),-[5])";
  functionString += " + TMath::Power(1 + (TMath::Power(2,1/[5])-1)*\
  TMath::Power(2*(x-3*TMath::Pi())/[4],2)/(2*[5]),-[5])) + [6]";

  TF1 * fit = new TF1(name.c_str(),functionString,-PI/2,3.0*PI/2);


  //name parameters
  fit->SetParName(0,"Y_NS");
  fit->SetParName(1,"Omega_NS");
  fit->SetParName(2,"Beta_NS");
```

```
36    fit->SetParName(3,"Y_AS");
37    fit->SetParName(4,"Omega_AS");
38    fit->SetParName(5,"Beta_AS");
39    fit->SetParName(6,"B");
```

Appendix D

π^0-identification plots

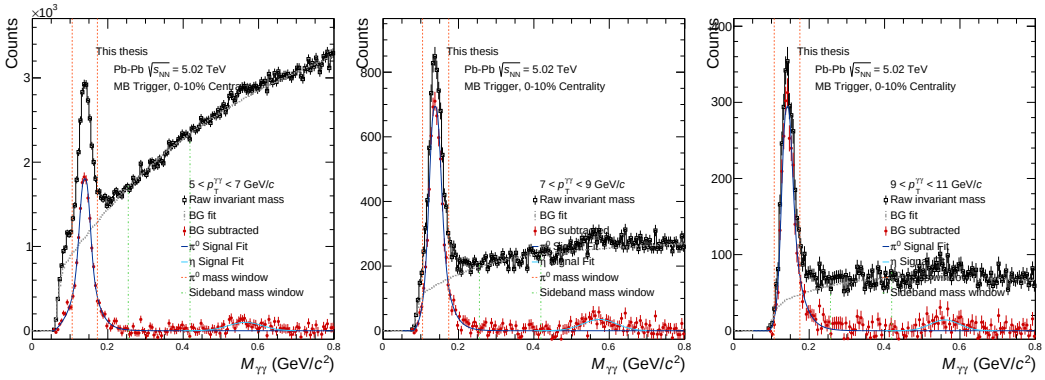

Figure D.1: Invariant Mass for the PbPb 15o Minimum Bias, Central 0-10% data set.

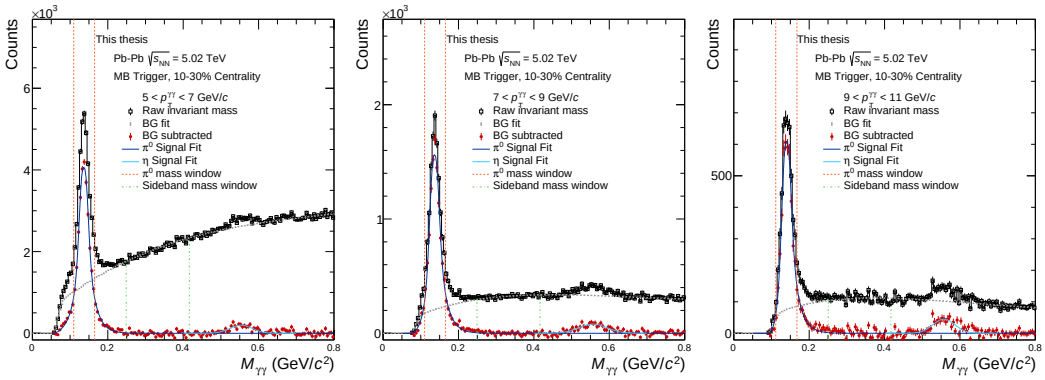

Figure D.2: Invariant Mass for the PbPb 15o Minimum Bias, Central 10-30% data set.

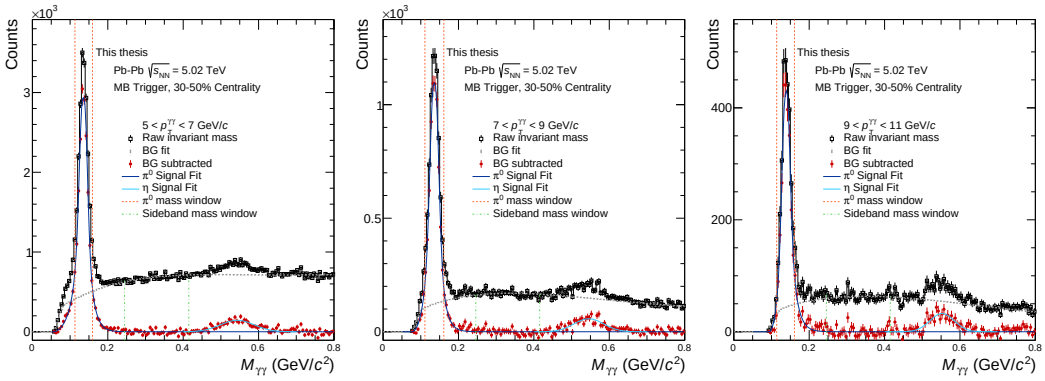

Figure D.3: Invariant Mass for the p_{T} ranges 5-7,7-9, and 9-11 GeV/c for the PbPb 15o Minimum Bias, Central 30-50% data set.

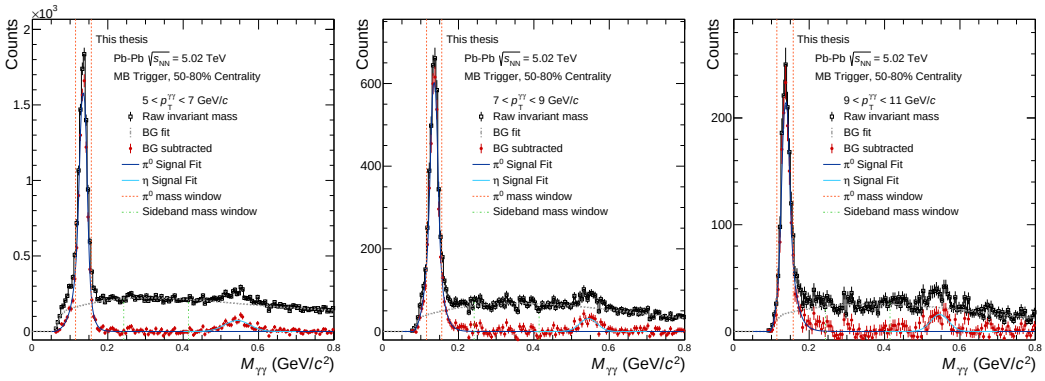

Figure D.4: Invariant Mass for the PbPb 15o Minimum Bias, Central 50-80% data set.

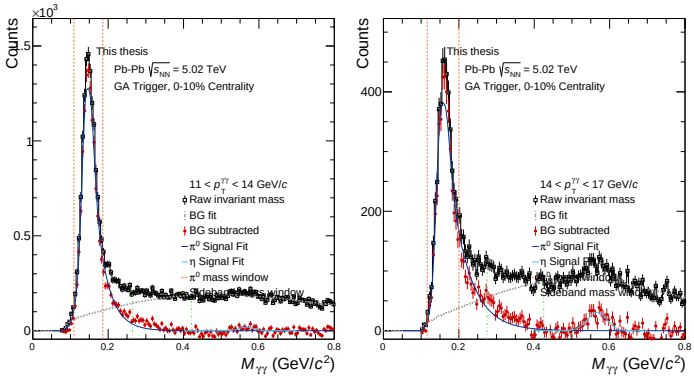

Figure D.5: Invariant Mass for the PbPb 15o EGA triggered event, Central 0-10% data set.

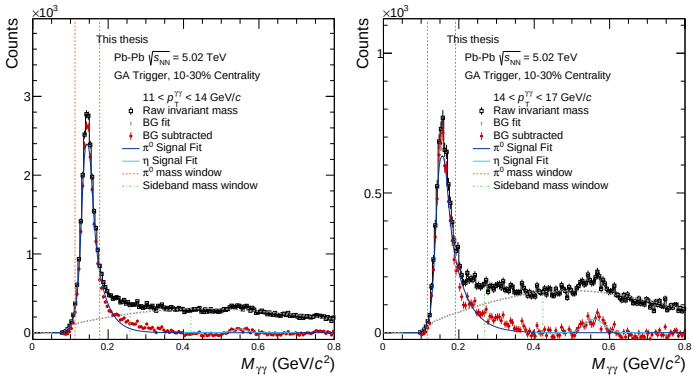

Figure D.6: Invariant Mass for the PbPb 15o EGA triggered event, Central 10-30% data set.

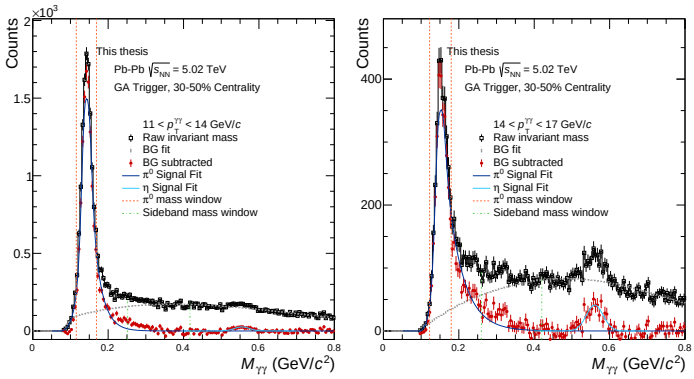

Figure D.7: Invariant Mass for the p_{T} ranges 11-14,14-17 GeV/c for the PbPb 15o EGA triggered event, Central 30-50% data set.

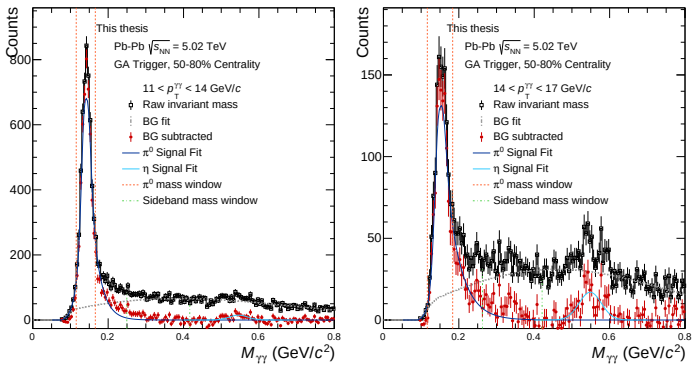

Figure D.8: Invariant Mass for the PbPb 15o EGA triggered event, Central 50-80% data set.

Appendix E

π^0-hadron Plots

E.1 Raw Correlations

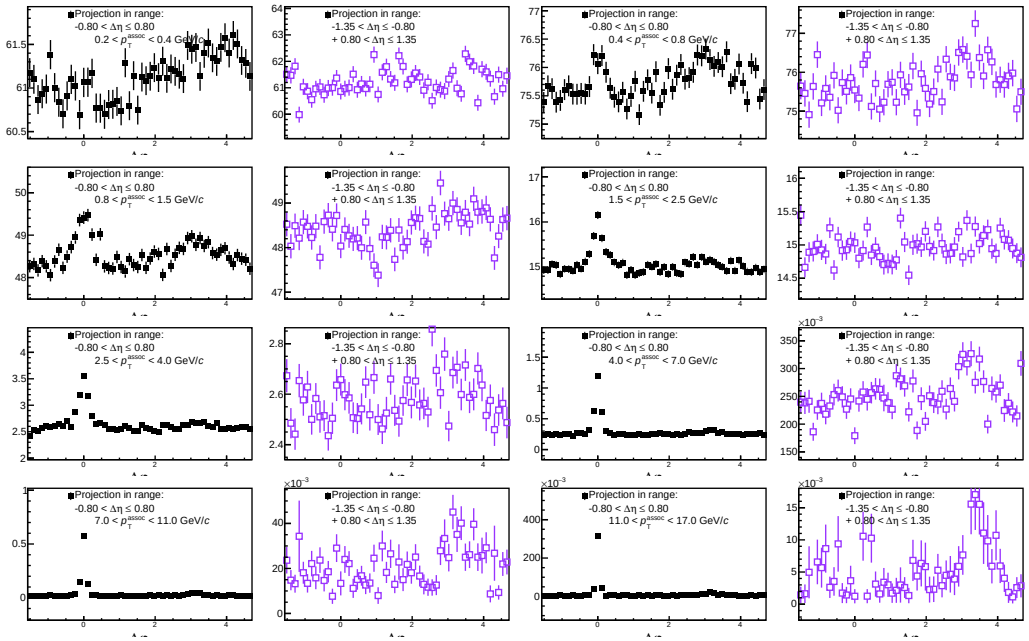

Figure E.1: Raw π^0-hadron correlations for trigger range 11-14 GeV/c, all-Angles, 0-10% Cent., EGA-trigger

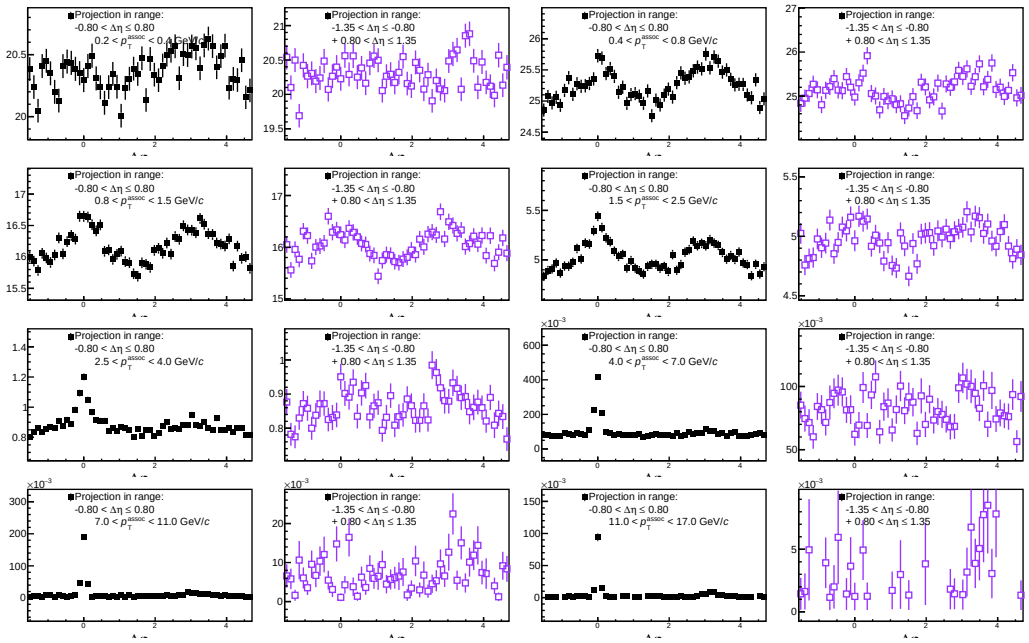

Figure E.2: Raw π^0-hadron correlations for trigger range 11-14 GeV/c, in-plane, 0-10% Cent., EGA-trigger

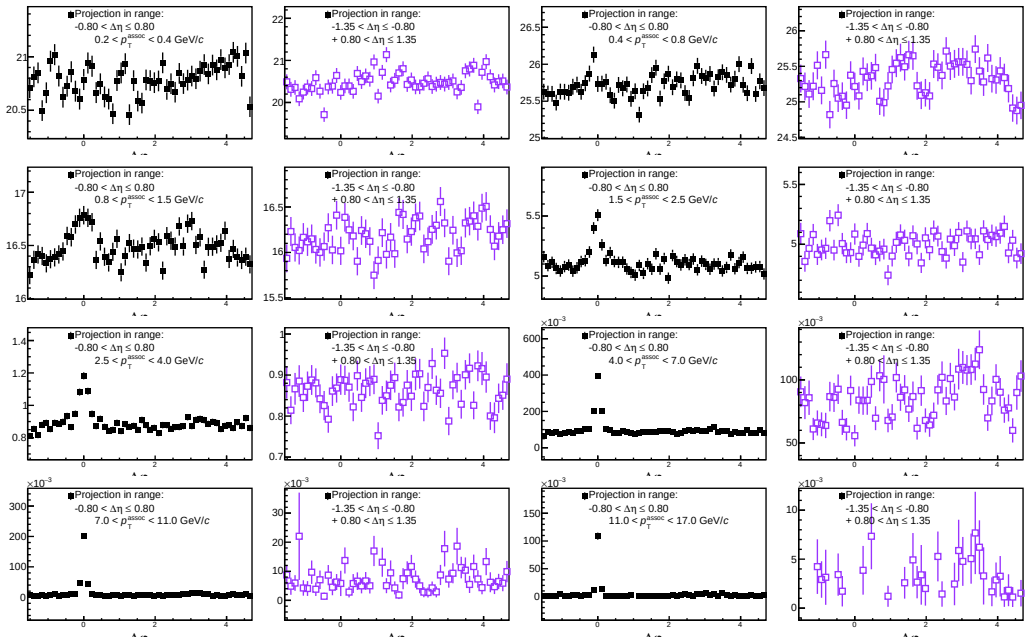

Figure E.3: Raw π^0-hadron correlations for trigger range 11-14 GeV/c, mid-plane, 0-10% Cent., EGA-trigger

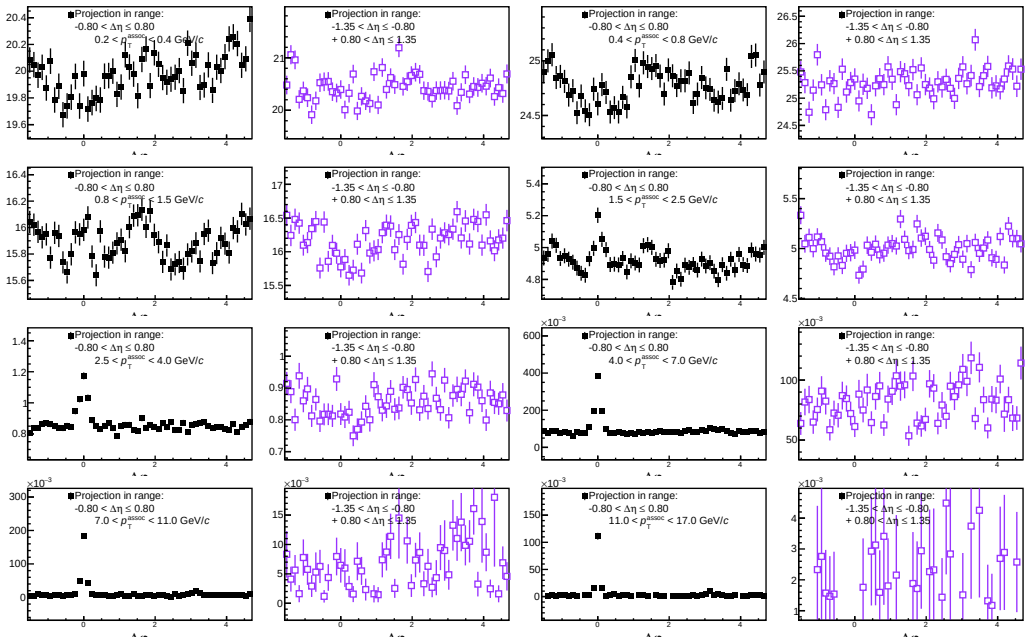

Figure E.4: Raw π^0-hadron correlations for trigger range 11-14 GeV/c, out-of-plane, 0-10% Cent., EGA-trigger

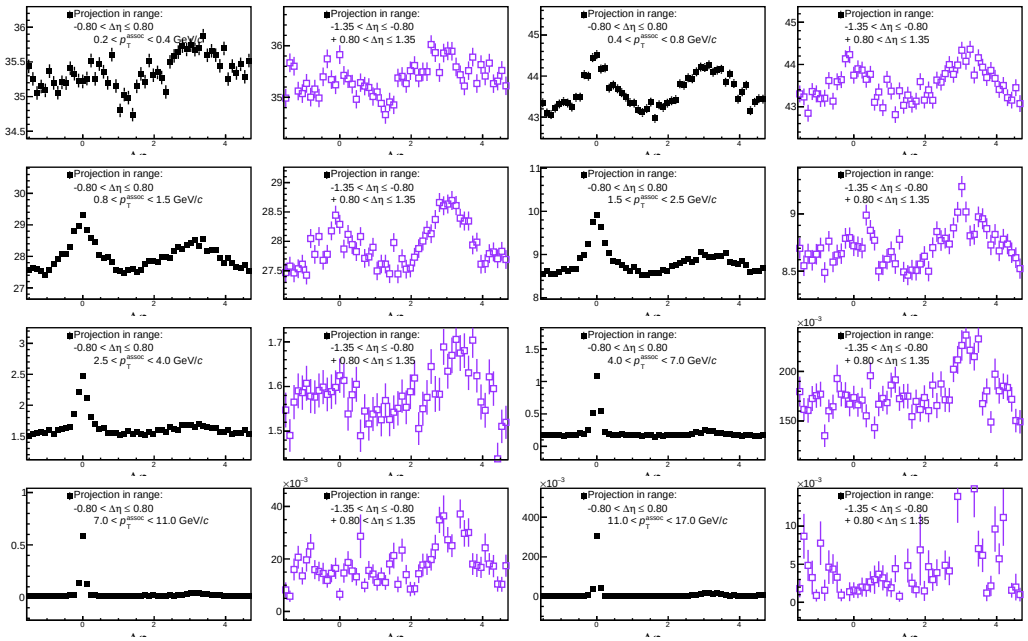

Figure E.5: Raw π^0-hadron correlations for trigger range 11-14 GeV/c, all-angles, 10-30% Cent., EGA-trigger

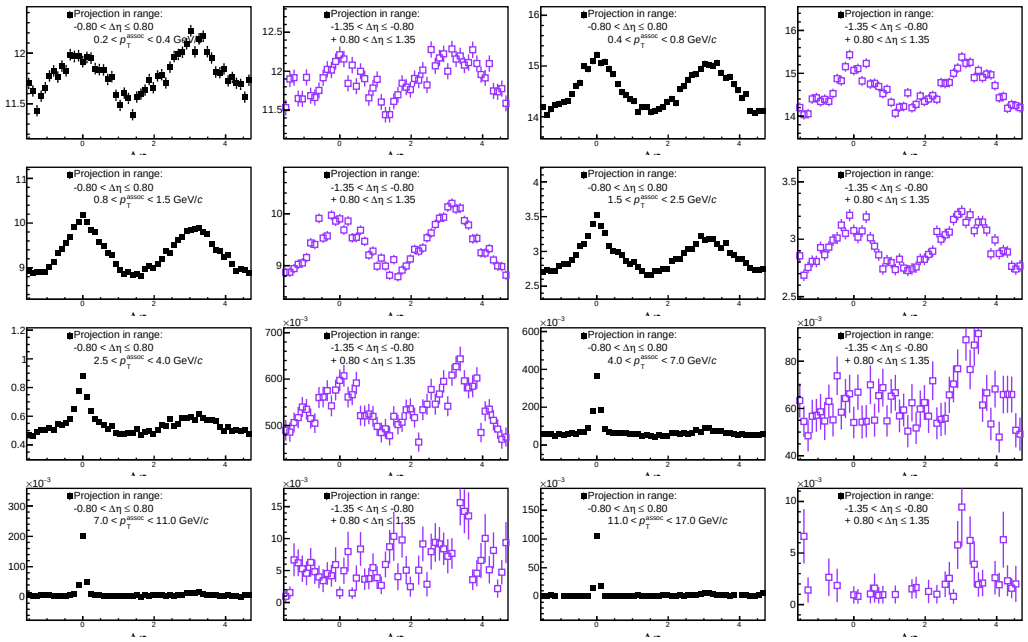

Figure E.6: Raw π^0-hadron correlations for trigger range 11-14 GeV/c, in-plane, 10-30% Cent., EGA-trigger

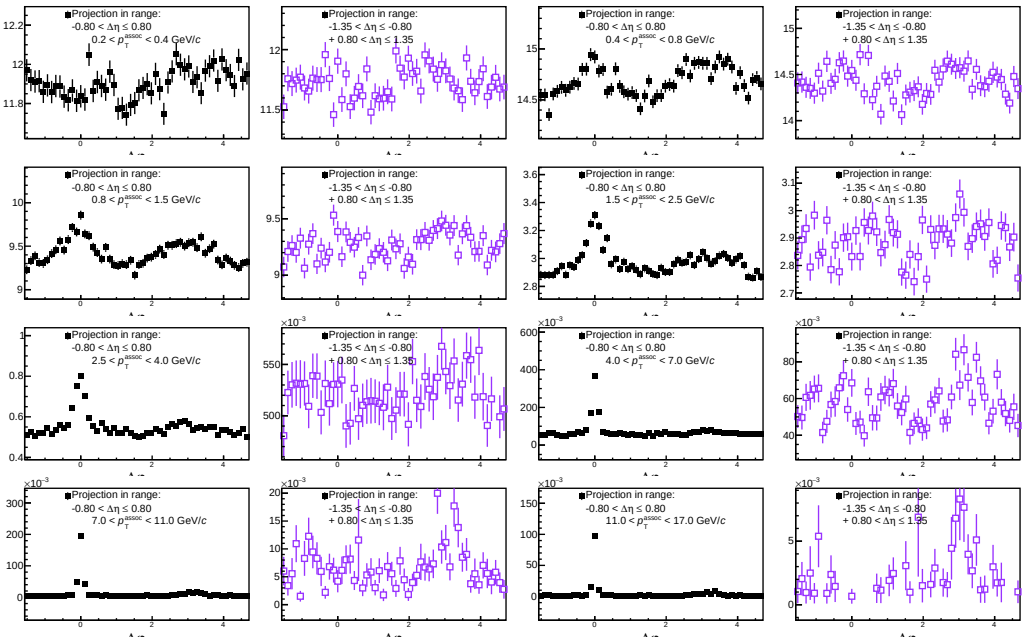

Figure E.7: Raw π^0-hadron correlations for trigger range 11-14 GeV/c, mid-plane, 10-30% Cent., EGA-trigger

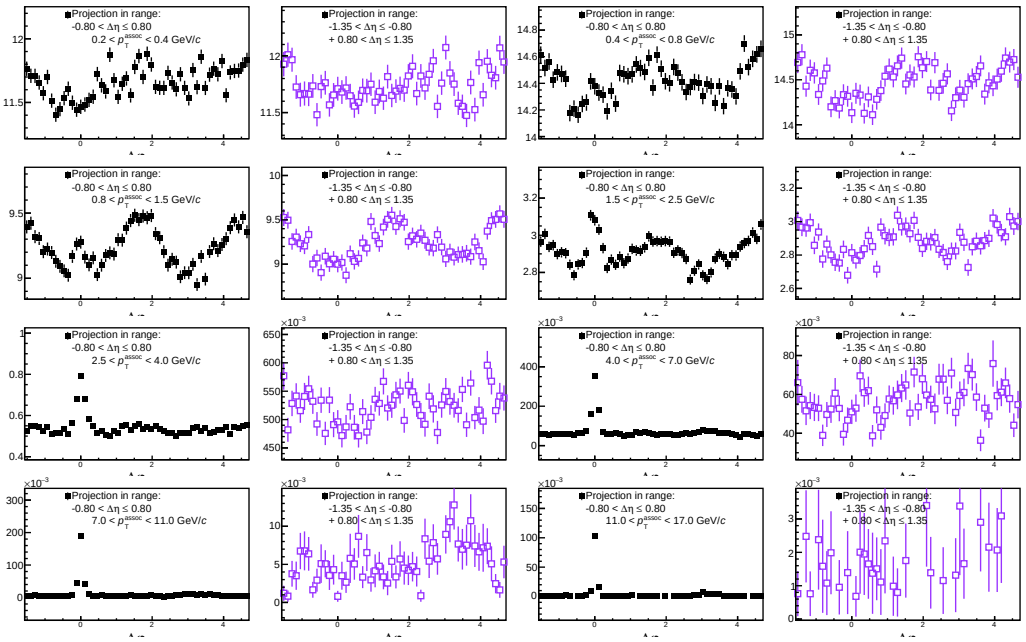

Figure E.8: Raw π^0-hadron correlations for trigger range 11-14 GeV/c, out-of-plane, 10-30% Cent., EGA-trigger

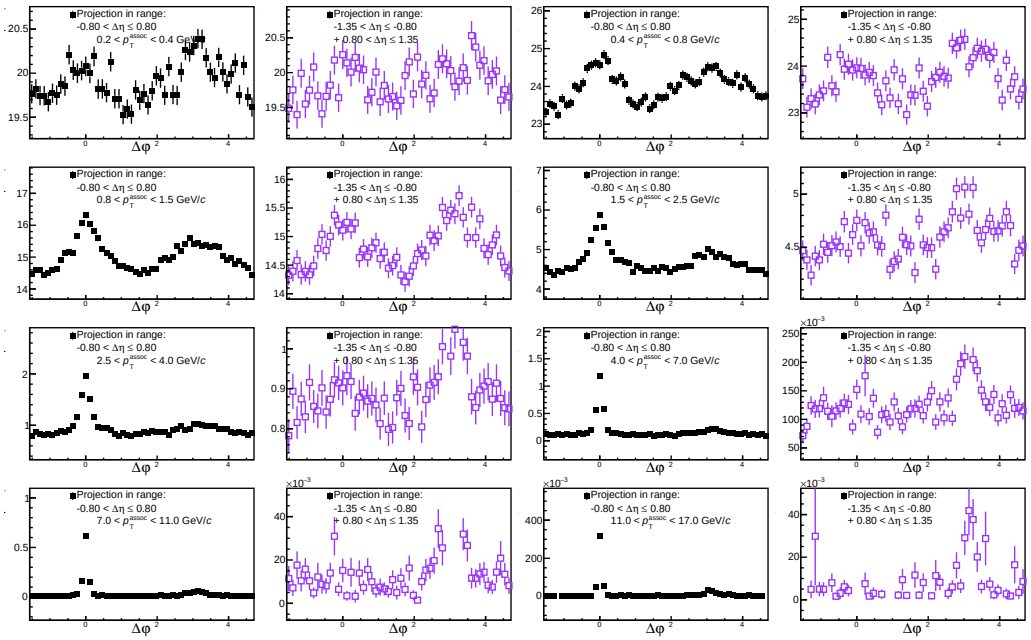

Figure E.9: Raw π^0-hadron correlations for trigger range 11-14 GeV/c, all-angles, 30-50% Cent., EGA-trigger

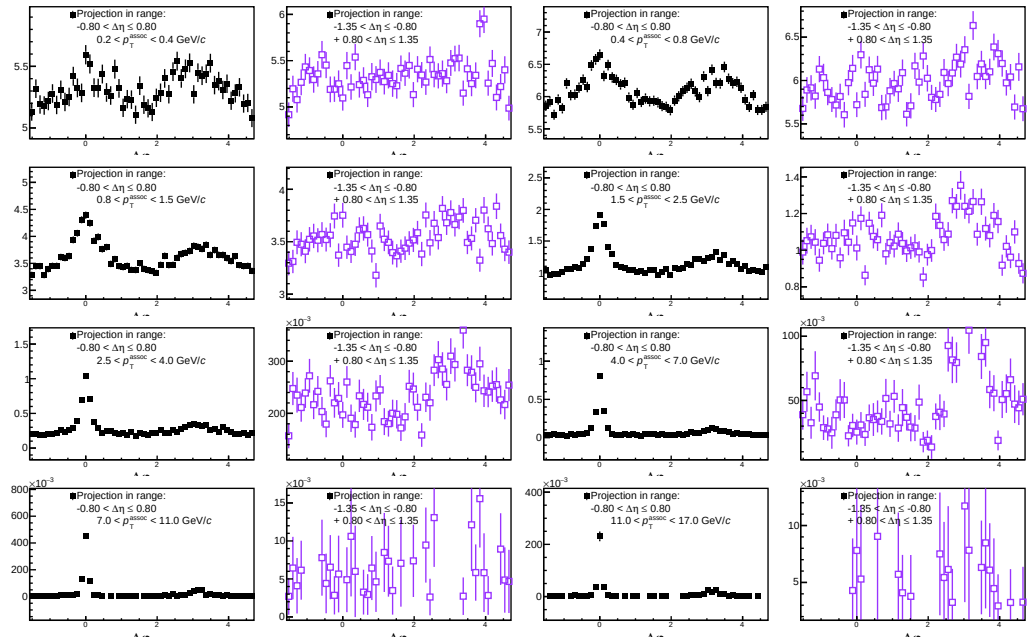

Figure E.10: Raw π^0-hadron correlations for trigger range 11-14 GeV/c, all-angles, 50-90% Cent., EGA-trigger

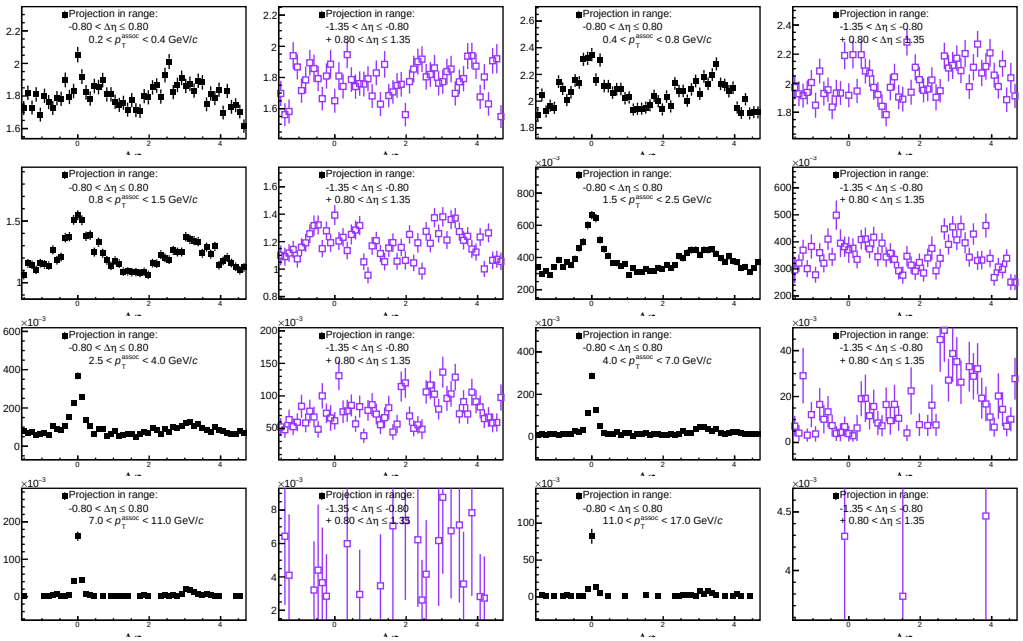

Figure E.11: Raw π^0-hadron correlations for trigger range 11-14 GeV/c, in-plane, 50-90% Cent., EGA-trigger

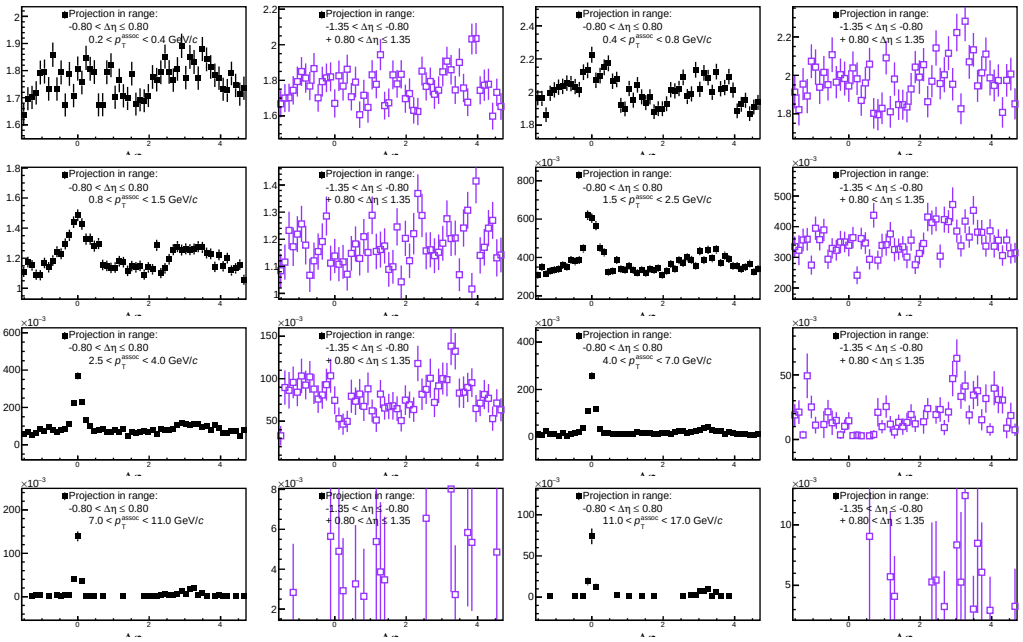

Figure E.12: Raw π^0-hadron correlations for trigger range 11-14 GeV/c, mid-plane, 50-90% Cent., EGA-trigger

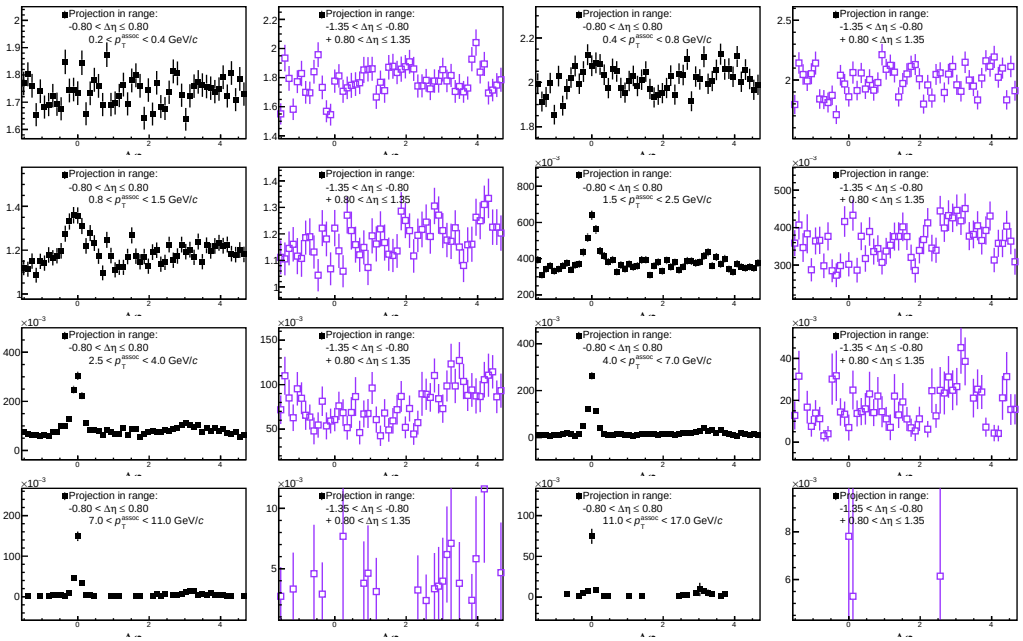

Figure E.13: Raw π^0-hadron correlations for trigger range 11-14 GeV/c, out-of-plane, 50-90% Cent., EGA-trigger

Appendix F

π^0 Impurity Correction Plots

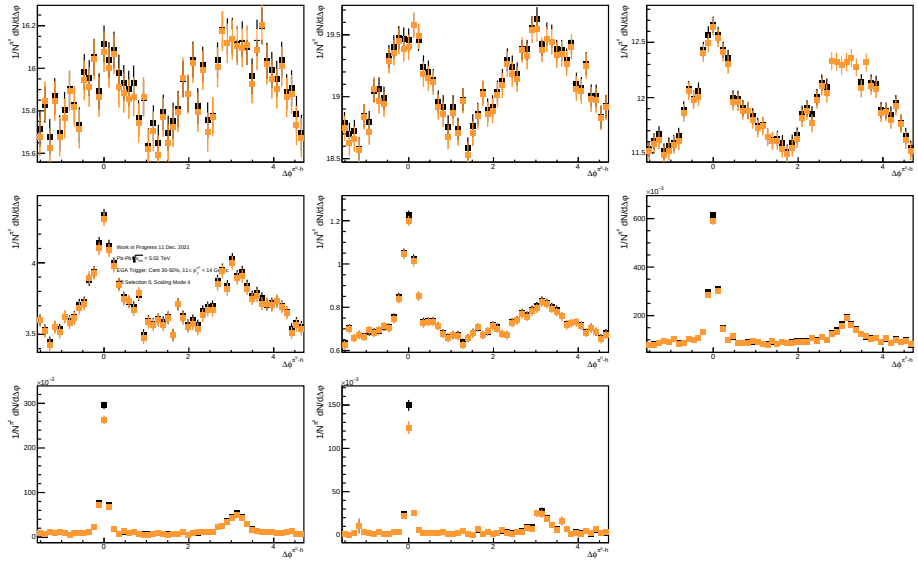

Figure F.1: Sideband subtraction in $\Delta\varphi$ with for π^0 in the p_{T} range 11-14 GeV/c. 30-50% centrality EGA-triggered events. From left to right and top to bottom, the plots increase in associated hadron p_{T}.

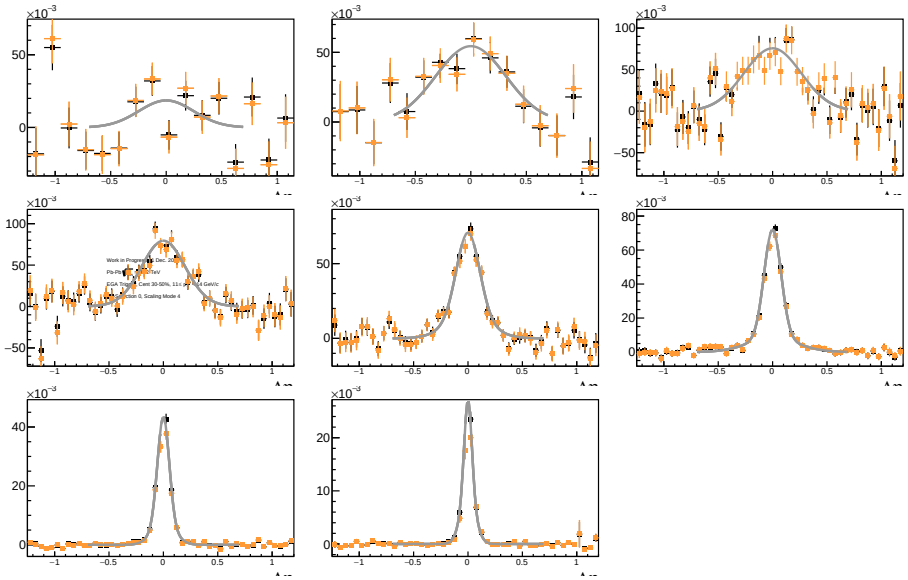

Figure F.2: Sideband subtraction in $\Delta\eta$ with for π^0 in the p_{T} range 11-14 GeV/c. 30-50% centrality EGA-triggered events. From left to right and top to bottom, the plots increase in associated hadron p_{T}.

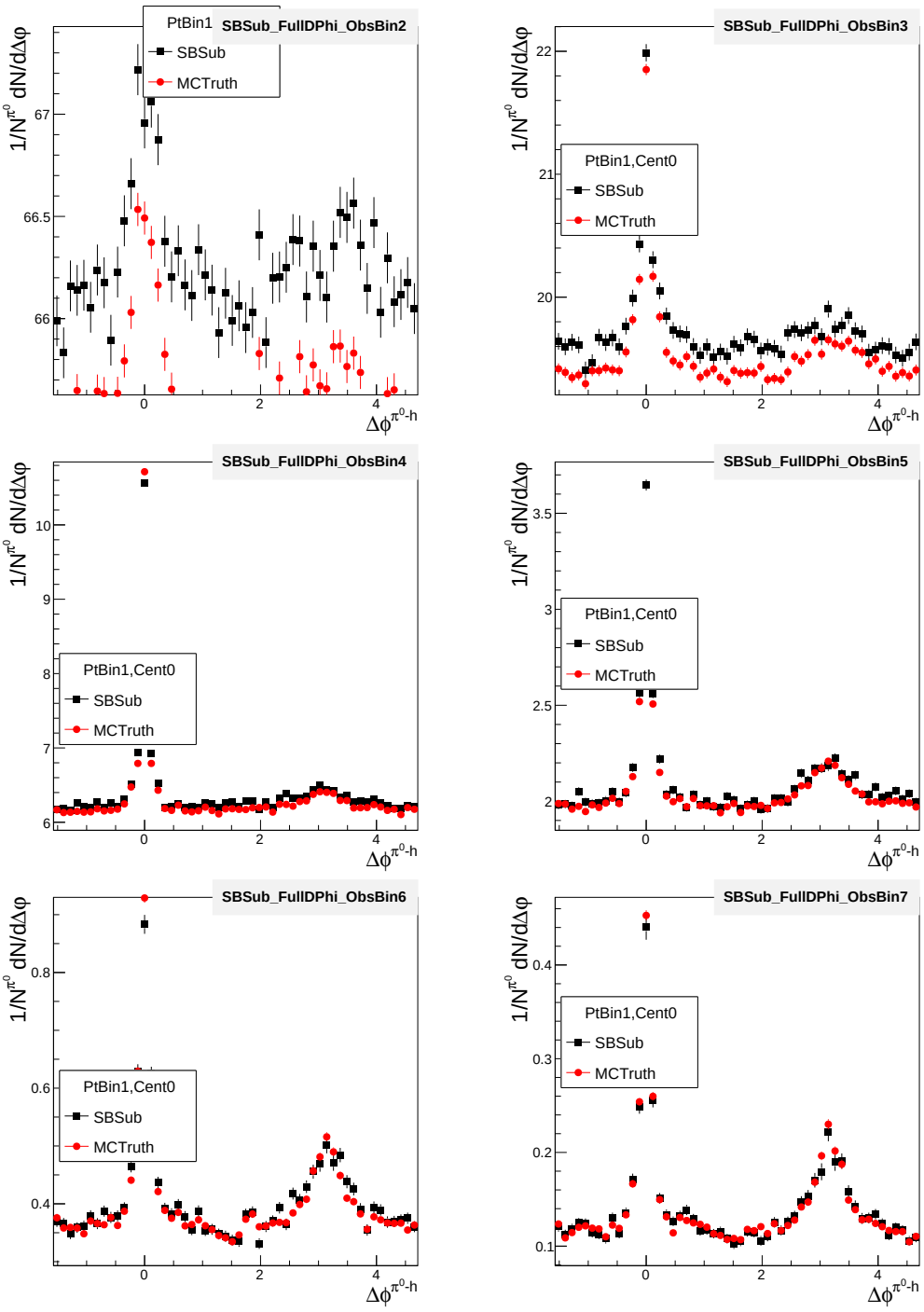

Figure F.3: Comparison of sideband-subtracted correlations in MC with the MC true π^0-hadron correlations. This is using extrapolation function 4, with all three sidebands. These correlations for triggers in the p_{T} range 11-14 GeV/c.

Appendix G

Flow Correction Plots

Plots of the χ^2/NDF and parameters used in the final version of the RPF used in this analysis are provided in plots

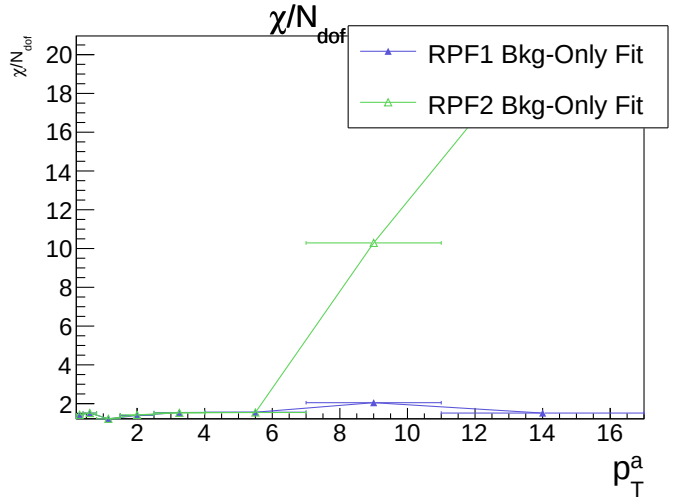

Figure G.1: χ^2/NDF for the Reaction Plane fit for π^0 triggers in the $11 - 14\mathrm{GeV}/c p_{\mathrm{T}}$ range, 30-50% centralEGA-triggered events.

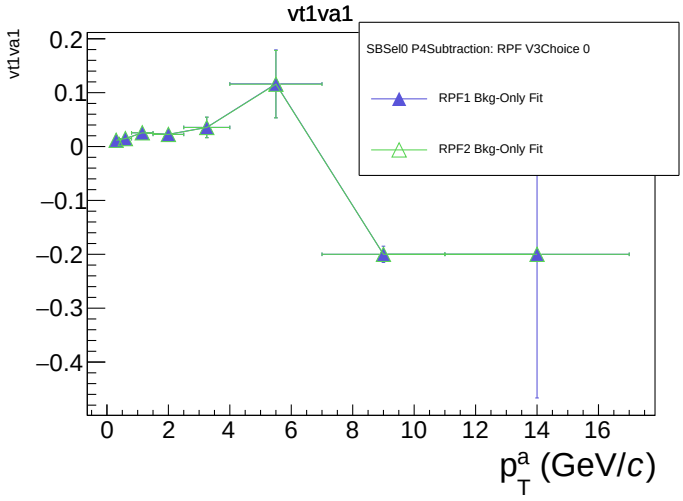

Figure G.2: $v_1^t v_1^a$ for the Reaction Plane fit for π^0 triggers in the $11 - 14\mathrm{GeV}/cp_\mathrm{T}$ range, 30-50% centralEGA-triggered events.

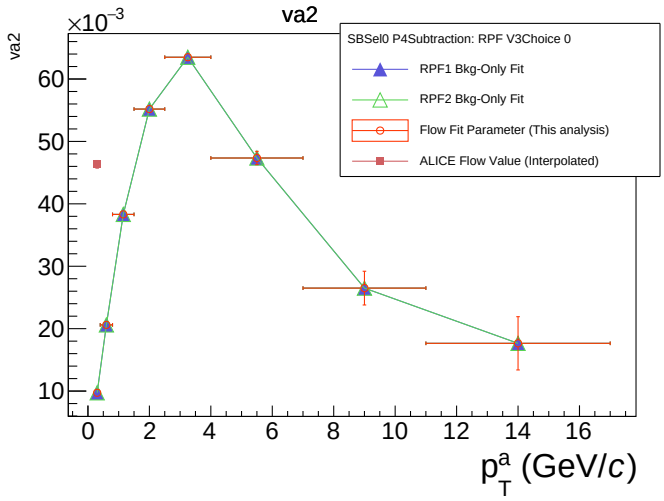

Figure G.3: v_2^a for the Reaction Plane fit for π^0 triggers in the $11 - 14\mathrm{GeV}/cp_\mathrm{T}$ range, 30-50% centralEGA-triggered events.

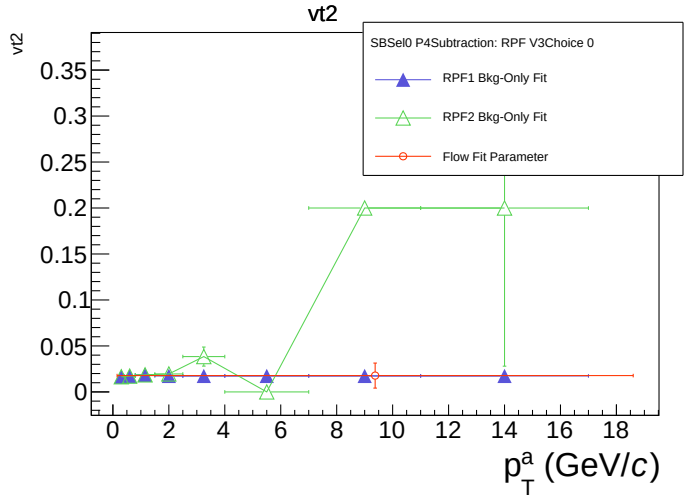

Figure G.4: v_2^a for the Reaction Plane fit for π^0 triggers in the $11 - 14\mathrm{GeV}/cp_\mathrm{T}$ range, 30-50% centralEGA-triggered events.

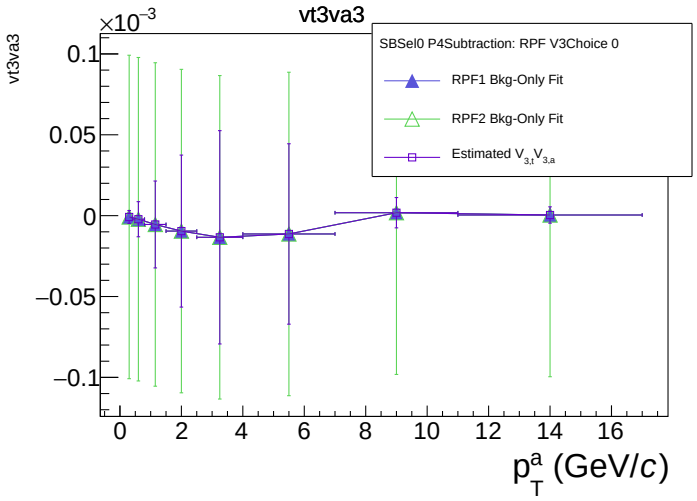

Figure G.5: $v_3^t v_3^a$ for the Reaction Plane fit for π^0 triggers in the $11 - 14\mathrm{GeV}/cp_\mathrm{T}$ range, 30-50% centralEGA-triggered events.

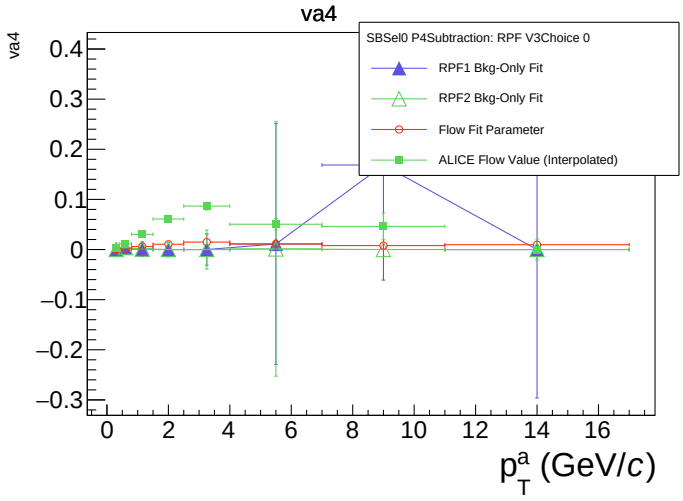

Figure G.6: v_2^a for the Reaction Plane fit for π^0 triggers in the $11 - 14\mathrm{GeV}/cp_\mathrm{T}$ range, 30-50% centralEGA-triggered events.

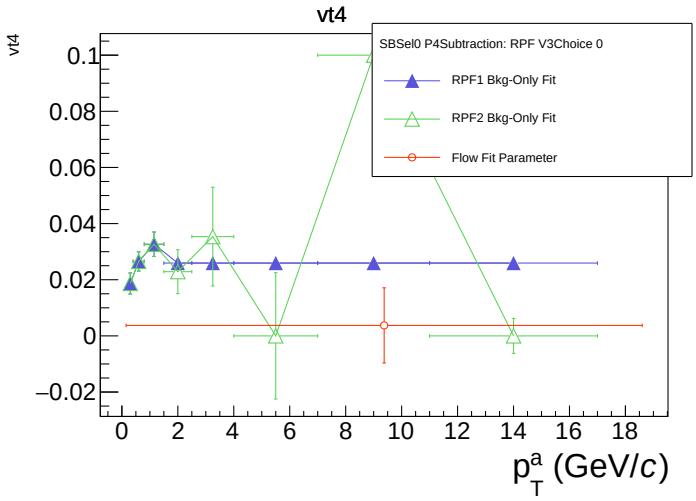

Figure G.7: v_2^a for the Reaction Plane fit for π^0 triggers in the $11 - 14\mathrm{GeV}/cp_\mathrm{T}$ range, 30-50% centralEGA-triggered events.

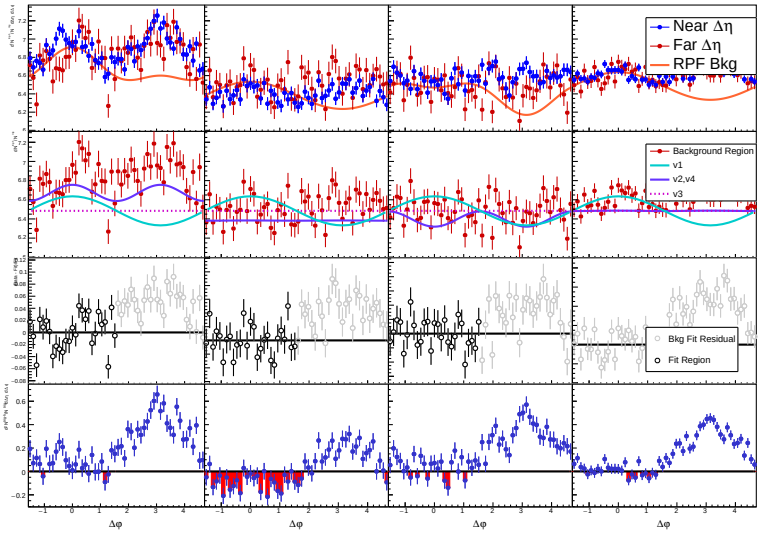

Figure G.8: 11-14 GeV/c π^0, 0.2-0.4 GeV/c $p_{\mathrm{T}}^{\mathrm{assoc}}$,30-50% central, EGA-triggered events

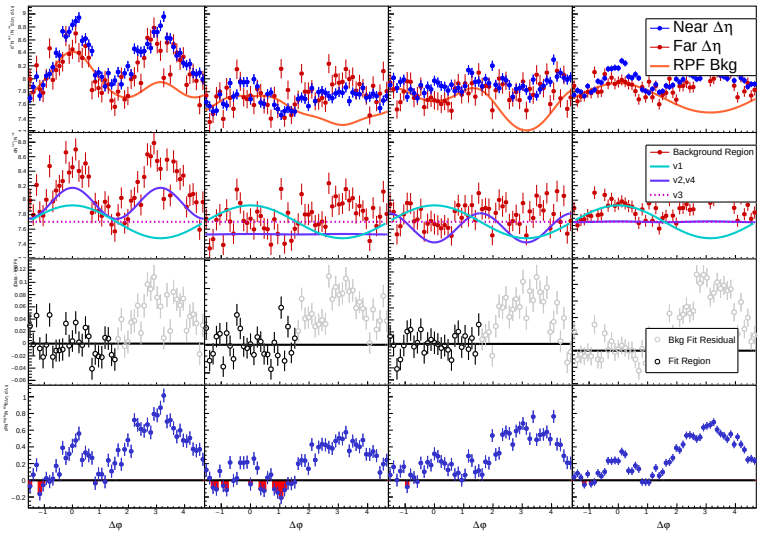

Figure G.9: 11-14 GeV/c π^0, 0.4-0.8 GeV/c $p_{\mathrm{T}}^{\mathrm{assoc}}$, 30-50% central, EGA-triggered events

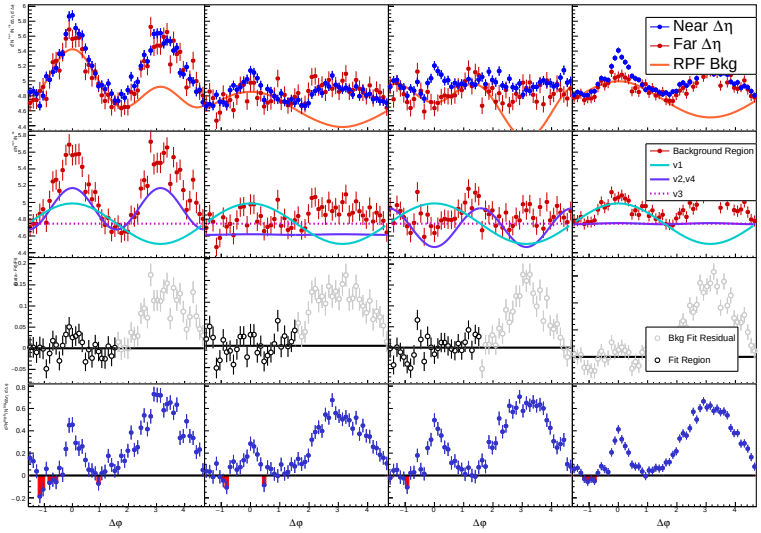

Figure G.10: 11-14 GeV/c π^0, 0.8-1.5 GeV/c $p_{\mathrm{T}}^{\mathrm{assoc}}$, 30-50% central, EGA-triggered events

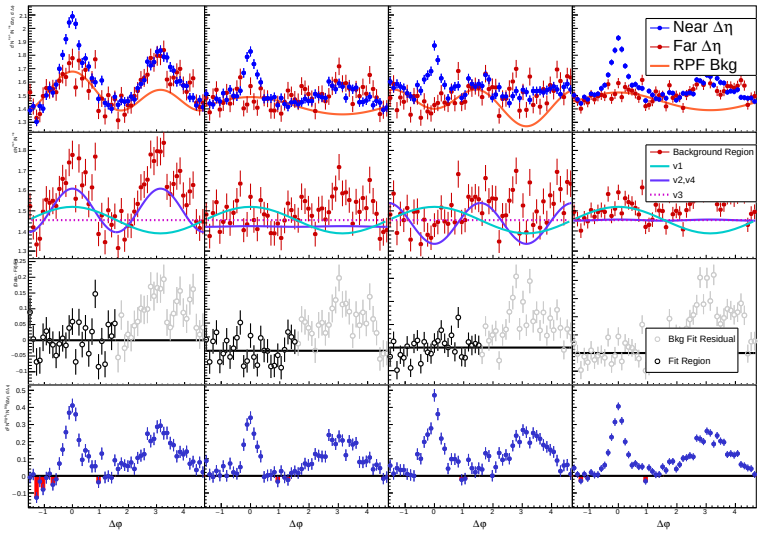

Figure G.11: 11-14 GeV/c π^0, 1.5-2.5 GeV/c $p_{\mathrm{T}}^{\mathrm{assoc}}$, 30-50% central, EGA-triggered events

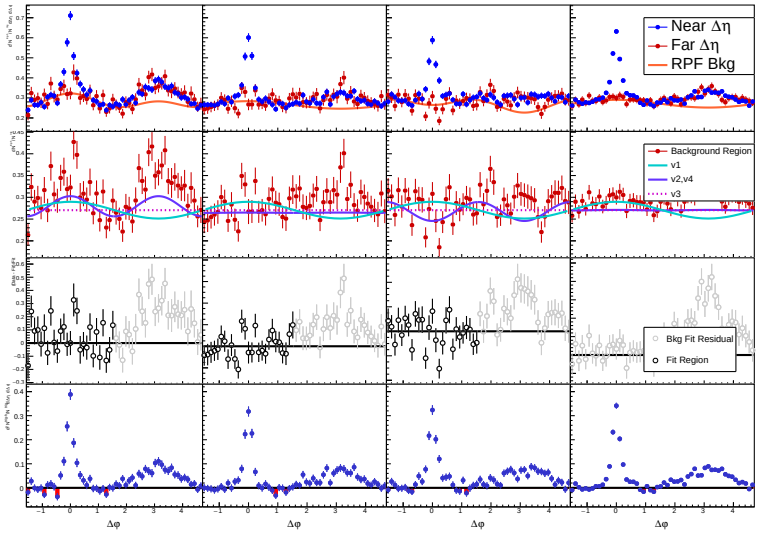

Figure G.12: 11-14 GeV/c π^0, 2.5-4 GeV/c $p_{\mathrm{T}}^{\mathrm{assoc}}$, 30-50% central, EGA-triggered events

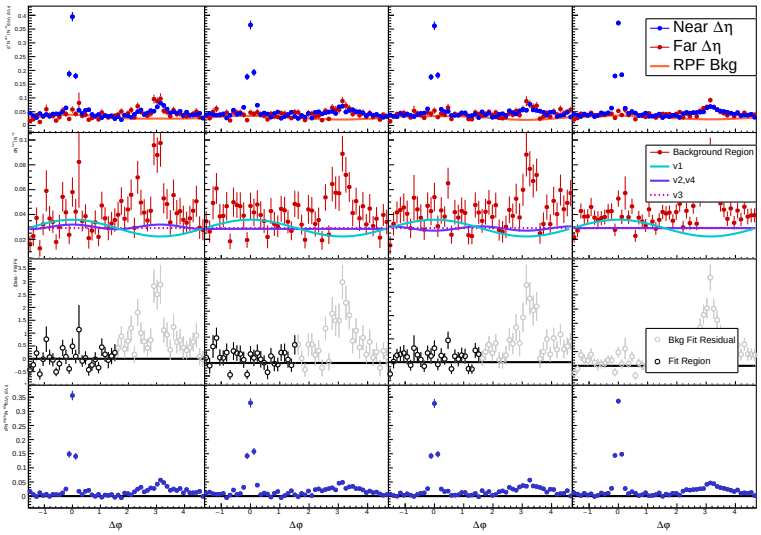

Figure G.13: 11-14 GeV/c π^0, 4-7 GeV/c $p_{\mathrm{T}}^{\mathrm{assoc}}$, 30-50% central, EGA-triggered events

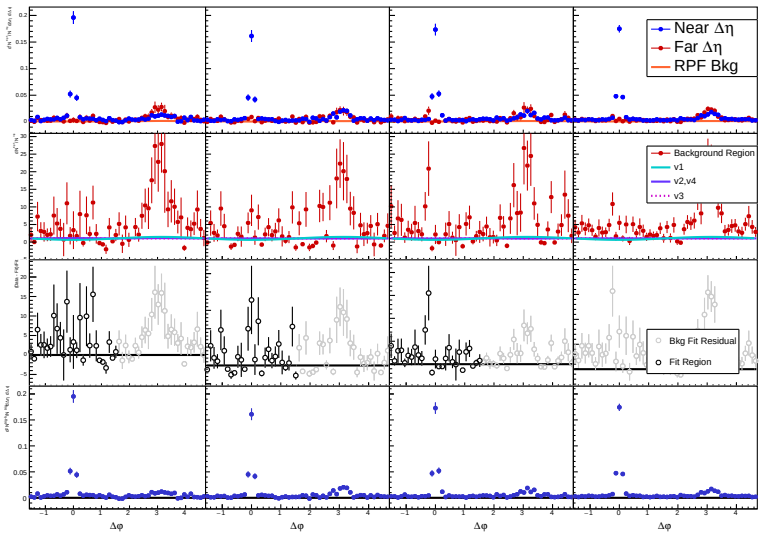

Figure G.14: 11-14 GeV/c π^0, 7-11 GeV/c $p_{\mathrm{T}}^{\mathrm{assoc}}$,30-50% central, EGA-triggered events

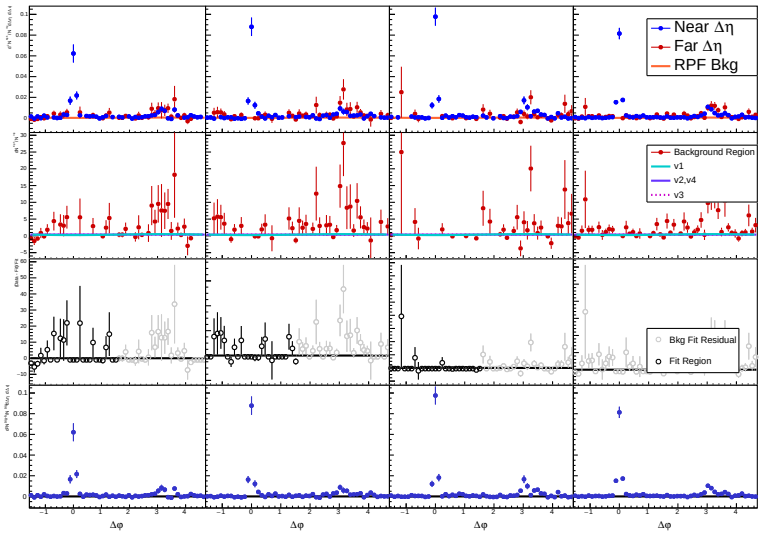

Figure G.15: 11-14 GeV/c π^0, 11-17 GeV/c $p_{\mathrm{T}}^{\mathrm{assoc}}$, 30-50% central, EGA-triggered events

G.1 Observables

G.1.1 Systematic uncertainties by source

The relative contributions of systematic uncertainty from different sources are provided for the near-side yields are provided in Figures G.16, G.17, and G.18, and those for the away-side yields are provided in Figures G.19, G.20, and G.21.

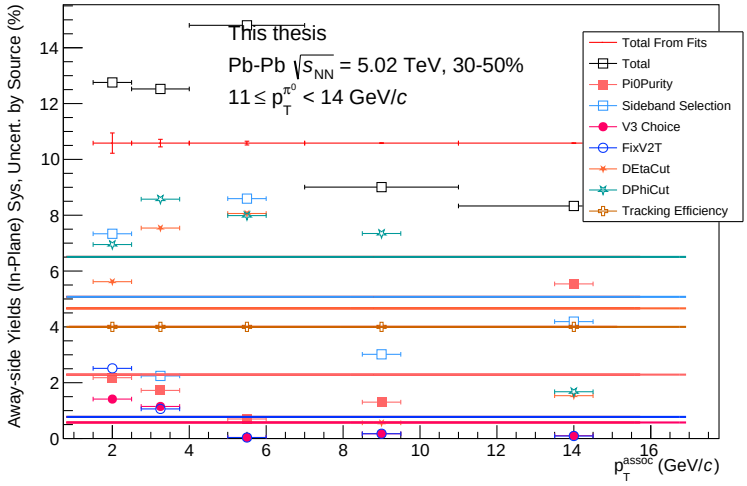

Figure G.16: Systematic uncertainties by source for near-side in-plane yields.

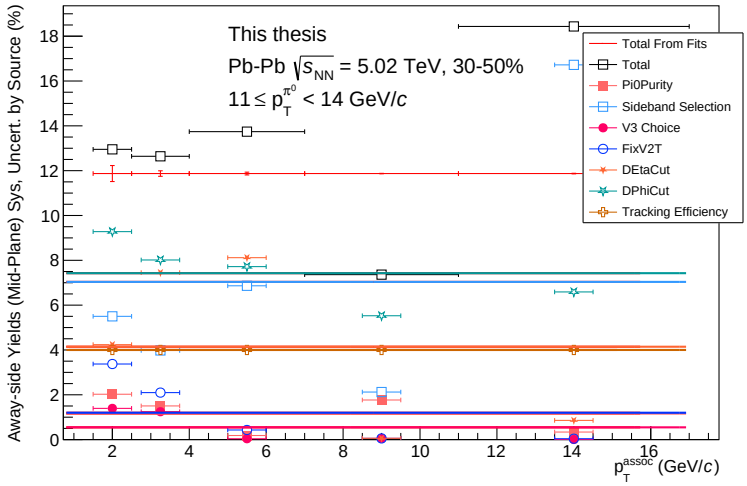

Figure G.17: Systematic uncertainties by source for near-side mid-plane yields.

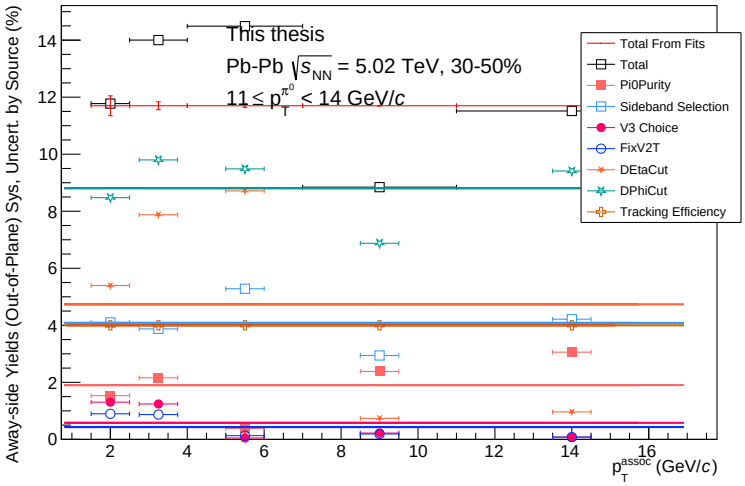

Figure G.18: Systematic uncertainties by source for near-side out-of-plane yields.

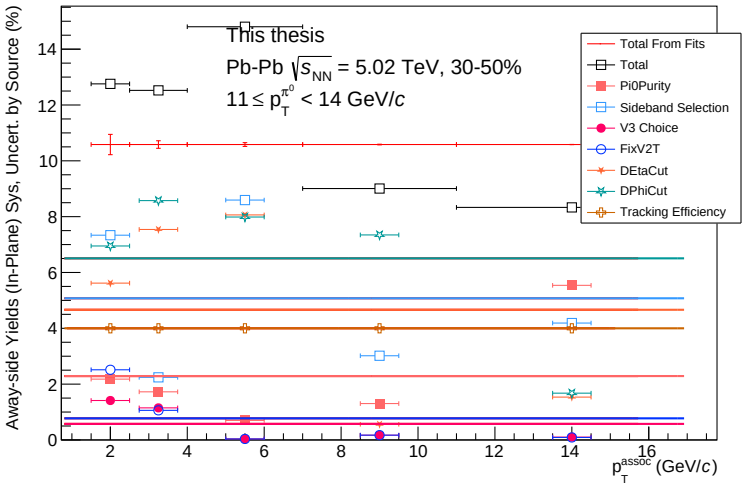

Figure G.19: Systematic uncertainties by source for away-side in-plane yields.

G.1.2 Yield Results by Event Plane

The raw yield results for the near-side yields in each event plane angle are provided in Figure G.22, while the away-side yields are provided in Figure G.23.

G.1.3 Yield Results by Event Plane with Model Comparisons

The raw yield results for the near-side yields with JEWEL model comparisons in each event plane angle are provided in Figure G.24, while those for the away-side are provided in Figure G.25.

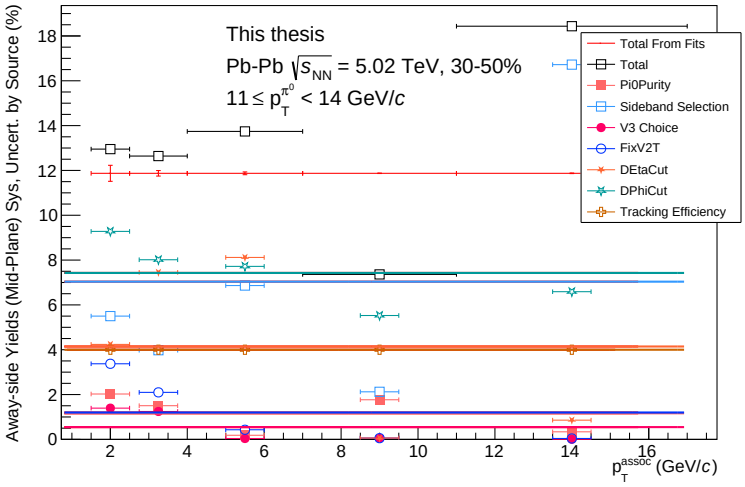

Figure G.20: Systematic uncertainties by source for away-side mid-plane yields.

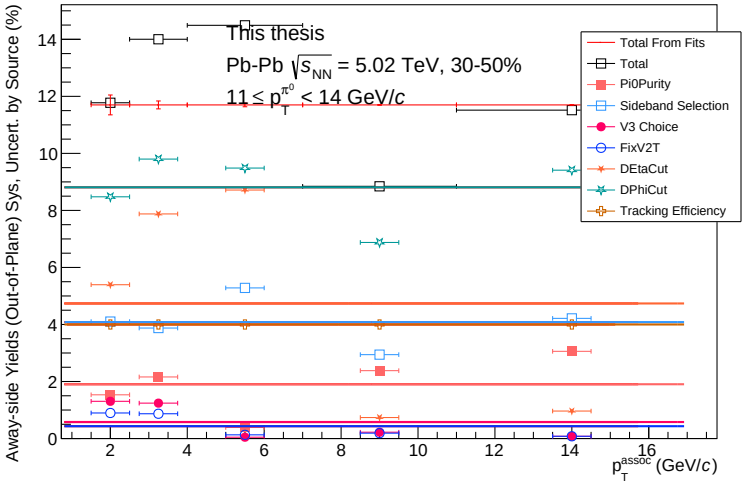

Figure G.21: Systematic uncertainties by source for away-side out-of-plane yields.

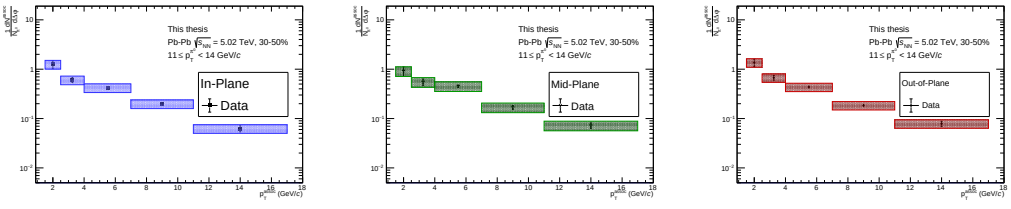

(a) In-plane (b) Mid-plane (c) Out-of-plane

Figure G.22: Nearside yields in each event plane bin.

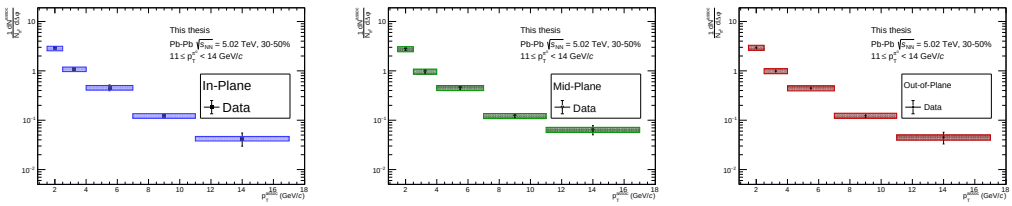

(a) In-plane (b) Mid-plane (c) Out-of-plane

Figure G.23: Awayside yields in each event plane bin.

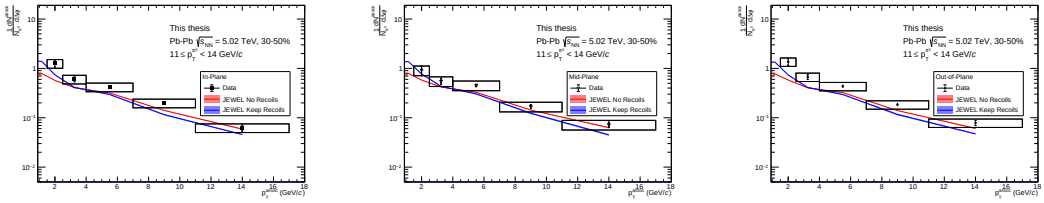

(a) In-plane (b) Mid-plane (c) Out-of-plane

Figure G.24: Nearside yields with JEWEL model comparison.

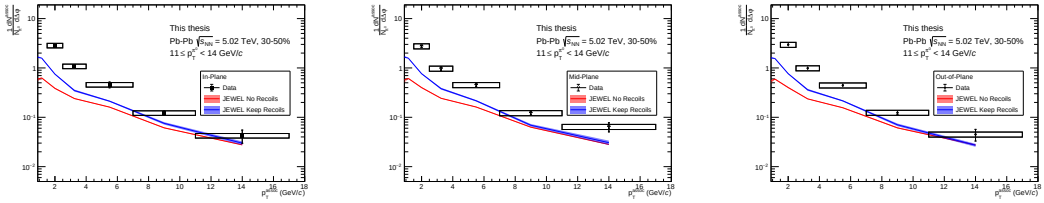

Figure G.25: Awayside yields in-plane, mid-plane, and out-of-plane with JEWEL comparison.

G.1.4 Sigma Widths by Event Plane

The σ width results for the near-side peaks in each event plane angle are provided in Figure G.26, while those for the away-side peaks are provided in Figure G.27.

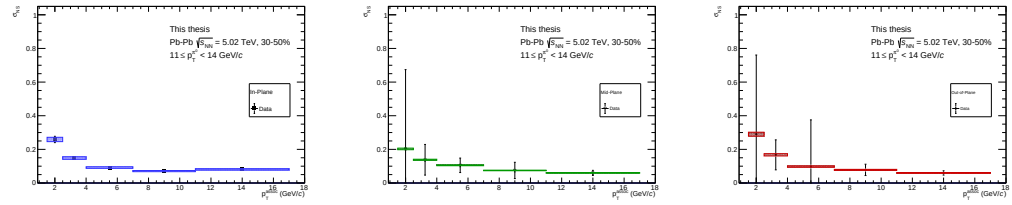

(a) In-plane (b) Mid-plane (c) Out-of-plane

Figure G.26: Near-side RMS widths in each event plane bin.

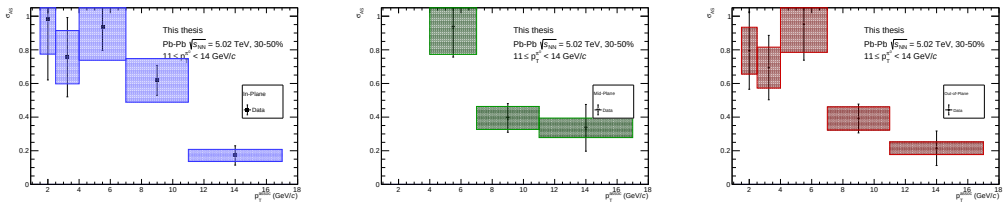

(a) In-plane (b) Mid-plane (c) Out-of-plane

Figure G.27: Awayside RMS widths in each event plane bin.

Appendix H

EMCal Trigger Simulation

All doctoral students in ALICE are required to provide 6 months of work for the collaboration, on tasks such as detector maintenance, calibration, and quality control. For this thesis, the service task was to update the simulation of the EMCal trigger in the ALICE code. Specifically, it was necessary to update the simulation for the updated geometry of the EMCal in run 2 of the LHC. Significant changes included the addition of the Dijet Calorimeter (DCal), extending the region needed to be simulated. Another change was a different geometric configuration of the trigger readout units within the EMCal supermodules. The final major change in run 2 was the implementation of a new underlying event subtraction method. In run 1, the impact of the underlying event, which could lower the effective threshold, was removed by subtracting energy based on the signal in the VZERO detectors. In the new algorithm, the median patch energy in each of the two sections of the EMCal are communicated to each other. This median patch energy is used to subtract the underlying event before testing the trigger threshold.

Another part of the task was implementing the proper simulation of noise in the trigger electronics. This is important for the EMCal Jet patch trigger, due to the size of the patch integrating more noise. This has the effect of lowering the effective threshold for the jet trigger and widening the trigger turn-on curve.

The accuracy of the trigger can be tested by measuring the trigger turn-on curve for neutral jets (jets composed entirely of EMCal clusters). By dividing the neutral jet spectra in events that activate the trigger by all events the efficiency of the trigger can be calculated. This can be done in simulation (done for this service task) and in data. This comparison was used to tune a noise parameter for the simulation, and the result with the final noise parameter is shown in figure H.1.

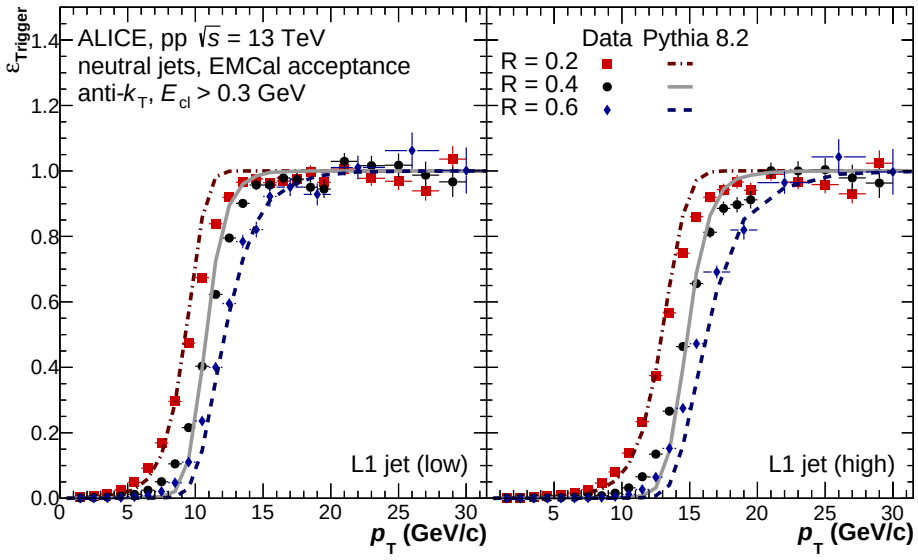

Figure H.1: Neutral jet turn-on curve for the EMCal Jet Patch trigger, with data drawn as markers and the results of the trigger simulation. Three different jet resolution parameters are used.

Bibliography

[1] P. Zyla, et al., Review of Particle Physics, PTEP 2020 (8) (2020) 083C01. doi:10.1093/ptep/ptaa104. vii, xv, 4, 28, 128, 129

[2] A. Bazavov, T. Bhattacharya, C. DeTar, H.-T. Ding, S. Gottlieb, R. Gupta, P. Hegde, U. Heller, F. Karsch, E. Laermann, L. Levkova, S. Mukherjee, P. Petreczky, C. Schmidt, C. Schroeder, R. Soltz, W. Soeldner, R. Sugar, M. Wagner, P. Vranas, Equation of state in (2+1)-flavor QCD, Physical Review D 90 (9). doi:10.1103/physrevd.90.094503.
URL http://dx.doi.org/10.1103/PhysRevD.90.094503 vii, 6

[3] T. Sakaguchi, Overview of latest results from PHENIX, PoS HardProbes2018 (2019) 035. doi:10.22323/1.345.0035. vii, 7

[4] T. Niida, Y. Miake, Signatures of QGP at RHIC and the LHC, AAPPS Bulletin 31 (2021) 12. doi:10.1007/s43673-021-00014-3.
URL https://doi.org/10.1007/s43673-021-00014-3 vii, 5, 6, 7, 11

[5] M. Connors, C. Nattrass, R. Reed, S. Salur, Jet measurements in heavy ion physics, Rev. Mod. Phys. 90 (2018) 025005. doi:10.1103/RevModPhys.90.025005.
URL https://link.aps.org/doi/10.1103/RevModPhys.90.025005 vii, 7, 8

[6] C. Gale, S. Jeon, B. Schenke, P. Tribedy, R. Venugopalan, Event-by-Event Anisotropic Flow in Heavy-ion Collisions from Combined Yang-Mills and Viscous Fluid Dynamics, Physical Review Letters 110 (1). doi:10.1103/physrevlett.110.012302.
URL http://dx.doi.org/10.1103/PhysRevLett.110.012302 vii, 8, 9

[7] A. Adare, S. Afanasiev, C. Aidala, N. N. Ajitanand, Y. Akiba, H. Al-Bataineh, J. Alexander, A. Al-Jamel, K. e. a. Aoki, Scaling Properties of Azimuthal Anisotropy in Au+Au and Cu+Cu Collisions at sNN=200 GeV, Physical Review Letters 98 (16). doi:10.1103/physrevlett.98.162301.
URL http://dx.doi.org/10.1103/PhysRevLett.98.162301 vii, 10

[8] J. Adam, D. Adamov, M. M. Aggarwal, G. A. Rinella, M. Agnello, N. Agrawal, Z. Ahammed, S. Ahmad, e. a. Ahn, S. U, Enhanced production of multi-strange hadrons in high-multiplicity protonproton collisions, Nature Physics 13 (6) (2017) 535539. doi:10.1038/nphys4111.
URL http://dx.doi.org/10.1038/nphys4111 vii, 11

[9] J. e. a. Adams, Evidence from $d + \mathrm{Au}$ measurements for final-state suppression of high-p_T hadrons in $\mathrm{Au} + \mathrm{Au}$ collisions at rhic, Phys. Rev. Lett. 91 (2003) 072304. doi:10.1103/PhysRevLett.91.072304.
URL https://link.aps.org/doi/10.1103/PhysRevLett.91.072304 vii, 13

[10] J. G. Milhano, K. C. Zapp, Origins of the di-jet asymmetry in heavy-ion collisions, The European Physical Journal C 76. doi:10.1140/epjc/s10052-016-4130-9.
URL https://doi.org/10.1140/epjc/s10052-016-4130-9 viii, 14, 15, 20, 155, 164

[11] L. Adamczyk, J. Adkins, G. Agakishiev, M. Aggarwal, Z. Ahammed, I. Alekseev, J. Alford, C. Anson, A. Aparin, D. Arkhipkin, E. Aschenauer, G. Averichev, A. Banerjee, et al., Jet-Hadron Correlations in sNN=200 GeV p+p and Central Au+Au Collisions, Physical Review Letters 112 (12). doi:10.1103/physrevlett.112.122301.
URL http://dx.doi.org/10.1103/PhysRevLett.112.122301 viii, xvii, 16, 17, 154

[12] J. Adam, D. Adamov, M. Aggarwal, G. Aglieri Rinella, M. Agnello, N. Agrawal, Z. Ahammed, S. Ahmad, S. Ahn, S. Aiola, A. Akindinov, S. Alam, D. Albuquerque, et al., Jet-like correlations with neutral pion triggers in pp and central PbPb collisions at 2.76 TeV, Physics Letters B 763 (2016) 238250. doi:10.1016/j.physletb.2016.10.048.
URL http://dx.doi.org/10.1016/j.physletb.2016.10.048 viii, 16, 17

[13] A. M. Sirunyan, A. Tumasyan, W. Adam, F. Ambrogi, E. Asilar, T. Bergauer, J. Brandstetter, E. Brondolin, M. Dragicevic, J. Er, A. Escalante Del Valle, M. Flechl, et al., Jet properties in PbPb and pp collisions at $\sqrt{s_{\mathrm{N\,N}}} = 5.02$ TeV, Journal of High Energy Physics 2018 (5). doi:10.1007/jhep05(2018)006.
URL http://dx.doi.org/10.1007/JHEP05(2018)006 viii, 19

[14] S. Acharya, et al., Jet-hadron correlations measured relative to the second order event plane in Pb-Pb collisions at $\sqrt{s_{NN}} = 2.76\,\mathrm{TeV}$, Phys. Rev. C 101 (2020) 064901. doi:10.1103/PhysRevC.101.064901.
URL https://link.aps.org/doi/10.1103/PhysRevC.101.064901 viii, xiii, 19, 20, 96, 126, 155, 163

[15] A. Collaboration, Measurements of azimuthal anisotropies of jet production in Pb+Pb collisions at $\sqrt{s_{NN}} = 5.02$ TeV with the ATLAS detector (2021). arXiv:2111.06606. viii, 20, 21

[16] P. Mouche, Overall view of the LHC. Vue d'ensemble du LHCGeneral Photo.
URL https://cds.cern.ch/record/1708847 viii, 23

[17] T. A. Collaboration, The ALICE experiment at the CERN LHC, Journal of Instrumentation 3 (08) (2008) S08002–S08002. doi:10.1088/1748-0221/3/08/s08002.
URL https://doi.org/10.1088/1748-0221/3/08/s08002 viii, 24, 27, 29, 30

[18] J. Allen, C. Bernard, O. Bourrion, M. Chala, M. Del Franio, O. Driga, F. Fichera, N. Giudice, A. Grimaldi, P. Laloux, Q. Li, F. Librizzi, G. Liu, C. Loizides, G. Marcotte, S. Muggeo, J. F. Muraz, F. Noto, A. Orlandi, V. Petrov, F. Pompei, W. Qian, J. Rasson, S. Sakai, M. Salemi, M. Sharma, V. Sparti, J. S. Stutzmann, A. Timmons, A. Viticchie, M. Wang, X. Xiang, F. Zhang, J. Zhou, X. Zhu, ALICE DCal: An Addendum to the EMCal Technical Design Report Di-Jet and Hadron-Jet correlation measurements in ALICE, Tech. rep. (Jun 2010).
URL http://cds.cern.ch/record/1272952 ix, 29, 31

[19] T. A. collaboration, Performance of the ALICE VZERO system, Journal of Instrumentation 8 (10) (2013) P10016P10016. doi:10.1088/1748-0221/8/10/p10016.
URL http://dx.doi.org/10.1088/1748-0221/8/10/P10016 ix, 31, 32

[20] J. Adam, D. Adamov, M. Aggarwal, G. Aglieri Rinella, M. Agnello, N. Agrawal, Z. Ahammed, Centrality Dependence of the Charged-Particle Multiplicity Density at Midrapidity in Pb-Pb Collisions at sNN = 5.02 TeV, Physical Review Letters 116 (22). doi:10.1103/physrevlett.116.222302.
URL http://dx.doi.org/10.1103/PhysRevLett.116.222302 ix, 38

[21] G. Conesa Balbastre, Study and emulation of cell energy cross-talk in EMCalInternal ALICE analysis note 837.
URL https://alice-notes.web.cern.ch/node/837 x, 45

[22] S. Acharya, F. T.-. Acosta, D. Adamov, J. Adolfsson, M. M. Aggarwal, G. Aglieri Rinella, M. Agnello, N. Agrawal, Z. Ahammed, S. U. Ahn, S. Aiola, A. Akindinov, et al., Energy dependence and fluctuations of anisotropic flow in Pb-Pb collisions at $\sqrt{s_{\rm NN}} = 5.02$ and 2.76 TeV, Journal of High Energy Physics 2018 (7). doi:10.1007/jhep07(2018)103.
URL http://dx.doi.org/10.1007/JHEP07(2018)103 xiv, 111

[23] R. Ehlers, reactionplanefit - RPF implementation (Nov. 2018). doi:10.5281/zenodo.1599239.
URL https://doi.org/10.5281/zenodo.1599239 xiv, 98, 113, 163

[24] R. K. Elayavalli, K. C. Zapp, Simulating V+jet processes in heavy ion collisions with JEWEL, The European Physical Journal C 76 (12). doi:10.1140/epjc/s10052-016-4534-6.
URL http://dx.doi.org/10.1140/epjc/s10052-016-4534-6 xvii, 151

[25] J. e. a. Adam, Centrality Dependence of the Charged-Particle Multiplicity Density at Midrapidity in Pb-Pb Collisions at $\sqrt{s_{NN}} = 5.02$ TeV, Phys. Rev. Lett. 116 (2016) 222302. doi:10.1103/PhysRevLett.116.222302.
URL https://link.aps.org/doi/10.1103/PhysRevLett.116.222302 xxii, 108

[26] T. A. Trainor, Zero yield at minimum (ZYAM) method and v2: Underestimating jet yields from dihadron azimuth correlations, Physical Review C 81 (1). doi:10.1103/physrevc.81.014905.
URL http://dx.doi.org/10.1103/PhysRevC.81.014905 xxii, 136, 137

[27] M. E. Peskin, D. V. Schroeder, An introduction to quantum field theory, Westview, Boulder, CO, 1995, includes exercises.
URL https://cds.cern.ch/record/257493 3

[28] P. Skands, Introduction to QCD (2017). arXiv:1207.2389. 5

[29] J. Bellm, et al., Herwig 7.0/Herwig++ 3.0 release note, Eur. Phys. J. C 76 (4) (2016) 196. arXiv:1512.01178, doi:10.1140/epjc/s10052-016-4018-8. 5

[30] T. Gleisberg, S. Hoeche, F. Krauss, A. Schalicke, S. Schumann, J.-C. Winter, SHERPA 1.alpha, a proof-of-concept version, JHEP 02 (2003) 056. 28 p, comments: 28 pages, three figures. doi:10.1088/1126-6708/2004/02/056.
URL https://cds.cern.ch/record/686287 5

[31] N. Cabibbo, G. Parisi, Exponential hadronic spectrum and quark liberation, Physics Letters B 59 (1) (1975) 67–69. doi:https://doi.org/10.1016/0370-2693(75)90158-6.
URL https://www.sciencedirect.com/science/article/pii/0370269375901586 6

[32] P. Shukla, Glauber model for heavy ion collisions from low energies to high energies (2001). doi:10.48550/ARXIV.NUCL-TH/0112039.
URL https://arxiv.org/abs/nucl-th/0112039 6

[33] P. Koch, B. Mller, J. Rafelski, From strangeness enhancement to quarkgluon plasma discovery, International Journal of Modern Physics A 32 (31) (2017) 1730024. doi:10.1142/s0217751x17300241.
URL http://dx.doi.org/10.1142/S0217751X17300241 10, 12

[34] T. Matsui, H. Satz, J/ψ Suppression by Quark-Gluon Plasma Formation, Phys. Lett. B 178 (1986) 416–422. doi:10.1016/0370-2693(86)91404-8. 10

[35] A. Majumder, M. van Leeuwen, The theory and phenomenology of perturbative QCD based jet quenching, Progress in Particle and Nuclear Physics 66 (1) (2011) 4192. doi:10.1016/j.ppnp.2010.09.001.
URL http://dx.doi.org/10.1016/j.ppnp.2010.09.001 12

[36] X.-N. Wang, M. Gyulassy, M. Plumer, The LPM effect in QCD and radiative energy loss in a quark gluon plasma, Phys. Rev. D 51 (1995) 3436–3446. arXiv:hep-ph/9408344, doi:10.1103/PhysRevD.51.3436. 13

[37] A. Adare, et al., Photon-hadron jet correlations in $p + p$ and $\mathrm{Au} + \mathrm{Au}$ collisions at $\sqrt{s_{NN}} = 200$ GeV, Phys. Rev. C 80 (2009) 024908. doi:10.1103/PhysRevC.80.024908.
URL https://link.aps.org/doi/10.1103/PhysRevC.80.024908 18

[38] U. Acharya, A. Adare, S. Afanasiev, C. Aidala, N. N. Ajitanand, Y. Akiba, R. Akimoto, H. Al-Bataineh, J. Alexander, H. Al-Taani, A. Angerami, K. Aoki, N. Apadula, et al., Measurement of jet-medium interactions via direct photon-hadron correlations in Au+Au and d+Au collisions at sNN = 200 GeV, Physical Review C 102 (5). doi:10.1103/physrevc.102.054910.
URL http://dx.doi.org/10.1103/PhysRevC.102.054910 18, 61

[39] C.-P. Wong, PHENIX results of π^0-hadron correlations, PoS High-pT2019 (2020) 004. doi:10.22323/1.355.0004. 18

[40] B. I. Abelev, M. M. Aggarwal, Z. A. et al, Parton energy loss in heavy-ion collisions via direct-photon and charged-particle azimuthal correlations, Physical Review C 82 (3). doi:10.1103/physrevc.82.034909.
URL https://doi.org/10.1103%2Fphysrevc.82.034909 18

[41] L. Adamczyk, J. Adkins, G. A. et al, Jet-like correlations with direct-photon and neutral-pion triggers at sNN=200 GeV, Physics Letters B 760 (2016) 689–696. doi:https://doi.org/10.1016/j.physletb.2016.07.046.
URL https://www.sciencedirect.com/science/article/pii/S0370269316303872 18

[42] N. Sharma, J. Mazer, M. Stuart, C. Nattrass, Background subtraction methods for precision measurements of di-hadron and jet-hadron correlations in heavy ion collisions, Phys. Rev. C 93 (2016) 044915. doi:10.1103/PhysRevC.93.044915.

URL https://link.aps.org/doi/10.1103/PhysRevC.93.044915 19, 96

[43] G. Aad, T. Abajyan, e. a. B. Abbott, Observation of a new particle in the search for the standard model higgs boson with the atlas detector at the lhc, Physics Letters B 716 (1) (2012) 1–29. doi:https://doi.org/10.1016/j.physletb.2012.08.020.
URL https://www.sciencedirect.com/science/article/pii/S037026931200857X 23

[44] S. Chatrchyan, V. Khachatryan, e. a. A.M. Sirunyan, Observation of a new boson at a mass of 125 gev with the cms experiment at the lhc, Physics Letters B 716 (1) (2012) 30–61. doi:https://doi.org/10.1016/j.physletb.2012.08.021.
URL https://www.sciencedirect.com/science/article/pii/S0370269312008581 23

[45] T. D. and, Centrality and collision event-plane determination in ALICE at the LHC, Journal of Physics: Conference Series 798 (2017) 012061. doi:10.1088/1742-6596/798/1/012061.
URL https://doi.org/10.1088/1742-6596/798/1/012061 26

[46] S. Acharya, F. T.-. Acosta, D. Adamov, J. Adolfsson, e. a. Aggarwal, Neutral pion and meson production at midrapidity in Pb-Pb collisions at sNN=2.76 tev, Physical Review C 98 (4). doi:10.1103/physrevc.98.044901.
URL http://dx.doi.org/10.1103/PhysRevC.98.044901 57

[47] N. van Eijndhoven, W. Wetzels, In-event background and signal reconstruction for two-photon invariant-mass analyses, Nuclear Instruments and Methods in Physics Research Section A: Accelerators, Spectrometers, Detectors and Associated Equipment 482 (1) (2002) 513–519. doi:https://doi.org/10.1016/S0168-9002(01)01558-3.
URL https://www.sciencedirect.com/science/article/pii/S0168900201015583 65

[48] Recommendations for the Modeling of Smooth Backgrounds, Tech. rep., CERN, Geneva, all figures including auxiliary figures are available at https://atlas.web.cern.ch/Atlas/GROUPS/PHYSICS/PUBNOTES/ATL-PHYS-PUB-2020-028 (Nov 2020).
URL https://cds.cern.ch/record/2743717 65

[49] S. Acharya, et al., Jet-hadron correlations measured relative to the second order event plane in pb-pb collisions at $\sqrt{s_{NN}} = 2.76\,\mathrm{TeV}$, Phys. Rev. C 101 (2020) 064901. doi:10.1103/PhysRevC.101.064901.
URL https://link.aps.org/doi/10.1103/PhysRevC.101.064901 95

[50] S. Acharya, D. Adamová, A. Adler, J. Adolfsson, M. M. Aggarwal, Measurements of inclusive jet spectra in pp and central Pb-Pb collisions at $\sqrt{s_{NN}} = 5.02\,\mathrm{TeV}$, Phys. Rev. C 101 (2020) 034911. doi:10.1103/PhysRevC.101.034911.
URL https://link.aps.org/doi/10.1103/PhysRevC.101.034911 108

[51] K. Zapp, Jewel 2.0.0: directions for use, The European Physical Journal C 74 (2). doi:10.1140/epjc/s10052-014-2762-1.
URL http://dx.doi.org/10.1140/epjc/s10052-014-2762-1 126, 127

[52] K. C. Zapp, F. Krauss, U. A. Wiedemann, A perturbative framework for jet quenching, Journal of High Energy Physics 2013 (3). doi:10.1007/jhep03(2013)080.
URL http://dx.doi.org/10.1007/JHEP03(2013)080 126, 127

[53] R. Ehlers, Jet-Hadron Correlations Measured in PbPb Collisions at sNN = 5.02 TeV with ALICE, Ph.D. thesis, Yale University, New Haven, CT (2020). 126, 146

[54] R. Kunnawalkam Elayavalli, K. C. Zapp, Medium response in JEWEL and its impact on jet shape observables in heavy ion collisions, Journal of High Energy Physics 2017 (7). doi:10.1007/jhep07(2017)141.
URL http://dx.doi.org/10.1007/JHEP07(2017)141 128

[55] M. Cacciari, G. P. Salam, G. Soyez, FastJet user manual, The European Physical Journal C 72 (3). doi:10.1140/epjc/s10052-012-1896-2.
URL http://dx.doi.org/10.1140/epjc/s10052-012-1896-2 133

[56] C. Nattrass, N. Sharma, J. Mazer, M. Stuart, A. Bejnood, Disappearance of the Mach cone in heavy-ion collisions, Physical Review C 94 (1). doi:10.1103/physrevc.94.011901.
URL http://dx.doi.org/10.1103/PhysRevC.94.011901 136

[57] J. H. Putschke, K. Kauder, E. Khalaj, A. Angerami, S. A. Bass, S. Cao, J. Coleman, L. Cunqueiro, T. Dai, L. Du, H. Elfner, D. Everett, W. Fan, R. J. Fries, C. Gale, Y. He, U. Heinz, B. V. Jacak, P. M. Jacobs, S. Jeon, W. Ke, M. K. I. au2, A. Kumar, T. Luo, A. Majumder, M. McNelis, J. Mulligan, C. Nattrass, D. Oliinychenko, D. Pablos, L. G. Pang, C. Park, J. F. Paquet, G. Roland, B. Schenke, L. Schwiebert, C. Shen, C. Sirimanna, R. A. Soltz, Y. Tachibana, G. Vujanovic, X. N. Wang, R. L. Wolpert, Y. Xu, Z. Yang, The jetscape framework (2019). arXiv:1903.07706. 165

[58] J. Casalderrey-Solana, D. C. Gulhan, J. G. Milhano, D. Pablos, K. Rajagopal, Predictions for boson-jet observables and fragmentation function ratios from a hybrid strong/weak coupling model for jet quenching, Journal of High Energy Physics 2016 (3). doi:10.1007/jhep03(2016)053.
URL http://dx.doi.org/10.1007/JHEP03(2016)053 166